



Doctorate Course in:

Energy and Environment Engineering Science

XXXII cycle

Thesis Title

“Pd/CeO₂ Methane Abatement Catalysts Prepared by
Solvent-free Mechano-chemical Synthesis”

PhD student

Maila Danielis

Advisor

Prof. Carla de Leitenburg

Co-advisors

Prof. Alessandro Trovarelli
Dr. Sara Colussi

Year 2020

The following dissertation was reviewed by:

Prof. Emiel J. M. Hensen, Eindhoven University of Technology

Dr. Sanjaya D. Senanayake, Brookhaven National Laboratory

Defense committee members:

Prof. Samir Bensaid, Politecnico di Torino

Dr. Davide Ferri, Paul Scherrer Institut

Abstract

The current socio-economic global environment strongly promotes the research towards sustainable energy generation and green chemical processes to reduce the anthropogenic footprint on Earth. In general, most of the greenhouse gases (GHGs) emissions are generated by energy production processes, which are required to satisfy the needs of the worldwide growing population and increased economic development of major countries. As such, their reduction is a complex issue that requires technical, economic and social solutions, feasible both in the short and in the long term. While renewable energy solutions are studied and developed, aiming at the substitution of fossil fuels and a zero-carbon emission target in the long term, a more careful utilization of the currently available fuel resources and the optimization of emissions control technology are measures that can be presently undertaken to improve air quality and reduce the environmental impact of human activities. Focus of this dissertation are improved after-treatment technologies for natural gas fueled vehicles (NGVs) and cleaner technologies for catalysts production. The results of my research will be reported in the following as collection of published or submitted papers, including the work in progress and future developments in the final chapters.

A novel solventless mechano-chemical synthesis was evaluated for the preparation of catalysts for unburned methane abatement in exhaust gases of natural gas fueled vehicles (NGVs). These vehicles, in fact, represent a temporary yet straightforward alternative to traditional gasoline and diesel fueled vehicles, enabling the reduction of CO₂, soot, NO_x and SO_x emissions from internal combustion engines by substituting gasoline and diesel with a cleaner fossil fuel, natural gas. Among the technical challenges arising from the transition, the release of unburned methane at tailpipe is cause of worry due to its global warming potential, ~25 times higher than CO₂, that ought to be controlled with specific emission control technology. In this work we focused on catalysts comprising palladium and ceria for the catalytic abatement of CH₄, a combination which was already known as promising for complete methane oxidation.

By preparing Pd/CeO₂ catalysts by the innovative mild milling procedure, novel materials characterized by a core-shell structure were obtained, displaying improved activity and stability compared to their state-of-the-art counterparts prepared by incipient wetness

impregnation. The enhanced Pd-Ce nanoscale interaction was characterized in depth and correlated to the improved methane oxidation activity (Chapter 3). The unique Pd-CeO₂ interplay and its role in methane combustion was further investigated by analyzing the effect of milling parameters on the obtained Pd-Ce interaction and palladium morphology (Chapter 4). Indeed, the unique synergy between palladium and ceria makes mild milling conditions both necessary and sufficient to produce nanoscale interaction between Pd and Ce ions, while in the literature mostly high energy milling processes are reported to induce alloying and/or strong interaction between different compounds.

The possibility of using palladium salt precursors was also explored, analyzing the obtained palladium species and the thermal treatments needed for synthesis optimization (Chapter 5). As suggested by the latest findings, a mixture of Pd⁰/Pd²⁺ species on the ceria surface proved to be the most active for the catalytic oxidation of methane, which could be achieved by using palladium acetate as Pd precursor and subsequently treating it under low oxygen partial pressure. Moreover, by using Pd(OAc)₂ instead of Pd black, an increased palladium content could be successfully deposited on ceria, thus achieving industrial requirements for methane abatement catalytic converters. Due to their industrial relevance, these materials were characterized by means of advanced *in-situ* and *ex-situ* techniques, with the aim of identifying the Pd-Ce active phases for CH₄ activation. The advanced characterization has been possible thanks to the collaboration with the Catalysis: Reactivity and Structure (CRS) group of the Chemistry Division at Brookhaven National Laboratory (BNL), Upton (NY). Tests were performed both in lean methane conditions (Chapter 6) and in reducing dry-reforming conditions (Chapter 7). Under methane oxidation conditions, a combination of Pd⁰/Pd²⁺ species appeared as extremely stable on the ceria surface and enabled methane oxidation at lower temperatures compared to samples prepared by wet synthesis, likely due to the mechanical stresses developed during milling and the resulting stabilized nanoscale environment. Under dry reforming conditions, the enhanced Pd-Ce interaction promoted by milling resulted in increased reactivity of metallic Pd species, undergoing rapid transitions during *in-situ* methane activation tests and displaying increased activity and stability in reducing environment compared to the impregnated reference sample.

Feasibility of the industrial application was studied by washcoating monoliths with Pd/CeO₂ powders prepared by dry milling and testing them in methane oxidation and steam reforming reactions, before and after simulated aging (Chapter 8). This part has been carried out in collaboration with Ford Motor Company, Dearborn (MI). While preliminary results

showed an activity improvement, the aging process and the limited composition (compared to fully formulated Pd-Rh/CeO₂-ZrO₂-Al₂O₃ three-way catalysts) hindered a real comparison. Nevertheless, considering the outlook of the European Union on sustainable processes, a comparable catalytic activity obtained by a cleaner and faster manufacturing process could represent an interesting alternative for catalysts production. Further studies, which lay outside of the scope of this dissertation, would be needed to optimize the scale-up of the synthesis and its application to fully formulated catalysts.

Given the scope of the study, i.e. catalytic converters for after-treatment applications, a support oxide able to withstand high temperature oscillations was necessary, thus catalysts were prepared using polycrystalline ceria calcined at temperatures higher than 1173 K prior to synthesis. In the first chapters of this dissertation (Chapter 3 to 8) activity results for methane activation showed that the enhanced activity of dry milled catalysts is due to an improved Pd-Ce interaction at the nanoscale with a combination of Pd⁰/Pd²⁺ species stabilized in and on the outermost layers of the ceria surface. To analyze the effect of the exposed ceria facets on this interaction, additional samples were prepared on ceria nanoparticles with defined morphology (Chapter 9). Preliminary results indicate that the preferential exposure of specific ceria planes (notably {100} and {110} of ceria nanocubes and nanorods, respectively) affects negatively the methane oxidation activity and influences the palladium spreading mechanism occurring during the dry milling process. Further investigation will be needed to understand the underlying motivations for poorer methane oxidation performance as well as the effect of exposed planes on the mechano-chemical synthesis.

In conclusion, a solventless, one-step mild milling synthesis was developed for the efficient preparation of methane oxidation Pd/CeO₂ catalysts. The enhanced Pd-Ce interaction, boosted by their synergistic properties and defects created by the shear stresses developed during milling, resulted in a promotional effect for methane activation, both in lean and rich methane conditions, favoring the application of these novel Pd/CeO₂ catalysts to the abatement of methane emitted from natural gas fueled vehicles. The fundamental approach followed in this thesis work allows for further studies of the prepared Pd/CeO₂ based materials in other methane activation reactions and for the application of the developed technique to other classes of materials.

Acknowledgements

I would like to thank Prof. Alessandro Trovarelli, Prof. Carla de Leitenburg and Dr. Sara Colussi for the inestimable mentoring and guidance throughout my PhD research work.

I would like to acknowledge the skilled contributions of Prof. Jordi Llorca, Dr. Luis Soler and Dr. Nuria J. Divins from Universitat Politecnica de Catalunya, Prof. José Rodriguez, Dr. Sanjaya D. Senanayake and Dr. Luis E. Betancourt from the CRS Group at the Chemistry Division of Brookhaven National Laboratory, Dr. Jeffrey Hepburn and Dr. Giovanni Cavataio from Ford Motor Company. The quality of this thesis wouldn't be the same without their help and assistance.

I would like to thank Ford Motor Company and Regione Friuli Venezia Giulia for financial support under the 2014-2195R URP Award “Three-way catalyst materials for compressed natural gas vehicles” and for PhD fellowship founding under the Operating Program of the European Social Fund 2014/2020.

Last but not least, I need to thank everyone who accompanied me in this journey, my family, friends and colleagues. I could not have done it without you. Thank you.

Index

ABSTRACT	I
-----------------	----------

ACKNOWLEDGEMENTS	IV
-------------------------	-----------

LIST OF ABBREVIATIONS	IX
------------------------------	-----------

1 BACKGROUND AND MOTIVATION	1
------------------------------------	----------

1.1 OVERVIEW	1
--------------	---

1.2 NATURAL GAS AS A TRANSPORTATION FUEL	5
------------------------------------------	---

1.2.1 MARINE APPLICATIONS	8
---------------------------	---

1.2.2 CURRENT EMISSION CONTROL TECHNOLOGY	9
-------------------------------------------	---

1.3 MECHANO-CHEMICAL SYNTHESIS	12
--------------------------------	----

1.3.1 MILLING EQUIPMENT	13
-------------------------	----

1.4 REFERENCES	16
----------------	----

2 EXPERIMENTAL METHODS	25
-------------------------------	-----------

2.1 SYNTHESIS OF CATALYTIC MATERIALS	25
--------------------------------------	----

2.1.1 SYNTHESIS OF SUPPORT OXIDES	25
-----------------------------------	----

2.1.2 PALLADIUM-BASED CATALYSTS	26
---------------------------------	----

2.2 CHARACTERIZATION	27
----------------------	----

2.2.1 SURFACE AREA AND PORE SIZE MEASUREMENTS	27
-----------------------------------------------	----

2.2.2 TEMPERATURE PROGRAMMED OXIDATION (TPO)	28
----------------------------------------------	----

2.2.3 TEMPERATURE PROGRAMMED REDUCTION (TPR)	28
----------------------------------------------	----

2.2.4 THERMO-GRAVIMETRIC ANALYSIS (TGA)	28
-----------------------------------------	----

2.2.5 TRANSMISSION ELECTRON MICROSCOPY (TEM)	28
----------------------------------------------	----

2.2.6 X-RAY PHOTOELECTRON SPECTROSCOPY (XPS)	29
----------------------------------------------	----

2.2.7 X-RAY DIFFRACTION ANALYSIS	29
----------------------------------	----

2.2.8 DIFFUSE REFLECTANCE INFRARED FOURIER TRANSFORM SPECTROSCOPY (DRIFTS)	30
----------------------------------------------------------------------------	----

2.2.9 RAMAN SPECTROSCOPY	31
--------------------------	----

2.2.10 ADDITIONAL CHARACTERIZATION	31
------------------------------------	----

2.3	CATALYTIC ACTIVITY	31
2.3.1	METHANE OXIDATION LIGHT-OFF ACTIVITY	31
2.3.2	METHANE OXIDATION STABILITY TESTS	33
2.3.3	METHANE OXIDATION REACTION RATE MEASUREMENTS	33
2.3.4	STEAM REFORMING (SR)	34
2.3.5	DRY REFORMING OF METHANE (DRM)	34
2.4	REFERENCES	35

3 OUTSTANDING METHANE OXIDATION PERFORMANCE OF Pd-EMBEDDED CERIA CATALYSTS PREPARED BY A ONE-STEP DRY BALL-MILLING METHOD **37**

	ABSTRACT	37
3.1	INTRODUCTION	38
3.2	EXPERIMENTAL	39
3.3	RESULTS AND DISCUSSION	39
3.4	CONCLUSIONS	54
3.5	REFERENCES	55

4 THE EFFECT OF MILLING PARAMETERS ON THE MECHANO-CHEMICAL SYNTHESIS OF Pd-CeO₂ METHANE OXIDATION CATALYSTS **58**

	ABSTRACT	58
4.1	INTRODUCTION	59
4.2	EXPERIMENTAL	60
4.3	RESULTS AND DISCUSSION	61
4.4	CONCLUSIONS	71
4.5	REFERENCES	73

5 THE ROLE OF PALLADIUM SALT PRECURSORS IN Pd-PdO/CeO₂ METHANE OXIDATION CATALYSTS PREPARED BY DRY MILLING **77**

	ABSTRACT	77
5.1	INTRODUCTION	78
5.2	EXPERIMENTAL	78
5.3	RESULTS AND DISCUSSION	79
5.4	CONCLUSIONS	92
5.5	REFERENCES	94

**6 Pd/CeO₂ CATALYSTS PREPARED BY MILLING PD ACETATE AND CERIA:
METHANE OXIDATION ACTIVITY, NANOSCALE MORPHOLOGY AND *IN-SITU***

<u>CHARACTERIZATION</u>	97
ABSTRACT	97
6.1 INTRODUCTION	98
6.2 EXPERIMENTAL	99
6.3 RESULTS	100
6.3.1 PHYSICO-CHEMICAL CHARACTERIZATION AND CATALYTIC ACTIVITY	100
6.3.2 HRTEM CHARACTERIZATION	106
6.3.3 TEMPERATURE PROGRAMMED OXIDATION (TPO) AND REDUCTION (TPR) TESTS	109
6.3.4 <i>IN-SITU</i> SYNCHROTRON XRD	112
6.3.5 RAMAN SPECTROSCOPY	118
6.3.6 <i>IN-SITU</i> DRIFTS	120
6.3.7 AMBIENT PRESSURE XPS	124
6.4 DISCUSSION	126
6.5 CONCLUSIONS	131
6.6 REFERENCES	132

**7 PRELIMINARY STUDY OF THE METHANE ACTIVATION PERFORMANCE OF
Pd/CeO₂ MILLED CATALYSTS IN DRY REFORMING OF METHANE**

ABSTRACT	137
7.1 INTRODUCTION	138
7.2 EXPERIMENTAL	139
7.3 RESULTS AND DISCUSSION	142
7.3.1 DRM CATALYTIC ACTIVITY	142
7.3.2 <i>IN-SITU</i> METHANE ACTIVATION	144
7.3.3 CATALYST STABILITY AND DEACTIVATION	152
7.4 CONCLUSIONS	157
7.5 REFERENCES	159

**8 METHANE OXIDATION AND STEAM REFORMING ACTIVITY OF Pd/CeO₂ MILLED
CATALYSTS IN NGVS AFTERTREATMENT APPLICATIONS**

ABSTRACT	162
8.1 INTRODUCTION	163
8.2 EXPERIMENTAL	164

8.3	RESULTS AND DISCUSSION	165
8.4	CONCLUSIONS	176
8.5	REFERENCES	177

9 PRELIMINARY STUDY ON THE EFFECT OF CERIA EXPOSED FACETS ON Pd/CEO₂ METHANE OXIDATION CATALYSTS **180**

	ABSTRACT	180
9.1	INTRODUCTION	181
9.2	EXPERIMENTAL	182
9.3	RESULTS	183
9.3.1	POLYCRYSTALLINE CeO ₂	185
9.3.2	CERIA NANOCUBES (CeNC)	190
9.3.3	CERIA NANORODS (CeNR)	195
9.4	DISCUSSION	199
9.5	CONCLUSIONS	201
9.6	REFERENCES	202

10 CONCLUDING REMARKS AND FUTURE PERSPECTIVES **207**

<u>APPENDIX A: INFLUENCE OF MASS AND HEAT TRANSFER LIMITATIONS</u>		A
	EXTERNAL MASS TRANSFER LIMITATIONS	B
	INTERNAL MASS TRANSFER LIMITATIONS	C
	HEAT TRANSFER LIMITATIONS	C
	REFERENCES	D

List of Abbreviations

NGV – Natural gas fueled vehicle
TWC – Three-way catalyst
OC – Oxidation catalyst
M – Milling
IW – Incipient wetness impregnation
SCS – Solution combustion synthesis
L – loose milling
G – Grinding
HM – High energy milling
BPR – Ball to powder weight ratio
BET – Brunauer–Emmett–Teller
BJH – Barrett-Joyner-Halenda
TPO – Temperature programmed oxidation
TPR – Temperature programmed reduction
TGA – Thermogravimetric analysis
TEM – Transmission electron microscopy
HRTEM – High resolution transmission electron microscopy
XPS – X-ray photoelectron spectroscopy
AP-XPS – Ambient pressure X-ray photoelectron spectroscopy
XRD – X-ray diffraction
DRIFTS – Diffuse reflectance infrared Fourier transform spectroscopy
TPC – Temperature programmed combustion
TOS – Time-on-stream
GHSV – Gas hourly space velocity
BNL – Brookhaven National Laboratory
APS – Advanced Photon Source

1 Background and Motivation

1.1 Overview

Climate change is globally recognized as an issue that needs to be urgently addressed, as it poses serious threats to environmental security, air quality, biodiversity, water, food and soil resources.^{1,2} The impending risks will become more critical as the world population increases, which is expected to grow to 10 bln in 2055¹ and this will be inevitably tied to an increase in energy consumption for housing, transportation, food and products. Among many interlinked causes for climate change, the anthropogenic release of greenhouse gases into the atmosphere is recognized as a big player in the global warming effect² and many actions have been undertaken to reduce its impact.^{3,4}

Since the industrial revolution, human population has started burning any fossil fuel available, transitioning from wood to coal and then oil, on a larger scale to obtain the energy needed for transportation and industrial production. The CO₂ emissions have therefore rapidly grown from null in 1820 to over 40 Gt CO₂-eq per year in 2010.⁵ The contribution to global emissions depends on the economic status of each country, with the most industrialized regions accounting for the highest degree of GHGs emissions,⁵ as seen in Figure 1.1. China and other developing countries have a great impact on the global GHG emissions due to large and growing population and economic growth, and their contribution has increased rapidly in the latest years. The second largest contributors are the US and the EU, whose emissions have been stable in the latest decades, despite economic growth. This is due to their self-imposed goals under the Kyoto Protocol⁴ and the Paris Agreement³ signed under the United Nations Framework Convention on Climate Change, whose objective included a reduction of emissions of Greenhouse Gases in order to stay below a 2°C global average temperature increase.

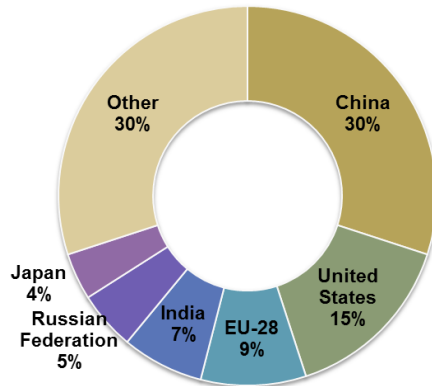


Figure 1.1: Global CO₂ emissions from Fossil Fuel Combustion and Industrial Processes in 2014.⁶

Focusing on the United States and European Union areas and breaking down their cumulative emissions by economic sector (Figure 1.2a and b, respectively), it can be seen that the main contributors are the transport and energy production sectors, followed by industrial manufacturing. In industry, GHGs emissions are equally due to fuel burning for energy requirements and feedstock materials. In these countries, statistics collected by organizations such as the United States Environmental Protection Agency (EPA) and the European Environment Agency (EEA) show that in 2016 roughly 30% of all GHGs emissions was caused by the transportation sector (including aviation and maritime transport), 30% from power generation, 20% from industrial processes and 10% from agriculture (Figure 1.2).

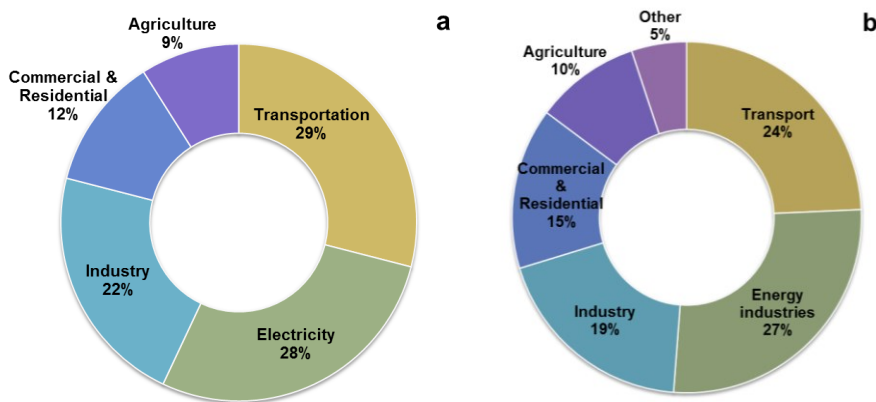


Figure 1.2: Greenhouse Gas emission by economic sector for the U.S. (a) and EU-28 (b) regions.⁷⁻⁹

By analyzing their evolution through time,⁷⁻⁹ it clearly appears how the stable CO₂-eq emission rate observed in the latest decades is actually a balance of the individual economic sectors, which have experienced very different growth rates. In fact, the transportation sector is the only one displaying a net increase in GHGs emissions, while energy generation experienced the strongest contraction. Such significant reduction was achieved by introducing renewable energies in the mix for electricity and heat generation, substituting mainly coal and nuclear power sources, and using more efficient technologies,^{8,10} thus successfully decoupling population growth and industrial production from their GHGs emissions.

This could not be achieved for the transportation sector, where the many constraints of mobile systems compared to stationary energy production sources, such as variable operation, size and weight limitations, fuel economy, re-fueling infrastructure, emission control technology, engine technology, price and aesthetic appeal pose many challenges to the employment of new fuels. All these factors have to be considered in the design of new mobile systems, while also ensuring that the engine and aftertreatment technology respect the regulations limiting emissions at tailpipe, such as LEV and TIER standards in the U.S. and the EURO standards in the European Union.^{11,12} While these regulations are needed to maintain and improve air quality in industrialized areas, they also affect the introduction of alternative and renewable sources in the energy mix for transportation fuels.

According to regulations, the “zero emission” vehicle would be represented by an electrical vehicle fueled by power exclusively obtained by renewable sources. Current limits on the required technologies, among others the high efficiency of power production from renewable source, reliable energy storage, and long lasting batteries, as well as the difficulties in the evaluation of environmental impact of such applications, pave the way to alternative solutions, a compromise between traditional internal combustion engines fueled by gasoline or diesel and electric vehicles. Several alternative technologies are possible, the more feasible being the substitution of liquid fossil fuels with biofuels and the transition to gaseous fuels such as natural gas or hydrogen. The advantages of liquid biofuels include easy substitution of traditional gasoline and diesel in the engine fuel injection system and a comparably high energy density, therefore representing a possible solution for freight transport. The EU promotes their production by setting up alternative fuel standards¹³ and goals of biofuels substitution percentages in the distributed diesel. On the other hand, increased biofuel production has caused a significant transition of land use, turning field

farming from edible to non-edible crops due to EU biofuel incentives,² therefore an increased production of the biofuel share should be considered with attention.

Gaseous fuels such as natural gas or hydrogen ensure a cleaner combustion inside the engine, producing lower amount of greenhouse gases (CO₂) and less pollutants such as volatile hydrocarbons, NO_x and SO_x. Nevertheless, their gaseous nature poses a challenge to fuel storage and the environmental impact of their production has to be considered as well. The most promising alternative fuel, with the current technology available, is natural gas, since it is readily available and fuel distribution grids for stationary applications are already well-developed. Moreover, its substitution by biomethane, entirely or in part, enables further reduction of its carbon footprint.^{2,14} The application of natural gas as a transportation fuel will be discussed in more detail in Section 1.2, but in general when talking about the environmental footprint of an automotive fuel there are some factors to be taken into account, namely its well-to-wheel impact, the noxious emissions and the catalytic system applied at tailpipe in order to meet the regulation limits on these emissions.

Besides energy generation and transport, the third large contributor to GHGs emission is industry and production (Figure 1.2), contributing to ca. 20% of the global greenhouse gases emitted. By analyzing its main subsectors, shown in Table 1.1, it can be noted that the chemical industry appears as one of the main contributors, despite its significant impact reduction since 1990. Consequently, it becomes more and more important to take into account the environmental impact of the chemicals manufacturing process, and this is true also for the catalytic systems to be used in the catalytic converters of transportation vehicles, alongside their catalytic efficiency and durability. These elements are slowly being considered in the life cycle analysis of products and chemical processes,¹⁵ and for this reason when investigating the development of novel and more efficient catalysts for automotive applications the sustainability of the catalyst production process should not be overlooked.

Within this framework, my PhD research work was aimed at studying a solvent-free, ecofriendly route for the production of catalysts for the abatement of methane from natural gas fueled vehicles, in order to find a potential way to minimize the overall environmental impact of the transportation sector while waiting for a mature technology to allow the diffusion of the “zero emission” vehicle.

Table 1.1: Greenhouse Gas Emissions from Industrial Processes and Products Use – Selected Sectors, EU-28, 1990 and 2016.⁸

Sector	Sector Code	Emissions (Mt CO ₂ -eq)		% Share in Total	
		1990	2016	1990	2016
Industrial Processes and Product Use	CRF2	517	374	100	100
Mineral Industry	CRF2A	145	108	28	29
Chemical Industry	CRF2B	212	62	41	17
Metal Industry	CRF2C	131	72	25	19
Refrigeration and Air Conditioning	CRF2F1	0	98	0	26

1.2 Natural Gas as a Transportation Fuel

The application of NG as a transportation fuel was promoted by the increased energy security that was guaranteed by fuel diversification,^{16–19} as well as its environmental benefits on GHGs emissions and air quality.^{17,20–24} In fact, despite being a fossil fuel, its composition allows a cleaner combustion compared to other hydrocarbons.^{25,26} Natural gas is comprised mostly by methane (80-96 vol%, depending on the source), which has the lowest C:H ratio among all hydrocarbons and therefore produces the lowest amount of CO₂ per mole burned, consequently per kWh produced, as reported in Table 1.2. It also lacks aromatic compounds and long-chained hydrocarbons, which are known carcinogens for humans and animals,²⁷ resulting in negligible formation of soot and non-methane volatile compounds originating from fuel (traces of soot and VOCs can be measured at tailpipe due to lubrication oil evaporation). Sulphur is present either in low concentrations or it can be easily removed from the gaseous fuel, thus reducing significantly the SO_x emissions.

Table 1.2: CO₂ emissions of different fuels with increasing C:H ratio.²⁸

Fuel	% hydrogen (weight)	LHV MJ/kg	g CO ₂ per kWh	Theoretical CO ₂ reduction (%) ^a
Methane (NG/biomethane)	25.0%	50.0	198.0	29.2
Propane (LPG)	18.2%	45.6	236.8	15.3
Butane (LPG)	17.2%	45.3	241.2	13.7
Diesel	13.5%	42.7	267.5	4.3
Gasoline	13.5%	42.4	279.5	0.0

a: CO₂ reduction compared to gasoline.

As a transportation fuel, natural gas can be used in compressed (CNG) or liquefied (LNG) state, to improve its low energy density.²⁹ The properties of CNG and LNG are compared in Table 1.3. The choice of fuel source thus depends on the application, with light-duty vehicles having strong limitations in size and weight and unable to include a refrigeration system for LNG, consequently relying on CNG. Conversely, adoption of a LNG-based technology is necessary for marine applications, where space is more easily available but greater fuel autonomy is needed.

Table 1.3: Properties of natural gas in compressed and liquefied state, given identical NG composition.²⁹

	CNG	LNG
Physical state	gas	liquid
Temperature in vehicle tank	ambient	111 K
Typical pressure in tank	17.3-24.9 MPa	170-446 kPa
Typical density in tank	130.6-189.9 kg/m ³	415.5 kg/m ³
Typical energy density (LHV)	6.5-9.5·10 ⁶ MJ/m ³	21·10 ⁶ MJ/m ³
Heat of vaporization	/	512 kJ/kg

Because of the many advantages provided by NG as an alternative fuel, natural gas fueled vehicles have experienced a great diffusion in the latest years, as shown in Figure 1.3, including both light- and heavy-duty vehicles (LDVs and HDVs, respectively) as well as vehicles for marine and rail transportation.

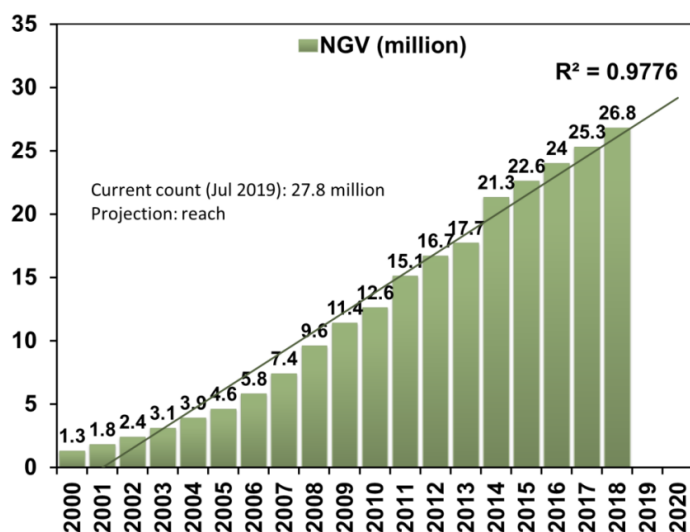


Figure 1.3: Total number of NGVs worldwide, 2000-2018 and projection to 2020.³⁰

In turn, the large current number of NGVs worldwide (ca. 28 mln in 2019) highlighted some critical issues for the use of natural gas as transportation fuel, including technical and environmental issues. The gaseous state of the fuel implies low energy density and high refueling volumes, lower volumetric and heat efficiency compared to gasoline engines,^{26,31} lower mileage and the subsequent need for an adequate well-developed refueling network. From the environmental point of view, the main issue relates to the methane leakage into the atmosphere, either in exhaust gases or through the natural gas fuel distribution system, as CH₄ has a global warming potential that is 25 times higher than CO₂ on a 100-year time window.⁷ Many studies are currently being carried out on this topic,^{32,33} as it was shown that methane leak into the atmosphere could possibly invalidate the CO₂ emission reduction advantage during use.^{17,23,34} Consequently, simultaneous efforts should be made towards the reduction of methane released during production and distribution and during vehicle use.

To reduce the emissions of unburned methane from exhaust gases of NGVs, stringent emission limits at tailpipe have been imposed by EURO standards and CAFE and LEV standards in the EU and US, respectively. The current EURO emission limits are reported in Table 1.4 and Table 1.5 for spark ignited (SI) vehicles, where methane is either listed individually or accounted for in the total unburned hydrocarbon (THC) limit. In Table 1.6, the CAFE and LEV standards are reported, where methane is indicated as a fleet average limit, like other GHG emissions (CO₂, N₂O).

Table 1.4: Euro VI emission limits for SI vehicles in World Harmonized Transient Cycle (WHTC) (EU Regulation 582/2011).

Limit values					
CO (mg/kWh)	NMHC (mg/kWh)	CH₄ (mg/kWh)	NO_x (mg/kWh)	NH₃ (ppm)	PM (mg/kWh)
4000	160	500	460	10	10

Table 1.5: Euro 6 emission limits for SI vehicles (EU Regulation 715/2007).

Vehicle weight (kg)	Limit values (mg/km)				
	CO	THC	NMHC	NO_x	PM
≤ 1305	1000	100	68	60	5
1305 - 1760	1810	130	90	75	5
> 1760	2270	160	108	82	5

Table 1.6: Tier 3 Certification Bin Standards and equivalent LEV III Emission Standards (Federal Test Procedure – FTP, durability 150'000 miles).

Federal Bin	Californian Emission Category	NMOG ^a +NO _x	PM	CO	HCHO
		mg/mile	mg/mile	g/mile	mg/mile
Bin 160	LEV160	160	3	4.2	4
Bin 125	ULEV125	125	3	2.1	4
Bin 70	ULEV70	70	3	1.7	4
Bin 50	ULEV50	50	3	1.7	4
Bin 30	SULEV30	30	3	1	4
Bin 20	SULEV20	20	3	1	4
Bin 0	-	0	0	0	0

a: 0.030 g/mile CH₄ emission limit is imposed, calculated on a fleet average.

1.2.1 Marine Applications

From the available statistics of GHG emissions, navigation appears to affect only marginally the global emissions of the transportation sector. Nevertheless, worldwide it accounts for ca. 2.5% of the overall GHGs emissions and it is expected to grow to 5% in 2050,³⁵ due to the lack of imposed emission limits at engine tailpipe and the difficulties in the management of an international sector.

The International Maritime Organization (IMO) has recently attempted to solve this issue by imposing new legislation on fuel economy for international marine transport, promoting more efficient fueling technology.³⁶ Moreover, the increasing concern on air and water quality in certain coastal regions,³⁷ denominated “Emission Control Areas” (ECAs) and designated under MARPOL Annex VI,³⁸ has further promoted the need for a transition from diesel to a cleaner alternative fuel. LNG has proved to be a successful substitute,³⁹ simultaneously reducing GHGs, NO_x and SO_x emissions.

Many studies have been undertaken to ensure that the refueling infrastructure and engine tank and injection systems would be less polluting than diesel engines,^{24,39,40} and so far many successful results have been considered. While the long-range autonomy remains a key point, many shorter range ships such as cruises and ferries have been successfully converted to single-fuel LNG, improving their environmental impact.^{39,41} For longer distances, international cargo ships can be equipped with dual-fuel LNG-diesel engines: by using LNG in coastal areas, the air quality limits are respected, while diesel is used in the open seas to guarantee the required fuel autonomy.

Due to the connection with diesel-fueled engines and the lack of space limitations on ships, in marine applications LNG is usually combusted in lean conditions inside the engine, enabling higher compression ratios and increased thermal outputs.^{31,42} Consequently, only an oxidative catalyst (OC) is used at tailpipe while secondary NO_x and SO_x removal systems are employed.

1.2.2 Current Emission Control Technology

Currently, for the abatement of unburned methane from exhaust gases there are two types of emission-control systems available depending on the engine technology, that is on the air-to-fuel (A/F) ratio used in the engine cylinders. Stoichiometric engines require a three-way catalyst (TWC) for the simultaneous abatement of CO, CH₄ and NO_x, while lean engine technology requires an oxidation catalyst (OC) only.^{43,44} Initially, lean combustion was the most popular engine technology employed due to its intrinsic simplicity of design and to the higher power and torque performances.²⁵ The excess oxygen in the air-fuel mixture reduced the NO_x concentration at tailpipe due to the cooler flame temperature, and a simple oxidation catalyst was needed to burn the residual HCs and CO in the exhausts. Moreover, due to the large O₂ availability no closed-loop technology was required to control the catalyst optimal working conditions, thus further simplifying the after-treatment system. Despite being very simple, this system was not able to satisfy the stricter emission limits imposed by the latest standards on light- or heavy-duty vehicles (EURO 6 and V-VI).^{45,46} Consequently the technology shifted towards stoichiometric engines, where NO_x emissions are reduced through EGR (Exhaust Gas Recirculation),^{31,47} which simultaneously decreases O₂ and N₂ content by introducing reaction products and reduces the flame temperature by absorbing heat. Total unburnt hydrocarbons concentration is lower due to higher flame stability, while carbon monoxide production increases.³¹ A three-way catalyst (TWC) is used at tailpipe to further reduce pollutant concentration below legislation limits and a closed-loop control is needed to keep the correct air-to-fuel ratio around the stoichiometric value (equal to 17 for methane). The overall system is more complex than the lean burn engine, but the technology is already mature and easily available based on that used for gasoline engines. In addition, recent studies have reported technical ways of improving the stoichiometric power and heat efficiency,⁴⁸ such as through the introduction of higher hydrogen content in natural gas⁴⁹ or by optimizing the fluidodynamic properties of the fuel introduction into the cylinder.⁴³

Irrespective of the engine combustion and after-treatment type, the key issue is the design of a catalyst able to abate unburned methane under the limits set by the legislation. The stringent constraints imposed on pollutant emissions and durability of the after-treatment system, coupled with the state-of-the-art technology, can be satisfied only by the expensive platinum-group metals.⁵⁰ The supported PGM acts solely as oxidative catalysts for lean burn engines or in synergy with NO_x-reduction catalysts (usually Rh-based) in three-way catalysts.^{44,51,52} The current state-of-the-art TWC are comprised by PGM dispersed by wet methods onto a ceria-zirconia-alumina (CZA) support oxide, which is then coated on a cordierite support by addition of an Al₂O₃-based binder. The exact metal/support oxide composition depends on manufacturers and on the requested specifications, but in general a noble metal loading around 4 wt% on the CZA support is needed to satisfy the abatement legislation at tailpipe.^{44,53} Consequently, the optimization of supported noble metals catalytic activity is increasingly important in order to reach the low limits imposed for CH₄ emissions with the lowest possible costs.

For methane oxidation it is known from the literature that the most active materials are those based on palladium.^{54–58} In fact, among the other PGMs, namely Pt, Rh or Ru, Pd displayed the higher activity for complete methane combustion and intensive studies were initially conducted on Pd-based catalysts for methane combustion at controlled temperatures in gas turbines.^{59–61} Nonetheless, Palladium shows a complex redox behavior with a noticeable thermal hysteresis between PdO decomposition and Pd re-oxidation, which proved to affect negatively its catalytic performance during the temperature oscillations experienced by the catalyst.^{62–65} Figure 1.4 shows the typical loss in methane conversion observed during a light-off cycle carried out on a commercial Pd/Al₂O₃ catalyst.

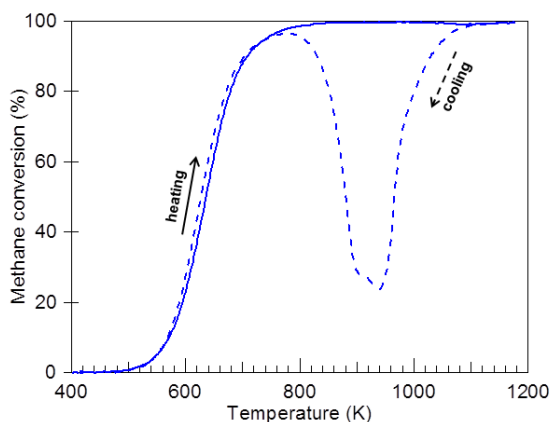


Figure 1.4: Methane conversion of a commercial Pd/Al₂O₃ catalyst; 2nd light-off cycle. Solid line: heating; dashed line: cooling.

Despite extensive studies, the variety of possible chemical and morphological states exhibited by palladium and their evolution during reaction prevented the univocal identification of the palladium active species for methane oxidation, thus hindering strategic design for optimized Pd-based catalysts. The most recent studies suggest the active phase at low temperature consists of a mixture of different Pd entities in an oxidized form (Pd^{2+} , PdO , PdO_x).^{56,66–70} The role of metallic Pd is more controversial and still debated, but in the high temperature range it is well established that Pd^0 is inactive, causing the typical activity loss observed for Pd-based catalysts between ca 973 K and 1173 K.^{62,63}

Among many known support oxides (Al_2O_3 , SnO_2 , ZrO_2) CeO_2 strongly promotes the catalytic activity of supported Pd in TWC, simultaneously stabilizing the PdO_x phases,^{66,68,71} reducing hysteresis at high temperatures^{72–74} and providing additional oxygen to the catalytic reaction.^{75,76} The promoting effect of ceria on Pd re-oxidation can be easily understood by looking at Figure 1.5, where the behavior of a commercial Pd/ Al_2O_3 catalyst is compared with that of a Pd/ CeO_2 sample. Consequently, Pd/ CeO_2 catalysts are considered as promising materials to improve the methane abatement performances of the catalytic systems to be applied on natural gas fueled vehicles, but, despite the considerable amount of work carried out on these systems, they still lack of fundamental understanding. Moreover, the synthesis procedures reported in the literature for their preparation often involve complex multi-step routes^{77–80} and/or techniques that are not easily scalable for an industrial production (SCS).^{66,68,81} These issues appeared to be an interesting challenge, and are the object of the study of this PhD research work.

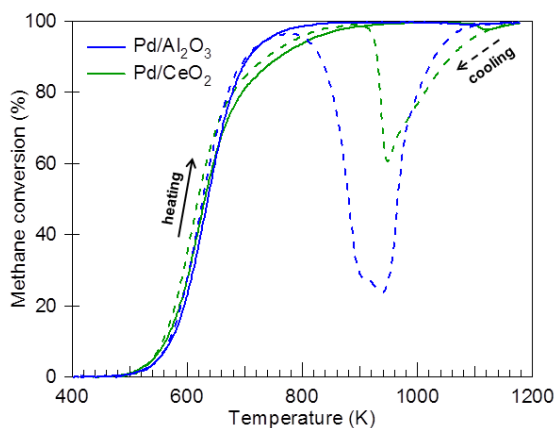


Figure 1.5: Comparison of the methane conversion measured on a commercial Pd/ Al_2O_3 catalyst and a Pd/ CeO_2 sample; 2nd light-off cycle. Solid line: heating; dashed line: cooling.

1.3 Mechano-chemical Synthesis

“Mechano-chemical” defines any process involving the use of mechanical energy to induce chemical transformations.^{82,83} The nature of the induced reaction is not specified and might refer to solid-solid or solid-liquid reactions for the synthesis of new materials as well as solid-gas, liquid-gas or even gas phase chemical reactions.^{84–86}

The mechanical energy is generally released by milling the desired reactants in a ball-mill apparatus, where the movement of the grinding bowl imposes kinetic and potential energy to the grinding balls loaded inside it. In turn, the grinding spheres release mechanical energy to the reactants through impacts occurring during milling. The energy transfer from the grinding media to the reactants and the effect of the milling parameters on the amount of energy released during the process have been widely studied in the literature,^{87–93} yet the complex behavior of the system and the huge variety of parameters hindered a comprehensive study of the mechanical forces occurring at the meso- and microscale. Nevertheless, many experimental studies were conducted to find the best milling conditions for each considered reactant system.

Due to its simplicity and versatility of use, the applications of mechano-chemical synthesis processes have been widely researched and recently they have been further promoted by the increased attention towards greener and more sustainable processes.¹⁰ Previously, the mechanical milling was mostly investigated for solid-solid reactions, i.e. for the solid synthesis of novel materials.^{94–98} In fact, by using mechanical energy instead of thermal energy the thermodynamic equilibrium of crystalline phases or multi-component alloy systems could be surpassed, inducing the formation of meta-stable phases. This resulted in the successful preparation of novel alloys or nanomaterials with enhanced magnetic or electric properties.^{85,99,100} The positive results obtained in the field were accompanied by a systematic study of the energies and forces developed during milling, often in combination with theoretical modelling approaches.^{88,91,92,101} To reduce the complexity of the system most models were developed on a series of assumptions strictly aimed at the specific application. In general, a planetary ball-mill geometry is considered and variables such as grinding ball size and weight, overall ball-to-powder weight ratio and rotation speed are investigated to maximize energy release.⁹³ The average mill size and the characteristic times necessary for the synthesis of the desired nanomaterials require the use of the discrete elements modelling (DEM) technique,^{87,89,90} whose time and space scales largely exceed the

ones relevant for chemical reactions and for surface stresses. As a consequence, a comprehensive theoretical background of the mechanical forces released during milling targeted to catalytic applications is so far lacking.

Nevertheless, the option to remove solvents and to overcome thermodynamic equilibria made the mechano-chemical process very attractive for the synthesis of catalytic materials, pushing for trial-and-error approaches for the application of mechano-chemistry in catalysis. Recently, this resulted in the preparation of novel catalytic materials with highly reactive meta-stable phases compared to conventionally prepared solid catalysts.^{102–108} Additional recent studies have focused on supported metal-metal oxides catalytic systems, where the possibility of depositing the metal on the support oxide and promoting the metal-support interaction was investigated with encouraging^{109–116} and less promising¹¹⁷ results, depending on the considered materials. This suggests that further work is needed in order to correlate the studies on the mechano-chemical process to the synthesis of supported heterogeneous catalysts, particularly because an understanding of the chemistry taking place at nanoscale induced by mechanical forces is missing.

Simultaneously, several groups have successfully highlighted the possibility of using the mechanical energy as a “catalyst”, either by inducing reactive meta-stable phases on the reactants, hence kickstarting reaction, or by modifying *in-situ* the state of a solid catalyst, promoting chemical reactions during milling.^{86,118,119} Such applications further open the way to more promising pathways towards greener chemical processes.

1.3.1 Milling Equipment

As many industrial processes rely on one or more milling steps, often with largely different purposes, a huge variety of milling equipment is available. Often, mills dedicated to industrial use work on very large mass scales, in the order of $10\text{-}10^3$ kg, and are required to release high mechanical energy. Most of the times, they are also designed in order to work continuously. Laboratory scale mills usually have a $10\text{-}10^2$ g mass scale, with mini-mills representing the smallest size available, and work as batch reactors. In both applications, the principal aim of the milling process is reduction and homogenization of the particle size, which is completely different from the application of mechanical milling for solid-solid reactions.

Another important parameter that discriminates milling equipment is the type of movement that is imposed on the bowl and, consequently, on the possible trajectories of the milling balls and the amount of energy released during the process. The bowl can move in one direction, like in vibratory mills or in three directions in shaker mills, or could rotate with one or more rotation centers, which is typical for planetary mills. Moreover, the most common type of milling media are milling spheres, whose material, size and weight can be decided by the user and further vary the process conditions, but other types of mills are available which rely on rolls, bars or plates.

The choice of support oxides, namely ceria, zirconia and alumina, requires the use of zirconia-based milling bowl and spheres. Yttria-stabilized Zirconia (YSZ) is commonly employed for its hardness and wear resistance. Three types of mills were used for the materials considered in this thesis: one vibratory mini-mill (Pulverisette 23, Fritsch), a shaker mill (Spex8000) and a planetary ball-mill (Pulverisette 6, Fritsch) for a preliminary scale-up of the synthesis. In the shaker mill, the YSZ bowl is closed into a clamp (Figure 1.6) and the spring at the base enables its movement in the three direction, with an overall run of 3 x 3 x 5 cm, increasing threefold the 875 rotations per minute of the mill engine. In the Pulverisette 23 Mini-mill, the bowl moves along a vertical axis, but its egg-shape allows the sphere to move internally in more directions, as shown in Figure 1.7. In the Pulverisette 6 planetary mill, the bowl is anchored on a rotating plate and moves around two centers (Figure 1.8) mimicking the planetary orbits, hence the name.



Figure 1.6: YSZ bowl in the Spex8000 shaker mill.

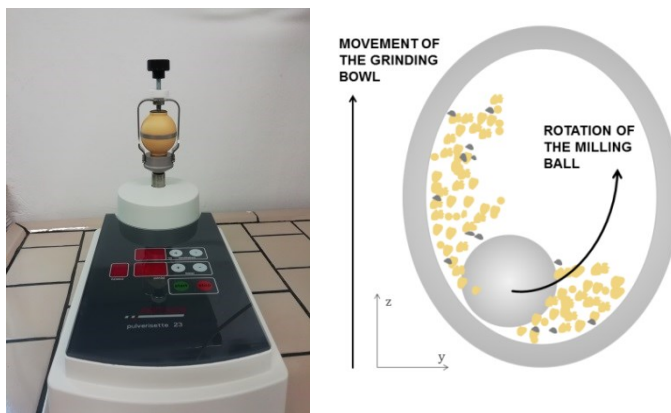


Figure 1.7: Fritsch Pulverisette 23 mill (left) and a schematic movement of the milling bowl and sphere (right).

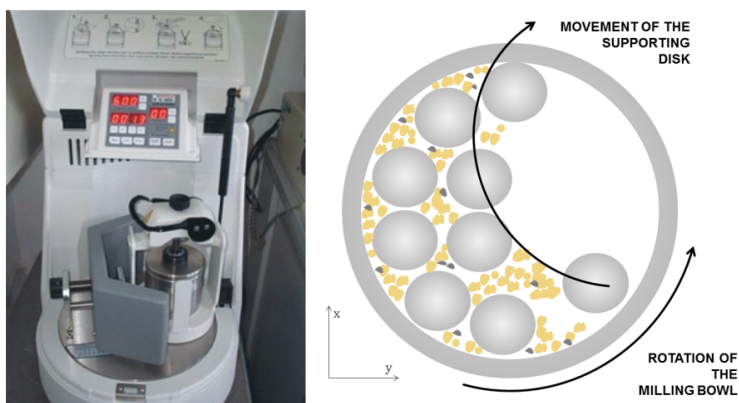


Figure 1.8: Fritsch Pulverisette 6 planetary ball mill (left) and a schematic movement of milling bowl and spheres (right).

Among many types of mills, it becomes quite difficult to choose the most appropriate equipment for the desired synthesis. The choice is usually guided by desired mass scale, considered materials, milling environment (air or inert gas, liquid or solid), and desired particle size distribution. For the synthesis of metal – metal oxide supported catalysts some of these parameters are not relevant, or not available, and as mentioned above the lack of a systematic study of the influence of milling parameters on the final metal-support interaction and on the chemical and mechanical events taking place at nanoscale makes the choice of milling conditions particularly challenging. Part of this thesis work has thus been devoted to the optimization of milling conditions in order to obtain the best catalytic performances for the synthesized materials.

1.4 References

- (1) Drivers of Environmental Change. In *Global Environment Outlook – GEO-6: Healthy Planet, Healthy People*; UN Environment, Ed.; Cambridge University Press, 2019; pp 20–55. <https://doi.org/10.1017/9781108627146.008>.
- (2) *Climate Change 2014: Mitigation of Climate Change: Working Group III Contribution to the Fifth Assessment Report of the Intergovernmental Panel on Climate Change*; Intergovernmental Panel on Climate Change, Edenhofer, O., Eds.; Cambridge University Press: New York, NY, 2014.
- (3) UNFCCC. *Paris Agreement*; 2016.
- (4) UNFCCC. *Kyoto Protocol*; 1997.
- (5) Chancel, L.; Piketty, T. *Carbon and Inequality: From Kyoto to Paris*; Paris School of Economics, 2015; p 50.
- (6) Boden, T. A.; Marland, G.; Andres, R. J. National CO₂ Emissions from Fossil-Fuel Burning, Cement Manufacture, and Gas Flaring: 1751-2014. **2017**. https://doi.org/10.3334/CDIAC/00001_V2017.
- (7) U.S. EPA. Global Greenhouse Gas Emissions Data <https://www.epa.gov/ghgemissions/global-greenhouse-gas-emissions-data> (accessed Oct 12, 2019).
- (8) Eurostat. Greenhouse gas emission statistics - emission inventories https://ec.europa.eu/eurostat/statistics-explained/index.php/Greenhouse_gas_emission_statistics.
- (9) Annual European Union Greenhouse Gas Inventory 1990–2017 and Inventory Report 2019. https://doi.org/10.1163/9789004322714_cclc_2016-0201-011.
- (10) Eurostat. *Sustainable Development in the European Union: Overview of Progress towards the SDGs in an EU Context.*; Publications Office of the European Union: Luxembourg, 2019.
- (11) *Regulation (EC) No 764/2008 of the European Parliament and of the Council*; 2015; pp 183–186. https://doi.org/10.1007/978-1-137-54482-7_19.
- (12) *Commission Regulation (EU) No 582/2011 of 25 May 2011 Implementing and Amending Regulation (EC) No 595/2009 of the European Parliament and of the Council with Respect to Emissions from Heavy Duty Vehicles (Euro VI) and Amending Annexes I and III to Directive 2007/46/EC of the European Parliament and of the Council Text with EEA Relevance*; 2011; p 168.
- (13) Ervine, C. Directive 2004/39/Ec of the European Parliament and of the Council of 21 April 2004. In *Core Statutes on Company Law*; Macmillan Education UK: London, 2015; pp 757–759. https://doi.org/10.1007/978-1-137-54507-7_21.
- (14) Han, J. W.; Mintz, M.; Wang, M. *Waste-to-Wheel Analysis of Anaerobic-Digestion-Based Renewable Natural Gas Pathways with the GREET Model*; ANL/ESD/11-6; Argonne National Laboratory, 2011; p 40.
- (15) Benavides, P. T.; Cronauer, D. C.; Adom, F.; Wang, Z.; Dunn, J. B. The Influence of Catalysts on Biofuel Life Cycle Analysis (LCA). *Sustainable Materials and Technologies* **2017**, *11*, 53–59. <https://doi.org/10.1016/j.susmat.2017.01.002>.
- (16) Rood Werpy, M.; Santini, D.; Burnham, A.; Mintz, M. *Natural Gas Vehicles: Status, Barriers, and Opportunities*; ANL/ESD/10-4; Argonne National Laboratory, 2010; p 59.

- (17) Nijboer, M. *The Contribution of Natural Gas Vehicles to Sustainable Transport*; IEA Energy Papers 2010/11; IEA: Paris Cedex 15, France, 2010. <https://doi.org/10.1787/5km4rm5c0pzp-en>.
- (18) *Energy Policy Act of 2005*; 2005.
- (19) *Energy Independence and Security Act of 2007*; 2007.
- (20) Yeh, S. An Empirical Analysis on the Adoption of Alternative Fuel Vehicles: The Case of Natural Gas Vehicles. *Energy Policy* **2007**, *35* (11), 5865–5875. <https://doi.org/10.1016/j.enpol.2007.06.012>.
- (21) Gonçalves, M.; Jiménez-Guerrero, P.; Baldasano, J. M. Emissions Variation in Urban Areas Resulting from the Introduction of Natural Gas Vehicles: Application to Barcelona and Madrid Greater Areas (Spain). *Science of The Total Environment* **2009**, *407* (10), 3269–3281. <https://doi.org/10.1016/j.scitotenv.2009.01.039>.
- (22) Thi Nguyen, H.; Kim, K.-H.; Ma, C.-J.; Cho, S.-J.; Ryeul Sohn, J. A Dramatic Shift in CO and CH₄ Levels at Urban Locations in Korea after the Implementation of the Natural Gas Vehicle Supply (NGVS) Program. *Environmental Research* **2010**, *110* (4), 396–409. <https://doi.org/10.1016/j.envres.2010.03.002>.
- (23) Wadud, Z.; Khan, T. Air Quality and Climate Impacts Due to CNG Conversion of Motor Vehicles in Dhaka, Bangladesh. *Environmental Science & Technology* **2013**, *47* (24), 13907–13916. <https://doi.org/10.1021/es402338b>.
- (24) Peterson, M. B.; Barter, G. E.; West, T. H.; Manley, D. K. A Parametric Study of Light-Duty Natural Gas Vehicle Competitiveness in the United States through 2050. *Applied Energy* **2014**, *125*, 206–217. <https://doi.org/10.1016/j.apenergy.2014.03.062>.
- (25) Cho, H. M.; He, B.-Q. Spark Ignition Natural Gas Engines—A Review. *Energy Conversion and Management* **2007**, *48* (2), 608–618. <https://doi.org/10.1016/j.enconman.2006.05.023>.
- (26) Pourkhesalian, A. M.; Shamekhi, A. H.; Salimi, F. Alternative Fuel and Gasoline in an SI Engine: A Comparative Study of Performance and Emissions Characteristics. *Fuel* **2010**, *89* (5), 1056–1063. <https://doi.org/10.1016/j.fuel.2009.11.025>.
- (27) Armstrong, B.; Hutchinson, E.; Fletcher, T.; Great Britain; Health and Safety Executive. *Cancer Risk Following Exposure to Polycyclic Aromatic Hydrocarbons (PAHs): A Meta-Analysis*; HSE Books: Sudbury, 2003.
- (28) NGVA Europe. Gas as a Transport Fuel <https://www.ngva.eu/gas-as-vehicle-fuel/> (accessed Oct 11, 2019).
- (29) Sinor, J. E. *Comparison of CNG and LNG Technologies for Transportation Applications*; United States, 1992. <https://doi.org/10.2172/5909852>.
- (30) NGV Global Knowledgebase. Statistics | NGV global knowledgebase <https://www.iangv.org/category/stats/>.
- (31) Korakianitis, T.; Namasivayam, A. M.; Crookes, R. J. Natural-Gas Fueled Spark-Ignition (SI) and Compression-Ignition (CI) Engine Performance and Emissions. *Progress in Energy and Combustion Science* **2011**, *37* (1), 89–112. <https://doi.org/10.1016/j.pecs.2010.04.002>.
- (32) Wang, M. Q.; Huang, H. S. *A Full Fuel-Cycle Analysis of Energy and Emissions Impacts of Transportation Fuels Produced from Natural Gas*; ANL/ESD--40, 750803; 2000. <https://doi.org/10.2172/750803>.

- (33) Clark, N. N.; McKain, D. L.; Johnson, D. R.; Wayne, W. S.; Li, H.; Akkerman, V.; Sandoval, C.; Covington, A. N.; Mongold, R. A.; Hailer, J. T.; et al. Pump-to-Wheels Methane Emissions from the Heavy-Duty Transportation Sector. *Environ. Sci. Technol.* **2017**, *51* (2), 968–976. <https://doi.org/10.1021/acs.est.5b06059>.
- (34) Camuzeaux, J. R.; Alvarez, R. A.; Brooks, S. A.; Browne, J. B.; Sterner, T. Influence of Methane Emissions and Vehicle Efficiency on the Climate Implications of Heavy-Duty Natural Gas Trucks. *Environmental Science & Technology* **2015**, *49* (11), 6402–6410. <https://doi.org/10.1021/acs.est.5b00412>.
- (35) European Commission. Reducing emissions from the shipping sector | Climate Action https://ec.europa.eu/clima/policies/transport/shipping_en.
- (36) IMO. Air Pollution, Energy Efficiency and Greenhouse Gas Emissions <http://www.imo.org/en/OurWork/Environment/PollutionPrevention/AirPollution/Pages/Default.aspx>.
- (37) IMO. Sulphur 2020 – cutting sulphur oxide emissions <http://www.imo.org/en/MediaCentre/HotTopics/Pages/Sulphur-2020.aspx> (accessed Sep 3, 2019).
- (38) IMO. Air Pollution <http://www.imo.org/en/OurWork/Environment/PollutionPrevention/AirPollution/Pages/Air-Pollution.aspx>.
- (39) IMO. *Studies on the Feasibility and Use of LNG as Fuel for Shipping*; Air Pollution and Energy Efficiency Study Series; 3; Micropress Printers: Suffolk, UK, 2016; p 290.
- (40) Arteconi, A.; Polonara, F. LNG as Vehicle Fuel and the Problem of Supply: The Italian Case Study. *Energy Policy* **2013**, *62*, 503–512. <https://doi.org/10.1016/j.enpol.2013.08.016>.
- (41) European Commission. Maritime <https://ec.europa.eu/inea/en/connecting-europe-facility/cef-transport/projects-by-transport-mode/maritime>.
- (42) Hajbabaie, M.; Karavalakis, G.; Johnson, K. C.; Lee, L.; Durbin, T. D. Impact of Natural Gas Fuel Composition on Criteria, Toxic, and Particle Emissions from Transit Buses Equipped with Lean Burn and Stoichiometric Engines. *Energy* **2013**, *62*, 425–434. <https://doi.org/10.1016/j.energy.2013.09.040>.
- (43) Chen, H.; He, J.; Zhong, X. Engine Combustion and Emission Fuelled with Natural Gas: A Review. *Journal of the Energy Institute* **2019**, *92* (4), 1123–1136. <https://doi.org/10.1016/j.joei.2018.06.005>.
- (44) Einewall, P.; Tunestål, P.; Johansson, B. Lean Burn Natural Gas Operation vs. Stoichiometric Operation with EGR and a Three Way Catalyst; 2005. <https://doi.org/10.4271/2005-01-0250>.
- (45) Yoon, S.; Collins, J.; Thiruvengadam, A.; Gautam, M.; Herner, J.; Ayala, A. Criteria Pollutant and Greenhouse Gas Emissions from CNG Transit Buses Equipped with Three-Way Catalysts Compared to Lean-Burn Engines and Oxidation Catalyst Technologies. *Journal of the Air & Waste Management Association* **2013**, *63* (8), 926–933. <https://doi.org/10.1080/10962247.2013.800170>.
- (46) Posada, F. *CNG Bus Emissions Roadmap: From Euro III to Euro VI*; International Council on Clean Transportation (ICCT), 2009; p 30.
- (47) Zhang, Q.; Li, M.; Li, G.; Shao, S.; Li, P. Transient Emission Characteristics of a Heavy-Duty Natural Gas Engine at Stoichiometric Operation with EGR and TWC. *Energy* **2017**, *132*, 225–237. <https://doi.org/10.1016/j.energy.2017.05.039>.

- (48) Tahir, M. Mohd.; Ali, M. S.; Salim, M. A.; Bakar, R. A.; Fudhail, A. M.; Hassan, M. Z.; Muhaimin, M. S. A. Performance Analysis of A Spark Ignition Engine Using Compressed Natural Gas (CNG) as Fuel. *Energy Procedia* **2015**, *68*, 355–362. <https://doi.org/10.1016/j.egypro.2015.03.266>.
- (49) Alrazen, H. A.; Ahmad, K. A. HCNG Fueled Spark-Ignition (SI) Engine with Its Effects on Performance and Emissions. *Renewable and Sustainable Energy Reviews* **2018**, *82*, 324–342. <https://doi.org/10.1016/j.rser.2017.09.035>.
- (50) Raj, B. A. Methane Emission Control. *Johnson Matthey Technology Review* **2016**, *60* (4), 228–235. <https://doi.org/10.1595/205651316X692554>.
- (51) Xi, Y.; Ottinger, N.; Liu, Z. G. Development of a Lab Reactor System for the Evaluation of Aftertreatment Catalysts for Stoichiometric Natural Gas Engines; 2017. <https://doi.org/10.4271/2017-01-0999>.
- (52) Bounechada, D.; Groppi, G.; Forzatti, P.; Kallinen, K.; Kinnunen, T. Effect of Periodic Lean/Rich Switch on Methane Conversion over a Ce–Zr Promoted Pd–Rh/Al₂O₃ Catalyst in the Exhausts of Natural Gas Vehicles. *Applied Catalysis B: Environmental* **2012**, *119–120*, 91–99. <https://doi.org/10.1016/j.apcatb.2012.02.025>.
- (53) Ferri, D.; Elsener, M.; Kröcher, O. Methane Oxidation over a Honeycomb Pd-Only Three-Way Catalyst under Static and Periodic Operation. *Applied Catalysis B: Environmental* **2018**, *220*, 67–77. <https://doi.org/10.1016/j.apcatb.2017.07.070>.
- (54) Lampert, J.; Kazi, M.; Farrauto, R. Palladium Catalyst Performance for Methane Emissions Abatement from Lean Burn Natural Gas Vehicles. *Applied Catalysis B: Environmental* **1997**, *14* (3–4), 211–223. [https://doi.org/10.1016/S0926-3373\(97\)00024-6](https://doi.org/10.1016/S0926-3373(97)00024-6).
- (55) Gélin, P.; Primet, M. Complete Oxidation of Methane at Low Temperature over Noble Metal Based Catalysts: A Review. *Applied Catalysis B: Environmental* **2002**, *39* (1), 1–37. [https://doi.org/10.1016/S0926-3373\(02\)00076-0](https://doi.org/10.1016/S0926-3373(02)00076-0).
- (56) Specchia, S.; Finocchio, E.; Busca, G.; Palmisano, P.; Specchia, V. Surface Chemistry and Reactivity of Ceria–Zirconia-Supported Palladium Oxide Catalysts for Natural Gas Combustion. *Journal of Catalysis* **2009**, *263* (1), 134–145. <https://doi.org/10.1016/j.jcat.2009.02.002>.
- (57) Farrauto, R. J. Low-Temperature Oxidation of Methane. *Science* **2012**, *337* (6095), 659–660. <https://doi.org/10.1126/science.1226310>.
- (58) Monai, M.; Montini, T.; Gorte, R. J.; Fornasiero, P. Catalytic Oxidation of Methane: Pd and Beyond: Catalytic Oxidation of Methane: Pd and Beyond. *European Journal of Inorganic Chemistry* **2018**, *2018* (25), 2884–2893. <https://doi.org/10.1002/ejic.201800326>.
- (59) Dalla Betta, R. A.; Schlatter, J. C.; Yee, D. K.; Loffler, D. G.; Shoji, T. Catalytic Combustion Technology to Achieve Ultra Low NO_x Emissions: Catalyst Design and Performance Characteristics. *Catalysis Today* **1995**, *26* (3–4), 329–335. [https://doi.org/10.1016/0920-5861\(95\)00155-6](https://doi.org/10.1016/0920-5861(95)00155-6).
- (60) Sekizawa, K.; Widjaja, H.; Maeda, S.; Ozawa, Y.; Eguchi, K. Low Temperature Oxidation of Methane over Pd/SnO₂ Catalyst. *Applied Catalysis A: General* **2000**, *200* (1–2), 211–217. [https://doi.org/10.1016/S0926-860X\(00\)00634-7](https://doi.org/10.1016/S0926-860X(00)00634-7).
- (61) Di Benedetto, A.; Landi, G.; Di Sarli, V.; Barbato, P. S.; Pirone, R.; Russo, G. Methane Catalytic Combustion under Pressure. *Catalysis Today* **2012**, *197* (1), 206–213. <https://doi.org/10.1016/j.cattod.2012.08.032>.

- (62) Farrauto, R. J.; Hobson, M. C.; Kennelly, T.; Waterman, E. M. Catalytic Chemistry of Supported Palladium for Combustion of Methane. *Applied Catalysis A: General* **1992**, *81* (2), 227–237. [https://doi.org/10.1016/0926-860X\(92\)80095-T](https://doi.org/10.1016/0926-860X(92)80095-T).
- (63) McCarty, J. G. Kinetics of PdO Combustion Catalysis. *Catalysis Today* **1995**, *26* (3–4), 283–293. [https://doi.org/10.1016/0920-5861\(95\)00150-7](https://doi.org/10.1016/0920-5861(95)00150-7).
- (64) Chin, Y.-H. (Cathy); Buda, C.; Neurock, M.; Iglesia, E. Consequences of Metal–Oxide Interconversion for C–H Bond Activation during CH₄ Reactions on Pd Catalysts. *Journal of the American Chemical Society* **2013**, *135* (41), 15425–15442. <https://doi.org/10.1021/ja405004m>.
- (65) Chin, Y.-H. (Cathy); García-Diéguez, M.; Iglesia, E. Dynamics and Thermodynamics of Pd–PdO Phase Transitions: Effects of Pd Cluster Size and Kinetic Implications for Catalytic Methane Combustion. *J. Phys. Chem. C* **2016**, *120* (3), 1446–1460. <https://doi.org/10.1021/acs.jpcc.5b06677>.
- (66) Colussi, S.; Gayen, A.; Farnesi Camellone, M.; Boaro, M.; Llorca, J.; Fabris, S.; Trovarelli, A. Nanofaceted Pd–O Sites in Pd–Ce Surface Superstructures: Enhanced Activity in Catalytic Combustion of Methane. *Angewandte Chemie International Edition* **2009**, *48* (45), 8481–8484. <https://doi.org/10.1002/anie.200903581>.
- (67) Mayernick, A. D.; Janik, M. J. Methane Oxidation on Pd–Ceria: A DFT Study of the Mechanism over Pd_xCe_{1-x}O₂, Pd, and PdO. *Journal of Catalysis* **2011**, *278* (1), 16–25. <https://doi.org/10.1016/j.jcat.2010.11.006>.
- (68) Meng, L.; Lin, J.-J.; Pu, Z.-Y.; Luo, L.-F.; Jia, A.-P.; Huang, W.-X.; Luo, M.-F.; Lu, J.-Q. Identification of Active Sites for CO and CH₄ Oxidation over PdO/Ce_{1-x}Pd_xO_{2-δ} Catalysts. *Applied Catalysis B: Environmental* **2012**, *119–120*, 117–122. <https://doi.org/10.1016/j.apcatb.2012.02.036>.
- (69) Senftle, T. P.; van Duin, A. C. T.; Janik, M. J. Methane Activation at the Pd/CeO₂ Interface. *ACS Catalysis* **2017**, *7* (1), 327–332. <https://doi.org/10.1021/acscatal.6b02447>.
- (70) Su, Y.-Q.; Liu, J.-X.; Filot, I. A. W.; Zhang, L.; Hensen, E. J. M. Highly Active and Stable CH₄ Oxidation by Substitution of Ce⁴⁺ by Two Pd²⁺ Ions in CeO₂(111). *ACS Catalysis* **2018**, *8* (7), 6552–6559. <https://doi.org/10.1021/acscatal.8b01477>.
- (71) Senftle, T. P.; van Duin, A. C. T.; Janik, M. J. Role of Site Stability in Methane Activation on Pd_xCe_{1-x}O_δ Surfaces. *ACS Catalysis* **2015**, *5* (10), 6187–6199. <https://doi.org/10.1021/acscatal.5b00741>.
- (72) Farrauto, R. J.; Lampert, J. K.; Hobson, M. C.; Waterman, E. M. Thermal Decomposition and Reformation of PdO Catalysts; Support Effects. *Applied Catalysis B: Environmental* **1995**, *6*(3),263–270.[https://doi.org/10.1016/0926-3373\(95\)00015-1](https://doi.org/10.1016/0926-3373(95)00015-1).
- (73) Groppi, G.; Cristiani, C.; Lietti, L.; Ramella, C.; Valentini, M.; Forzatti, P. Effect of Ceria on Palladium Supported Catalysts for High Temperature Combustion of CH₄ under Lean Conditions. *Catalysis Today* **1999**, *50* (2), 399–412. [https://doi.org/10.1016/S0920-5861\(98\)00518-5](https://doi.org/10.1016/S0920-5861(98)00518-5).
- (74) Colussi, S.; Trovarelli, A.; Groppi, G.; Llorca, J. The Effect of CeO₂ on the Dynamics of Pd–PdO Transformation over Pd/Al₂O₃ Combustion Catalysts. *Catalysis Communications* **2007**, *8* (8), 1263–1266. <https://doi.org/10.1016/j.catcom.2006.11.020>.
- (75) McCabe, R. W.; Trovarelli, A. Forty Years of Catalysis by Ceria: A Success Story. *Applied Catalysis B: Environmental* **2016**, *197*, 1. <https://doi.org/10.1016/j.apcatb.2016.04.044>.

- (76) Farrauto, R. J.; Deeba, M.; Alerasool, S. Gasoline Automobile Catalysis and Its Historical Journey to Cleaner Air. *Nat Catal* **2019**, *2* (7), 603–613. <https://doi.org/10.1038/s41929-019-0312-9>.
- (77) Cargnello, M.; Montini, T.; Polizzi, S.; Wieder, N. L.; Gorte, R. J.; Graziani, M.; Fornasiero, P. Novel Embedded Pd@CeO₂ Catalysts: A Way to Active and Stable Catalysts. *Dalton Trans.* **2010**, *39* (8), 2122–2127. <https://doi.org/10.1039/B916035C>.
- (78) Cargnello, M.; Jaen, J. J. D.; Garrido, J. C. H.; Bakhmutsky, K.; Montini, T.; Gamez, J. J. C.; Gorte, R. J.; Fornasiero, P. Exceptional Activity for Methane Combustion over Modular Pd@CeO₂ Subunits on Functionalized Al₂O₃. *Science* **2012**, *337* (6095), 713–717. <https://doi.org/10.1126/science.1222887>.
- (79) Ma, J.; Lou, Y.; Cai, Y.; Zhao, Z.; Wang, L.; Zhan, W.; Guo, Y.; Guo, Y. The Relationship between the Chemical State of Pd Species and the Catalytic Activity for Methane Combustion on Pd/CeO₂. *Catal. Sci. Technol.* **2018**, *8* (10), 2567–2577. <https://doi.org/10.1039/C8CY00208H>.
- (80) Peng, H.; Rao, C.; Zhang, N.; Wang, X.; Liu, W.; Mao, W.; Han, L.; Zhang, P.; Dai, S. Confined Ultrathin Pd-Ce Nanowires with Outstanding Moisture and SO₂ Tolerance in Methane Combustion. *Angewandte Chemie International Edition* **2018**, *57* (29), 8953–8957. <https://doi.org/10.1002/anie.201803393>.
- (81) Khader, M.; Al-Marri, M.; Ali, S.; Abdelmoneim, A. Active and Stable Methane Oxidation Nano-Catalyst with Highly-Ionized Palladium Species Prepared by Solution Combustion Synthesis. *Catalysts* **2018**, *8* (2), 66. <https://doi.org/10.3390/catal8020066>.
- (82) Takacs, L. The Historical Development of Mechanochemistry. *Chemical Society Reviews* **2013**, *42* (18), 7649. <https://doi.org/10.1039/c2cs35442j>.
- (83) Baláž, P.; Achimovičová, M.; Baláž, M.; Billik, P.; Cherkezova-Zheleva, Z.; Criado, J. M.; Delogu, F.; Dutková, E.; Gaffet, E.; Gotor, F. J.; et al. Hallmarks of Mechanochemistry: From Nanoparticles to Technology. *Chemical Society Reviews* **2013**, *42* (18), 7571. <https://doi.org/10.1039/c3cs35468g>.
- (84) Davis, R. M.; McDermott, B.; Koch, C. C. Mechanical Alloying of Brittle Materials. *Metallurgical Transactions A* **1988**, *19* (12), 2867–2874. <https://doi.org/10.1007/BF02647712>.
- (85) Enayati, M. H.; Mohamed, F. A. Application of Mechanical Alloying/Milling for Synthesis of Nanocrystalline and Amorphous Materials. *International Materials Reviews* **2014**, *59* (7), 394–416. <https://doi.org/10.1179/1743280414Y.0000000036>.
- (86) Bolm, C.; Hernández, J. G. Mechanochemistry of Gaseous Reactants. *Angewandte Chemie International Edition* **2019**, *58* (11), 3285–3299. <https://doi.org/10.1002/anie.201810902>.
- (87) Dong, H.; Moys, M. H. Assessment of Discrete Element Method for One Ball Bouncing in a Grinding Mill. *International Journal of Mineral Processing* **2002**, *65* (3–4), 213–226. [https://doi.org/10.1016/S0301-7516\(01\)00083-7](https://doi.org/10.1016/S0301-7516(01)00083-7).
- (88) Gilardi, G.; Sharf, I. Literature Survey of Contact Dynamics Modelling. *Mechanism and Machine Theory* **2002**, *37* (10), 1213–1239. [https://doi.org/10.1016/S0094-114X\(02\)00045-9](https://doi.org/10.1016/S0094-114X(02)00045-9).

- (89) Feng, Y. T.; Han, K.; Owen, D. R. J. Discrete Element Simulation of the Dynamics of High Energy Planetary Ball Milling Processes. *Materials Science and Engineering: A* **2004**, 375–377, 815–819. <https://doi.org/10.1016/j.msea.2003.10.162>.
- (90) Chen, W.; Schoenitz, M.; Ward, T.; Dave, R. N.; Dreizin, E. L. Numerical Simulation of Mechanical Alloying in a Shaker Mill by Discrete Element Method. *KONA* **2005**, 23 (0), 152–162. <https://doi.org/10.14356/kona.2005018>.
- (91) Rosenkranz, S.; Breitung-Faes, S.; Kwade, A. Experimental Investigations and Modelling of the Ball Motion in Planetary Ball Mills. *Powder Technology* **2011**, 212 (1), 224–230. <https://doi.org/10.1016/j.powtec.2011.05.021>.
- (92) Burmeister, C. F.; Kwade, A. Process Engineering with Planetary Ball Mills. *Chem. Soc. Rev.* **2013**, 42 (18), 7660. <https://doi.org/10.1039/c3cs35455e>.
- (93) Razavi-Tousi, S. S.; Szpunar, J. A. Effect of Ball Size on Steady State of Aluminum Powder and Efficiency of Impacts during Milling. *Powder Technology* **2015**, 284, 149–158. <https://doi.org/10.1016/j.powtec.2015.06.035>.
- (94) Trovarelli, A.; Zamar, F.; Llorca, J.; Leitenburg, C. de; Dolcetti, G.; Kiss, J. T. Nanophase Fluorite-Structured CeO₂-ZrO₂ Catalysts Prepared by High-Energy Mechanical Milling. *Journal of Catalysis* **1997**, 169 (2), 490–502. <https://doi.org/10.1006/jcat.1997.1705>.
- (95) Šepelák, V.; Bégin-Colin, S.; Le Caër, G. Transformations in Oxides Induced by High-Energy Ball-Milling. *Dalton Transactions* **2012**, 41 (39), 11927. <https://doi.org/10.1039/c2dt30349c>.
- (96) Šepelák, V.; Düvel, A.; Wilkening, M.; Becker, K.-D.; Heitjans, P. Mechanochemical Reactions and Syntheses of Oxides. *Chemical Society Reviews* **2013**, 42 (18), 7507. <https://doi.org/10.1039/c2cs35462d>.
- (97) Furlani, E.; Aneggi, E.; de Leitenburg, C.; Maschio, S. High Energy Ball Milling of Titania and Titania-Ceria Powder Mixtures. *Powder Technology* **2014**, 254, 591–596. <https://doi.org/10.1016/j.powtec.2014.01.075>.
- (98) Do, J.-L.; Frišić, T. Mechanochemistry: A Force of Synthesis. *ACS Central Science* **2017**, 3 (1), 13–19. <https://doi.org/10.1021/acscentsci.6b00277>.
- (99) Enayati, M. H. Formation of Nanoscale Layered Structures and Subsequent Transformations during Mechanical Alloying of Ni₆₀Nb₄₀ Powder Mixture in a Low Energy Ball Mill. *KONA Powder and Particle Journal* **2015**, 32 (0), 196–206. <https://doi.org/10.14356/kona.2015010>.
- (100) Da Silva, K. L.; Menzel, D.; Feldhoff, A.; Kübel, C.; Bruns, M.; Paesano, A.; Düvel, A.; Wilkening, M.; Ghafari, M.; Hahn, H.; et al. Mechanothesized BiFeO₃ Nanoparticles with Highly Reactive Surface and Enhanced Magnetization. *The Journal of Physical Chemistry C* **2011**, 115 (15), 7209–7217. <https://doi.org/10.1021/jp110128t>.
- (101) Chen, W.; Dave, R. N.; Pfeffer, R.; Walton, O. Numerical Simulation of Mechanofusion System. *Powder Technology* **2004**, 146 (1–2), 121–136. <https://doi.org/10.1016/j.powtec.2004.07.014>.
- (102) Buyanov, R. A.; Molchanov, V. V.; Boldyrev, V. V. Mechanochemical Activation as a Tool of Increasing Catalytic Activity. *Catalysis Today* **2009**, 144 (3–4), 212–218. <https://doi.org/10.1016/j.cattod.2009.02.042>.

- (103) Muñoz-Batista, M. J.; Rodriguez-Padron, D.; Puente-Santiago, A. R.; Luque, R. Mechanochemistry: Toward Sustainable Design of Advanced Nanomaterials for Electrochemical Energy Storage and Catalytic Applications. *ACS Sustainable Chemistry & Engineering* **2018**, *6* (8), 9530–9544. <https://doi.org/10.1021/acssuschemeng.8b01716>.
- (104) Ralphs, K.; Hardacre, C.; James, S. L. Application of Heterogeneous Catalysts Prepared by Mechanochemical Synthesis. *Chemical Society Reviews* **2013**, *42* (18), 7701. <https://doi.org/10.1039/c3cs60066a>.
- (105) Xu, C.; De, S.; Balu, A. M.; Ojeda, M.; Luque, R. Mechanochemical Synthesis of Advanced Nanomaterials for Catalytic Applications. *Chemical Communications* **2015**, *51* (31), 6698–6713. <https://doi.org/10.1039/C4CC09876E>.
- (106) Yang, Y.; Zhang, S.; Wang, S.; Zhang, K.; Wang, H.; Huang, J.; Deng, S.; Wang, B.; Wang, Y.; Yu, G. Ball Milling Synthesized MnO_x as Highly Active Catalyst for Gaseous POPs Removal: Significance of Mechanochemically Induced Oxygen Vacancies. *Environmental Science & Technology* **2015**, *49* (7), 4473–4480. <https://doi.org/10.1021/es505232f>.
- (107) Zhan, W.; Yang, S.; Zhang, P.; Guo, Y.; Lu, G.; Chisholm, M. F.; Dai, S. Incorporating Rich Mesoporosity into a Ceria-Based Catalyst via Mechanochemistry. *Chemistry of Materials* **2017**, *29* (17), 7323–7329. <https://doi.org/10.1021/acs.chemmater.7b02206>.
- (108) Zhao, B.; Tong, Y.; Zhao, Y.; Yang, T.; Yang, F.; Hu, Q.; Zhao, C. Preparation of Ultra-Fine Sm_{0.2}Ce_{0.8}O_{1.9} Powder by a Novel Solid State Reaction and Fabrication of Dense Sm_{0.2}Ce_{0.8}O_{1.9} Electrolyte Film. *Ceramics International* **2015**, *41* (8), 9686–9691. <https://doi.org/10.1016/j.ceramint.2015.04.037>.
- (109) Borchers, C.; Martin, M. L.; Vorobjeva, G. A.; Morozova, O. S.; Firsova, A. A.; Leonov, A. V.; Kurmaev, E. Z.; Kukhareenko, A. I.; Zhidkov, I. S.; Cholakh, S. O. Cu–CeO₂ Nanocomposites: Mechanochemical Synthesis, Physico-Chemical Properties, CO-PROX Activity. *Journal of Nanoparticle Research* **2016**, *18* (11). <https://doi.org/10.1007/s11051-016-3640-6>.
- (110) Maeda, Y.; Akita, T.; Kohyama, M. High Activity of Gold/Tin-Dioxide Catalysts for Low-Temperature CO Oxidation: Application of a Reducible Metal Oxide to a Catalyst Support. *Catalysis Letters* **2014**, *144* (12), 2086–2090. <https://doi.org/10.1007/s10562-014-1376-4>.
- (111) Tang, C.; Sun, B.; Sun, J.; Hong, X.; Deng, Y.; Gao, F.; Dong, L. Solid State Preparation of NiO-CeO₂ Catalyst for NO Reduction. *Catalysis Today* **2017**, *281*, 575–582. <https://doi.org/10.1016/j.cattod.2016.05.026>.
- (112) Kamolphop, U.; Taylor, Sarah. F. R.; Breen, J. P.; Burch, R.; Delgado, J. J.; Chansai, S.; Hardacre, C.; Hengrasme, S.; James, S. L. Low-Temperature Selective Catalytic Reduction (SCR) of NO_x with *n*-Octane Using Solvent-Free Mechanochemically Prepared Ag/Al₂O₃ Catalysts. *ACS Catalysis* **2011**, *1* (10), 1257–1262. <https://doi.org/10.1021/cs200326m>.
- (113) Kondrat, S. A.; Shaw, G.; Freakley, S. J.; He, Q.; Hampton, J.; Edwards, J. K.; Miedziak, P. J.; Davies, T. E.; Carley, A. F.; Taylor, S. H.; et al. Physical Mixing of Metal Acetates: A Simple, Scalable Method to Produce Active Chloride Free Bimetallic Catalysts. *Chemical Science* **2012**, *3* (10), 2965. <https://doi.org/10.1039/c2sc20450a>.

- (114) Lin, Y.; Watson, K. A.; Fallbach, M. J.; Ghose, S.; Smith, J. G.; Delozier, D. M.; Cao, W.; Crooks, R. E.; Connell, J. W. Rapid, Solventless, Bulk Preparation of Metal Nanoparticle-Decorated Carbon Nanotubes. *ACS Nano* **2009**, *3* (4), 871–884. <https://doi.org/10.1021/nn8009097>.
- (115) Siamaki, A. R.; Lin, Y.; Woodberry, K.; Connell, J. W.; Gupton, B. F. Palladium Nanoparticles Supported on Carbon Nanotubes from Solventless Preparations: Versatile Catalysts for Ligand-Free Suzuki Cross Coupling Reactions. *Journal of Materials Chemistry A* **2013**, *1* (41), 12909. <https://doi.org/10.1039/c3ta12512b>.
- (116) Zhou, M.; Zhao, J.; Zhang, P.; Chen, N.; Yang, S. Solvent-Free and Rapid Synthesis of Mesoporous Pt–Iron Oxide Catalysts *via* Mechanochemical Assembly. *Catalysis Science & Technology* **2019**, *9* (15), 3907–3913. <https://doi.org/10.1039/C9CY00970A>.
- (117) Ismagilov, Z. R.; Kuntsevich, S. V.; Shikina, N. V.; Kuznetsov, V. V.; Kerzhentsev, M. A.; Ushakov, V. A.; Rogov, V. A.; Boronin, A. I.; Zaikovskiy, V. I. Characterization of Alumina-Supported Uranium Oxide Catalysts in Methane Oxidation. *Catalysis Today* **2010**, *157* (1–4), 217–222. <https://doi.org/10.1016/j.cattod.2010.02.020>.
- (118) Eckert, R.; Felderhoff, M.; Schüth, F. Preferential Carbon Monoxide Oxidation over Copper-Based Catalysts under In Situ Ball Milling. *Angewandte Chemie International Edition* **2017**, *56* (9), 2445–2448. <https://doi.org/10.1002/anie.201610501>.
- (119) Ralphs, K.; Zhang, C.; James, S. L. Solventless Mechanochemical Metallation of Porphyrins. *Green Chemistry* **2017**, *19* (1), 102–105. <https://doi.org/10.1039/C6GC02420C>.

2 Experimental Methods

Purpose of this chapter is to give an overview of the experimental methods employed throughout the PhD research work. The solventless mechano-chemical synthesis was optimized for each set of samples based on the starting materials considered, therefore details on synthesis parameters, metal precursors and support oxides will be given at the beginning of each chapter. Here a more general description of the synthesis will be reported, together with an overview of characterization methods and testing conditions employed.

2.1 Synthesis of Catalytic Materials

2.1.1 Synthesis of Support Oxides

CeO₂ and ZrO₂ polycrystalline supports were synthesized by precipitation in presence of H₂O₂, following a procedure developed previously in our group.¹ Briefly, a 0.2 M solution of cerium nitrate exahydrate (Ce(NO₃)₃·6H₂O) or zirconyl nitrate (ZrO(NO₃)₂) (Treibacher Industrie AG) was prepared, then hydrogen peroxide (H₂O₂, Aldrich, 35%) was poured into the solution to obtain a molar M:H₂O₂ ratio of 3. To induce precipitation, an appropriate amount of ammonia solution (NH₄OH, Sigma Aldrich, 30%) was added until pH reached a value of 10.5. The slurry was maintained under stirring for 4 hours and then it was filtered, washed with distilled water, dried in static air at 393 K for 15 hours and eventually calcined in static air at 1173 K for 3 hours. The surface area after calcination was 2.6 m²/g for ceria and 5.2 m²/g for zirconia. γ-Al₂O₃ was prepared by calcination of pseudoboehmite in static air at 1173 K for 3 hours (BET surface area 146 m²/g).

Other commercial supports were used in Chapters 4 and 5. Commercial ceria (Treibacher Industrie. AG) and ZrO₂ (Grace) powders were used after calcination in static air at 1173 K, resulting in BET surface area of 3 m²/g and 20 m²/g, respectively. To explore the effect of higher surface area, a thermally stable CeO₂ gently provided by Ford Motor Company, Dearborn (MI), was used after calcination at 1173 K (BET surface area 25 m²/g) and 1473 K (3 m²/g) in Chapters 6 - 8.

Ceria with defined morphology was prepared by hydrothermal methods following an established procedure.^{2,3} Ceria nanocubes (CeNC) were prepared starting from a cerium nitrate solution (5.21 g of $\text{Ce}(\text{NO}_3)_3 \cdot 6\text{H}_2\text{O}$ in 30 mL of distilled water). 210 ml of a 6.9M NaOH solution (57.60 g of NaOH dissolved in 210 mL of distilled water) was then added dropwise under vigorous mixing. The obtained suspension was then transferred in a 300 ml Teflon-lined Parr 4843 autoclave and heated at 453 K for 24 hours. After cooling, the precipitate was recovered by centrifugation and washed three times in distilled water and ethanol for further purification and separation. Ceria nanorods (CeNR) were synthesized by adding dropwise 200 ml of a 9.45M NaOH solution into a solution of $\text{CeCl}_3 \cdot 7\text{H}_2\text{O}$ (5.36 g in 40 mL of distilled water). After precipitation, the mixture was transferred to the autoclave, heated at 373 K for 48 h, cooled and centrifuged to obtain the separated cake. For both syntheses, the obtained precipitate was dried overnight at 333 K and calcined at 723 K for 4 hours prior to their use.

2.1.2 Palladium-based Catalysts

Reference catalytic materials were prepared by conventional incipient wetness impregnation (IW). For the preparation of the reference PdCeIW catalysts, an aqueous solution of $\text{Pd}(\text{NO}_3)_2$ (Aldrich, 99,999%) was used in appropriate amount to reach the desired nominal Pd loading (1 wt% or 4 wt%). The solution was impregnated drop by drop on the ceria support. The catalyst was then dried at 393 K overnight and calcined at 1173 K for 3 hours in static air.

Object of the current study are samples prepared by dry mechano-chemical synthesis, which was carried out in different conditions and setups. Details of the synthesis are reported in the following and summarized in each chapter. Milling of Pd black (Aldrich, surface area 40 m^2/g , mean particle size 10 μm) and ceria powders was carried out in a Pulverisette 23 Mini-Mill for 10 min at a frequency of 15 Hz to obtain a nominal Pd loading of 1 wt%. The powders (990 mg of CeO_2 and 10 mg of Pd) were put in a 15 ml zirconia bowl with 1 grinding ball made of ZrO_2 (diameter = 15 mm, weight = 10 g, Ball Powder Ratio, BPR = 10). The samples so obtained were denoted as PdCeM. For comparison, other samples were prepared using PdO (Aldrich, surface area 74 m^2/g , mean particle size <10 μm) on ceria and Pd supported on zirconia. 11.5 mg of PdO or 10 mg of Pd were mixed with 990 mg of CeO_2 or ZrO_2 in the same milling setup, and the samples are denoted as PdOCeM and PdZrM, respectively. After milling, the powders were recovered and used without further treatments.

A different class of materials was prepared using palladium salt precursors, such as palladium nitrate (Johnson Matthey, 41.54% Pd) and palladium acetate (Sigma Aldrich, 99.99%). The appropriate amount of salt was milled with the desired support oxide in two milling steps of 10 minutes each at 15 Hz in the same experimental setup. The activation of the catalyst was carried out in reaction conditions to obtain the best catalytic activity, as discussed in detail in Chapter 5. Under the conditions described above, no trace of ZrO_2 from the milling apparatus were found on the final material.

To investigate the effect of the milling parameters, other Pd-ceria formulations were prepared by mixing the two components (Pd black and commercial ceria) with lower or higher intensity with respect to PdCeM. Low intensity mixing was achieved when palladium nanoparticles and ceria powders were loosely mixed inside the jar in the absence of grinding balls (denoted as PdCeL) or simply grinded in an agate mortar for 10 minutes (PdCeG). On the medium-high intensity side, one sample was prepared by milling for 1 hour in the same conditions as PdCeM (Pulverisette 23 Minimill, 15 Hz and one zirconia ball, named PdCeM 1h), while other samples were prepared in a Spex8000 Mixer Mill rotating at 875 rpm, referred to as PdCeHM (High-intensity Milling). These samples PdCeHM were prepared by loading 1.188 g of CeO_2 and 12 mg of Pd into a 50 ml YSZ grinding bowl with 9 zirconia balls (diameter = 10 mm, weight = 3 g, BPR = 22) for milling times ranging from 5 minutes to 8 hours. The obtained powders were tested without further treatments.

2.2 Characterization

In order to investigate in depth the structure-activity correlation, structural, textural and redox properties of the prepared materials were studied by several *ex-situ* and *in-situ* techniques.⁴ Details will be given in the following.

2.2.1 Surface Area and Pore Size Measurements

Evaluation of the catalysts surface area was carried out in a Micrometrics Tristar Porosimeter by analyzing N_2 adsorption isotherms at 77 K using the Brunauer-Emmett-Teller method (BET). Pore size measurements were performed in the same setup using the Barrett-Joyner-Halenda method (BJH) on desorption isotherms. Catalyst samples were degassed at 423 K for 1.5 hours prior to analysis.

2.2.2 Temperature Programmed Oxidation (TPO)

TPO analysis was carried out to analyze the palladium oxidation and decomposition behavior⁵ in the same setup used for activity measurements (Scheme 2.2). For TPO tests, 150 mg of powder catalyst were placed in a quartz reactor supported on a quartz wool bed. The sample was then exposed to a flowing mixture (60 ml/min) containing 2 vol% O₂ in N₂, and the oxygen release and consumption was monitored with an on-line ABB Magnos 106 paramagnetic analyzer during 3 heating/cooling cycles from RT to 1273 K (10 K/min heating/cooling rate). Data were recorded every 10 seconds.

2.2.3 Temperature Programmed Reduction (TPR)

TPR experiments were carried out in a Micromeritics AutoChem II 2920 analyzer on 50 mg of catalyst, loaded in a U-shaped quartz micro-reactor. The fresh sample was pretreated in air at 723 K for 1 h, then cooled to 193 K under N₂ flow by pumping liquid nitrogen in the furnace. The analysis was performed under a flowing reducing mixture of 4.5% H₂ in N₂ (flow rate = 35 ml/min), heating the sample from 193 K to 1233 K at a heating rate of 10 K/min. TPR tests on post-reaction samples were performed without any pretreatment.

2.2.4 Thermo-gravimetric Analysis (TGA)

To analyze the decomposition behavior of palladium precursor salts supported on ceria, thermogravimetric analyses were carried out in a Q500 - TA Instruments thermobalance. Usually, ~15 mg of sample were loaded on a platinum pan with 60 ml/min of gas flowing horizontally over the sample surface. The sample was gradually heated at 10 K/min from RT to 1173 K, then cooled to 373 K. Weight loss profiles could be measured under synthetic air (20.9% O₂/N₂), inert gas (N₂), low oxygen partial pressure (2% O₂/N₂) and under reaction conditions (0.5 vol% CH₄, 2 vol% O₂ in He), with a total gas flow of 60 ml/min.

2.2.5 Transmission Electron Microscopy (TEM)

Microstructural characterization by High Resolution Transmission Electron Microscopy (HRTEM)⁶ was carried out at the Universitat Politècnica de Catalunya, in Barcelona, thanks to the collaboration with prof. Jordi Llorca. Images were collected at 200 kV with a JEOL JEM-2010F electron microscope equipped with a field emission gun. The point-to-point resolution was 0.19 nm and the resolution between lines was 0.14 nm. Samples were dispersed in alcohol in an ultrasonic bath, and a drop of supernatant suspension was poured onto a holey carbon-coated grid.

To investigate the morphology of nano-shaped ceria particles, transmission electron microscopy (TEM) analysis was carried out by a Zeiss LIBRA 200FE microscope equipped with a 200 kV FEG source. Prior to introduction in the instrument, the samples were ultrasonically dispersed in isopropyl alcohol and a drop of the suspension was deposited onto a lacey carbon copper grid (300 mesh).

2.2.6 X-ray Photoelectron Spectroscopy (XPS)

Ex-situ X-ray photoelectron spectroscopy (XPS) was performed at the Universitat Politècnica de Catalunya, Barcelona, with a SPECS system using an Al X-ray source (150 W) and a 9-channel Phoibos detector at a pressure below 10^{-6} Pa. Quantification was carried out using Shirley baselines and Gaussian-Lorentzian lineshapes.

Ambient Pressure XPS (AP-XPS) measurements⁷ were performed at the Chemistry Division of Brookhaven National Laboratory (BNL), in Upton (NY), with a commercial SPECS AP-XPS chamber equipped with a Phoibos 150 EP MCD-9 analyzer. The evaluated powder catalyst was pressed on an aluminum plate and then loaded into the AP-XPS chamber. Methane oxidation tests were carried out under a 10 mTorr CH₄, 40 mTorr O₂ atmosphere, after pretreatment in 20 mTorr O₂ at 673 K for 30 min. The O 1s, Ce 3d, C 1s and Pd 3d XPS regions were collected from RT to 673 K at a 100 K interval. The Ce 3d photoemission line with the strongest Ce⁴⁺ feature (916.9 eV) was used for the energy calibration.

2.2.7 X-ray Diffraction Analysis

XRD analysis was performed *ex-situ* in a Philips X'Pert diffractometer equipped with an X'Celerator detector using Ni-filtered Cu K α radiation ($\lambda = 1.542$ Å). Data were recorded in the 2θ range of 20-100° with a step size of 0.02° and a counting time per step of 40 s. Fitting of the crystalline phases was performed using the Philips X'Pert HighScore program. Particle size was estimated using the Scherrer equation⁸ (eq. 2.1) using the {220} ceria peak at $2\theta = 47.48^\circ$ and the instrumental peak widening correction measured for a silica standard.

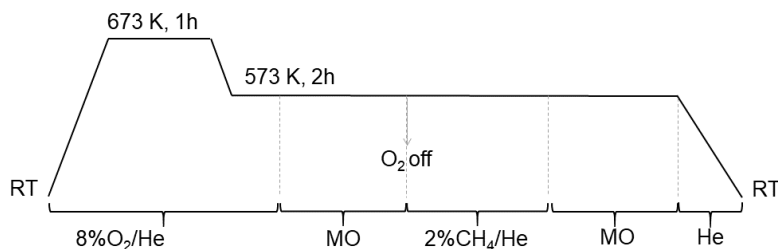
$$d_p(\text{Å}) = \frac{K \lambda}{\sqrt{B_{obs}^2 - B_{strum}^2} \cos\theta} \quad (\text{eq. 2.1})$$

In-situ XRD analysis was performed at 17BM beamline at the Advanced Photon Source (APS) of Argonne National Laboratory, in Argonne (IL). The powdered sample was loaded in a 0.9mm ID, 1.1mm OD quartz capillary between quartz wool and mounted in a Clausen cell.⁹ Through individual mass flow controllers, 10 ml/min of the required gas mixture were

introduced in the capillary. Samples were stepwise heated at 10 K/min to 773 K for methane oxidation tests or to 973 K in dry reforming tests and the gaseous species at the outlet were monitored with an on-line residual gas analyzer. Data were collected throughout reaction at a $\lambda = 0.24169 \text{ \AA}$ beam radiation length (51.298 keV) every 60 s with a PerkinElmer Si flat panel detector. Elaboration of the recorded two-dimensional XRD images to Intensity-vs-2 θ diagrams and Rietveld analyses were carried out with GSAS-II software.¹⁰

2.2.8 Diffuse Reflectance Infrared Fourier Transform Spectroscopy (DRIFTS)

In-situ DRIFTS spectra were collected in absorbance mode using a Bruker Vertex 70 FTIR spectrometer equipped with a Harrick-Praying Mantis cell at the Chemistry Department of Brookhaven National Laboratory, Upton (NY). *In-situ* methane oxidation and CO chemisorption measurements were carried out to investigate the adsorbed species on the catalysts surface. Powder samples were loaded in the reaction cell above a quartz wool bed under 50 ml/min total gas flow. An on-line residual gas analyzer (RGA) was employed to measure gas concentrations at the outlet (O_2 , CH_4 , CO , CO_2 , H_2 , H_2O) during reaction. Before reaction, the sample was pretreated in low oxygen pressure (8% O_2 in He) at 673 K for 1 hour. After cooling at the reaction temperature, the background was collected with 256 scans. As DRIFTS probes the adsorbed species on the catalyst surface, the fluidic- and thermo-dynamic properties of the commercial cell do not correspond to the conditions in the activity measurements reactor,¹¹ therefore experimental conditions needed to be optimized for the set-up. For methane oxidation tests, a gas mixture containing 2 vol% CH_4 and 8 vol% O_2 in He/ N_2 was employed and the sample heated following Scheme 2.1. For CO adsorption tests, a 5% CO/He mixture was used (40 ml/min total gas flow). The sample was held under CO containing mixture for 10 minutes at RT, then purged in He for 30 min. Spectra were collected with 128 scans every 60 s during CO adsorption and after purging.



Scheme 2.1: Experimental detail of the in-situ DRIFTS methane oxidation (MO) tests. Heating/cooling ramps: 20 K/min; reaction mixture: 2% $\text{CH}_4/8\%\text{O}_2/\text{He}$.

2.2.9 Raman Spectroscopy

Raman spectra¹² were collected with an Xplora Plus Micro-Raman system (Horiba, Kyoto, Japan). The samples were excited with the 532 nm radiation at room temperature and the spectra were acquired with a resolution of 1 cm^{-1} and 2 accumulations of 10 s with a 50x LWD objective. Mapping of the sample surface was performed on a $12 \times 12\ \mu\text{m}^2$ grid, with 3 μm spacing between acquisition points. The intensity ratio between the B_{1g} vibrational mode of PdO at 650 cm^{-1} and the F_{2g} vibrational mode of CeO_2 at $\sim 460\text{ cm}^{-1}$ ($I_{\text{PdO}}/I_{\text{CeO}_2}$) was plotted to analyze the PdO distribution and uniformity on the mesoscale.

2.2.10 Additional Characterization

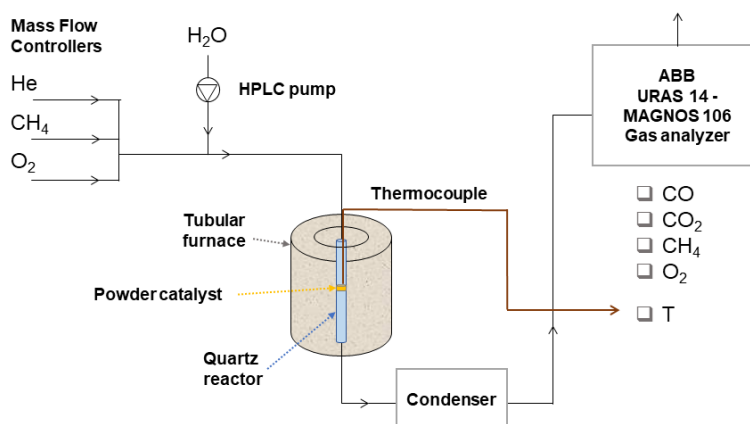
ICP-mass elemental analysis was used to measure the actual loading of palladium on prepared samples. Particle size distributions of Pd and PdO powders were determined by laser scattering using a Horiba LA950 laser scattering particle size analyzer. Analyses were carried out in water after 7 min sonication.¹³

2.3 Catalytic Activity

The catalytic activity of prepared samples in powder form was evaluated in a lab-scale reactor for the complete oxidation of methane in transient and stationary conditions under excess of oxygen. Further methane activation mechanisms in reducing atmosphere were investigated, such as steam and dry reforming. Additional methane oxidation and steam reforming tests were carried out on washcoated monoliths in order to test them in more realistic conditions thanks to the collaboration with Ford Motor Company, Dearborn (MI).

2.3.1 Methane Oxidation Light-off Activity

Catalytic methane combustion activity was measured in a lab-scale setup illustrated in Scheme 2.2.



Scheme 2.2: Experimental setup for methane combustion tests.

Methane oxidation tests were performed in lean conditions, in dry or wet atmosphere. Usually, 120 mg of catalyst in powder form was loaded in the quartz reactor on a quartz wool bed and 180 ml/min of a gas mixture containing 0.5 vol% CH₄, 2 vol% O₂ in He were introduced, resulting in a gas hourly space velocity (GHSV) of ca. $2 \cdot 10^5 \text{ h}^{-1}$. For wet experiments, 10 vol% H₂O was added to the gas feed to simulate the steam content measured at NGV tailpipe and investigate the deactivation behavior of prepared samples.¹⁴ Water was introduced by a Waters 515 HPLC pump in liquid form and transformed to water vapor through heated lines. During transient tests, the temperature was increased at 10 K/min from RT to 1173 K, and then cooled; the cycle was repeated twice. The second heating/cooling cycle is most representative of the catalytic activity¹⁵ and thus will be reported in the following chapters for comparison, unless otherwise stated. Reactants and products were monitored with an on-line ABB Uras 14 infrared gas analyzer, and the temperature was measured with a K-type thermocouple placed at the top of the catalytic bed. Comparative light-off experiments were carried out at higher space velocity by loading 60 mg of sample under the same experimental conditions.

Methane oxidation tests were also carried out at Ford Motor Company, Dearborn (MI), on powder and monolith samples. Powder catalysts were pressed and sieved, then diluted with ground up cordierite at a 1:1 weight ratio. 1 g of mixed sample was then loaded in a 0.50"OD quartz reactor tube between two beds of quartz wool and tested under 2L/min of reaction mixture (0.1% CH₄, 1% O₂, 5% H₂O, 5% CO₂ in N₂, $\lambda=1.03$), heating the sample from 373 K to 1173 K for three consecutive heating/cooling cycles. An oxidative or reducing pretreatment at 1173 K was performed before reaction by adding 1% O₂ or 1% CO

to 0.1% CH₄, 5% H₂O, 5%CO₂ in N₂. Monoliths were prepared by depositing the prepared dry-milled catalysts on a cordierite core to reach a final washcoat loading of 3 gci. A 0.70”D x 1.0” L sized core was inserted in a quartz tube and exposed to the same reaction atmosphere and powder experiments to reach a final GHSV of 19000 h⁻¹. Monolithic samples were tested fresh (or de-greened) and after synthetic aging. The synthetic aging process consisted in holding the sample at 1223 K for 50 hours, repeating 60-second-long cycles of 54s lean (4%O₂/ 10%H₂O) and 6s rich pulses (3%CO/ 1%H₂/ 10% H₂O).

2.3.2 Methane Oxidation Stability Tests

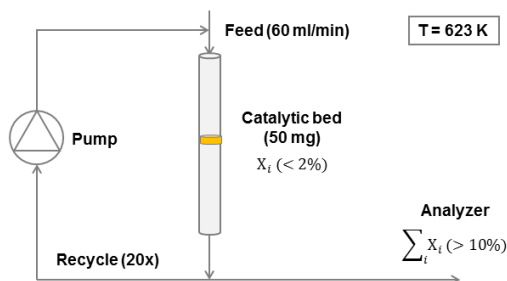
Time-on-Stream (TOS) tests were carried out in stationary conditions to evaluate the stability and durability of prepared samples. Tests were performed in the same experimental setup as transient tests, illustrated above in Scheme 2.2. Catalysts were held at 723 K for 24 hours either in dry atmosphere or in wet conditions, i.e. with 10 vol% steam added to the gas feed. Before reaction, one dry combustion cycle up to 1173 K was performed as pre-treatment. After cooling to RT, water was added to the gas feed, if necessary, and the temperature was ramped at 10 K/min to 723 K and held for 24 hours. The catalyst deactivation during the isothermal period was monitored by analyzing the normalized methane conversion (eq. 2.2):

$$X_{norm,CH_4} = \frac{X_{CH_4}(t)}{X_{CH_4}(t=0)} \quad (eq. 2.2)$$

where X_{CH₄}(t) is the conversion at time t and X_{CH₄}(t=0) is the initial conversion measured at 723 K.

2.3.3 Methane Oxidation Reaction Rate Measurements

Reaction rates measurements were carried out in a recycle reactor set-up,¹⁶ illustrated in Scheme 2.3. For rate evaluation tests, 50 mg of sample were placed in a quartz reactor (6 mm internal diameter) over a quartz wool bed and exposed to the same lean reaction mixture as standard combustion tests (0.5 vol% CH₄, 2 vol% O₂ in He) flowing at 60 ml/min. One heating/cooling cycle up to 1173 K was performed as a pre-treatment. After cooling, the gases were recirculated with a recycle ratio ~20, to ensure that the catalyst was working in differential conditions (conversion per step < 2%). The temperature was raised up to 623 K and held for 10 minutes while recording methane conversion. This value was used for the calculation of the reaction rate, and the verification of kinetic regime is reported in Appendix A.



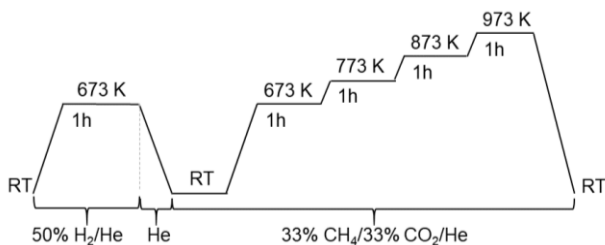
Scheme 2.3: Recycle reactor.

2.3.4 Steam Reforming (SR)

Steam reforming activity tests were carried out in collaboration with Ford Motor Company at Ford Research and Innovation Center in Dearborn (MI). Tests were carried out both on powdered catalysts and on monoliths, in the same setup used for methane oxidation tests (section 2.3.1). For SR tests, an oxidative pretreatment at 1173 K under 0.1% CH₄, 1% O₂, 5% H₂O, 5%CO₂ in N₂ was performed before reaction, then oxygen was removed and 0.15% CO was added to the gas feed ($\lambda=0.99$). Methane conversion on fresh (de-greened) and aged samples was evaluated during three consecutive heating/cooling cycles from 373 to 1173 K.

2.3.5 Dry Reforming of Methane (DRM)

The activity of prepared samples was tested for the dry reforming of methane at Brookhaven National Laboratory. 10 mg of powder catalyst, diluted with 10 mg of pre-calcined SiO₂ (1173 K, 400-800 μ m) were loaded in a quartz reactor and pretreated at 673 K for 1 h in 50%H₂/N₂ (20 ml/min). After cooling, the sample was heated stepwise from RT to 973 K under a 1:1:1 CH₄:CO₂:N₂ mixture (30 ml/min), as shown in Scheme 2.4. Their DRM activity was measured at 673 K, 773 K, 873 K and 973 K, holding the temperature for 1 hour at each step. The evolution of reaction products was analyzed with an on-line gas chromatography instrument Agilent 7890A. Stability tests were performed holding the sample at 973 K for 24 hours after H₂ pre-treatment.



Scheme 2.4 : Experimental detail of the dry reforming activity test.

2.4 References

- (1) Moser, M.; Vilé, G.; Colussi, S.; Krumeich, F.; Teschner, D.; Szentmiklósi, L.; Trovarelli, A.; Pérez-Ramírez, J. Structure and Reactivity of Ceria–Zirconia Catalysts for Bromine and Chlorine Production via the Oxidation of Hydrogen Halides. *Journal of Catalysis* **2015**, *331*, 128–137. <https://doi.org/10.1016/j.jcat.2015.08.024>.
- (2) Aneggi, E.; Wiater, D.; de Leitenburg, C.; Llorca, J.; Trovarelli, A. Shape-Dependent Activity of Ceria in Soot Combustion. *ACS Catalysis* **2014**, *4* (1), 172–181. <https://doi.org/10.1021/cs400850r>.
- (3) Mai, H.-X.; Sun, L.-D.; Zhang, Y.-W.; Si, R.; Feng, W.; Zhang, H.-P.; Liu, H.-C.; Yan, C.-H. Shape-Selective Synthesis and Oxygen Storage Behavior of Ceria Nanopolyhedra, Nanorods, and Nanocubes. *The Journal of Physical Chemistry B* **2005**, *109* (51), 24380–24385. <https://doi.org/10.1021/jp055584b>.
- (4) Che, M.; Védrine, J. C. *Characterization of Solid Materials and Heterogeneous Catalysts: From Structure to Surface Reactivity*. Eds.; Wiley-VCH Verlag GmbH & Co. KGaA: Weinheim, Germany, 2012. <https://doi.org/10.1002/9783527645329>.
- (5) Farrauto, R. J.; Hobson, M. C.; Kennelly, T.; Waterman, E. M. Catalytic Chemistry of Supported Palladium for Combustion of Methane. *Applied Catalysis A: General* **1992**, *81* (2), 227–237. [https://doi.org/10.1016/0926-860X\(92\)80095-T](https://doi.org/10.1016/0926-860X(92)80095-T).
- (6) Maiti, S.; Llorca, J.; Dominguez, M.; Colussi, S.; Trovarelli, A.; Priolkar, K. R.; Aquilanti, G.; Gayen, A. Combustion Synthesized Copper-Ion Substituted FeAl_2O_4 ($\text{Cu}_{0.1}\text{Fe}_{0.9}\text{Al}_2\text{O}_4$): A Superior Catalyst for Methanol Steam Reforming Compared to Its Impregnated Analogue. *Journal of Power Sources* **2016**, *304*, 319–331. <https://doi.org/10.1016/j.jpowsour.2015.11.066>.
- (7) Palomino, R. M.; Hamlyn, R.; Liu, Z.; Grinter, D. C.; Waluyo, I.; Rodriguez, J. A.; Senanayake, S. D. Interfaces in Heterogeneous Catalytic Reactions: Ambient Pressure XPS as a Tool to Unravel Surface Chemistry. *Journal of Electron Spectroscopy and Related Phenomena* **2017**, *221*, 28–43. <https://doi.org/10.1016/j.elspec.2017.04.006>.
- (8) Jenkins, R.; Snyder, R. L. *Introduction to X-Ray Powder Diffractometry*; Wiley: New York, 1996.
- (9) Chupas, P. J.; Chapman, K. W.; Kurtz, C.; Hanson, J. C.; Lee, P. L.; Grey, C. P. A Versatile Sample-Environment Cell for Non-Ambient X-Ray Scattering Experiments. *Journal of Applied Crystallography* **2008**, *41* (4), 822–824. <https://doi.org/10.1107/S0021889808020165>.
- (10) Toby, B. H.; Von Dreele, R. B. GSAS-II: The Genesis of a Modern Open-Source All Purpose Crystallography Software Package. *Journal of Applied Crystallography* **2013**, *46* (2), 544–549. <https://doi.org/10.1107/S0021889813003531>.
- (11) Meunier, F. C. The Design and Testing of Kinetically-Appropriate Operando Spectroscopic Cells for Investigating Heterogeneous Catalytic Reactions. *Chemical Society Reviews* **2010**, *39* (12), 4602. <https://doi.org/10.1039/b919705m>.
- (12) Larkin, P. Introduction. In *Infrared and Raman Spectroscopy*; Elsevier, 2011; pp 1–5. <https://doi.org/10.1016/B978-0-12-386984-5.10001-1>.
- (13) Li, H.; Li, J.; Bodycomb, J.; Patience, G. S. Experimental Methods in Chemical Engineering: Particle Size Distribution by Laser Diffraction—PSD. *The Canadian Journal of Chemical Engineering* **2019**, *97* (7), 1974–1981. <https://doi.org/10.1002/cjce.23480>.

- (14) Gholami, R.; Alyani, M.; Smith, K. Deactivation of Pd Catalysts by Water during Low Temperature Methane Oxidation Relevant to Natural Gas Vehicle Converters. *Catalysts* **2015**, *5* (2), 561–594. <https://doi.org/10.3390/catal5020561>.
- (15) Danielis, M.; Colussi, S.; de Leitenburg, C.; Soler, L.; Llorca, J.; Trovarelli, A. Outstanding Methane Oxidation Performance of Palladium-Embedded Ceria Catalysts Prepared by a One-Step Dry Ball-Milling Method. *Angewandte Chemie International Edition* **2018**, *57* (32), 10212–10216. <https://doi.org/10.1002/anie.201805929>.
- (16) Colussi, S.; Gayen, A.; Llorca, J.; de Leitenburg, C.; Dolcetti, G.; Trovarelli, A. Catalytic Performance of Solution Combustion Synthesized Alumina- and Ceria-Supported Pt and Pd Nanoparticles for the Combustion of Propane and Dimethyl Ether (DME). *Industrial & Engineering Chemistry Research* **2012**, *51* (22), 7510–7517. <https://doi.org/10.1021/ie2016625>.

3 Outstanding Methane Oxidation Performance of Pd-embedded Ceria Catalysts Prepared by a One-step Dry Ball-milling Method

Abstract

By carefully mixing Pd metal nanoparticles with CeO₂ polycrystalline powder under dry conditions a new unpredicted arrangement of the Pd-O-Ce interface is obtained, where an amorphous shell containing Pd species dissolved in ceria is covering a core of CeO₂ particles. The robust contact that is generated at nanoscale, along with mechanical forces generated during mixing, promotes the redox exchange between Pd and CeO₂ and creates highly reactive and stable sites constituted by PdO_x embedded into CeO₂ surface layers. This specific arrangement outperforms conventional Pd/CeO₂ reference catalysts in methane oxidation, by lowering light-off temperature by more than 50 degrees and boosting reaction rate. The origin of the outstanding activity is traced back to the structural properties of the interface, modified at nanoscale by mechano-chemical interaction, and it is unraveled by a combined set of experimental data including high resolution transmission electron microscopy and supported by recent computational studies.

This was published as:

Danielis, M.; Colussi, S.; de Leitenburg, C.; Soler, L.; Llorca, J.; Trovarelli, A. Outstanding Methane Oxidation Performance of Palladium-Embedded Ceria Catalysts Prepared by a One-Step Dry Ball-Milling Method. *Angewandte Chemie International Edition* **2018**, *57* (32), 10212–10216. <https://doi.org/10.1002/anie.201805929>.

3.1 Introduction

The increasing concern over the abundant emissions of greenhouse gases from motor vehicles is pushing towards the development of more efficient catalysts for their abatement. This is particularly true for natural gas fueled vehicles, for which the exponential growth of the market and the concern for methane global warming potential urge for the design of catalytic systems with improved activity at low temperature and higher resistance to deactivation under operating conditions.¹ An efficient low temperature activation of the CH₄ molecule would also be a significant advancement in the field of methane utilization, an issue that is now attracting several efforts due to the increased supplies of shale gas and the consequent availability of natural gas as a feedstock.² Pd-based formulations are the most effective for methane oxidation, and the use of ceria as support confers additional benefits to the catalysts due to its unique redox features and to the level of Pd-Ce interfacial interactions.³⁻⁷ It is reported from experimental^{4,8-10} and computational^{11,12} studies that an enhanced Pd-ceria interaction can improve significantly the catalytic activity of these materials. In particular, the presence of Pd into ceria lattice can lead to the formation of highly reactive Pd^{2+/4+} sites which show lower methane activation barriers compared to isolated PdO_x units. Interestingly, differently from what happens on PdO_x clusters, on these ionic Pd species methane activation proceeds via hydrogen abstraction, a route that is potentially very important for methane utilization.¹¹

We have already reported the increased activity of a Pd/CeO₂ catalyst prepared by solution combustion synthesis in which the substitution of Pd²⁺ ions into ceria lattice caused the formation of ordered arrays of oxygen vacancies and highly reactive undercoordinated oxygen atoms.¹³ More recently we also investigated the milling of CeO₂-based materials with carbon, originating a 2D carbon layer, covering the ceria particles, and improving the interfacial redox exchange between the two materials.¹⁴ Here, by combining the above mentioned approaches, we use a controlled one-step dry milling procedure where Pd metal nanoparticles are put in contact with ceria particles to prepare a methane oxidation catalyst that outperforms traditional Pd/CeO₂ due to the unique structural arrangements that characterize metal/support interface at nanoscale. In addition, avoiding the use of Pd nitrate or chloride solution significantly reduces waste generation ensuring lower environmental impact. The characteristics of the preparation method, the properties and performances of the catalyst have been investigated in detail; the data suggest a correlation between the

unusual morphology developed at nanoscale and the high catalytic activity observed, and this correlation is supported by most recent theoretical simulations.^{11,12}

3.2 Experimental

The details on samples preparation with milling parameters, the detailed description of characterization methods and testing conditions are reported in Chapter 2 (Sections 2.1, 2.2 and 2.3, respectively). Briefly, the mechanically mixed samples (denoted with M) were prepared by mixing together metallic Pd nanoparticles with CeO₂ powder aged at 1173 K in a mini ball mill, to obtain a nominal Pd loading of 1% wt. (PdCeM). Reference catalysts with the same nominal Pd loading were also synthesized by incipient wetness impregnation on the same CeO₂ support (PdCeIW) and by solution combustion synthesis (PdCeSCS). An additional catalyst, where PdO nanoparticles were used in substitution of Pd metal in the milling procedure, was also prepared for comparison (PdOCeM). To check the effect of the support, comparison of PdCeM with Pd supported on ZrO₂ (PdZrM) prepared by the same procedure was also carried out. Catalytic activity was evaluated in methane oxidation tests under lean conditions (0.5% CH₄, 2% O₂ in He) heating the sample up to 1173 K. Stability under reaction conditions and durability were tested in comparison to PdCeIW following six reaction cycles up to 1173 K and monitoring time on stream behavior also under hydrothermal conditions.

3.3 Results and Discussion

The crystalline phases and oxidation state of palladium on PdCeIW and PdCeM were evaluated by means of X-ray diffraction and temperature programmed reduction tests. The comparison of XRD spectra and TPR profiles of PdCeM and PdCeIW are reported in Figure 3.1 and Figure 3.2, respectively. Due to the low Pd loading in all catalysts the Pd/PdO diffraction signals are barely visible. After reaction a small peak at ca. 34 degrees is detected due to PdO in all samples (see inset in Figure 3.1). In Figure 3.2 temperature programmed reduction of catalysts pretreated in air at 623 K shows reduction of PdO and evolution of hydrogen due to Pd hydride formation and decomposition.¹⁵ In PdCeM the reduction of PdO is shifted to 25 degrees to lower temperature compared to PdCeIW. Without pretreatment in air, only a negligible reduction peak is observed and Pd is present mainly in the form of small Pd metal nanoclusters (inset).

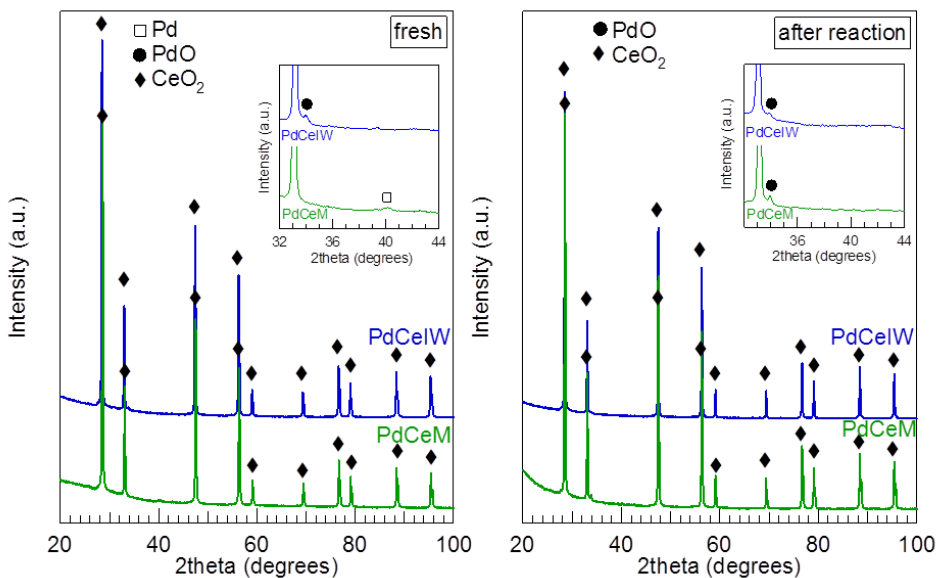


Figure 3.1: XRD spectra of PdCeM and PdCeIW. Left: spectra collected on fresh samples; right: spectra of the samples after reaction. In the inset, the range $2\theta = 32\text{--}44^\circ$ is magnified to focus on the Pd (40.2°) and PdO (34.0°) peaks.

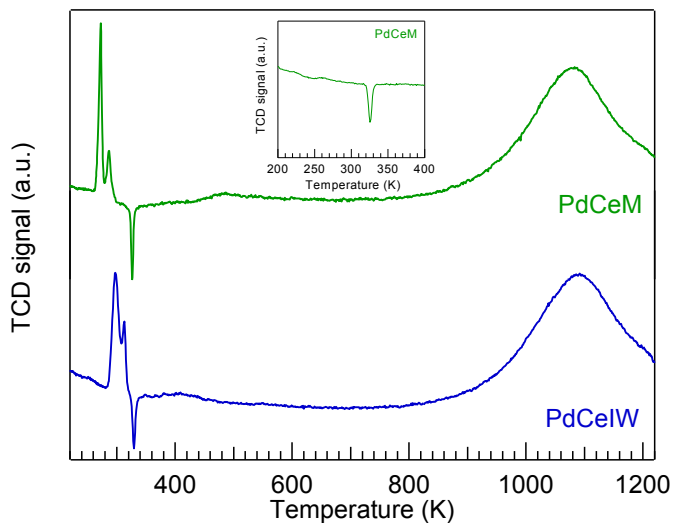


Figure 3.2: H_2 -TPR profiles of PdCeM and PdCeIW. Inset: H_2 -TPR profile of PdCeM without pretreatment in air.

The light-off curves of methane combustion under lean atmosphere for the different Pd-ceria formulations are shown in Figure 3.3, along with the corresponding cooling part of the cycle. In these experiments the catalysts were cycled under reaction conditions between room temperature and 1173 K for 2 heating/cooling cycles and the second cycle was

selected as representative of the catalytic behavior, unless otherwise stated. Interestingly, the overall performance of the M samples strongly depends on the nature of the palladium precursor. PdCeM has a much higher activity than PdOCeM in the whole temperature range, and its behavior outperforms significantly that of the impregnated sample and of the catalyst made by solution combustion synthesis, which was reported as one of the best literature examples.^{4,13} This can be seen either by the lower light-off temperature or by the higher reaction rate measured for the PdCeM sample in a recycle reactor, as reported in Table 3.1. The better performance of PdCeM is maintained also in the cooling portion of the cycle, where the drop of activity due to the dynamics of Pd-PdO transformation follows the order PdCeM < PdCeSCS < PdOCeM < PdCeIW.

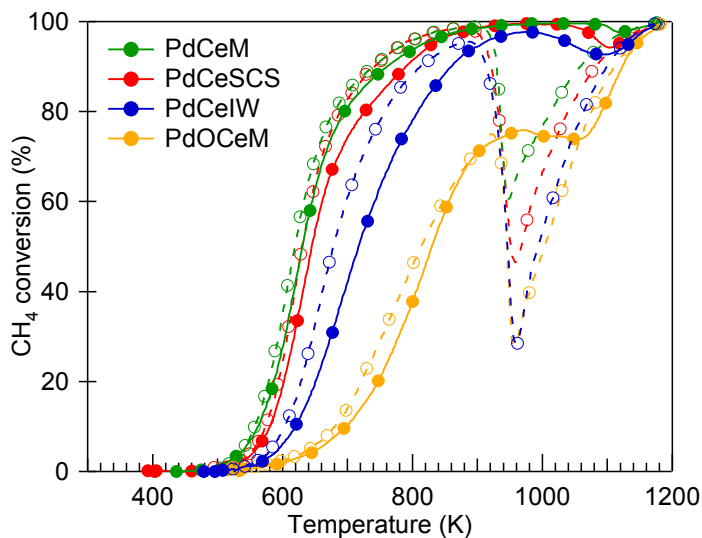


Figure 3.3: Light-off curves for Pd-CeO₂ catalysts (2nd cycle). Solid line, closed symbols: heating part of the cycle; dashed line, open symbols: cooling part of the cycle. Conditions: GHSV ca. 200000 h⁻¹, 0.5% CH₄, 2% O₂, He to balance.

Table 3.1: Physico-chemical properties and activity parameters for methane combustion.

Sample	Pd loading (wt%) ^a	Surface area (m ² /g)	T ₁₀ ^b (K)	Reaction rate ^c (μmol/gPd·s)
PdCeM	0.81	3.2	564	208
PdOCeM	0.80	4.1	700	16
PdCeIW	0.97	2.3	619	32
PdCeSCS	0.93	5.9	581	112

a: measured by ICP elemental analysis; b: temperature for 10% conversion; c: measured at 623 K in a recycle reactor.

The catalyst stability has been successfully checked over six light-off cycles (Figure 3.5) where it can be seen that PdCeM shows a stable CH₄ conversion behavior from the third cycle onward, after which the temperature corresponding to 10% methane conversion (T_{10}) reaches a stable value (Figure 3.5). Time on stream behavior has also been investigated both under reaction conditions (Figure 3.6) and in the presence of large excess of water (Figure 3.7), which is known to accelerate deactivation in Pd-based catalysts.¹⁶ Catalysts prepared by milling are more stable with an overall activity loss of ca. 25% after 24 h on stream, compared with a loss of 70% observed in reference PdCeIW.

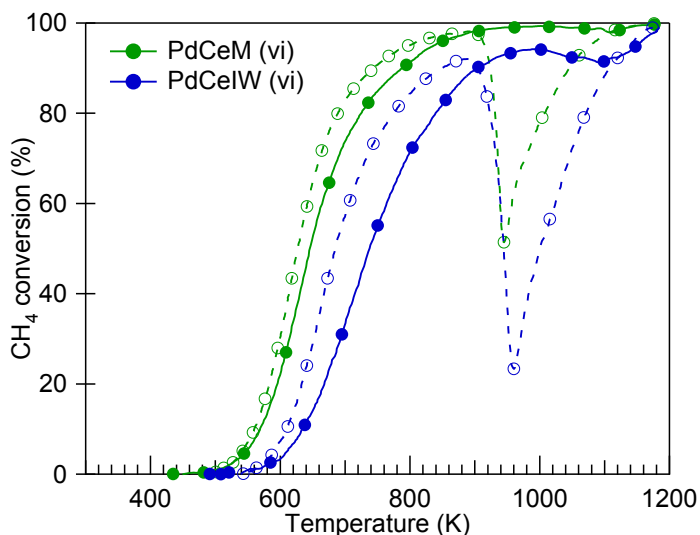


Figure 3.4: Catalytic activity of PdCeM and PdCeIW, after six light-off cycles.

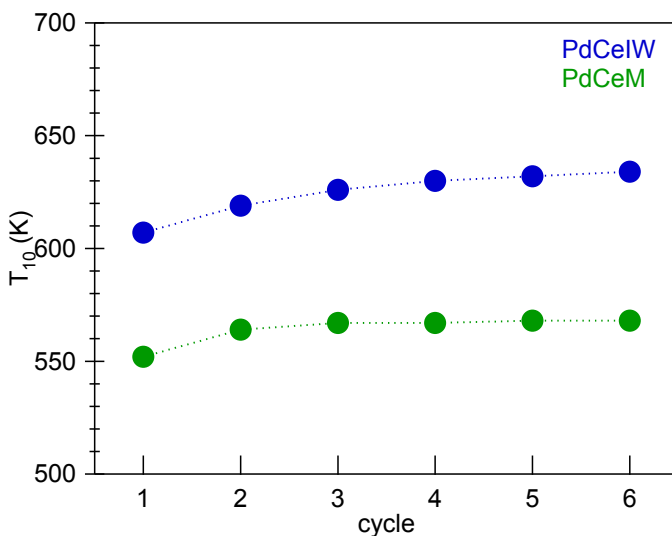


Figure 3.5: Temperatures corresponding to 10% CH₄ conversion (T_{10}) for six consecutive light-off cycles, for PdCeM and PdCeIW samples.

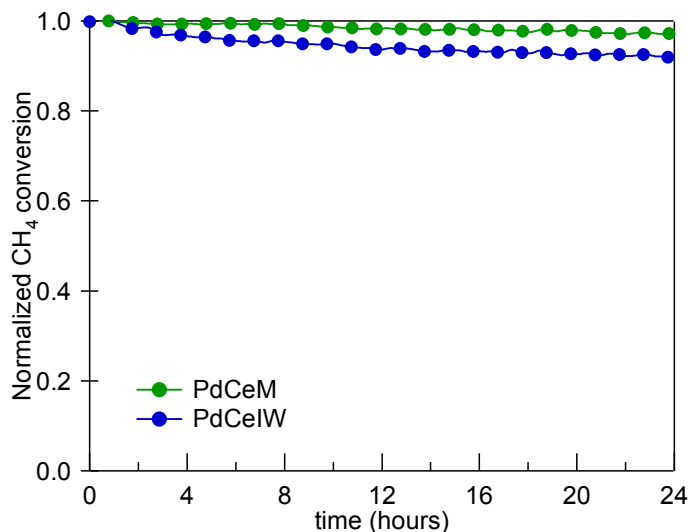


Figure 3.6: Normalized catalytic activity of PdCeM and PdCeIW during time-on-stream tests in dry atmosphere at 723 K.

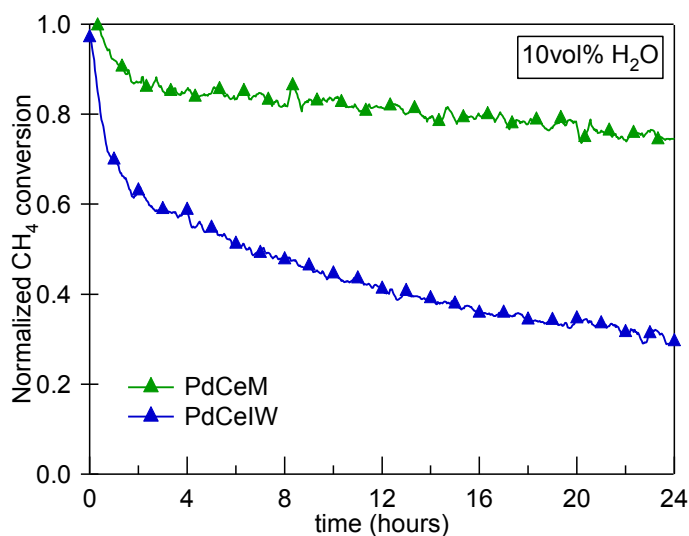


Figure 3.7: Normalized catalytic activity of PdCeM and PdCeIW during time-on-stream tests in wet atmosphere (10 vol% H₂O) at 723 K.

Light-off activity behavior of PdCeM is also affected by the modification of milling parameters. It is observed that, increasing milling intensity, the overall light-off profiles of the catalyst shift to higher temperatures, indicating a drop of reaction rates compared to our standard PdCeM sample (see Figure 3.8). This will be further investigated in Chapter 4.

The uniqueness of the newly found Pd-ceria interaction under the mild milling conditions employed is further confirmed by the study of a PdCe sample obtained by milling Pd and CeO₂ in the same conditions of the M samples but without using the zirconia balls (PdCe loose - L). Figure 3.9 shows the comparison of the light-off curves obtained for PdCeM, PdCeL and unsupported Pd. This last material was tested by mixing the appropriate amount of Pd powder with inert quartz beads, in order to have in the reactor the same weight loading of palladium. It is worth noting that even the loose contact between Pd and ceria gives rise to an outstanding catalytic performance up to about 950 K, better than the one observed for unsupported Pd and equal to PdCeM. Above 950 K, PdCeL suffers from a dramatic deactivation, due to the lack of nanoscale interactions between Pd and ceria and subsequent extensive sintering at higher temperatures. Still, the loss in conversion of PdCeL is significantly smaller than the one of unsupported Pd. Moreover, the loose sample recovers its activity during the cooling branch much more than pure Pd, even if its methane conversion remains extremely low compared to PdCeM. TPO profiles (Figure 3.10) evidence the absence of the reoxidation peak in the cooling portion of the first cycle for Pd and PdCeL which is likely due to extensive Pd sintering at high temperature with the loss of most of the Pd active sites. The dynamics of PdO/Pd transformation is almost disappeared in the second cycle for the above samples. This shows that the choice of our milling parameters for PdCeM sample (10 minutes milling at an oscillation frequency of 15 Hz with a ball to powder ratio of 10) optimizes activity performances.

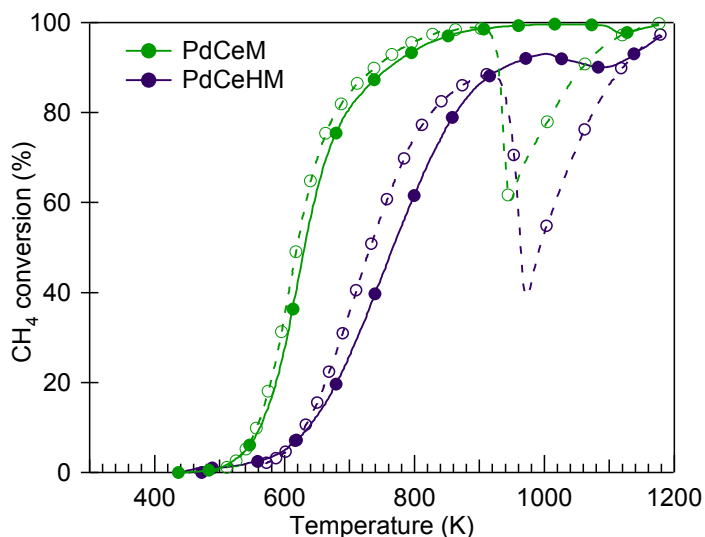


Figure 3.8: Second light-off cycle for PdCeM compared with a PdCe sample obtained by milling at a higher intensity (PdCeHM).

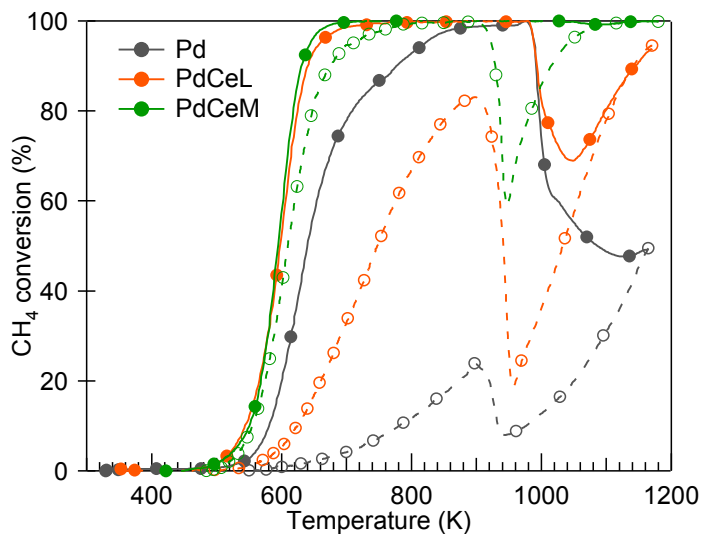


Figure 3.9: Light-off curves for different Pd-based formulations.

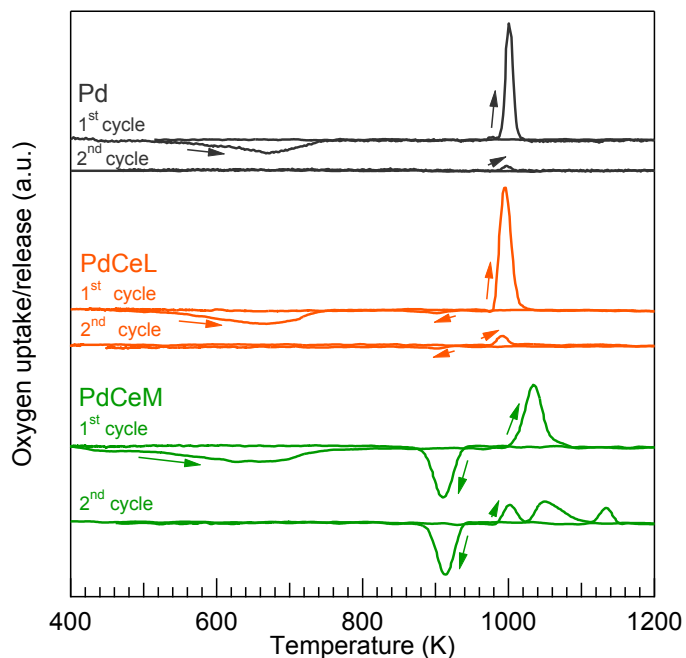


Figure 3.10: First and second TPO cycles for different Pd-based formulations.

Methane oxidation light-off profiles were also collected on the corresponding ZrO_2 supported catalysts, and they did not evidence any significant difference among samples prepared by impregnation and by mechanical milling (Figure 3.11). This strongly supports the fact that the origin of the unique activity of PdCeM must be found in a specific

characteristic of the Pd-CeO₂ interface that is promoted during milling, and not in a more general behavior of samples prepared by a mechano-chemical procedure.

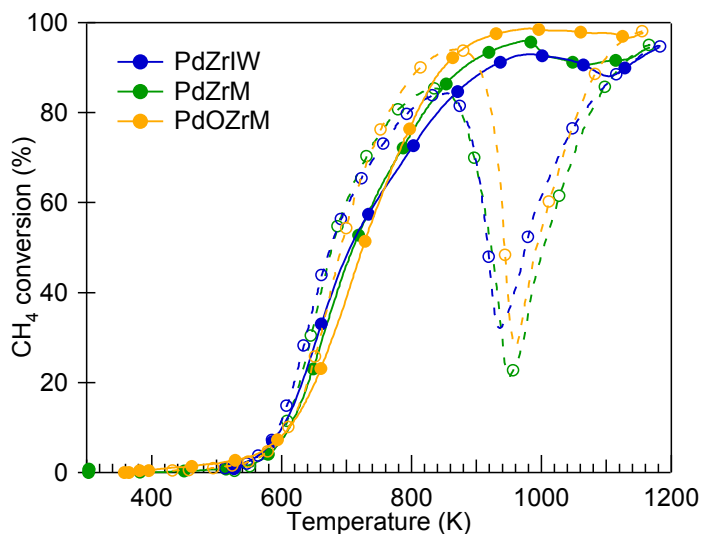


Figure 3.11: Second light-off cycle for PdZrM, PdOZrM and PdZrIW.

In parallel to light-off cycles, temperature programmed oxidation experiments (Figure 3.12) showed for fresh PdCeM the oxidation of Pd at low temperature (cycle 1), and the presence of at least three PdO decomposition peaks (cycles 2 and 3), indicating the coexistence of different palladium species. Quantitative re-oxidation of Pd during cooling occurs in one single peak at ca. 910 K.

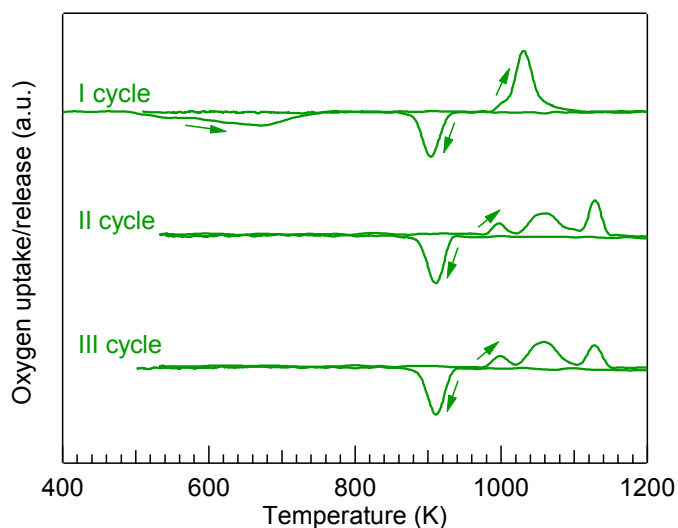


Figure 3.12: TPO profiles for PdCeM over three consecutive heating/cooling cycles.

A comparison with PdCeIW, which presents only two oxygen release peaks, is shown in Figure 3.13. On PdCeIW the high temperature decomposition peak, linked to palladium species in close contact with the support surface,¹⁷ is also significantly smaller than the one observed on PdCeM, suggesting a less intimate Pd-Ce interaction on the sample prepared by incipient wetness impregnation method.

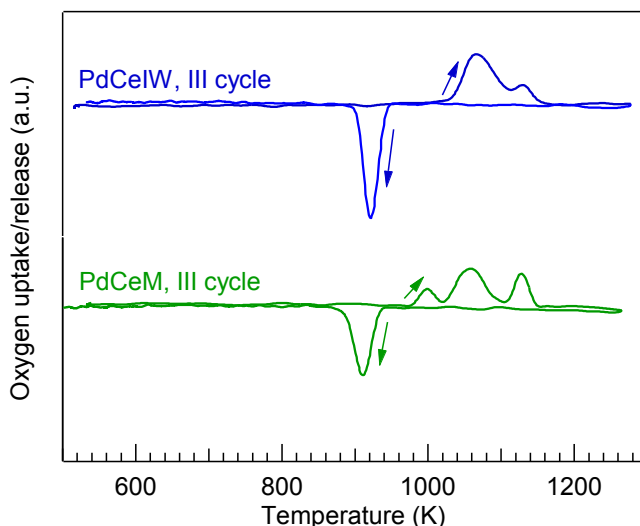


Figure 3.13: Comparison between the third TPO cycles on PdCeM and PdCeIW.

Details on the Pd-CeO₂ morphology were obtained by HRTEM analysis on the fresh samples. Figure 3.14(A,B) shows the surface of PdCeIW where, as expected, small Pd nanoparticles (ca. 2 nm) are well dispersed over a clean ceria surface. In contrast, PdCeM is characterized by ceria crystallites that are covered by an amorphous layer measuring between 2 and 5 nm in thickness (Figure 3.14(C-F)). This amorphous shell is compact and perfectly defined, following the perimeter of the ceria particles (Figure 3.14(C-D)). Interestingly, the ceria crystallites covered by this layer present a more rounded morphology, suggesting that the spreading of Pd by mechanical mixing affects their surface. Ceria nanoparticles show well-defined lattice fringes at 3.12 and 2.71 Å in both samples, which correspond to the {111} and {200} crystallographic planes of CeO₂, respectively. In Figure 3.14(D) the EDX analysis of the shell is reported, which contains both ceria and Pd (the Cu signal originates from the TEM grid), indicating that the shell is comprised of a mixed Pd-Ce phase. In addition to this amorphous layer, some smaller particles measuring less than 5 nm are also detected, mostly decorating the ceria crystallites (Figure 3.14(E,F)).

Lattice fringe analysis of these nanoparticles (see insets “c” and “d” corresponding to FT images of “a” and “b”, respectively, in Figure 3.14(F)) shows fringes at 2.25 and 1.95 Å. They correspond to the {111} and {200} crystallographic planes of Pd metal. Noticeably, these Pd nanoparticles are embedded in the amorphous shell, which suggests that the shell is produced by the distribution of Pd metal nanoparticles over the ceria support upon mechanical mixing. Figure 3.14(E) represents nicely this situation: a very small nanoparticle (less than 2 nm) diffuses into the shell at the edges, still preserving some crystallographic order (see the FT image in inset “a” showing fringes of Pd metal).

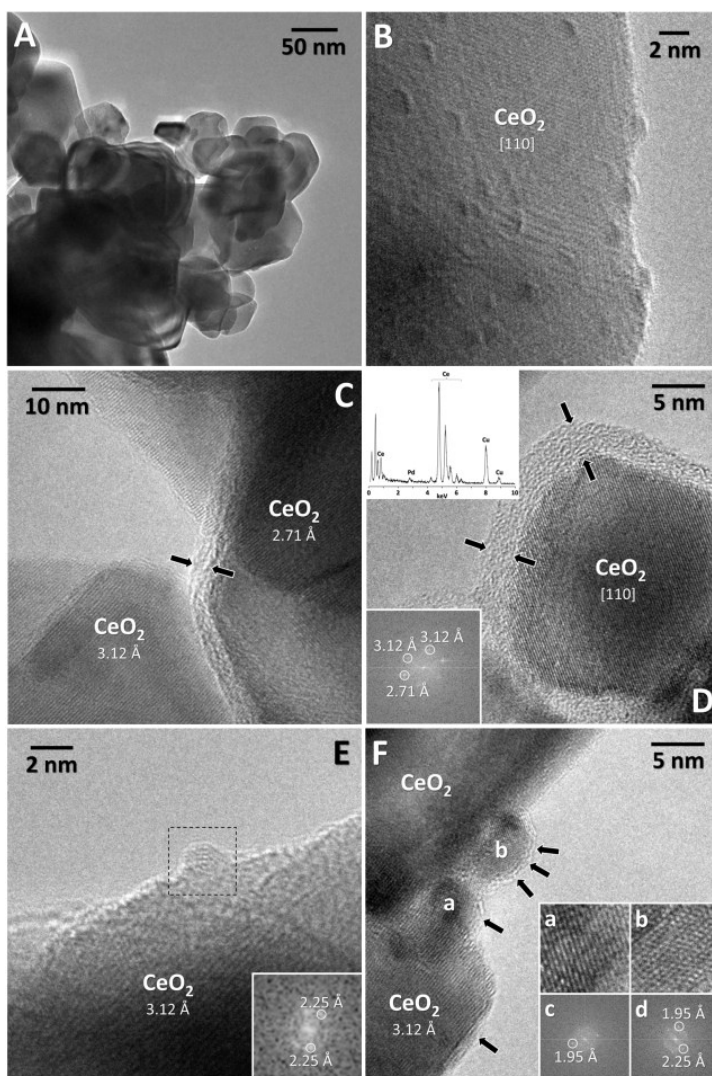


Figure 3.14: HRTEM images of PdCeIW (A,B) and PdCeM (C-F).

Remarkably, this morphology is not observed on PdOCeM and PdZrM where well defined PdO and Pd nanoparticles are respectively found over the support (see Figure 3.15(A,B) for representative samples). Moreover, the mechanical milling of pure CeO₂ under the same conditions does not induce any change of the surface (Figure 3.15(C)) indicating that surface amorphization takes place only upon mixing of Pd and ceria.

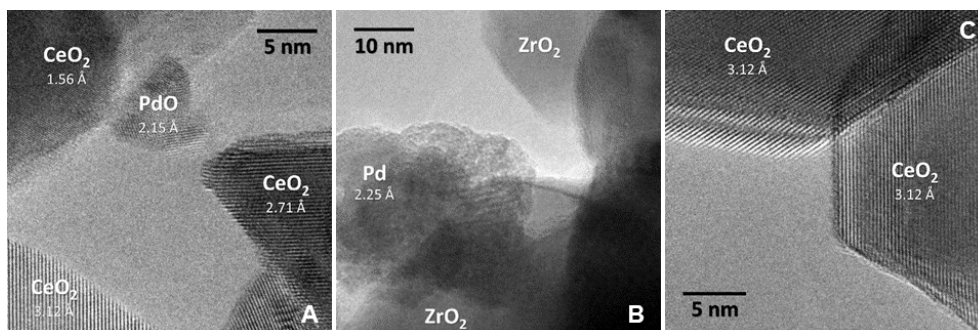


Figure 3.15: Representative HRTEM image of PdOCeM sample (A), PdZrM sample (B), and CeO₂ support after mechanical grinding (C).

A similar core-shell structure where Pd covers SnO₂ particles was observed on a Pd/SnO₂ catalyst prepared by wet impregnation,¹⁸ however, the Pd-Sn alloy-based shell disappeared under an oxidizing atmosphere. Conversely, the amorphous shell observed on PdCeM is also stable under reaction conditions, as demonstrated by the HRTEM image of the used sample after two cycles (Figure 3.16(A,B)) in which it is possible to recognize the presence of two fringes, one at 3.1 Å corresponding to the {111} crystallographic planes of the ceria substrate, and another one at a greater spacing likely due to inclusion of PdO within ceria lattice, where Pd is strongly interacting with the support. This is in accordance with the existence of small domains of Pd completely embedded in the amorphous shell, as discussed above for the fresh PdCeM sample. Figure 3.16(C,D) shows representative images of the shell around ceria after 6 reaction cycles, which is marked between arrows along with the crystallographic planes exposed by the ceria crystallites. From these images it is clear that the shell is preserved after the sixth cycle. Interestingly, no remaining Pd containing particles have been identified indicating that all Pd is still spread within the layer surrounding the ceria particles. Similarly, time on stream behavior under hydrothermal conditions does not alter the structure of the layer, indicating stability also in the presence of excess of water (Figure 3.17).

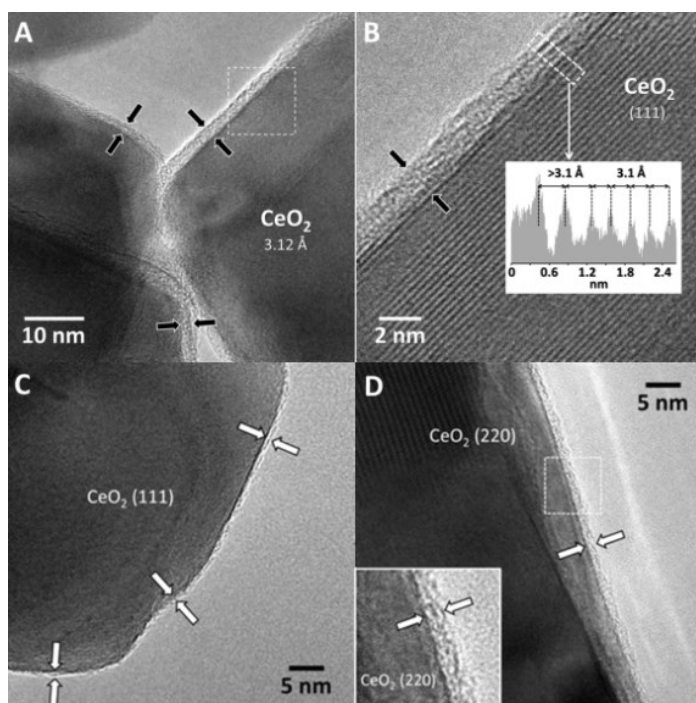


Figure 3.16: HRTEM images of PdCeM after two (A, B) and six (C, D) methane oxidation tests.

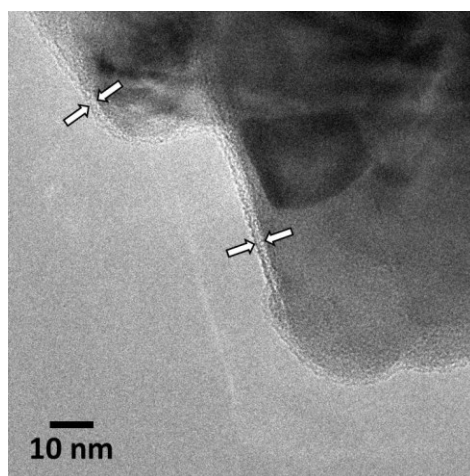


Figure 3.17: Representative HRTEM image of PdCeM after 24 hours in time on stream experiment in wet atmosphere (10 vol% H₂O).

The reasons behind the structural rearrangement of the surface in PdCeM during milling are not straightforward and should be the result of a combination of different elements. Some interesting indications on the phenomena that might take place during the mechanical mixing of Pd and ceria powders come from the studies on solid state amorphization.¹⁹ In

these studies it is evidenced that mechanical alloying increases vacancies, chemical disordering at atomic level and nanocrystalline grain boundaries, which in turn raise the free energy of the crystalline phase favoring the stabilization of the amorphous state, particularly at nanometer scale. This process usually starts with the amorphization of the edges, and in some cases proceeds through the formation of a crystalline solid solution which is then transformed into the amorphous phase. Interestingly, the formation of point and lattice defects by milling has been proposed as the rate limiting step for amorphization.²⁰

It should be observed though that, in general, in the studies dealing with solid state amorphization the energies employed are much higher than those of our dry mixing method, nevertheless in the case of palladium and ceria the process might be speeded up by other factors, like the specific interaction between Pd and CeO₂.²¹⁻²³ This interaction, which could account for an easier solid state reaction between the two components, involves the formation of vacancies and/or more active oxygen states at the metal-oxide interface as observed for other systems after milling.²⁴⁻²⁷ In addition, it has been reported that the oxidation state of cerium ions in solid solutions can be altered at room temperature by changing mechanically the local stress state, and that the distribution of Ce³⁺/Ce⁴⁺ can be influenced by stress gradients.^{28,29}

Indeed, XPS studies carried out on PdCeM and PdCeIW after one reaction cycle (Table 3.2) show that the ratio between Ce³⁺ and Ce⁴⁺ is higher on the sample prepared by mechanical grinding compared to the impregnated one, and also to pure milled CeO₂ (sample CeM). This indicates that the interplay between Pd and ceria on PdCeM is stronger and induces a higher degree of ceria reduction. In addition, a better and more homogeneous Pd distribution is also observed in milled samples which is maintained after the first reaction cycles.

Table 3.2: Data from XPS analysis.

Sample	Pd/Ce	Ce ³⁺ /Ce	Pd ⁰ (%)	Pd ²⁺ (%)	Pd ⁴⁺ (%)
CeM	-	0.16	-	-	-
PdCeM ^a	0.19 (0.18) ^b	0.24 (0.12)	0 (0)	82 (78)	18 (22)
PdCeIW ^a	0.15 (0.15)	0.15 (0.12)	0 (0)	76 (87)	24 (13)

a: collected after one reaction cycle; b: in parentheses data collected after six reaction cycles.

Characterization after six reaction cycles shows an increase of Pd⁴⁺ in milled sample compared to PdCeIW while the amount of Ce³⁺ become similar, likely due to prolonged oxidation cycles at high temperature. In addition, the better Pd distribution of PdCeM is

maintained after stability tests. This is also confirmed by comparing the Raman spectra obtained by mapping $144 \mu\text{m}^2$ of the surface of PdCeM and PdCeIW (Figure 3.18). In both samples the more intense signal is due to the F_{2g} vibrational mode of CeO_2 (461 cm^{-1}), but a signal originating from the B_{1g} vibrational mode of PdO is also observed (646 cm^{-1}). Collecting several spectra, it is clearly seen that the intensity ratio between the two signals is rather constant for PdCeM (Figure 3.18b), indicating a more homogeneous spreading of Pd over CeO_2 , as it can be expected from its distribution within the surface layer. A broad Raman signal covering the region between $550\text{-}600 \text{ cm}^{-1}$ is also detected in PdCeM; peaks in this region are attributed to surface defects in ceria^{30,31} that might include those generated by close interaction and inclusion of Pd into CeO_2 lattice. A more recent study³² confirmed by DFT calculations and experimental evidence that the broad band observed could be a combination of $\text{Ce}^{3+}\text{-O-Ce}^{4+}$ with oxygen defects, vibrating at 560 cm^{-1} , and Pd inclusions in the ceria lattice ($\sim 600 \text{ cm}^{-1}$).

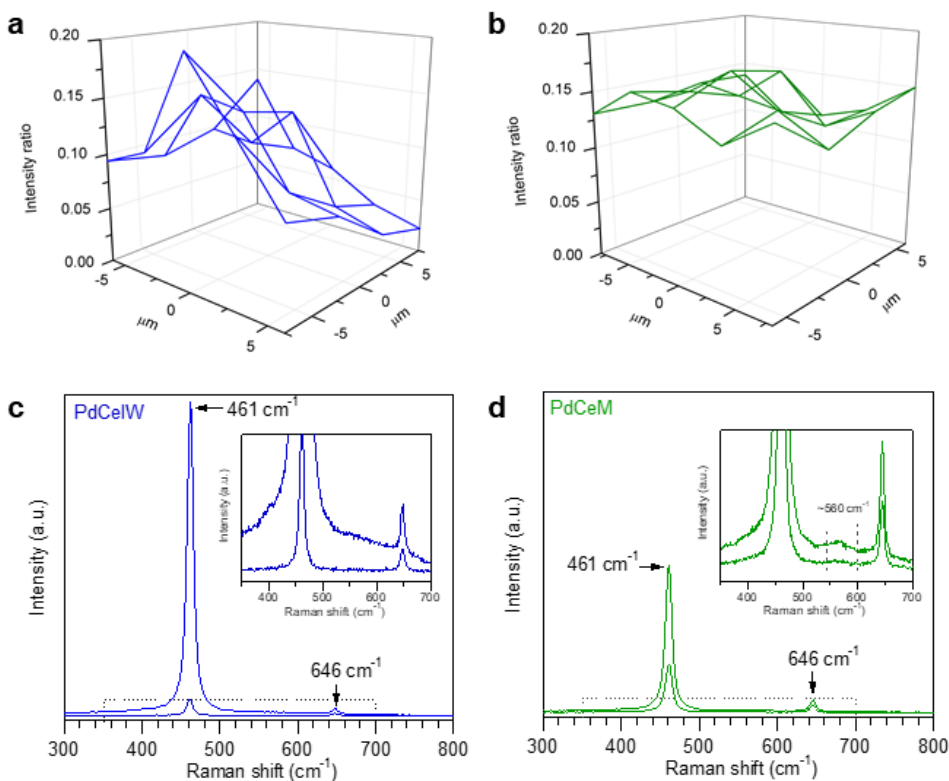


Figure 3.18: (a,b) Intensity ratio between the B_{1g} vibrational mode of PdO (646 cm^{-1}) and the F_{2g} vibrational mode of CeO_2 (461 cm^{-1}) collected by mapping a $12 \times 12 \mu\text{m}$ grid on PdCeIW (a) and PdCeM (b) samples after 6 combustion cycles. (c, d) Raman spectra corresponding to the minimum and maximum intensity ratio on PdCeIW (c) and PdCeM (d).

The information gathered from HRTEM and XPS studies show that on PdCeM there is a unique arrangement of Pd and ceria that is not observed on samples prepared by conventional routes. This arrangement is the result of an interaction between Pd and ceria promoted by mechanical milling and by the redox characteristics of the two components. It was recently reported that the milling of ceria with carbon soot results in the formation of a CeO₂ core wrapped in a soft carbon shell;¹⁴ the nanoscale arrangement created by mixing was promoted by the different hardness of the two materials that helps the spreading of the softer carbon particles on the surface of ceria. This might explain why the core-shell structure observed here is obtained only when mixing Pd metal nanoparticles and ceria and not when harder materials like PdO and/or ZrO₂ are used (0.6 vs 4 GPa for Pd metal and ceria, respectively, against 8 for zirconia^{33,34}). It is true in fact that the adhesive force between two compressed particles varies inversely with their hardness.³⁵

The high reactivity for methane oxidation over Pd/CeO₂ interfacial sites was recently described by the group of Janik, using integrated DFT and empirical reactive force field methods.¹² In their study partially embedded Pd clusters are shown to favor the formation of metastable transient Pd⁴⁺ ions inserted into ceria lattice which are indicated as the most reactive for methane activation. The authors predict that, starting from supported Pd clusters, Pd atoms can migrate across the ceria surface and assume a higher oxygen coordination being incorporated into the lattice when encountering steps, vacancies and/or grain boundaries, forming active oxidized Pd species. It is remarkable to observe that this description well agrees with our HRTEM observation of nanometer scale Pd clusters embedded in an amorphous Pd-CeO₂ shell (Figure 3.14(E,F)), as if this layer would be originated by the dissolution of Pd nanoclusters into the ceria lattice. A similar situation, with copper clusters dispersed into the ceria lattice at atomic scale, has been recently reported following the mechanical mixing of cerium and copper complexes.³⁶ This unique embedded configuration might explain the reasons why active Pd⁴⁺ centers in PdCeM are more efficient than in PdCeIW, where the presence of Pd⁴⁺ (also detected by XPS) is not characterized by the same nanoscale environment. This picture might also explain why promotion of activity is not observed for PdZrM and PdOCeM. Thanks to the oxygen exchange properties of ceria, Pd⁴⁺ ions are formed on CeO₂ under conditions much different from other supports.¹² Moreover, the appearance of these species is prompted by the migration of Pd atoms in the lattice from metallic Pd clusters on the surface,¹² a situation that likely could not be feasible in presence of stable PdO clusters.

3.4 Conclusions

By using an independently developed solventless mild milling procedure, a Pd/CeO₂ catalyst with a peculiar core-shell morphology was obtained, which resulted in improved methane oxidation activity compared to the traditional state-of-the-art incipient wetness impregnation (IW) synthesis and outperforming the solution combustion synthesized (SCS) samples, previously reported as the most active in the literature.^{13,37} In fact, the observed formation of a specific nanoscale arrangement, with Pd moieties embedded in the outer surface layers of ceria, promotes methane activation at much lower temperature compared to conventional Pd/CeO₂ catalysts. Interestingly, this feature is only obtained when metallic palladium is milled with cerium oxide, as their chemical properties likely play a fundamental role in the creation of the Pd-Ce amorphous shell during milling. The shear stresses developed during the mechanical mixing process result in a higher density of surface defects compared to the wet synthesized samples, as observed by XPS and Raman characterization, which may promote the nanoscale intermixing of Pd and Ce atoms and thus result in the stabilization of the amorphous shell structure. These experimental results, supported by a strong theoretical background developed independently,^{11,12} open the way to the design of highly active Pd-ceria catalytic systems via sustainable mechanical synthesis routes. In addition, and perhaps more importantly, they put the accent on the role of mechanical stress in modifying at nanoscale the properties of ceria, which can offer a powerful tool in the design of materials with undisclosed properties.

3.5 References

- (1) Farrauto, R. J. Low-Temperature Oxidation of Methane. *Science* **2012**, *337* (6095), 659–660. <https://doi.org/10.1126/science.1226310>.
- (2) Tang, P.; Zhu, Q.; Wu, Z.; Ma, D. Methane Activation: The Past and Future. *Energy Environ. Sci.* **2014**, *7* (8), 2580–2591. <https://doi.org/10.1039/C4EE00604F>.
- (3) Colussi, S.; Trovarelli, A.; Cristiani, C.; Lietti, L.; Groppi, G. The Influence of Ceria and Other Rare Earth Promoters on Palladium-Based Methane Combustion Catalysts. *Catalysis Today* **2012**, *180* (1), 124–130. <https://doi.org/10.1016/j.cattod.2011.03.021>.
- (4) Cargnello, M.; Jaen, J. J. D.; Garrido, J. C. H.; Bakhmutsky, K.; Montini, T.; Gamez, J. J. C.; Gorte, R. J.; Fornasiero, P. Exceptional Activity for Methane Combustion over Modular Pd@CeO₂ Subunits on Functionalized Al₂O₃. *Science* **2012**, *337* (6095), 713–717. <https://doi.org/10.1126/science.1222887>.
- (5) Fouladvand, S.; Schernich, S.; Libuda, J.; Grönbeck, H.; Pingel, T.; Olsson, E.; Skoglundh, M.; Carlsson, P.-A. Methane Oxidation Over Pd Supported on Ceria–Alumina Under Rich/Lean Cycling Conditions. *Topics in Catalysis* **2013**, *56* (1–8), 410–415. <https://doi.org/10.1007/s11244-013-9988-2>.
- (6) Nilsson, J.; Carlsson, P.-A.; Fouladvand, S.; Martin, N. M.; Gustafson, J.; Newton, M. A.; Lundgren, E.; Grönbeck, H.; Skoglundh, M. Chemistry of Supported Palladium Nanoparticles during Methane Oxidation. *ACS Catalysis* **2015**, *5* (4), 2481–2489. <https://doi.org/10.1021/cs502036d>.
- (7) Su, Y.-Q.; Liu, J.-X.; Filot, I. A. W.; Zhang, L.; Hensen, E. J. M. Highly Active and Stable CH₄ Oxidation by Substitution of Ce⁴⁺ by Two Pd²⁺ Ions in CeO₂ (111). *ACS Catalysis* **2018**, *8* (7), 6552–6559. <https://doi.org/10.1021/acscatal.8b01477>.
- (8) Meng, L.; Lin, J.-J.; Pu, Z.-Y.; Luo, L.-F.; Jia, A.-P.; Huang, W.-X.; Luo, M.-F.; Lu, J.-Q. Identification of Active Sites for CO and CH₄ Oxidation over PdO/Ce_{1-x}Pd_xO_{2-δ} Catalysts. *Applied Catalysis B: Environmental* **2012**, *119–120*, 117–122. <https://doi.org/10.1016/j.apcatb.2012.02.036>.
- (9) Zhu, Y.; Zhang, S.; Shan, J.; Nguyen, L.; Zhan, S.; Gu, X.; Tao, F. (Feng). In Situ Surface Chemistries and Catalytic Performances of Ceria Doped with Palladium, Platinum, and Rhodium in Methane Partial Oxidation for the Production of Syngas. *ACS Catalysis* **2013**, *3* (11), 2627–2639. <https://doi.org/10.1021/cs400070y>.
- (10) Colussi, S.; Gayen, A.; Boaro, M.; Llorca, J.; Trovarelli, A. Influence of Different Palladium Precursors on the Properties of Solution-Combustion-Synthesized Palladium/Ceria Catalysts for Methane Combustion. *ChemCatChem* **2015**, *7* (14), 2222–2229. <https://doi.org/10.1002/cctc.201500390>.
- (11) Senftle, T. P.; van Duin, A. C. T.; Janik, M. J. Role of Site Stability in Methane Activation on Pd_xCe_{1-x}O_δ Surfaces. *ACS Catalysis* **2015**, *5* (10), 6187–6199. <https://doi.org/10.1021/acscatal.5b00741>.
- (12) Senftle, T. P.; van Duin, A. C. T.; Janik, M. J. Methane Activation at the Pd/CeO₂ Interface. *ACS Catalysis* **2017**, *7* (1), 327–332. <https://doi.org/10.1021/acscatal.6b02447>.
- (13) Colussi, S.; Gayen, A.; Farnesi Camellone, M.; Boaro, M.; Llorca, J.; Fabris, S.; Trovarelli, A. Nanofaceted Pd-O Sites in Pd-Ce Surface Superstructures: Enhanced Activity in Catalytic Combustion of Methane. *Angewandte Chemie International Edition* **2009**, *48* (45), 8481–8484. <https://doi.org/10.1002/anie.200903581>.

- (14) Aneggi, E.; Rico-Perez, V.; de Leitenburg, C.; Maschio, S.; Soler, L.; Llorca, J.; Trovarelli, A. Ceria-Zirconia Particles Wrapped in a 2D Carbon Envelope: Improved Low-Temperature Oxygen Transfer and Oxidation Activity. *Angewandte Chemie International Edition* **2015**, *54* (47), 14040–14043. <https://doi.org/10.1002/anie.201507839>.
- (15) Lieske, H.; Voelter, J. Palladium Redispersion by Spreading of Palladium(II) Oxide in Oxygen Treated Palladium/Alumina. *The Journal of Physical Chemistry* **1985**, *89* (10), 1841–1842. <https://doi.org/10.1021/j100256a001>.
- (16) Gholami, R.; Alyani, M.; Smith, K. Deactivation of Pd Catalysts by Water during Low Temperature Methane Oxidation Relevant to Natural Gas Vehicle Converters. *Catalysts* **2015**, *5* (2), 561–594. <https://doi.org/10.3390/catal5020561>.
- (17) Colussi, S.; Trovarelli, A.; Vesselli, E.; Baraldi, A.; Comelli, G.; Groppi, G.; Llorca, J. Structure and Morphology of Pd/Al₂O₃ and Pd/CeO₂/Al₂O₃ Combustion Catalysts in Pd–PdO Transformation Hysteresis. *Applied Catalysis A: General* **2010**, *390* (1–2), 1–10. <https://doi.org/10.1016/j.apcata.2010.09.033>.
- (18) Kamiuchi, N.; Muroyama, H.; Matsui, T.; Kikuchi, R.; Eguchi, K. Nano-Structural Changes of SnO₂-Supported Palladium Catalysts by Redox Treatments. *Applied Catalysis A: General* **2010**, *379* (1–2), 148–154. <https://doi.org/10.1016/j.apcata.2010.03.019>.
- (19) Enayati, M. H.; Mohamed, F. A. Application of Mechanical Alloying/Milling for Synthesis of Nanocrystalline and Amorphous Materials. *International Materials Reviews* **2014**, *59* (7), 394–416. <https://doi.org/10.1179/1743280414Y.0000000036>.
- (20) Schwarz, R. B.; Koch, C. C. Formation of Amorphous Alloys by the Mechanical Alloying of Crystalline Powders of Pure Metals and Powders of Intermetallics. *Appl. Phys. Lett.* **1986**, *49* (3), 146–148. <https://doi.org/10.1063/1.97206>.
- (21) Yang, Z.; Lu, Z.; Luo, G.; Hermansson, K. Oxygen Vacancy Formation Energy at the Pd/CeO₂(111) Interface. *Physics Letters A* **2007**, *369* (1–2), 132–139. <https://doi.org/10.1016/j.physleta.2007.04.068>.
- (22) Liu, B.; Liu, J.; Li, T.; Zhao, Z.; Gong, X.-Q.; Chen, Y.; Duan, A.; Jiang, G.; Wei, Y. Interfacial Effects of CeO₂-Supported Pd Nanorod in Catalytic CO Oxidation: A Theoretical Study. *J. Phys. Chem. C* **2015**, *119* (23), 12923–12934. <https://doi.org/10.1021/acs.jpcc.5b00267>.
- (23) Slavinskaya, E. M.; Kardash, T. Yu.; Stonkus, O. A.; Gulyaev, R. V.; Lapin, I. N.; Svetlichnyi, V. A.; Boronin, A. I. Metal–Support Interaction in Pd/CeO₂ Model Catalysts for CO Oxidation: From Pulsed Laser-Ablated Nanoparticles to Highly Active State of the Catalyst. *Catal. Sci. Technol.* **2016**, *6* (17), 6650–6666. <https://doi.org/10.1039/C6CY00319B>.
- (24) Maeda, Y.; Akita, T.; Kohyama, M. High Activity of Gold/Tin-Dioxide Catalysts for Low-Temperature CO Oxidation: Application of a Reducible Metal Oxide to a Catalyst Support. *Catalysis Letters* **2014**, *144* (12), 2086–2090. <https://doi.org/10.1007/s10562-014-1376-4>.
- (25) Yang, Y.; Zhang, S.; Wang, S.; Zhang, K.; Wang, H.; Huang, J.; Deng, S.; Wang, B.; Wang, Y.; Yu, G. Ball Milling Synthesized MnO_x as Highly Active Catalyst for Gaseous POPs Removal: Significance of Mechanochemically Induced Oxygen Vacancies. *Environmental Science & Technology* **2015**, *49* (7), 4473–4480. <https://doi.org/10.1021/es505232f>.

- (26) Borchers, C.; Martin, M. L.; Vorobjeva, G. A.; Morozova, O. S.; Firsova, A. A.; Leonov, A. V.; Kurmaev, E. Z.; Kukharenko, A. I.; Zhidkov, I. S.; Cholakh, S. O. Cu–CeO₂ Nanocomposites: Mechanochemical Synthesis, Physico-Chemical Properties, CO-PROX Activity. *Journal of Nanoparticle Research* **2016**, *18* (11). <https://doi.org/10.1007/s11051-016-3640-6>.
- (27) Tang, C.; Sun, B.; Sun, J.; Hong, X.; Deng, Y.; Gao, F.; Dong, L. Solid State Preparation of NiO-CeO₂ Catalyst for NO Reduction. *Catalysis Today* **2017**, *281*, 575–582. <https://doi.org/10.1016/j.cattod.2016.05.026>.
- (28) Sayle, T. X. T.; Cantoni, M.; Bhatta, U. M.; Parker, S. C.; Hall, S. R.; Möbus, G.; Molinari, M.; Reid, D.; Seal, S.; Sayle, D. C. Strain and Architecture-Tuned Reactivity in Ceria Nanostructures; Enhanced Catalytic Oxidation of CO to CO₂. *Chemistry of Materials* **2012**, *24* (10), 1811–1821. <https://doi.org/10.1021/cm3003436>.
- (29) Munnings, C.; Badwal, S. P. S.; Fini, D. Spontaneous Stress-Induced Oxidation of Ce Ions in Gd-Doped Ceria at Room Temperature. *Ionics* **2014**, *20* (8), 1117–1126. <https://doi.org/10.1007/s11581-014-1079-2>.
- (30) Spanier, J. E.; Robinson, R. D.; Zhang, F.; Chan, S.-W.; Herman, I. P. Size-Dependent Properties of CeO_{2-y} Nanoparticles as Studied by Raman Scattering. *Physical Review B* **2001**, *64* (24). <https://doi.org/10.1103/PhysRevB.64.245407>.
- (31) Filtschew, A.; Hofmann, K.; Hess, C. Ceria and Its Defect Structure: New Insights from a Combined Spectroscopic Approach. *The Journal of Physical Chemistry C* **2016**, *120* (12), 6694–6703. <https://doi.org/10.1021/acs.jpcc.6b00959>.
- (32) Xu, Y.; Wang, F.; Liu, X.; Liu, Y.; Luo, M.; Teng, B.; Fan, M.; Liu, X. Resolving a Decade-Long Question of Oxygen Defects in Raman Spectra of Ceria-Based Catalysts at Atomic Level. *The Journal of Physical Chemistry C* **2019**, *123* (31), 18889–18894. <https://doi.org/10.1021/acs.jpcc.9b00633>.
- (33) Maschio, S.; Sbaizero, O.; Meriani, S. Mechanical Properties in the Ceria-Zirconia System. *Journal of the European Ceramic Society* **1992**, *9* (2), 127–132. [https://doi.org/10.1016/0955-2219\(92\)90054-H](https://doi.org/10.1016/0955-2219(92)90054-H).
- (34) Samsonov, G. V. *Handbook of the Physicochemical Properties of the Elements*; Springer US: Boston, 1968.
- (35) Krupp, H. Particle Adhesion Theory and Experiment. *Advances in Colloid and Interface Science* **1967**, *1*(2), 111–239. [https://doi.org/10.1016/0001-8686\(67\)80004-6](https://doi.org/10.1016/0001-8686(67)80004-6).
- (36) Zhan, W.; Yang, S.; Zhang, P.; Guo, Y.; Lu, G.; Chisholm, M. F.; Dai, S. Incorporating Rich Mesoporosity into a Ceria-Based Catalyst via Mechanochemistry. *Chemistry of Materials* **2017**, *29* (17), 7323–7329. <https://doi.org/10.1021/acs.chemmater.7b02206>.
- (37) Toso, A.; Colussi, S.; Padigapaty, S.; de Leitenburg, C.; Trovarelli, A. High Stability and Activity of Solution Combustion Synthesized Pd-Based Catalysts for Methane Combustion in Presence of Water. *Applied Catalysis B: Environmental* **2018**, *230*, 237–245. <https://doi.org/10.1016/j.apcatb.2018.02.049>.

4 The Effect of Milling Parameters on the Mechano-chemical Synthesis of Pd-CeO₂ Methane Oxidation Catalysts

Abstract

The preparation of catalytic materials via mechanochemical routes is a very promising alternative to complex wet chemical syntheses due to its simplicity, versatility and ecological advantages. The mechanical mixing of Pd nanoparticles and CeO₂ results in very active methane oxidation catalysts; here we explore the effect of milling parameters on the overall performance of Pd-ceria catalysts. The high methane combustion activity is the result of nanoscale interaction between palladium and cerium oxide and it is shown to be strongly dependent on the intensity of milling. This was investigated through methane combustion tests up to 1173 K and characterized by means of temperature programmed oxidation and reduction experiments. The morphological features of the obtained materials were investigated by HRTEM analysis and correlated to the catalytic behavior.

This was published as:

Danielis, M.; Colussi, S.; de Leitenburg, C.; Soler, L.; Llorca, J.; Trovarelli, A. The Effect of Milling Parameters on the Mechanochemical Synthesis of Pd–CeO₂ Methane Oxidation Catalysts. *Catal. Sci. Technol.* **2019**, *9* (16), 4232–4238. <https://doi.org/10.1039/C9CY01098J>.

4.1 Introduction

The discovery of untapped natural gas deposits and the possible valorization of waste through biogas production have prompted the development of new technologies for natural gas utilization, among which its use as fuel for transportation or for distributed small-scale power generation. This in turn has focused the attention on the possible dangers of methane leak into the atmosphere, since CH_4 is a strong greenhouse gas, and consequently on methane abatement. Due to the intrinsic unreactive nature of the CH_4 molecule, the oxidation of methane has always represented a challenge, and numerous studies have been published.¹⁻⁵ Nevertheless, its increasing application to natural gas fueled vehicles emission control,³ reduction of secondary pollutants from controlled natural gas combustion⁶ and methane activation for the production of feedstock molecules^{7,8} is continuously pushing towards the development of catalytic systems with increased activity and stability.

Palladium is known as one of the most active metals for methane activation, and CeO_2 addition proved to lead to a synergetic effect on Pd-based catalysts.⁹⁻¹² In particular, ionic Pd species in strong interaction with ceria are reported both theoretically¹³⁻¹⁵ and experimentally¹⁶ as extremely active for methane combustion, enabling activation also by the hydrogen abstraction route.¹⁷ In addition, this configuration appears able to hinder the steam deactivation, as reported recently by our group.¹⁸ Water vapor in fact is known as a strong inhibitor for methane combustion¹⁹⁻²¹ and it represents an especially important issue for automotive after-treatment applications, since exhaust gases contain around 10-15 vol% of water vapor produced by fuel combustion in the engine chamber.

Among the variety of chemical synthesis approaches, mechano-chemistry is the oldest known method for the preparation of materials, as the very simple act of mixing different compounds together to transform them into a new product was already experienced in the prehistoric times.^{22,23} Fast forward to the modern times, the mechano-chemical route for the synthesis of products or for promoting chemical reaction (even in gas-phase)²⁴ has been developed mostly in the material science field. Mechanical energy enables the creation of metastable structures bypassing the thermodynamic and chemical equilibria and it is of particular interest for the synthesis of new alloys or nanocomposite materials.²⁵⁻²⁷ In the latest decades, the advances in mechano-chemical technology have spread to other fields such as catalysis, where it has been successfully applied to the synthesis of advanced nanomaterials for electrochemical applications,^{28,29} mixed oxides,^{30,31} metallorganic

materials³² and many others.^{33–36} Nevertheless, its wide range of variable parameters and the combination of mechanical and chemical effects has hindered the straightforward application to oxide-supported metal catalysts.^{37,38} Often an experimental trial-and-error approach is needed to find the best synthesis conditions, depending on the choice of the precursors and on the desired applications.³⁹ In general, high energies are employed in order to induce interaction and alloying at nanoscale.

We recently reported an extremely active methane oxidation Pd-CeO₂ catalyst prepared by a mild milling process.⁴⁰ The low intensity milling brought to the creation of an amorphous Pd-Ce layer covering the ceria crystallites, where the enhanced nanoscale interaction was at the origin of an outstanding methane oxidation activity. Here, we investigate the effect of milling conditions on this catalytic system in order to further study the resulting Pd-CeO₂ interaction. Starting from metallic palladium and cerium oxide powders, we varied the milling time and energy and analyzed their effect on the morphological features and the methane oxidation activity.

4.2 Experimental

The detailed description of catalyst preparation, characterization and testing is reported in Chapter 2. For easier reference, a brief summary of evaluated samples and preparation methods is proposed. All catalysts considered in this work contain 1 wt% Pd and were prepared using Pd black (Sigma Aldrich, BET surface area 40 m²/g) as palladium precursor and pure CeO₂ calcined at 1173 K as support oxide (Treibacher Industrie, BET surface area 3 m²/g). The preparation of Pd/CeO₂ was carried out by mixing of the powders under different milling conditions. The reference PdCeM sample was synthesized in a Pulverisette 23 Minimill by milling Pd and ceria powders for 10 minutes at 15 Hz in a 15 ml jar using one zirconia ball (15 mm diameter, 10 g, Ball-to-Powder Ratio = 10).⁴⁰ For comparison, other Pd-ceria formulations were prepared by mixing the two components with lower or higher intensity with respect to PdCeM. Low intensity mixing was achieved when palladium nanoparticles and ceria powders were loosely mixed inside the jar in the absence of grinding balls (denoted as PdCeL) or simply grinded in an agate mortar for 10 minutes (PdCeG). On the medium-high intensity side, one sample was prepared by milling for 1 hour in the same conditions as PdCeM (Pulverisette 23 Minimill, 15 Hz and one zirconia ball, named PdCeM 1h), while other samples were prepared in a Spex8000 Mixer Mill rotating at 875 rpm in a 50 ml jar with 9 zirconia balls (10 mm diameter, total BPR = 20) for milling times ranging

from 5 minutes to 8 hours. These last samples are referred to as PdCeHM (High-intensity Milling).

4.3 Results and Discussion

Table 4.1 and Figure 4.1 show respectively BET surface area and powder X-ray diffraction profiles of all the samples investigated. The mixing of ceria and Pd at low intensity (PdCeL and PdCeG) results in samples having a surface area in the range 2-4 m²/g, similar to the initial support surface area. Also with PdCeM textural properties are not affected, while an increase of surface area to 5 m²/g is observed in the sample milled at low intensity for 1h. Milling at a higher energy causes a significant increase of surface area, which is typically observed in high-energy milling of powders.²⁷ This is due to continuous fragmentation of particles during milling with consequent reduction of crystallite size down to a few nanometers, as can be measured from peak enlargement in the X-ray diffraction profiles of high-energy milled powders (Table 4.1).

Table 4.1: Characterization and activity data of samples prepared in this study.

Sample ^a	Pd loading (wt%)	BET Surface area (m ² /g)	Crystallite size (nm) ^b	Reaction rate (μmol/g _{Pd} ·s)
CeO ₂	-	2.6	47.2	-
PdCeL	1 ^c	2.9	47.1	35.7 ^e
PdCeG	0.8 ^d	3.2	47.1	205 ^f
PdCeM	0.8 ^d	3.5	47.0	208 ^f
PdCeM 1 h	0.82 ^d	5.0	42.1	206 ^f
PdCeHM 5 min	0.87 ^d	11.6	28.9	52.6 ^e
PdCeHM 30 min	1 ^c	23.1	12.3	11.6 ^e
PdCeHM 1 h	1 ^c	23.7	11.6	9.1 ^e
PdCeHM 8 h	1 ^c	25.6	9.5	0.8 ^e

a: L (loosely mixed in a Pulverisette Minimill without grinding balls), G (mixed in an agate mortar for 10 minutes), M (mixed in a Pulverisette Minimill at 15 Hz using one 15 mm diameter zirconia ball and a Ball/Powder Ratio of 10), HM (mixed in a Spex8000 Mixer Mill rotating at 875 rpm with nine 10 mm diameter zirconia balls and a Ball/Powder Ratio of 20); b: estimated using Scherrer equation;⁴¹ c: nominal loading; d: measured by ICP; e: measured at 623 K in a flow reactor under 5% conversion; f: calculated under differential conditions in a recycle reactor at 623 K.

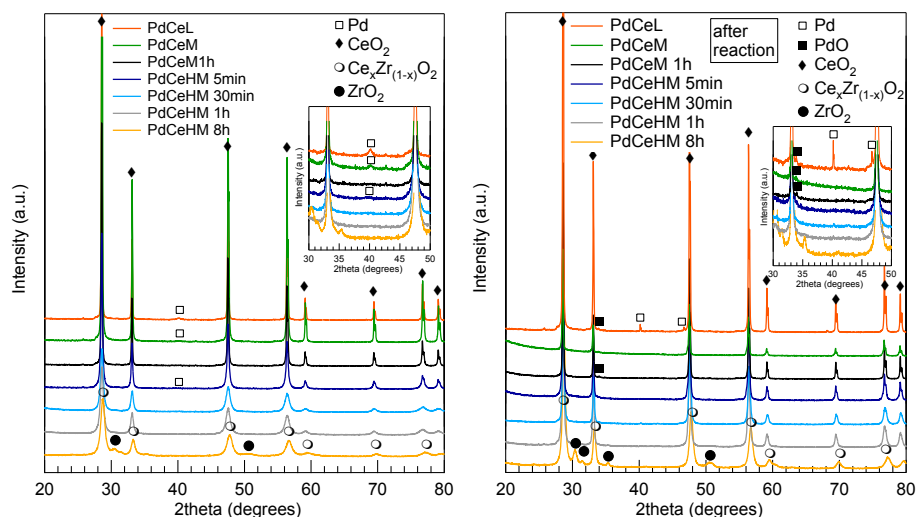


Figure 4.1: XRD spectra of milled samples, as prepared (left) and after reaction (right). Inset: focus on the Pd-PdO 2theta range.

X-ray diffraction profiles for all samples show peaks belonging to main reflections of CeO_2 fluorite phase. In one sample only (PdCeHM8h) a slight shift of the diffraction profile at higher angles indicates formation of solid solution between CeO_2 and ZrO_2 originating from the milling media. The high energy impact and friction that characterize milling in this sample can explain the leaching of ZrO_2 from the grinding balls and jar with insertion of Zr inside CeO_2 lattice, as already observed under similar milling conditions.^{31,42} For the same reason diffraction peaks belonging to free ZrO_2 are also detected. Weak XRD signals due to Pd are also distinguished in the fresh samples (see inset Figure 4.1).

In Figure 4.2 the light-off curves of combustion tests measured under the same conditions are reported for all prepared samples. The heating and cooling ramps are shown separately and refer to the second combustion cycle, where the catalytic behavior is usually stabilized.⁴⁰ To better compare the activity, in Figure 4.3 are reported the temperatures at which 10% CH_4 conversion was achieved (T_{10}) during combustion tests. Figure 4.3 shows also reaction rates measured at 623 K for all samples as reported in Table 4.1. As it can be observed there is a narrow window of optimal milling conditions which result in highly active Pd/ CeO_2 catalyst. These conditions depend heavily on the characteristics of the milling and on the milling time. Mild grinding in an agate mortar (PdCeG) or milling in a Minimill (PdCeM milled at 15 Hz with one single grinding ball) for up to 1h led to the lowest ignition temperatures, as seen by the light-off curves in Figure 4.2 and the corresponding T_{10} reported in Figure 4.3.

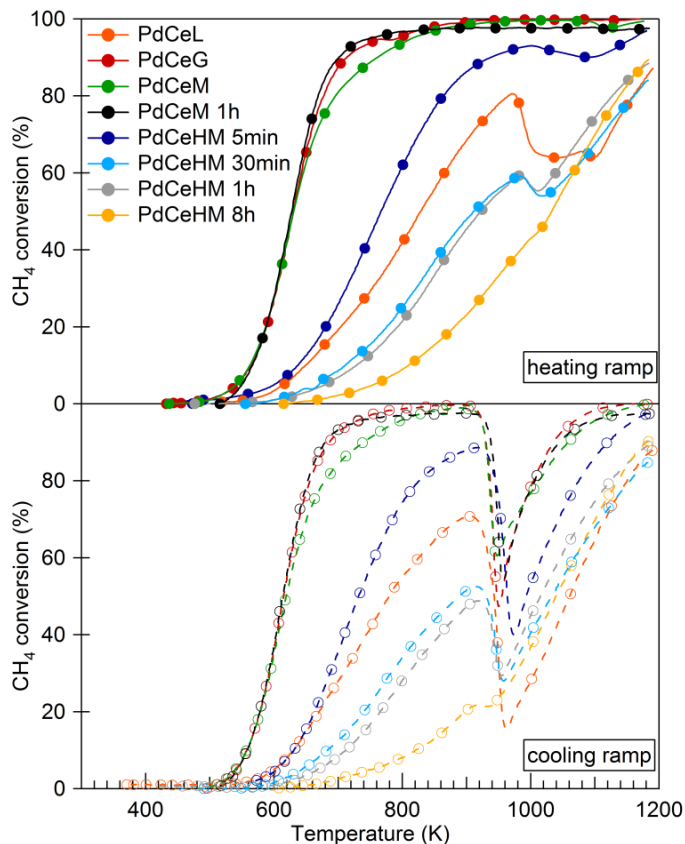


Figure 4.2: Methane oxidation tests; second combustion cycle. Solid line: heating; dashed line: cooling.

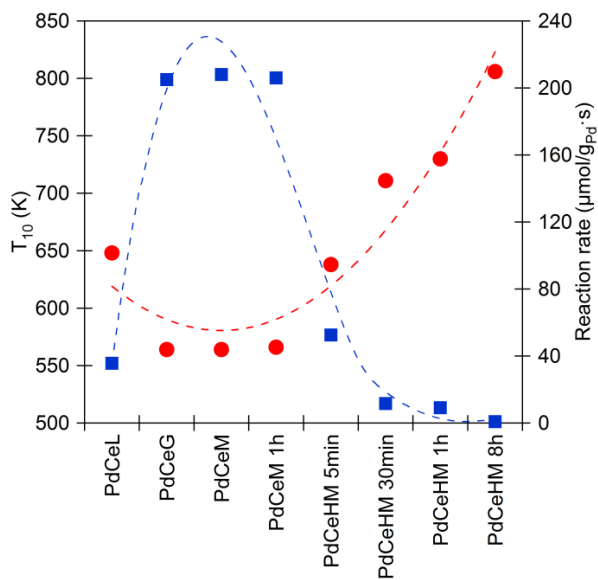


Figure 4.3: Temperatures of 10% methane conversion in the second TPC cycle (red circles) and reaction rates measured at 623 K (blue squares).

Conversely, milling in the high energy Spex 8000 mill brought to very different results. While the overall rpm and BPR were similar to the P23 Minimill conditions (i.e. 900 rpm and BPR = 10), the increased amount of grinding balls brought to an exponential increase of ball-to-ball impacts.⁴³ Since the milling spheres possess high kinetic energy, the impacts among them confer a much higher energy to the milled powders compared to ball-to-wall impacts, as the jar walls have kinetic energy equal to zero.⁴⁴ As a consequence, in the Spex8000 mill the powders are subjected to more frequent and energetic collisions, while in the Minimill arrangement and in the agate mortar mostly shear stresses are developed due to the friction of the single ball or the pestle on the walls.

At nanoscale, this may influence the fracture-relaxation phenomena occurring at the interface²² with a strong effect on the properties of the catalytic materials obtained. In fact, as evidenced by data in Figure 4.3 and the light-off curves in Figure 4.2, the HM samples display poor methane oxidation activity which further decreases with prolonged milling times. It can also be observed from Table 4.1 that these impacts are able to break down the particles with a decrease in crystallite size and a consequent increase of surface area. In addition, at longer milling time, impacts can partially transfer zirconium ions from the milling media to the powder, thus leading to a contamination of the support. Both phenomena are typically observed when milling powders under similar conditions.^{28,31}

The different interaction developed between ceria and palladium was further characterized by Temperature Programmed Oxidation (TPO) tests and HRTEM investigation. Figure 4.4 shows TPO profiles of the most representative samples in the first two heating/cooling cycles. Further TPO cycles do not modify the overall profile and the second TPO is therefore indicative of the behavior of the sample under catalytic conditions. PdCeM profile shows a broad oxygen uptake in the first cycle during heating between 450 K and 750 K. This is common to all samples investigated, excluding PdCeHM8h, and it is due to the complete oxidation of the metallic Pd nanoparticles to PdO as quantitatively shown in Table 4.2 with an oxygen uptake ranging from 41.9 to 51.5 $\mu\text{moles O}_2$ per gram of catalyst that is close to the oxidation of ca. 100% of metallic Pd to PdO (Uptake 0 in Table 2). At ca. 1040 K the decomposition of PdO to Pd takes place in one single peak (Release 1). During cooling reformation of PdO occurs at lower temperature (ca. 910 K, Uptake 1) showing the typical hysteresis of Pd/PdO formation/decomposition.⁴⁵ In the second cycle, decomposition of PdO to Pd occurs in three successive steps (Release 2) suggesting the presence of strongly interacting Pd-Ce-O species which decompose at high temperatures (1120 K) and

that are usually related to a high methane oxidation activity.⁴⁶ Reformation of PdO during cooling (Uptake 2) is qualitatively and quantitatively similar to PdO formation in the first cycle (Uptake 1). In all cases the quantity of oxygen uptake or released correspond to the oxidation or decomposition of ca. 100% of Pd/PdO. In PdCeL quantitative low temperature oxidation of Pd to PdO and high temperature decomposition of PdO to Pd is observed, with the latter occurring at slightly lower temperature than in PdCeM. However, only ca. 10% of loaded Pd is able to undergo oxidation during cooling, while in the following second cycle Pd has substantially lost its cycling capabilities. This is likely due to the insufficient contact established between the metal and the support during loose mixing which causes most of the Pd not in contact with ceria to sinter at high temperature and become inactive.

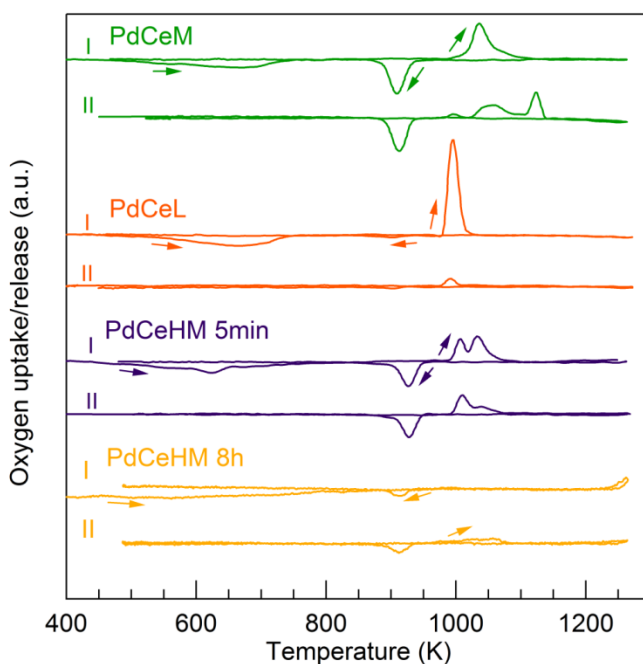


Figure 4.4: Oxygen uptake and release profiles, first and second TPO cycle.

Table 4.2: Quantitative analysis of TPO profiles.

Sample name	I cycle			II cycle	
	Uptake 0 ($\mu\text{moles O}_2/\text{g}$)	Release 1 ($\mu\text{moles O}_2/\text{g}$)	Uptake 1 ($\mu\text{moles O}_2/\text{g}$)	Release 2 ($\mu\text{moles O}_2/\text{g}$)	Uptake 2 ($\mu\text{moles O}_2/\text{g}$)
PdCeM	41.9 (110)	37.4 (99)	33.4 (89)	36.2 (96)	34.1 (91)
PdCeL	44.2 (94) ^a	43.5 (93)	6.4 (13)	6.7 (14)	4.5 (9)
PdCeHM 5min	51.5 (126)	30.5 (75)	20.9 (51)	18.8 (46)	21.0 (51)
PdCeHM 8h	-	0.2 (0)	7.5 (16)	10 (21)	11.5 (24)

a: the amount of Pd (% of total Pd) that is involved in oxidation/decomposition is reported in parentheses.

This explains the lower activity of PdCeL shown in Figure 4.2; on this sample the interaction between palladium and ceria is weak and during the first heating cycle at temperatures higher than 970 K, PdO decomposes to Pd metal (Figure 4.5), likely followed by the sintering of metal particles. During cooling their increased size prevents re-oxidation, thus losing active sites for the subsequent combustion cycles. Indeed, XRD measurements after reaction reveal the presence of highly crystalline metallic Pd (see Figure 4.1). Likely, the absence of the grinding ball hinders the creation of surface defects⁴⁷ or highly reactive sites⁴⁸ on the ceria surface, hence providing few anchoring sites for insertion and spreading of Pd. It is interesting, though, that even this very gentle mixing of Pd and ceria provides some interaction between the two components, as the catalytic behavior of PdCeL is better than that of bare Pd nanoparticles loosely mixed with quartz (Figure 4.6), where the activity heavily dropped at ca. 1173 K and does not recover in subsequent cycles.

On the samples milled at higher energy a progressive decrease in the amount of cycling Pd can be observed. On the PdCeHM 5min sample two distinct palladium oxide decomposition peaks appear in the first heating ramp, accounting for only 75% of all loaded Pd. During cooling, around 50% of the loaded metal is re-oxidized, which again decomposes in the second heating ramp in two steps between 1010 K and 1040 K. These peaks are usually attributed in the literature to superficial and bulk palladium oxide.⁴⁶ On the sample milled for 8 hours a negligible decomposition peak can be observed at 1000 K. During cooling, the characteristic O₂ absorption peak for Pd re-oxidation appears at slightly lower temperatures compared to other ceria-supported samples due to the inclusion of zirconium ions from the milling media in the ceria lattice.¹⁰ The quantitative analysis of the oxygen uptake and release in the second heating/cooling cycle indicates that only ca. 20% of all loaded Pd participates in the decomposition/re-oxidation cycle.

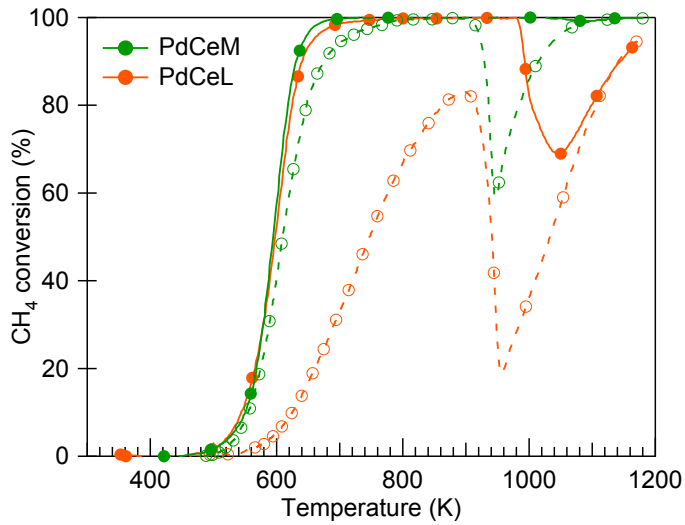


Figure 4.5: Methane conversion of PdCeM and PdCeL samples, 1st heating/cooling cycle.

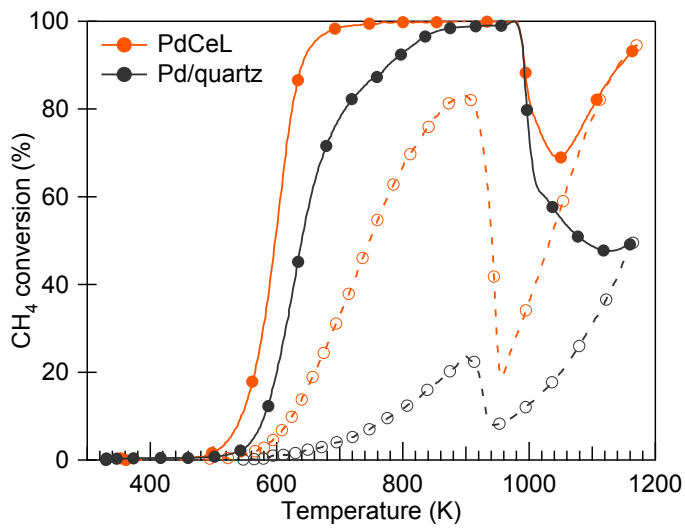


Figure 4.6: Methane conversion of PdCeL and unsupported Pd (mixed with quartz), 1st heating/cooling cycle.

HRTEM characterization allows us to observe in more detail the morphological characteristics of Pd-ceria catalysts as a function of milling parameters. When the contact energy is too low, Pd aggregates appear in weak contact with ceria, as shown in Figure 4.7(A,B). On the other hand, when Pd and CeO₂ are subject to soft milling and mostly shear stresses, the characteristic amorphous layer with embedded Pd is observed,⁴⁰ both in PdCeM and PdCeG samples (Figure 4.7(C) and (D), respectively). Under hard milling conditions, i.e. with a higher number of grinding balls, the palladium particles appear well defined and partially embedded inside the ceria lattice. On the PdCeHM 5min sample large Pd particles can be observed either in a flattened form (Figure 4.7(E)) or strongly anchored to the support crystal lattice (Figure 4.7(F)). It is possible that part of these particles are so strongly embedded inside the ceria lattice that, once oxidized in the first heating ramp in combustion or oxidation tests, they are not reactive anymore and do not participate in the typical PdO-Pd-PdO hysteresis behavior at high temperature. The remaining part, in weaker contact with ceria, is likely the one contributing to the oxygen uptake and release shown in Figure 4.4 and responsible for the relatively poor catalytic activity observed. Prolonged milling times, as in the PdCeHM 8h sample, lead to the insertion of these palladium particles inside the support. Figure 4.7(G,H) illustrate profile views of the sample where PdO particles are present and covered by a ceria layer. These HRTEM images suggest that the high mechanical energy developed is not only able to break ceria crystallites in smaller ones, as seen by the high surface area of this sample, but also to oxidize Pd particles to PdO which remains entrapped within ceria. The enclosed palladium is therefore not available for methane oxidation, which is in agreement with the progressive loss of activity with increasing milling times observed in light-off curves (Figure 4.2 and Figure 4.3).

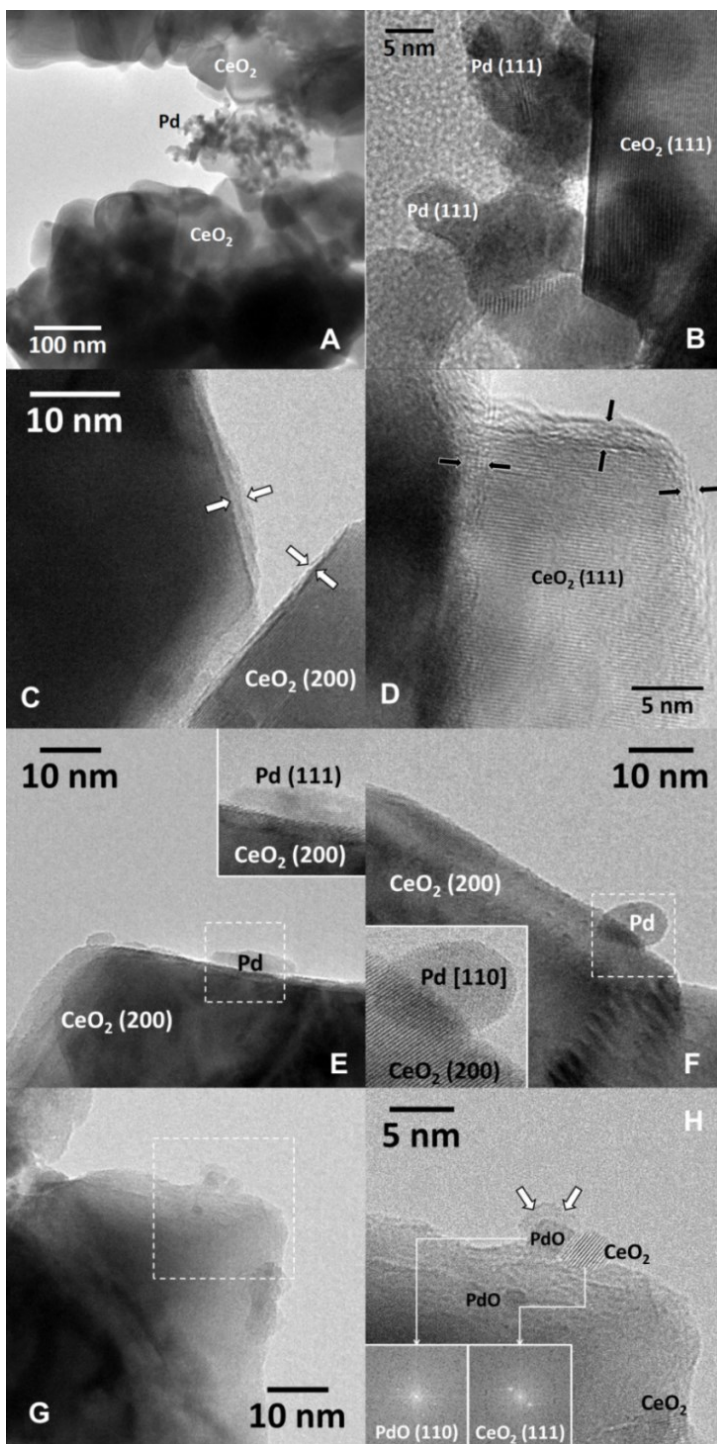


Figure 4.7: HRTEM images of (A,B) PdCeL, (C) PdCeM, (D) PdCeG, (E,F) PdCeHM 5min, (G,H) PdCeHM 8h.

Interestingly, after exposure of this sample under oxidizing conditions at high temperatures (1273 K), HRTEM observations evidence that part of the palladium oxide is disclosed and becomes exposed on the ceria surface. Indeed, the resulting PdO particles can be seen by HRTEM images in Figure 4.8(A,B): they lack any encapsulation and are characterized by a relatively large average dimension (around 10 nm). Some smaller features can also be observed on the ceria surface (Figure 4.8(C)), likely attributed to other palladium oxide species but too small for further HRTEM analysis. The newly exposed palladium is poorly active towards methane oxidation, as seen in Figure 4.9 that compares the light-off behavior of PdCeHM 8h before and after treatment at 1273 K. The lack of activity recovery might be due to the fact that not all the encapsulated palladium segregates to the surface after the thermal treatment, and/or to the low activity of bulk PdO in the low temperature region.^{4,40}

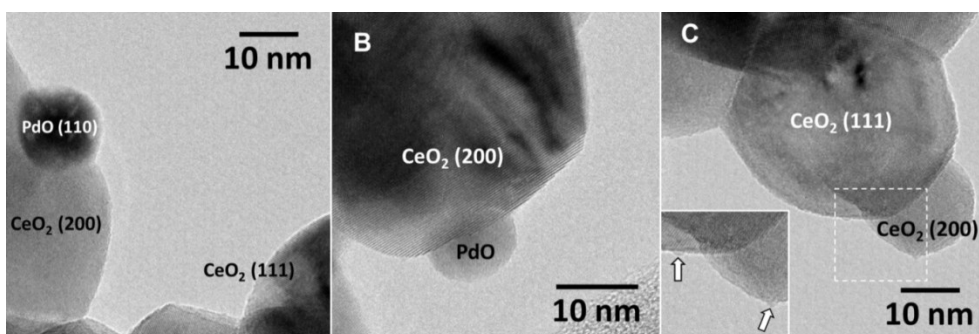


Figure 4.8: HRTEM images of PdCeHM 8h after oxidation test performed up to 1273 K.

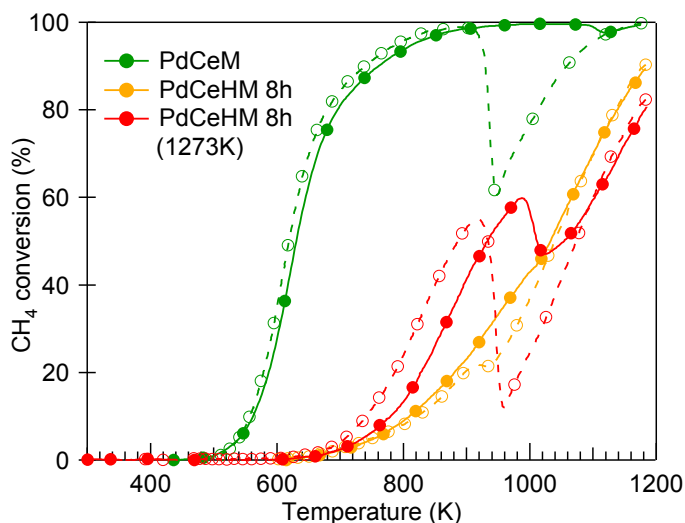


Figure 4.9: Catalytic activity of PdCeHM 8h before and after oxidation test (at 1273K). PdCeM is reported for comparison.

The encapsulation of PdO during high energy milling followed by its extraction when treated at high temperatures can be also followed by Raman spectroscopy. Spectra collected on PdCeHM 8h as prepared and after combustion (1173 K) and oxidation tests (1273 K) are illustrated in Figure 4.10. On the fresh milled sample the characteristic PdO peak at around 650 cm^{-1} is absent, and the same profile is obtained on the PdCeHM 8h sample after combustion reaction up to 1173 K. It is possible that under these conditions the signal of the small PdO entities embedded inside the ceria particles, observed by HRTEM in Figure 4.7, is too attenuated and therefore escapes detection. On the other hand, by thermally treating the sample at 1273 K these palladium species are oxidized and conglomerate in large PdO particles; as a result, the peak at 646 cm^{-1} corresponding to the B_{1g} vibrational mode of PdO is clearly observed. On all samples, the F_{2g} mode of CeO_2 is shifted to 468 cm^{-1} , compared to 461 cm^{-1} observed in fresh ceria, likely due to physical stresses on the ceria surface induced by the high intensity milling process⁴⁹ and the inclusion of some Zr^{4+} ions in the ceria lattice.⁵⁰

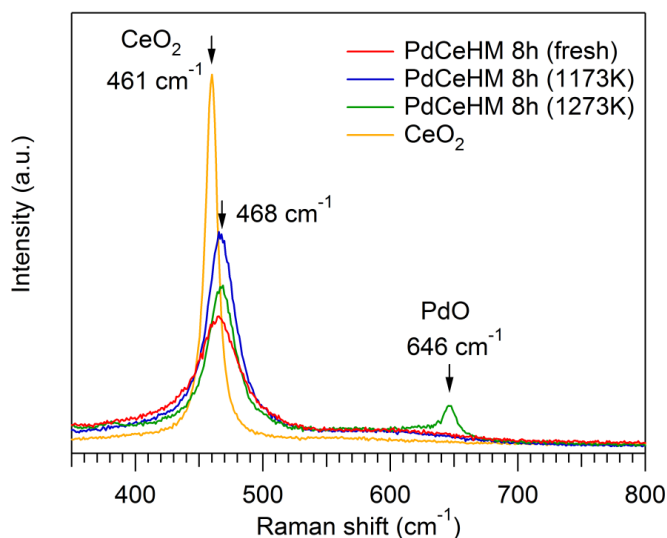


Figure 4.10: Raman spectra collected on PdCeHM 8h fresh, after combustion test at 1173 K and after oxidation test at 1273 K.

4.4 Conclusions

The milling of Pd and CeO_2 results in catalytic materials with very different performance in methane combustion. A correlation between the intensity of contact and the properties at nanoscale of Pd and CeO_2 is observed. To prepare active materials an appropriate shear energy must be developed during milling which ensures the embedding and dissolution of

metallic Pd particles in an amorphous Pd-ceria layer covering the ceria crystallites.⁴⁰ When the energy is insufficient, the palladium particles aggregate in grape-like clusters and display a very low interaction with the support oxide, producing catalysts which initial good activity but leading to a strong activity deterioration during reaction. On the other hand, highly energetic direct impacts flatten and embed large oxidized Pd particles inside of the ceria lattice, making them unavailable for methane activation. High temperature treatment partially reverses this process, with only a limited recovery of activity.

The obtained results differ from the general trends reported in the literature, where usually a high energy is needed in order to induce atomic interactions. Possibly, the peculiar affinity between palladium and ceria combined with their physico-chemical properties ensures that soft shear-like stresses, as those obtained simply grinding in an agate mortar, are enough to have superficial alloying of the two phases in an amorphous layer surrounding the support, which is the key factor for the stabilization of a high methane oxidation activity observed on these materials.

4.5 References

- (1) Monai, M.; Montini, T.; Gorte, R. J.; Fornasiero, P. Catalytic Oxidation of Methane: Pd and Beyond: Catalytic Oxidation of Methane: Pd and Beyond. *European Journal of Inorganic Chemistry* **2018**, *2018* (25), 2884–2893. <https://doi.org/10.1002/ejic.201800326>.
- (2) Satsuma, A.; Osaki, K.; Yanagihara, M.; Ohyama, J.; Shimizu, K. Low Temperature Combustion over Supported Pd Catalysts – Strategy for Catalyst Design. *Catalysis Today* **2015**, *258*, 83–89. <https://doi.org/10.1016/j.cattod.2015.03.047>.
- (3) Farrauto, R. J. Low-Temperature Oxidation of Methane. *Science* **2012**, *337* (6095), 659–660. <https://doi.org/10.1126/science.1226310>.
- (4) Ciuparu, D.; Lyubovsky, M. R.; Altman, E.; Pfefferle, L. D.; Datye, A. Catalytic Combustion of Methane over Palladium-based Catalysts. *Catalysis Reviews* **2002**, *44* (4), 593–649. <https://doi.org/10.1081/CR-120015482>.
- (5) Lampert, J.; Kazi, M.; Farrauto, R. Palladium Catalyst Performance for Methane Emissions Abatement from Lean Burn Natural Gas Vehicles. *Applied Catalysis B: Environmental* **1997**, *14* (3–4), 211–223. [https://doi.org/10.1016/S0926-3373\(97\)00024-6](https://doi.org/10.1016/S0926-3373(97)00024-6).
- (6) Nemitallah, M. A.; Rashwan, S. S.; Mansir, I. B.; Abdelhafez, A. A.; Habib, M. A. Review of Novel Combustion Techniques for Clean Power Production in Gas Turbines. *Energy & Fuels* **2018**, *32* (2), 979–1004. <https://doi.org/10.1021/acs.energyfuels.7b03607>.
- (7) Wang, B.; Albarracín-Suazo, S.; Pagán-Torres, Y.; Nikolla, E. Advances in Methane Conversion Processes. *Catalysis Today* **2017**, *285*, 147–158. <https://doi.org/10.1016/j.cattod.2017.01.023>.
- (8) Kondratenko, E. V.; Peppel, T.; Seeburg, D.; Kondratenko, V. A.; Kalevaru, N.; Martin, A.; Wohlrab, S. Methane Conversion into Different Hydrocarbons or Oxygenates: Current Status and Future Perspectives in Catalyst Development and Reactor Operation. *Catalysis Science & Technology* **2017**, *7* (2), 366–381. <https://doi.org/10.1039/C6CY01879C>.
- (9) Fouladvand, S.; Schernich, S.; Libuda, J.; Grönbeck, H.; Pingel, T.; Olsson, E.; Skoglundh, M.; Carlsson, P.-A. Methane Oxidation Over Pd Supported on Ceria–Alumina Under Rich/Lean Cycling Conditions. *Topics in Catalysis* **2013**, *56* (1–8), 410–415. <https://doi.org/10.1007/s11244-013-9988-2>.
- (10) Colussi, S.; Trovarelli, A.; Cristiani, C.; Lietti, L.; Groppi, G. The Influence of Ceria and Other Rare Earth Promoters on Palladium-Based Methane Combustion Catalysts. *Catalysis Today* **2012**, *180* (1), 124–130. <https://doi.org/10.1016/j.cattod.2011.03.021>.
- (11) Cargnello, M.; Jaen, J. J. D.; Garrido, J. C. H.; Bakhmutsky, K.; Montini, T.; Gamez, J. J. C.; Gorte, R. J.; Fornasiero, P. Exceptional Activity for Methane Combustion over Modular Pd@CeO₂ Subunits on Functionalized Al₂O₃. *Science* **2012**, *337* (6095), 713–717. <https://doi.org/10.1126/science.1222887>.
- (12) Groppi, G.; Cristiani, C.; Lietti, L.; Ramella, C.; Valentini, M.; Forzatti, P. Effect of Ceria on Palladium Supported Catalysts for High Temperature Combustion of CH₄ under Lean Conditions. *Catalysis Today* **1999**, *50* (2), 399–412. [https://doi.org/10.1016/S0920-5861\(98\)00518-5](https://doi.org/10.1016/S0920-5861(98)00518-5).

- (13) Su, Y.-Q.; Filot, I. A. W.; Liu, J.-X. Stable Pd-Doped Ceria Structures for CH₄ Activation and CO Oxidation. *ACS Catalysis* **2018**, *8* (1), 75–80. <https://doi.org/10.1021/acscatal.7b03295>.
- (14) Senftle, T. P.; van Duin, A. C. T.; Janik, M. J. Methane Activation at the Pd/CeO₂ Interface. *ACS Catalysis* **2017**, *7* (1), 327–332. <https://doi.org/10.1021/acscatal.6b02447>.
- (15) Mayernick, A. D.; Janik, M. J. Methane Oxidation on Pd–Ceria: A DFT Study of the Mechanism over Pd_xCe_{1-x}O₂, Pd, and PdO. *Journal of Catalysis* **2011**, *278* (1), 16–25. <https://doi.org/10.1016/j.jcat.2010.11.006>.
- (16) Colussi, S.; Gayen, A.; Farnesi Camellone, M.; Boaro, M.; Llorca, J.; Fabris, S.; Trovarelli, A. Nanofaceted Pd-O Sites in Pd-Ce Surface Superstructures: Enhanced Activity in Catalytic Combustion of Methane. *Angewandte Chemie International Edition* **2009**, *48* (45), 8481–8484. <https://doi.org/10.1002/anie.200903581>.
- (17) Senftle, T. P.; van Duin, A. C. T.; Janik, M. J. Role of Site Stability in Methane Activation on Pd_xCe_{1-x}O_δ Surfaces. *ACS Catalysis* **2015**, *5* (10), 6187–6199. <https://doi.org/10.1021/acscatal.5b00741>.
- (18) Toso, A.; Colussi, S.; Padigapaty, S.; de Leitenburg, C.; Trovarelli, A. High Stability and Activity of Solution Combustion Synthesized Pd-Based Catalysts for Methane Combustion in Presence of Water. *Applied Catalysis B: Environmental* **2018**, *230*, 237–245. <https://doi.org/10.1016/j.apcatb.2018.02.049>.
- (19) Gholami, R.; Alyani, M.; Smith, K. Deactivation of Pd Catalysts by Water during Low Temperature Methane Oxidation Relevant to Natural Gas Vehicle Converters. *Catalysts* **2015**, *5* (2), 561–594. <https://doi.org/10.3390/catal5020561>.
- (20) Schwartz, W. R.; Ciuparu, D.; Pfefferle, L. D. Combustion of Methane over Palladium-Based Catalysts: Catalytic Deactivation and Role of the Support. *The Journal of Physical Chemistry C* **2012**, *116* (15), 8587–8593. <https://doi.org/10.1021/jp212236e>.
- (21) Persson, K.; Pfefferle, L. D.; Schwartz, W.; Ersson, A.; Järås, S. G. Stability of Palladium-Based Catalysts during Catalytic Combustion of Methane: The Influence of Water. *Applied Catalysis B: Environmental* **2007**, *74* (3–4), 242–250. <https://doi.org/10.1016/j.apcatb.2007.02.015>.
- (22) Baláž, P.; Achimovičová, M.; Baláž, M.; Billik, P.; Cherkezova-Zheleva, Z.; Criado, J. M.; Delogu, F.; Dutková, E.; Gaffet, E.; Gotor, F. J.; et al. Hallmarks of Mechanochemistry: From Nanoparticles to Technology. *Chemical Society Reviews* **2013**, *42* (18), 7571. <https://doi.org/10.1039/c3cs35468g>.
- (23) Takacs, L. The Historical Development of Mechanochemistry. *Chemical Society Reviews* **2013**, *42* (18), 7649. <https://doi.org/10.1039/c2cs35442j>.
- (24) Bolm, C.; Hernández, J. G. Mechanochemistry of Gaseous Reactants. *Angewandte Chemie International Edition* **2019**, *58* (11), 3285–3299. <https://doi.org/10.1002/anie.201810902>.
- (25) Enayati, M. H.; Mohamed, F. A. Application of Mechanical Alloying/Milling for Synthesis of Nanocrystalline and Amorphous Materials. *International Materials Reviews* **2014**, *59* (7), 394–416. <https://doi.org/10.1179/1743280414Y.0000000036>.
- (26) Šepelák, V.; Düvel, A.; Wilkening, M.; Becker, K.-D.; Heitjans, P. Mechanochemical Reactions and Syntheses of Oxides. *Chemical Society Reviews* **2013**, *42* (18), 7507. <https://doi.org/10.1039/c2cs35462d>.

- (27) Šepelák, V.; Bégin-Colin, S.; Le Caër, G. Transformations in Oxides Induced by High-Energy Ball-Milling. *Dalton Transactions* **2012**, 41 (39), 11927. <https://doi.org/10.1039/c2dt30349c>.
- (28) Kawaguchi, T.; Nakamura, H.; Watano, S. Parametric Study of Dry Coating Process of Electrode Particle with Model Material of Sulfide Solid Electrolytes for All-Solid-State Battery. *Powder Technology* **2017**, 305, 241–249. <https://doi.org/10.1016/j.powtec.2016.09.085>.
- (29) Zhao, B.; Tong, Y.; Zhao, Y.; Yang, T.; Yang, F.; Hu, Q.; Zhao, C. Preparation of Ultra-Fine $\text{Sm}_{0.2}\text{Ce}_{0.8}\text{O}_{1.9}$ Powder by a Novel Solid State Reaction and Fabrication of Dense $\text{Sm}_{0.2}\text{Ce}_{0.8}\text{O}_{1.9}$ Electrolyte Film. *Ceramics International* **2015**, 41 (8), 9686–9691. <https://doi.org/10.1016/j.ceramint.2015.04.037>.
- (30) Enayati, M. H. Formation of Nanoscale Layered Structures and Subsequent Transformations during Mechanical Alloying of $\text{Ni}_{60}\text{Nb}_{40}$ Powder Mixture in a Low Energy Ball Mill. *KONA Powder and Particle Journal* **2015**, 32 (0), 196–206. <https://doi.org/10.14356/kona.2015010>.
- (31) Trovarelli, A.; Zamar, F.; Llorca, J.; Leitenburg, C. de; Dolcetti, G.; Kiss, J. T. Nanophase Fluorite-Structured $\text{CeO}_2\text{-ZrO}_2$ Catalysts Prepared by High-Energy Mechanical Milling. *Journal of Catalysis* **1997**, 169 (2), 490–502. <https://doi.org/10.1006/jcat.1997.1705>.
- (32) Ralphs, K.; Zhang, C.; James, S. L. Solventless Mechanochemical Metallation of Porphyrins. *Green Chemistry* **2017**, 19 (1), 102–105. <https://doi.org/10.1039/C6GC02420C>.
- (33) Muñoz-Batista, M. J.; Rodriguez-Padron, D.; Puente-Santiago, A. R.; Luque, R. Mechanochemistry: Toward Sustainable Design of Advanced Nanomaterials for Electrochemical Energy Storage and Catalytic Applications. *ACS Sustainable Chemistry & Engineering* **2018**, 6 (8), 9530–9544. <https://doi.org/10.1021/acssuschemeng.8b01716>.
- (34) Do, J.-L.; Frišičić, T. Mechanochemistry: A Force of Synthesis. *ACS Central Science* **2017**, 3 (1), 13–19. <https://doi.org/10.1021/acscentsci.6b00277>.
- (35) Xu, C.; De, S.; Balu, A. M.; Ojeda, M.; Luque, R. Mechanochemical Synthesis of Advanced Nanomaterials for Catalytic Applications. *Chemical Communications* **2015**, 51 (31), 6698–6713. <https://doi.org/10.1039/C4CC09876E>.
- (36) Ralphs, K.; Hardacre, C.; James, S. L. Application of Heterogeneous Catalysts Prepared by Mechanochemical Synthesis. *Chemical Society Reviews* **2013**, 42 (18), 7701. <https://doi.org/10.1039/c3cs60066a>.
- (37) Ismagilov, Z. R.; Kuntsevich, S. V.; Shikina, N. V.; Kuznetsov, V. V.; Kerzhentsev, M. A.; Ushakov, V. A.; Rogov, V. A.; Boronin, A. I.; Zaikovskiy, V. I. Characterization of Alumina-Supported Uranium Oxide Catalysts in Methane Oxidation. *Catalysis Today* **2010**, 157 (1–4), 217–222. <https://doi.org/10.1016/j.cattod.2010.02.020>.
- (38) Kawabata, T.; Matsuoka, H.; Shishido, T.; Li, D.; Tian, Y.; Sano, T.; Takehira, K. Steam Reforming of Dimethyl Ether over ZSM-5 Coupled with $\text{Cu/ZnO/Al}_2\text{O}_3$ Catalyst Prepared by Homogeneous Precipitation. *Applied Catalysis A: General* **2006**, 308, 82–90. <https://doi.org/10.1016/j.apcata.2006.04.032>.
- (39) Lin, Y.; Watson, K. A.; Fallbach, M. J.; Ghose, S.; Smith, J. G.; Delozier, D. M.; Cao, W.; Crooks, R. E.; Connell, J. W. Rapid, Solventless, Bulk Preparation of Metal Nanoparticle-Decorated Carbon Nanotubes. *ACS Nano* **2009**, 3 (4), 871–884. <https://doi.org/10.1021/nn8009097>.

- (40) Danielis, M.; Colussi, S.; de Leitenburg, C.; Soler, L.; Llorca, J.; Trovarelli, A. Outstanding Methane Oxidation Performance of Palladium-Embedded Ceria Catalysts Prepared by a One-Step Dry Ball-Milling Method. *Angewandte Chemie International Edition* **2018**, *57* (32), 10212–10216. <https://doi.org/10.1002/anie.201805929>.
- (41) Jenkins, R.; Snyder, R. L. *Introduction to X-Ray Powder Diffractometry*; Wiley: New York, 1996.
- (42) Aneggi, E.; Rico-Perez, V.; de Leitenburg, C.; Maschio, S.; Soler, L.; Llorca, J.; Trovarelli, A. Ceria-Zirconia Particles Wrapped in a 2D Carbon Envelope: Improved Low-Temperature Oxygen Transfer and Oxidation Activity. *Angewandte Chemie International Edition* **2015**, *54* (47), 14040–14043. <https://doi.org/10.1002/anie.201507839>.
- (43) Davis, R. M.; McDermott, B.; Koch, C. C. Mechanical Alloying of Brittle Materials. *Metallurgical Transactions A* **1988**, *19* (12), 2867–2874. <https://doi.org/10.1007/BF02647712>.
- (44) Jiang, X.; Trunov, M. A.; Schoenitz, M.; Dave, R. N.; Dreizin, E. L. Mechanical Alloying and Reactive Milling in a High Energy Planetary Mill. *Journal of Alloys and Compounds* **2009**, *478* (1–2), 246–251. <https://doi.org/10.1016/j.jallcom.2008.12.021>.
- (45) Farrauto, R. J.; Lampert, J. K.; Hobson, M. C.; Waterman, E. M. Thermal Decomposition and Reformation of PdO Catalysts; Support Effects. *Applied Catalysis B: Environmental* **1995**, *6*(3), 263–270. [https://doi.org/10.1016/0926-3373\(95\)00015-1](https://doi.org/10.1016/0926-3373(95)00015-1).
- (46) Colussi, S.; Trovarelli, A.; Vesselli, E.; Baraldi, A.; Comelli, G.; Groppi, G.; Llorca, J. Structure and Morphology of Pd/Al₂O₃ and Pd/CeO₂/Al₂O₃ Combustion Catalysts in Pd–PdO Transformation Hysteresis. *Applied Catalysis A: General* **2010**, *390* (1–2), 1–10. <https://doi.org/10.1016/j.apcata.2010.09.033>.
- (47) Yang, Y.; Zhang, S.; Wang, S.; Zhang, K.; Wang, H.; Huang, J.; Deng, S.; Wang, B.; Wang, Y.; Yu, G. Ball Milling Synthesized MnO_x as Highly Active Catalyst for Gaseous POPs Removal: Significance of Mechanochemically Induced Oxygen Vacancies. *Environmental Science & Technology* **2015**, *49* (7), 4473–4480. <https://doi.org/10.1021/es505232f>.
- (48) Sayle, T. X. T.; Cantoni, M.; Bhatta, U. M.; Parker, S. C.; Hall, S. R.; Möbus, G.; Molinari, M.; Reid, D.; Seal, S.; Sayle, D. C. Strain and Architecture-Tuned Reactivity in Ceria Nanostructures; Enhanced Catalytic Oxidation of CO to CO₂. *Chemistry of Materials* **2012**, *24* (10), 1811–1821. <https://doi.org/10.1021/cm3003436>.
- (49) Li, H.; Zhang, P.; Li, G.; Lu, J.; Wu, Q.; Gu, Y. Stress Measurement for Nonstoichiometric Ceria Films Based on Raman Spectroscopy. *Journal of Alloys and Compounds* **2016**, *682*, 132–137. <https://doi.org/10.1016/j.jallcom.2016.04.272>.
- (50) Xu, Y.; Wang, F.; Liu, X.; Liu, Y.; Luo, M.; Teng, B.; Fan, M.; Liu, X. Resolving a Decade-Long Question of Oxygen Defects in Raman Spectra of Ceria-Based Catalysts at Atomic Level. *The Journal of Physical Chemistry C* **2019**, *123* (31), 18889–18894. <https://doi.org/10.1021/acs.jpcc.9b00633>.

5 The Role of Palladium Salt Precursors in Pd-PdO/CeO₂ Methane Oxidation Catalysts Prepared by Dry Milling

Abstract

Heterogeneous catalysts comprising palladium as active phase are widely used to promote a variety of reactions due to the easy tuning of Pd particle size and its oxidation state. When Pd is combined with CeO₂, specific structural arrangements at the nanoscale level can strongly impact on activity and durability, especially in methane oxidation. In this work, the effect of different palladium salt precursors on the final state of a Pd/CeO₂ catalyst prepared by dry milling was studied by coupling thermogravimetric characterization and temperature programmed reaction methods. The combination of palladium acetate and a mild oxidative thermal treatment proved successful in generating an appropriate Pd⁰/Pd²⁺ mixture on the ceria surface with improved methane oxidation activity.

This was published as:

Danielis, M.; Colussi, S.; de Leitenburg, C.; Trovarelli, A. The Role of Palladium Salt Precursors in Pd-PdO/CeO₂ Catalysts Prepared by Dry Milling for Methane Oxidation. *Catalysis Communications* **2020**, *135*, 105899. <https://doi.org/10.1016/j.catcom.2019.105899>.

5.1 Introduction

Palladium is an extremely versatile noble metal and its intrinsic properties make it active in a variety of reactions, ranging from complete oxidation of methane and other hydrocarbons¹⁻³ to hydrogenation^{4,5} and C-C coupling reactions.^{6,7} In particular, its ability to activate methane at low temperatures is making palladium-based materials especially attractive for the production of higher-value feedstock from abundant natural gas sources⁸ and widely employed in three-way catalytic converters for spark-ignited engines.^{9,10} Consequently, its popularity and widespread use have increased its market price, promoting the recycling from end-of-life products¹¹ and leading manufacturers towards further optimization of the palladium active phase.

Heterogeneous catalysts are usually prepared by wet syntheses followed by calcination and activation treatments.¹² The effect of different palladium precursors and solvents employed has been often explored in the literature,^{4,13-17} since the anion properties play a big role in the obtained noble metal dispersion, particle size and oxidation state that are usually key factors for increased activity and selectivity, as evidenced by advanced operando studies.^{16,18} For methane oxidation, it is suggested that the active phase at low temperature consists of a mixture of different Pd entities in an oxidized form (Pd²⁺, PdO, PdO_x).¹⁹ The role of metallic Pd is more controversial and still debated, but in the high temperature range it is well established that Pd⁰ is inactive, causing the typical activity loss observed for Pd-based catalysts between ca 973 K and 1173 K.²⁰

In this chapter we investigate the role of palladium precursors on Pd/CeO₂ catalysts prepared by a dry milling procedure developed in our lab^{21,22} and utilized for the catalytic oxidation of methane. In the previous works, we observed how the success of the preparation was strongly dependent on the milling parameters²² and on the choice of palladium precursor,²¹ either metallic or palladium oxide nanoparticles, the latter resulting in materials with extremely poor activity. Here we explore the effect of palladium salts as precursors for the synthesis of Pd/CeO₂ catalytic materials by dry milling, their role in the obtained Pd species on the ceria surface and the related methane combustion activity.

5.2 Experimental

Samples containing 1 wt% Pd were prepared using commercial ceria as support oxide (Treibacher Industrie AG), calcined at 1173 K in static air prior to synthesis with a final

surface area of 3 m²/g. Two precursor salts were used, palladium acetate (Sigma Aldrich, 99.9%) and palladium nitrate (Johnson Matthey, 41.54% Pd). For the dry milled samples (M), the solid salts were milled with ceria powder in a Pulverisette 23 Mini-mill for 20 minutes at 15 Hz, following the recently reported mechano-chemical synthesis.²¹ As reference, two samples were prepared by incipient wetness impregnation (IW) on the same ceria support using a commercial palladium nitrate solution (Sigma Aldrich, 99.999%) and palladium acetate dissolved in acetone. After impregnation, the IW samples were dried at 373 K overnight and calcined in static air at 1173 K for 3 hours. Other catalytic samples were prepared by milling the palladium salts with commercial ZrO₂ (Grace) and alumina prepared in our laboratory by calcination of pseudoboehmite. Both support oxides were calcined at 1173 K for 3 hours before synthesis, resulting in a BET surface area of 20 m²/g and 146 m²/g for ZrO₂ and γ -Al₂O₃, respectively. The samples were denoted as PdAc(PdN)Al M and PdAcZr M.

The decomposition properties and behavior of the precursor salts were analyzed by thermogravimetric analysis (TGA) in a Q500 - TA Instruments. Temperature programmed oxidation (TPO) tests were carried out to analyze the palladium decomposition/re-oxidation behavior by monitoring the oxygen uptake and release during heating and cooling cycles. Catalytic methane oxidation was used as test reaction to assess the reactivity of prepared samples. TGA experiments were carried out under synthetic air (20.9% O₂/N₂) and reaction conditions (0.5% CH₄, 2% O₂ in He), total gas flow 60 ml/min, by heating the sample at 10 K/min from RT to 1173 K and gradually cooling it to 400 K. XRD analysis was performed in a Philips X'Pert diffractometer equipped with an X'Celerator detector using Ni-filtered Cu K α radiation ($\lambda = 1.542 \text{ \AA}$). XRD measurements were performed after activation of the samples at 1173 K in air and reaction conditions. TPO and methane combustion (TPC) tests were carried out in a lab scale setup,²¹ following an established procedure, described in detail in Chapter 2, Sections 2.2 and 2.3.

5.3 Results and Discussion

A summary of the catalytic samples and commercial solid precursors used in this study is reported in Table 5.1, together with the abbreviated sample name that will be used in the following.

Table 5.1: Summary of evaluated salts and catalytic samples.

Sample name	Composition	Nominal Pd content (wt%)	Preparation
PdN	$\text{Pd}(\text{NO}_3)_2$	41.54	Commercial (Johnson Matthey)
PdAc	$\text{Pd}(\text{OAc})_2$	47.4	Commercial (Sigma Aldrich)
CeO₂	$\text{CeO}_2(1173 \text{ K})$	-	Commercial (Treibacher)
PdN/CeIW	$\text{Pd}(\text{NO}_3)_2/\text{CeO}_2$	1	Incipient wetness impregnation (IW)
PdAc/CeIW	$\text{Pd}(\text{OAc})_2/\text{CeO}_2$	1	Incipient wetness impregnation (IW)
PdN/CeM	$\text{Pd}(\text{NO}_3)_2/\text{CeO}_2$	1	Milling (M)
PdAc/CeM	$\text{Pd}(\text{OAc})_2/\text{CeO}_2$	1	Milling (M)

The properties of the pure solid palladium salts were evaluated in TGA under air and reaction mixture (2% O₂, 0.5% CH₄ in He) to analyze the effect of the oxygen partial pressure on their intrinsic decomposition behavior. The weight loss profiles are shown in Figure 5.1. The high temperature weight loss (above 900 K), highlighted by a grey bar in Figure 5.1, corresponds to the decomposition of PdO to Pd and was used as reference for the semi-quantitative evaluation of the Pd species obtained during the precursor salt decomposition at around 400-500 K. For PdN and PdAc the measured weight loss above 900 K is equal to 5.8 wt% and 6.3 wt%, respectively, corresponding to ca. 90% of the theoretical oxygen released for the complete decomposition of PdO to Pd.

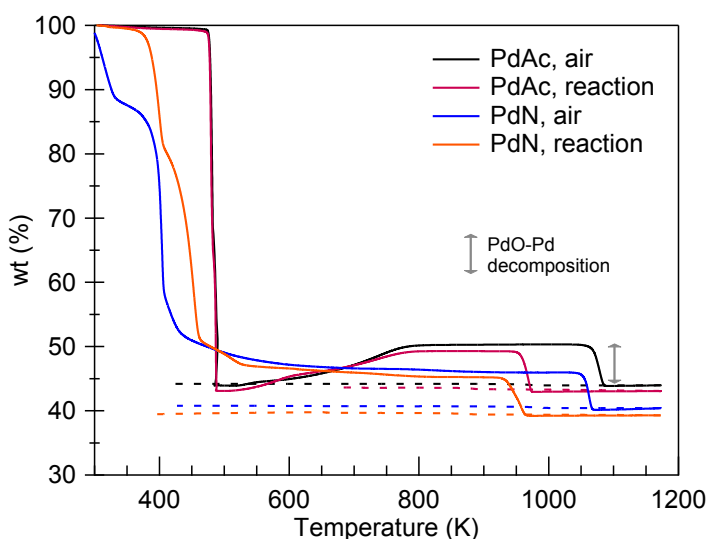


Figure 5.1: TGA profiles of unsupported palladium acetate and palladium nitrate, recorded under air (21% O₂ in N₂) and reaction conditions (0.5% CH₄, 2%O₂ in He). Solid line: heating; dashed line: cooling.

Considering the first decomposition step in Figure 5.1, a prominent difference can be observed between the two precursors: while palladium nitrate gradually reaches a fully oxidized state, palladium acetate exhibits a more complex behavior with a sudden drop to metallic Pd at around 480 K and a subsequent, slow re-oxidation to PdO completed at around 800 K. This behavior was already observed in the literature, showing how palladium nitrate decomposes thermally to PdO,²³ while palladium acetate tends to decompose to metallic Pd.²⁴ The organic anion decomposes in a mixture of volatile compounds, such as CO₂, CO and acetic acid, which are immediately further oxidized releasing more heat and adding complexity to the system. Interestingly, this behavior appears to be independent from the oxygen partial pressure, whose effect can be instead observed on the PdO decomposition temperature above 900 K (compare the profile under air and under reaction mixture).

The high temperature redox behavior of palladium is a complex phenomenon, with its thermodynamically stable phase turning from the oxide to the metal. The $2\text{PdO} \rightarrow 2\text{Pd} + \text{O}_2$ transition depends on particle size and oxygen partial pressure^{20,25,26} and can be shifted to higher temperatures by increasing O₂ content or by providing a support oxide with oxygen exchange capacity.^{27,28} During cooling, the re-oxidation of the metallic phase is kinetically limited and occurs at lower temperatures with respect to the decomposition,²⁸ giving rise to the well-known hysteresis behavior of palladium.²⁹ If no anchoring sites are offered by the support, metallic particles are free to sinter, thus inhibiting re-oxidation; indeed, for unsupported salts no weight increase can be measured during cooling at around 900-950 K, reflecting the absence of oxygen uptake in temperature-programmed oxidation tests observed in our previous work²¹ for unsupported Pd nanoparticles.

When the salts are dry milled on a reducible support, like CeO₂, both their decomposition behavior and Pd-PdO hysteresis cycles are partially modified, as clearly illustrated in Figure 5.2. This is most likely due to the oxygen storage capacity of ceria, which is further promoted by defects originating from mechanical stresses developed during milling.^{21,30} Focusing on the low temperature region, it can be observed that the formation of oxidized PdO species from PdAc decomposition is favored when supported on ceria, compared to the unsupported salt. The oxidation degree depends on oxygen partial pressure: when PdAcCeM is heated in air the salt is immediately fully oxidized, while an intermediate Pd/PdO mixture is obtained under 2% O₂ pressure (indicated by the 0.048% weight uptake at 550 K compared to the 0.114% weight loss at 950 K). The low Pd loading and the little amount of tested sample result in a significant experimental error on the measured final weight.

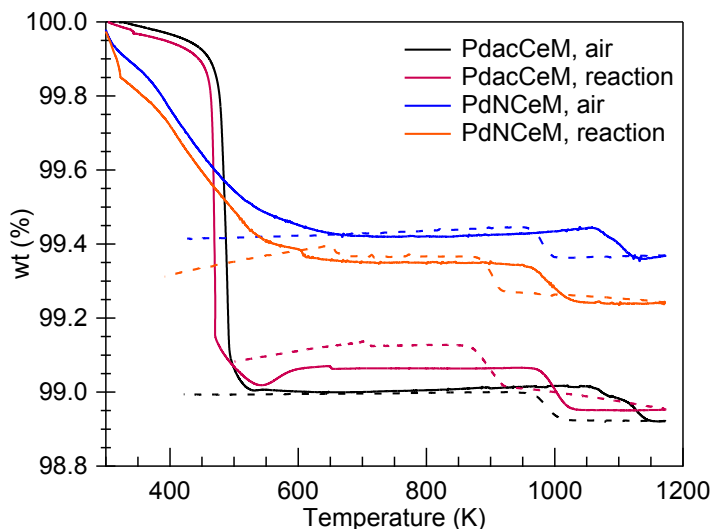


Figure 5.2: TGA profiles of PdAcCeM and PdNCeM dry-milled samples under air (21% O₂ in N₂) and reaction conditions (0.5% CH₄, 2% O₂ in He). Solid line: heating; dashed line: cooling.

Consequently, to provide a comparison with a smaller experimental error, a sample with increased Pd loading (4%) was prepared and tested (Figure 5.3). The 4PdAcCeM sample exhibited the same behavior as PdAcCeM, with a full oxidation in air and a partial oxidation state under reaction conditions. During heating in reaction conditions, the quantitative analysis shows that at 470 K an intermediate Pd/PdO status is reached, with a subsequent 0.29% weight uptake at 550 K corresponding to the oxidation of 50% of the loaded palladium. The decomposition of PdO to Pd at high temperature is indicated by a grey bar in Figure 5.3; the 0.52% weight loss measured at 950 K corresponds to 90% of the loaded metal. In air, the relative weight measured at 480 K and 1173 K, 96.3% and 95.73%, correspond to a fully oxidized and reduced state, respectively.

The strong interaction between Pd and CeO₂ developed on PdAcCeM can be observed even under N₂, as shown in Figure 5.4, where the presence of ceria delays the complete decomposition of PdAc, which occurs slowly between 450 K and 600 K. Conversely, the palladium nitrate behavior is not modified and, as for the unsupported salt, only palladium oxide is formed under either 2% or 20% oxygen (Figure 5.2).

In the high temperature region the ceria support effect on PdO stabilization can be observed by comparing the high temperature profiles in Figure 5.1 and Figure 5.2. Palladium oxide decomposition is shifted to higher temperatures and full re-oxidation occurs during cooling,

as expected by the known promotional effect of ceria against supported metal sintering.^{31,32} Nevertheless, on PdNCeM the onset of PdO decomposition is slightly anticipated compared to PdAcCeM, suggesting a weaker interaction of the palladium species with the support.²⁸

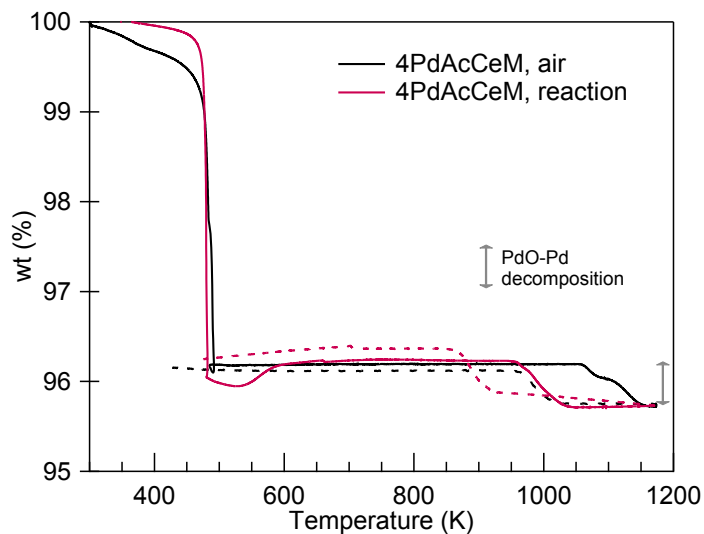


Figure 5.3: Thermogravimetric analysis of 4PdAcCeM under air and reaction conditions. Solid line: heating; dashed line: cooling.

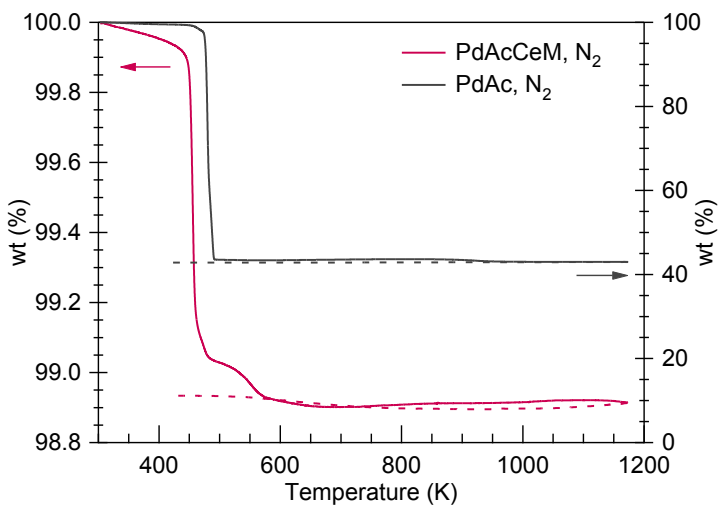


Figure 5.4: Thermogravimetric analysis of unsupported PdAc and PdAcCeM under N₂. Solid line: heating; dashed line: cooling.

The different baseline drifts observed during heating (in air) and during cooling (in reaction mixture) are due to the different properties of the carrier gas, as shown in Figure 5.5. In fact, verification of the carrier gas effect was carried out using a 5%O₂/He mixture to exclude a possible interaction of methane with the salt decomposition. The resulting weight loss profiles in Figure 5.5 show the same weight drift during cooling, which is not observed when N₂ is used as carrier gas. The differences in PdAc decomposition at 550 K are attributed to the increased O₂ content of the methane-free mixture.

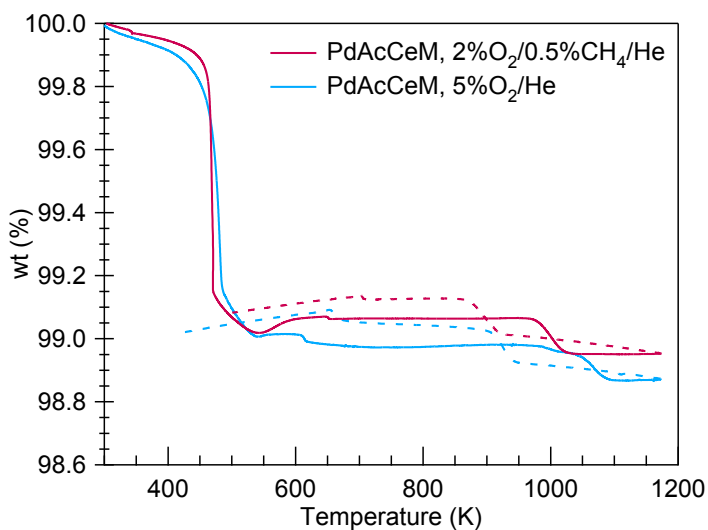


Figure 5.5: Weight loss profiles of PdAcCeM measured using He as carrier gas, with and without CH₄ in the feed.

The differences in decomposition behavior disappear on samples prepared by incipient wetness impregnation, as illustrated in Figure 5.6. When the salts are dissolved in a solution before synthesis, they appear to lose the peculiar properties of their solid precursors and always result in the complete oxidation of the supported Pd species into PdO, regardless of precursor and O₂ partial pressure. This may be due to a weaker metal-support interaction developed under wet conditions, which is unable to stabilize active Pd⁰/Pd²⁺ couples on the ceria surface.³³

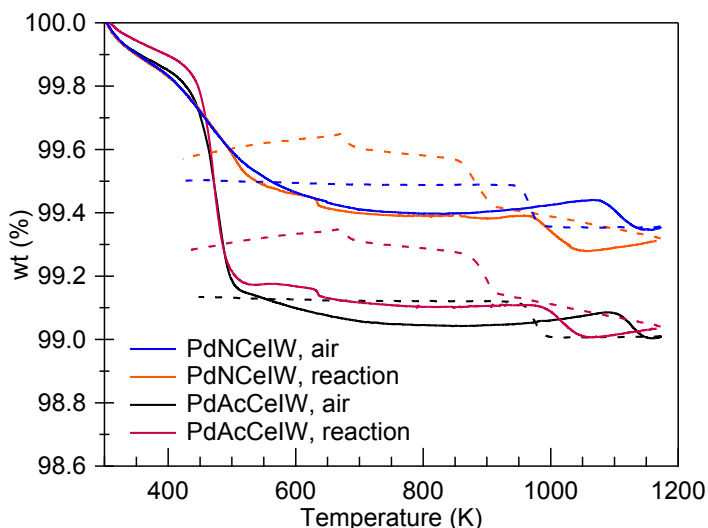


Figure 5.6: TGA profiles of 1wt%Pd/CeO₂ samples prepared by incipient wetness impregnation prior to calcination, under air (21% O₂ in N₂) and reaction conditions (0.5% CH₄, 2%O₂ in He). Solid line: heating; dashed line: cooling.

In order to investigate the properties of the obtained Pd species, the milled catalysts were tested for methane oxidation and compared with their reference sample prepared by incipient wetness impregnation. In all samples, palladium is highly dispersed as revealed by powder XRD spectra (Figure 5.7). Methane oxidation catalytic activity is reported in Figure 5.8 and Figure 5.9 for samples prepared starting from PdN and PdAc, respectively, and the reaction rates are compared in Table 5.2.

No significant differences in activity can be observed in Figure 5.8 for PdN/CeO₂ samples, regardless of the preparation route or the salt decomposition atmosphere. This is in accordance with the decomposition profiles recorded in Figure 5.2 and Figure 5.6, where the same behavior could be observed for the dry and wet synthesized samples. Conversely, in Figure 5.9 a remarkable improvement of the low temperature methane activation can be noted on the sample milled with palladium acetate and decomposed under reaction conditions. It is worth highlighting that this sample is the only one where a Pd/PdO mixture is formed at low temperature, while all other samples are characterized by fully oxidized palladium species (Figure 5.2 and Figure 5.6). More interestingly, a minimum activity loss due to the PdO-Pd-PdO decomposition and re-oxidation behavior at high temperature can be observed, unattained by any other considered sample (Inset in Figure 5.9) and not reported in the literature for Pd/CeO₂-only samples at this high space velocity ($\sim 2 \cdot 10^5 \text{ h}^{-1}$).³⁴ The

remarkably small activity loss observed during cooling might be related to the intrinsic higher activity of this sample, as a consequence of the different palladium species formed on its surface. Indeed, when the reaction is performed at higher space velocity (at a GHSV $\sim 2 \cdot 10^6 \text{ h}^{-1}$), a larger activity loss appears during cooling (Figure 5.10), the catalytic performance advantage on the reference PdCeIW sample being maintained.

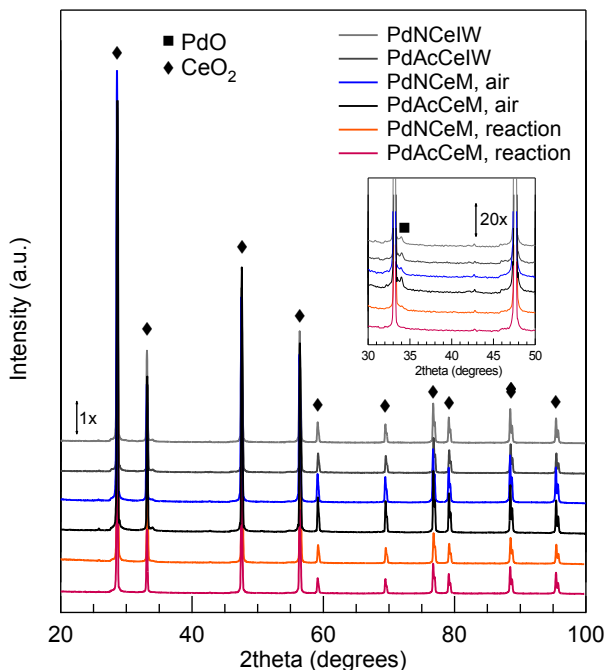


Figure 5.7: XRD spectra of all samples tested for methane oxidation.

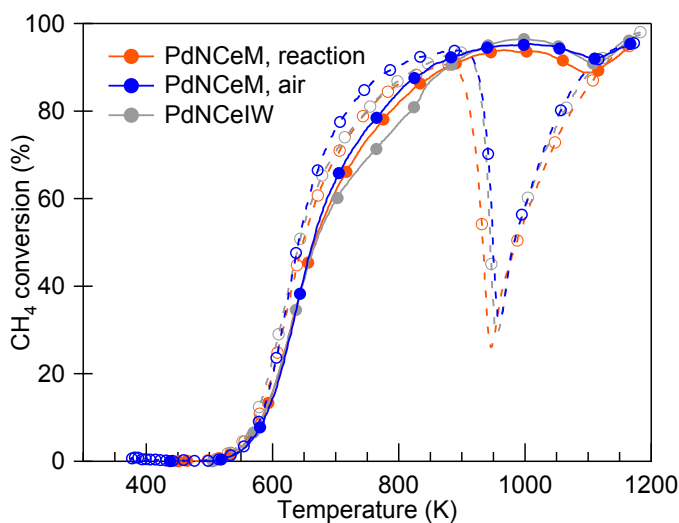


Figure 5.8: Catalytic activity of samples prepared starting from palladium nitrate, 2nd heating/cooling cycle. Solid line: heating; dashed line: cooling.

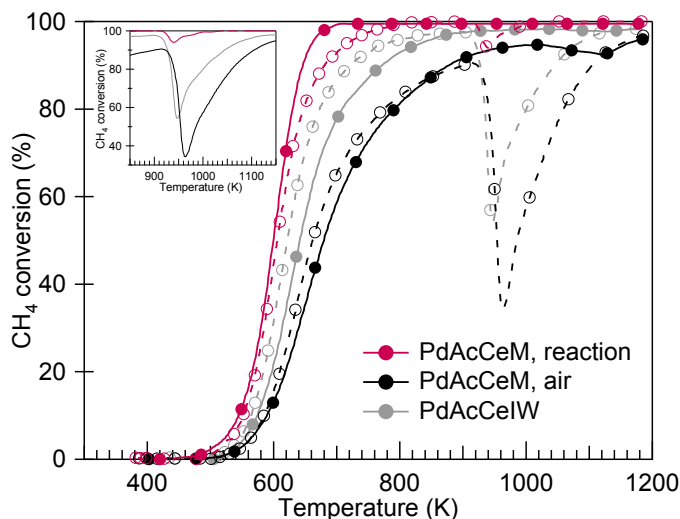


Figure 5.9: Catalytic activity of samples prepared starting from palladium acetate, 2nd heating/cooling cycle. Solid line: heating; dashed line: cooling. Inset: focus on the activity loss during cooling.

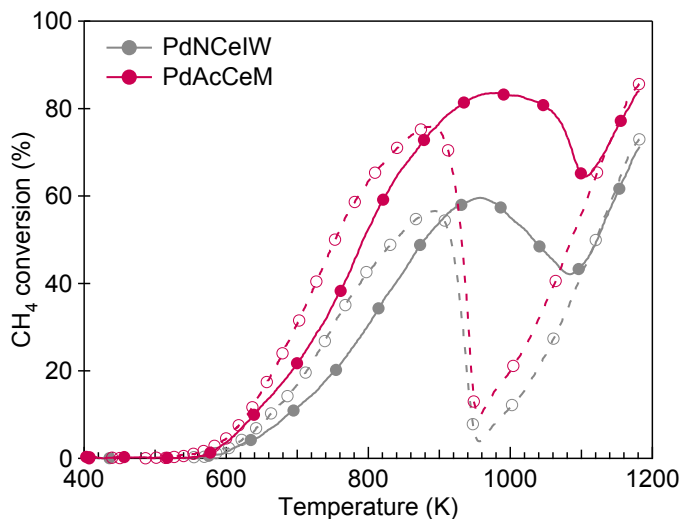


Figure 5.10: Methane combustion activity of PdAcCeM and PdNCEIW at $\text{GHSV} \approx 2 \cdot 10^6 \text{ h}^{-1}$. Solid line: heating; dashed line: cooling.

The enhanced catalytic activity of PdAcCeM is also shown by comparing the calculated reaction rates, reported in Table 5.2 for all samples. Reaction rate values clearly show how all samples display similar activity at 540 K, with the exception of PdAcCeM activated in reaction mixture, whose rate is almost double already at 520 K (the different temperatures being due to the need of carrying out the measurements under differential conditions, i.e. for CH_4 conversion below 5%).

Table 5.2: Reaction rates of M and IW samples calculated from light-off curves at conversions < 5%.

Sample name	Measured Pd loading (wt%)	Activation treatment	Reaction rate ($\mu\text{mol/g}_{\text{Pd}}\cdot\text{s}$)
PdAcCeM	1.01	air	10.6 ^a
PdAcCeM	1.01	reaction mixture	25.1 ^b
PdAcCeIW	1 ^c	air	14.7 ^a
PdNCeM	0.91	air	10.0 ^a
PdNCeM	0.91	reaction mixture	13.8 ^a
PdNCeIW	0.93	air	11.3 ^a

a: measured at 540 K. b: measured at 520 K. c: nominal Pd loading.

Possibly, the presence of stabilized metallic Pd species on PdO/Pd²⁺ clusters promotes methane activation at low temperature, as suggested by *operando* studies carried out on ceria-zirconia or alumina,^{33,35} while fully oxidized PdO species are less active. Moreover, Pd⁰ species on ceria might also enhance the Pd-Ce nanoscale interaction, as already observed in samples prepared by milling with metallic Pd,²¹ contributing to the reduction of high temperature activity loss. In fact, TPO experiments (Figure 5.11) show that the high temperature decomposition peak corresponding to highly stable Pd oxide species in close interaction with ceria,²⁸ highlighted by an asterisk in Figure 5.11, is negligible on both PdNCeIW and PdNCeM, while being significant on PdAcCeM. The amount of cycling palladium calculated by quantitative analysis of the O₂ released during heating and consumed during cooling corresponds to only ~ 80% of the loaded metal, as reported in more detail in Table 5.3, in agreement with the semi-quantitative analysis of the high temperature weight loss and uptake of TGA experiments.

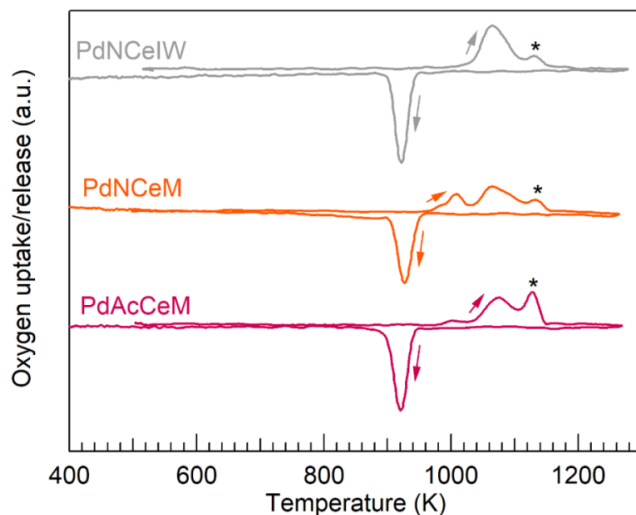


Figure 5.11: Oxygen uptake/release profiles of samples prepared by milling using palladium acetate and nitrate as precursors; 3rd heating/cooling cycle. The conventional PdNCEIW sample is reported for reference. The high temperature decomposition peak is highlighted by an asterisk.

Table 5.3: Quantitative analysis of TPO profiles, 3rd heating/cooling cycle.

Sample	Measured Pd loading (wt%)	O ₂ release (μmoles O ₂ /g) ^a	O ₂ uptake (μmoles O ₂ /g)
PdNCEIW	0.93	35.9 (82)	35.3 (81)
PdNCEM	0.91	34.7 (82)	32.0 (75)
PdAcCEM	1.01	38.3 (81)	34.9 (74)

a: the amount of Pd (% of total Pd) that is involved in oxidation/decomposition is reported in parentheses.

The uniqueness of such interaction was further evaluated by analyzing the effect of the palladium salt properties on other non-reducible supports such as γ -Al₂O₃ and ZrO₂. It was previously shown that the milling of metallic Pd on these support oxides did not result in particularly active catalysts.²¹ By changing the palladium precursor, the obtained dry-milled catalysts exhibited higher activity compared to their IW counterparts (Figure 5.12 and Figure 5.13 for alumina and zirconia, respectively), regardless of the starting salt (Figure 5.12). This may be attributed to a more physical mechanism, where the milling of a precursor salt, softer than metallic Pd, on the support oxide powders enables an improved distribution of metal clusters and nanoparticles.¹² In fact, other examples of dry milling of precursor salts on high surface area supports (Al₂O₃, zeolites, activated carbon) are reported

in the literature, resulting in catalysts with very high metal dispersion and high catalytic activity.^{5,6,36,37}

Despite their higher surface area (20 m²/g for ZrO₂ and 146 m²/g for γ -Al₂O₃ after calcination at 1173 K), the samples prepared by PdAc are outperformed by the PdAcCeM sample (3 m²/g) (Figure 5.14), which displays a light-off temperature 20 K lower than the other catalysts and a negligible activity loss during cooling. This suggests that the palladium acetate properties are mostly enhanced by ceria and confirms the unique synergistic properties of a Pd⁰/Pd²⁺/CeO₂ combination, that plays a fundamental role in the improvement of methane oxidation activity at low temperatures. The stronger Pd-support interaction obtained on ceria can be also observed by TPO experiments: the oxygen uptake and release profiles reported in Figure 5.15 underline how no peak corresponding to PdO_x species in close contact with the support (i.e. the one observed at higher temperature) can be detected on the non-reducible supports.

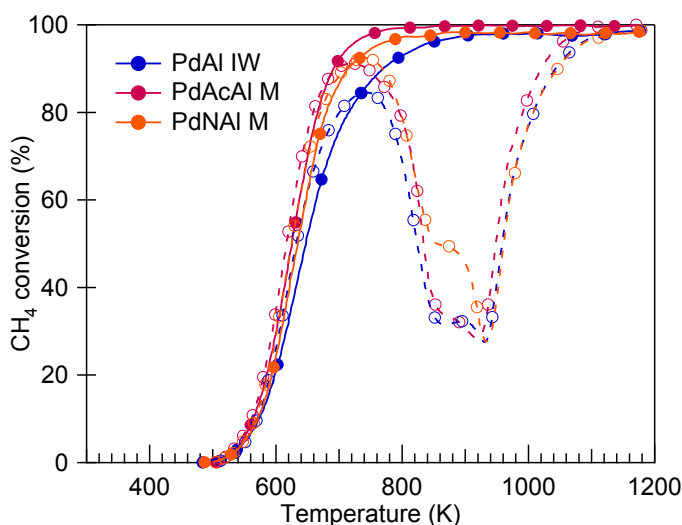


Figure 5.12: Methane combustion activity of dry milled samples on γ -Al₂O₃, prepared from different precursors (PdN, PdAc) compared to the reference IW catalyst. Solid line: heating; dashed line: cooling.

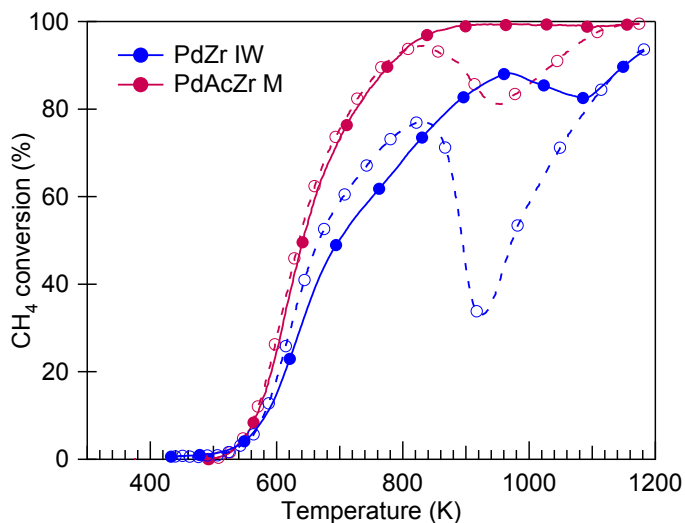


Figure 5.13: Methane combustion activity of PdAcZrO₂ M and the reference IW catalyst. Solid line: heating; dashed line: cooling.

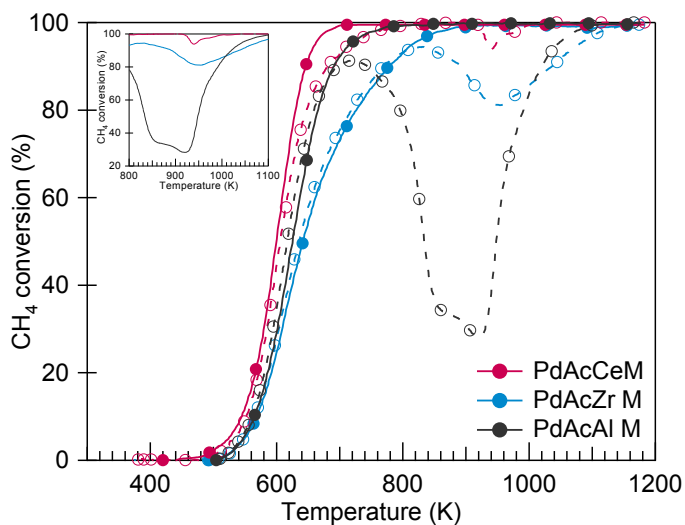


Figure 5.14: Methane combustion activity of dry milled samples prepared with PdAc on all considered supports (CeO₂, ZrO₂, Al₂O₃). Solid line: heating; dashed line: cooling. Inset: focus on the activity loss during cooling.

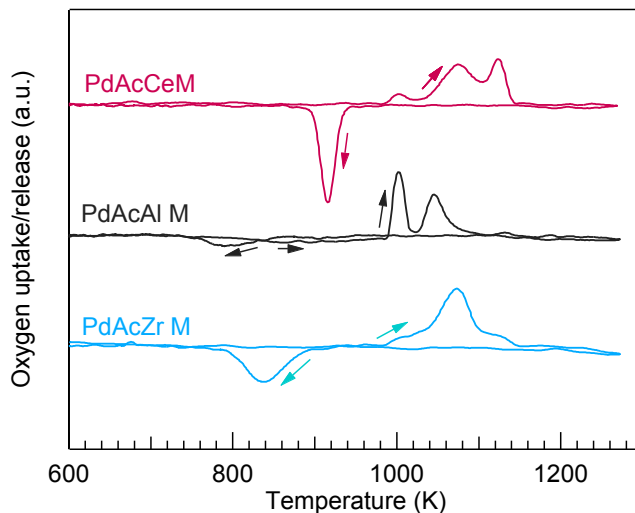


Figure 5.15: Oxygen uptake/release profiles of samples prepared by milling PdAc on CeO_2 , ZrO_2 and Al_2O_3 ; 3rd heating/cooling cycle.

5.4 Conclusions

The different decomposition pathways of solid Pd salt precursors have a strong influence on the palladium species and Pd-ceria interactions developed during and after the dry milling synthesis of Pd-ceria catalysts. Palladium nitrate was observed to always decompose into PdO ,²³ resulting in oxide species on the ceria surface comparable to the ones obtained by incipient wetness impregnation. No significant differences could be detected in the PdN decomposition behavior from IW and milled samples and among the catalytic activities of PdNCeM and PdNCeIW.

Pristine palladium acetate has the peculiar characteristic of decomposing to Pd^0 first and then gradually oxidizing to PdO , depending on the atmosphere.²⁴ This property is exhibited only by the solid salt and can be modified by the oxygen storage capacity of ceria, which promotes its oxidation to PdO . When the PdAc/ CeO_2 M sample is treated at low O_2 partial pressure, an intermediate $\text{Pd}^0/\text{Pd}^{2+}$ state is reached which proved to be extremely active in the low temperature oxidation of methane, resulting in an increased reaction rate and lower light-off temperature. On the other hand, a fully oxidized PdO state, either obtained by treatment in air of PdAcCeM or present on the reference sample prepared by incipient wetness impregnation, was shown to be detrimental for the catalytic activity towards methane oxidation.

The unique properties of ceria and its interaction with the formed Pd species were confirmed by comparing the PdAcCeM sample with equivalent catalysts supported on other non-reducible oxides, such as alumina and zirconia. PdAcCeM displayed the highest low temperature activity, outperforming all other samples by ca. 20 K, and the smallest high temperature activity loss, with a 92% minimum CH₄ conversion during cooling. In general, the dry-milling synthesis resulted in catalysts with improved activity compared to their IW reference materials on all evaluated support oxides, suggesting that a wider application of the developed mild milling procedure can be approached by using metal precursor salts.

5.5 References

- (1) Gélin, P.; Primet, M. Complete Oxidation of Methane at Low Temperature over Noble Metal Based Catalysts: A Review. *Applied Catalysis B: Environmental* **2002**, *39* (1), 1–37. [https://doi.org/10.1016/S0926-3373\(02\)00076-0](https://doi.org/10.1016/S0926-3373(02)00076-0).
- (2) Colussi, S.; Gayen, A.; Llorca, J.; de Leitenburg, C.; Dolcetti, G.; Trovarelli, A. Catalytic Performance of Solution Combustion Synthesized Alumina- and Ceria-Supported Pt and Pd Nanoparticles for the Combustion of Propane and Dimethyl Ether (DME). *Industrial & Engineering Chemistry Research* **2012**, *51* (22), 7510–7517. <https://doi.org/10.1021/ie2016625>.
- (3) Khudorozhkov, A. K.; Chetyrin, I. A.; Bukhtiyarov, A. V.; Prosvirin, I. P.; Bukhtiyarov, V. I. Propane Oxidation Over Pd/Al₂O₃: Kinetic and In Situ XPS Study. *Top Catal* **2017**, *60* (1–2), 190–197. <https://doi.org/10.1007/s11244-017-0733-0>.
- (4) Shen, W.-J.; Ichihashi, Y.; Ando, H.; Okumura, M.; Haruta, M.; Matsumura, Y. Influence of Palladium Precursors on Methanol Synthesis from CO Hydrogenation over Pd/CeO₂ Catalysts Prepared by Deposition–Precipitation Method. *Applied Catalysis A: General* **2001**, *217* (1–2), 165–172. [https://doi.org/10.1016/S0926-860X\(01\)00606-8](https://doi.org/10.1016/S0926-860X(01)00606-8).
- (5) Shen, Y.; Bo, X.; Tian, Z.; Wang, Y.; Guo, X.; Xie, M.; Gao, F.; Lin, M.; Guo, X.; Ding, W. Fabrication of Highly Dispersed/Active Ultrafine Pd Nanoparticle Supported Catalysts: A Facile Solvent-Free in Situ Dispersion/Reduction Method. *Green Chem.* **2017**, *19* (11), 2646–2652. <https://doi.org/10.1039/C7GC00262A>.
- (6) Siamaki, A. R.; Lin, Y.; Woodberry, K.; Connell, J. W.; Gupton, B. F. Palladium Nanoparticles Supported on Carbon Nanotubes from Solventless Preparations: Versatile Catalysts for Ligand-Free Suzuki Cross Coupling Reactions. *Journal of Materials Chemistry A* **2013**, *1* (41), 12909. <https://doi.org/10.1039/c3ta12512b>.
- (7) Amoroso, F.; Colussi, S.; Del Zotto, A.; Llorca, J.; Trovarelli, A. PdO Hydrate as an Efficient and Recyclable Catalyst for the Suzuki–Miyaura Reaction in Water/Ethanol at Room Temperature. *Catalysis Communications* **2011**, *12* (6), 563–567. <https://doi.org/10.1016/j.catcom.2010.11.026>.
- (8) Tang, P.; Zhu, Q.; Wu, Z.; Ma, D. Methane Activation: The Past and Future. *Energy Environ. Sci.* **2014**, *7* (8), 2580–2591. <https://doi.org/10.1039/C4EE00604F>.
- (9) Lampert, J.; Kazi, M.; Farrauto, R. Palladium Catalyst Performance for Methane Emissions Abatement from Lean Burn Natural Gas Vehicles. *Applied Catalysis B: Environmental* **1997**, *14* (3–4), 211–223. [https://doi.org/10.1016/S0926-3373\(97\)00024-6](https://doi.org/10.1016/S0926-3373(97)00024-6).
- (10) Farrauto, R. J.; Deeba, M.; Alerasool, S. Gasoline Automobile Catalysis and Its Historical Journey to Cleaner Air. *Nat Catal* **2019**, *2* (7), 603–613. <https://doi.org/10.1038/s41929-019-0312-9>.
- (11) Hagelüken, C.; Lee-Shin, J.; Carpentier, A.; Heron, C. The EU Circular Economy and Its Relevance to Metal Recycling. *Recycling* **2016**, *1* (2), 242–253. <https://doi.org/10.3390/recycling1020242>.
- (12) Munnik, P.; de Jongh, P. E.; de Jong, K. P. Recent Developments in the Synthesis of Supported Catalysts. *Chem. Rev.* **2015**, *115* (14), 6687–6718. <https://doi.org/10.1021/cr500486u>.

- (13) Lomot, D.; Juszczyk, W.; Karpiński, Z.; Bozon-Verduraz, F. Evolution of Pd/SiO₂ Catalysts Prepared from Chlorine-Free Precursors. *J. Chem. Soc., Faraday Trans.* **1997**, *93* (10), 2015–2021. <https://doi.org/10.1039/A608616K>.
- (14) Marques, R.; Mazri, L.; Da Costa, S.; Delacroix, F.; Djéga-Mariadassou, G.; Da Costa, P. Selective Reduction of NO_x by Hydrogen and Methane in Natural Gas Stationary Sources over Alumina-Supported Pd, Co and Co/Pd Catalysts. *Catalysis Today* **2008**, *137* (2–4), 179–184. <https://doi.org/10.1016/j.cattod.2007.11.025>.
- (15) Kinnunen, N. M.; Suvanto, M.; Moreno, M. A.; Savimäki, A.; Kallinen, K.; Kinnunen, T.-J. J.; Pakkanen, T. A. Methane Oxidation on Alumina Supported Palladium Catalysts: Effect of Pd Precursor and Solvent. *Applied Catalysis A: General* **2009**, *370* (1–2), 78–87. <https://doi.org/10.1016/j.apcata.2009.09.018>.
- (16) Lopes, C. W.; Cerrillo, J. L.; Palomares, A. E.; Rey, F.; Agostini, G. An *in Situ* XAS Study of the Activation of Precursor-Dependent Pd Nanoparticles. *Phys. Chem. Chem. Phys.* **2018**, *20* (18), 12700–12709. <https://doi.org/10.1039/C8CP00517F>.
- (17) Colussi, S.; Gayen, A.; Boaro, M.; Llorca, J.; Trovarelli, A. Influence of Different Palladium Precursors on the Properties of Solution-Combustion-Synthesized Palladium/Ceria Catalysts for Methane Combustion. *ChemCatChem* **2015**, *7* (14), 2222–2229. <https://doi.org/10.1002/cctc.201500390>.
- (18) Dann, E. K.; Gibson, E. K.; Catlow, R. A.; Collier, P.; Eralp Erden, T.; Gianolio, D.; Hardacre, C.; Kroner, A.; Raj, A.; Goguet, A.; et al. Combined *In Situ* XAFS/DRIFTS Studies of the Evolution of Nanoparticle Structures from Molecular Precursors. *Chem. Mater.* **2017**, *29* (17), 7515–7523. <https://doi.org/10.1021/acs.chemmater.7b02552>.
- (19) Meng, L.; Lin, J.-J.; Pu, Z.-Y.; Luo, L.-F.; Jia, A.-P.; Huang, W.-X.; Luo, M.-F.; Lu, J.-Q. Identification of Active Sites for CO and CH₄ Oxidation over PdO/Ce_{1-x}Pd_xO_{2-δ} Catalysts. *Applied Catalysis B: Environmental* **2012**, *119–120*, 117–122. <https://doi.org/10.1016/j.apcatb.2012.02.036>.
- (20) McCarty, J. G. Kinetics of PdO Combustion Catalysis. *Catalysis Today* **1995**, *26* (3–4), 283–293. [https://doi.org/10.1016/0920-5861\(95\)00150-7](https://doi.org/10.1016/0920-5861(95)00150-7).
- (21) Danielis, M.; Colussi, S.; de Leitenburg, C.; Soler, L.; Llorca, J.; Trovarelli, A. Outstanding Methane Oxidation Performance of Palladium-Embedded Ceria Catalysts Prepared by a One-Step Dry Ball-Milling Method. *Angewandte Chemie International Edition* **2018**, *57* (32), 10212–10216. <https://doi.org/10.1002/anie.201805929>.
- (22) Danielis, M.; Colussi, S.; de Leitenburg, C.; Soler, L.; Llorca, J.; Trovarelli, A. The Effect of Milling Parameters on the Mechanochemical Synthesis of Pd–CeO₂ Methane Oxidation Catalysts. *Catal. Sci. Technol.* **2019**, *9* (16), 4232–4238. <https://doi.org/10.1039/C9CY01098J>.
- (23) Yuvaraj, S.; Fan-Yuan, L.; Tsong-Huei, C.; Chuin-Tih, Y. Thermal Decomposition of Metal Nitrates in Air and Hydrogen Environments. *The Journal of Physical Chemistry B* **2003**, *107* (4), 1044–1047. <https://doi.org/10.1021/jp026961c>.
- (24) Gallagher, P. K.; Gross, M. E. The Thermal Decomposition of Palladium Acetate. *Journal of Thermal Analysis* **1986**, *31* (6), 1231–1241. <https://doi.org/10.1007/BF01914636>.
- (25) Datye, A. K.; Bravo, J.; Nelson, T. R.; Atanasova, P.; Lyubovsky, M.; Pfefferle, L. Catalyst Microstructure and Methane Oxidation Reactivity during the Pd↔PdO Transformation on Alumina Supports. *Applied Catalysis A: General* **2000**, *198* (1–2), 179–196. [https://doi.org/10.1016/S0926-860X\(99\)00512-8](https://doi.org/10.1016/S0926-860X(99)00512-8).

- (26) Chin, Y.-H. (Cathy); García-Diéguez, M.; Iglesia, E. Dynamics and Thermodynamics of Pd–PdO Phase Transitions: Effects of Pd Cluster Size and Kinetic Implications for Catalytic Methane Combustion. *J. Phys. Chem. C* **2016**, *120* (3), 1446–1460. <https://doi.org/10.1021/acs.jpcc.5b06677>.
- (27) Farrauto, R. J.; Lampert, J. K.; Hobson, M. C.; Waterman, E. M. Thermal Decomposition and Reforming of PdO Catalysts; Support Effects. *Applied Catalysis B: Environmental* **1995**, *6*(3), 263–270. [https://doi.org/10.1016/0926-3373\(95\)00015-1](https://doi.org/10.1016/0926-3373(95)00015-1).
- (28) Colussi, S.; Trovarelli, A.; Vesselli, E.; Baraldi, A.; Comelli, G.; Groppi, G.; Llorca, J. Structure and Morphology of Pd/Al₂O₃ and Pd/CeO₂/Al₂O₃ Combustion Catalysts in Pd–PdO Transformation Hysteresis. *Applied Catalysis A: General* **2010**, *390* (1–2), 1–10. <https://doi.org/10.1016/j.apcata.2010.09.033>.
- (29) Farrauto, R. J.; Hobson, M. C.; Kennelly, T.; Waterman, E. M. Catalytic Chemistry of Supported Palladium for Combustion of Methane. *Applied Catalysis A: General* **1992**, *81* (2), 227–237. [https://doi.org/10.1016/0926-860X\(92\)80095-T](https://doi.org/10.1016/0926-860X(92)80095-T).
- (30) Sayle, T. X. T.; Cantoni, M.; Bhatta, U. M.; Parker, S. C.; Hall, S. R.; Möbus, G.; Molinari, M.; Reid, D.; Seal, S.; Sayle, D. C. Strain and Architecture-Tuned Reactivity in Ceria Nanostructures; Enhanced Catalytic Oxidation of CO to CO₂. *Chemistry of Materials* **2012**, *24* (10), 1811–1821. <https://doi.org/10.1021/cm3003436>.
- (31) Su, Y.-Q.; Liu, J.-X.; Filot, I. A. W.; Hensen, E. J. M. Theoretical Study of Ripening Mechanisms of Pd Clusters on Ceria. *Chemistry of Materials* **2017**, *29* (21), 9456–9462. <https://doi.org/10.1021/acs.chemmater.7b03555>.
- (32) Farmer, J. A.; Campbell, C. T. Ceria Maintains Smaller Metal Catalyst Particles by Strong Metal-Support Bonding. *Science* **2010**, *329* (5994), 933–936. <https://doi.org/10.1126/science.1191778>.
- (33) Nilsson, J.; Carlsson, P.-A.; Fouladvand, S.; Martin, N. M.; Gustafson, J.; Newton, M. A.; Lundgren, E.; Grönbeck, H.; Skoglundh, M. Chemistry of Supported Palladium Nanoparticles during Methane Oxidation. *ACS Catalysis* **2015**, *5* (4), 2481–2489. <https://doi.org/10.1021/cs502036d>.
- (34) Cargnello, M.; Jaen, J. J. D.; Garrido, J. C. H.; Bakhmutsky, K.; Montini, T.; Gamez, J. J. C.; Gorte, R. J.; Fornasiero, P. Exceptional Activity for Methane Combustion over Modular Pd@CeO₂ Subunits on Functionalized Al₂O₃. *Science* **2012**, *337* (6095), 713–717. <https://doi.org/10.1126/science.1222887>.
- (35) Ciuparu, D.; Lyubovsky, M. R.; Altman, E.; Pfefferle, L. D.; Datye, A. Catalytic Combustion of Methane over Palladium-based Catalysts. *Catalysis Reviews* **2002**, *44* (4), 593–649. <https://doi.org/10.1081/CR-120015482>.
- (36) Lin, Y.; Watson, K. A.; Fallbach, M. J.; Ghose, S.; Smith, J. G.; Delozier, D. M.; Cao, W.; Crooks, R. E.; Connell, J. W. Rapid, Solventless, Bulk Preparation of Metal Nanoparticle-Decorated Carbon Nanotubes. *ACS Nano* **2009**, *3* (4), 871–884. <https://doi.org/10.1021/nn8009097>.
- (37) Kondrat, S. A.; Shaw, G.; Freakley, S. J.; He, Q.; Hampton, J.; Edwards, J. K.; Miedziak, P. J.; Davies, T. E.; Carley, A. F.; Taylor, S. H.; et al. Physical Mixing of Metal Acetates: A Simple, Scalable Method to Produce Active Chloride Free Bimetallic Catalysts. *Chemical Science* **2012**, *3* (10), 2965. <https://doi.org/10.1039/c2sc20450a>.

6 Pd/CeO₂ Catalysts Prepared by Milling Pd Acetate and Ceria: Methane Oxidation Activity, Nanoscale Morphology and *In-situ* Characterization

Abstract

The preparation of Pd/CeO₂ methane oxidation catalysts by dry mechanical milling of Pd and ceria nanopowders has been shown to be very effective in obtaining active and stable materials with strong surface and subsurface interaction between the two components. Here we investigate Pd/CeO₂ catalysts prepared by milling palladium acetate and ceria and varying Pd loading and CeO₂ surface area. These catalysts show superior activity compared to the ones prepared starting from metallic Pd. *In-situ* synchrotron X-ray diffraction (XRD) and X-ray absorption fine structure (XAFS) characterization techniques, coupled with ambient pressure XPS analysis, have been used to deeply characterize the samples, and allowed to identify various Pd species with different degrees of interaction with ceria and different morphology. These Pd species are likely generated by the mechanical and electronic interplay taking place over ceria surface during milling and are indicated as the responsible of the enhanced catalytic activity.

6.1 Introduction

One of the main goals of the current research involving metal-oxide systems for catalytic applications is the optimization of the interaction between the metal and the support at nanoscale level, due to its implications in the catalytic activity for different reactions.¹⁻⁴ In the case of metal-ceria formulations the strong interplay between the two components at the interface can lead to very interesting catalytic properties.^{5,6} Recent studies have highlighted different aspects of metal-ceria interaction, with a significant amount of work dedicated to palladium-ceria systems for which a higher activity and/or stability is often observed when Pd is somehow embedded or substituted into ceria lattice. Pd/CeO₂ catalysts have been extensively investigated for the catalytic abatement of methane,⁷⁻¹⁵ and their peculiar characteristics have been found promising also for other reactions.¹⁶⁻²¹ Theoretical investigations have given strong support to experimental results by demonstrating that various Pd-ceria embedded configurations are extremely stable and provide low energy barriers for molecular activation.²²⁻²⁶

The synthesis of catalysts with strong metal-ceria interaction at nanoscale usually requires preparation methods in wet environment with subsequent thermal treatments, or methods which are not easily applicable at large scale.^{7,8,10,14} In Chapter 3 I have described a Pd/ceria catalyst (PdCeM) prepared by simple dry milling of metallic Pd and CeO₂ powders, which showed increased catalytic activity for methane oxidation with respect to an analogous sample prepared by traditional incipient wetness impregnation.¹³ This improved activity was attributed to the formation of a mixed Pd-CeO₂ amorphous layer on the surface, whose configuration resembles the one predicted by DFT calculations in which the dissolution of palladium clusters into CeO₂ lattice yields a unique interface assembly with low methane activation barrier.²⁵ Here, by applying a similar milling procedure, a Pd/ceria formulation obtained by milling solid palladium acetate salt with ceria powder is disclosed. This catalyst still presents the amorphous Pd-Ce-O shell surrounding ceria nanoparticles and outperforms the one prepared starting from Pd metal for methane oxidation. Moreover, the use of Pd acetate allows to incorporate higher Pd loadings (up to 10%) on ceria compared to Pd metal powder. Differently from metallic palladium, Pd acetate is effective also in obtaining very good catalytic performances on ceria with high thermal stability, i.e. with higher surface area at high temperature, which is very important in light of a wider range of possible applications for Pd/CeO₂ catalysts prepared by dry milling. *In-situ* synchrotron x-ray diffraction (XRD) and x-ray absorption fine structure (XAFS) characterization techniques,

coupled with ambient pressure x-ray photoelectron spectroscopy and Fourier transform infrared spectroscopy, were used to get deeper insights on this promising material and to identify the Pd active phase by following the Pd-Ce interaction at nanoscale during reaction.

6.2 Experimental

Catalytic samples with a Pd loading of 1wt%, 4wt% and 10wt% were prepared using Pd acetate salt ($\text{Pd}(\text{O}_2\text{CCH}_3)_2$, Sigma Aldrich, 99.99%) and a commercial CeO_2 sample gently provided by Ford Motor Company (Dearborn, MI), calcined at 1173 K (Ce1173) or at 1473 K (Ce1473) prior to synthesis. The two components were milled in a Pulverisette 23 Minimill operating at 15 Hz in two subsequent 10-minute steps, separated by a manual mixing of the powder with a spatula inside the milling jar to avoid the formation of big agglomerates. The prepared samples were denoted as $x\text{PdAcCe}(1173)\text{M}$ and $x\text{PdAcCe}(1473)\text{M}$, respectively, where x indicates the nominal Pd loading. Other samples were synthesized for comparison on Ce(1173) and Ce(1473), prepared by dry milling starting from commercial Pd black and PdO nanopowders (Sigma Aldrich), namely $x\text{PdCe}(1173)\text{M}$, $x\text{PdCe}(1473)\text{M}$ and $x\text{PdOCe}(1173)\text{M}$, as well as reference samples prepared by conventional incipient wetness impregnation ($x\text{PdCe}(1173)\text{IW}$, $x\text{PdCe}(1473)\text{IW}$). For experimental details of the synthesis procedure refer to Chapter 2, section 2.1.2.

All samples were characterized by means of BET surface area and pore size measurements, ICP-mass elemental analysis, High Resolution Transmission Electron Microscopy (HRTEM) and Temperature Programmed Oxidation (TPO) and Reduction (TPR) tests. The best performing samples with increased Pd loading were further characterized by means of advanced *in-situ* techniques. *In-situ* synchrotron x-ray diffraction was performed at Advanced Photon Source (APS), Argonne (IL), to follow the evolution of bulk Pd and PdO species during reaction. Ambient Pressure XPS analysis and *in-situ* Diffuse Reflectance Infrared Fourier Transform Spectroscopy (DRIFTS) were carried out at the Chemistry Division of Brookhaven National Laboratory (BNL), Upton (NY), to investigate respectively the electronic states and evolution of the surface Pd and Ce species during reaction²⁷ and the reaction intermediates during methane oxidation at low temperature and the palladium state under CH_4 or CO only. *Ex-situ* Raman spectra were collected with an Xplora Plus Micro-Raman system (Horiba, Kyoto, Japan) to evaluate the nature of PdO and

CeO₂ structures on prepared catalysts after reaction. Mapping of the surface was carried out to analyze the PdO distribution and uniformity on the mesoscale.

All samples were tested for complete methane oxidation in a lab-scale flow reactor setup. Combustion tests were performed in transient or stationary conditions on 120 mg of sample under 180 ml/min of a 0.5%CH₄/2%O₂/He gas mixture, for a final GHSV of ca. 180'000 h⁻¹. Additional experiments were carried out in “wet” conditions by adding 10 vol% water vapor to the gas feed. Reaction rates in dry atmosphere were calculated at methane conversion values ≤ 5% measured during the heating ramp of the 2nd light off cycle, in differential conditions.^{28–30} Details on the characterization techniques and catalytic tests are reported in Chapter 2, sections 2.2 and 2.3, respectively.

6.3 Results

6.3.1 Physico-chemical Characterization and Catalytic activity

The surface area and Pd loading of the samples prepared on ceria support calcined at 1473 K and 1173 K are reported in Table 6.1. As expected, the surface area is low (~4 m²/g) for all samples with a slight increase for the milled samples containing 1 wt% of palladium, likely due to the breakdown of bigger agglomerates into smaller particles during the milling process,^{31,32} as shown by the granulometric analysis of the pure support oxide and milled powders reported in Figure 6.1. The accumulated quantity curves clearly show that after the milling process some particle aggregates larger than 10 μm are broken down to 1–4 μm. Ceria calcined at lower temperature (Ce1173) is characterized by higher surface area, ~25 m²/g, which is maintained on the milled samples while a significant loss is observed on 4PdCe(1173)IW. Indication of pore occlusion on this sample is observed by the analysis of pore size distribution, performed on desorption isotherms at 77 K using the BJH method (Figure 6.2). The measured Pd loading is close to the nominal one for all samples, with the exception of the sample prepared using metallic Pd (as already reported in Chapter 3).

Table 6.1: BET surface area, Pd loading and calculated reaction rates of samples prepared on ceria calcined at 1473 K and 1173 K.

Sample	BET surface area (m ² /g)	Measured Pd loading (wt%)	Reaction rate (μmol/g _{Pd} ·s) ^a
CeO ₂ (1473)	3.8	-	-
1PdAcCe1473M	5.2	1.01	25.1
1PdCe1473M	4.8	0.81	14.1
1PdCe1473IW	3.7	0.97	6.4
4PdAcCe1473M	3.1	4.03	8.5
4PdCe1473M	4.7	3.58	0.9
4PdCe1473IW	4.1	3.97	0.9
CeO ₂ (1173)	23.4	-	-
4PdAcCe1173M	22.1	3.92	8.2
4PdCe1173M	25.1	3.69	0.7
4PdCe1173IW	14.6	3.94	3.3
4PdOCe1173M	26.7	3.83	0

a: calculated at 520 K from the 2nd heating cycle of light-off curves.

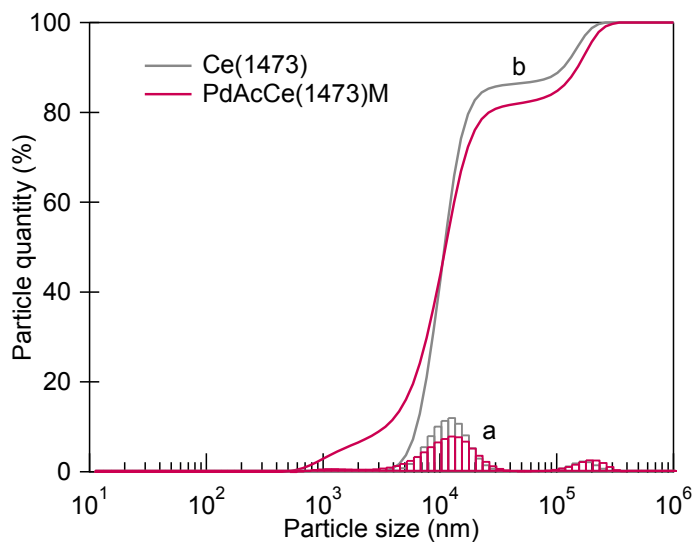


Figure 6.1: Particle size distribution diagrams (a) and accumulated quantity curves (b) of 1PdAcCe(1473)M and the oxide support Ce(1473).

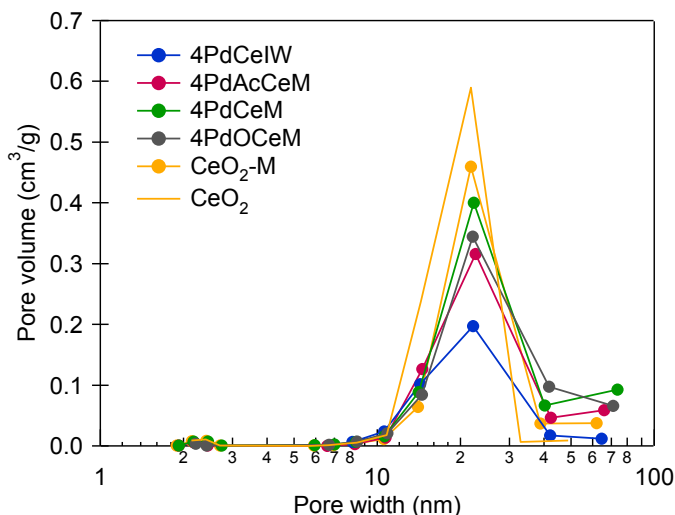


Figure 6.2: Pore size distribution of 4wt.%Pd/CeO₂(1173) samples and the CeO₂(1173) support, as prepared and after milling (CeO₂-M).

The result of the catalytic activity testing of sample 1PdAcCe(1473)M for lean methane oxidation is reported in Figure 6.3, in comparison with the light-off curves of the samples prepared by incipient wetness (1PdCe(1473)IW) and by using Pd metal as precursor (1PdCe(1473)M), and the reaction rates calculated at 520 K are reported in Table 6.1. The activity of the Pd metal-based and impregnated catalysts well compares with that of analogous samples, prepared on similar ceria support, already described in our published works.^{13,33} As it can be observed, the use of palladium acetate as precursor improves significantly the overall catalytic activity, with a decrease of T_{10} (temperature to achieve 10% methane conversion) of about 15 K, and a remarkable improvement of the conversion at high temperature in the cooling branch of the light-off curve. In particular, the typical loss in methane conversion usually present on Pd-based catalysts (and clearly visible for 1PdCe(1473)IW and 1PdCe(1473)M) is strongly reduced, the minimum being of ca. 92% for 1PdAcCe(1473)M against 40-50% for the reference samples.

The catalyst prepared from Pd acetate was tested also for stability over time-on-stream (Figure 6.4) and in presence of water in the feed (Figure 6.6 and Figure 6.5). In both cases the activity and stability of 1PdAcCe(1473)M are comparable, or even better than those of 1PdCe(1473)M which, in turn, was found to be much better than the conventional impregnated sample (see Chapter 3). The light-off curve shift to higher temperatures (ca. 80 K) is due to the inhibiting effect of steam on low temperature methane oxidation.^{30,34}

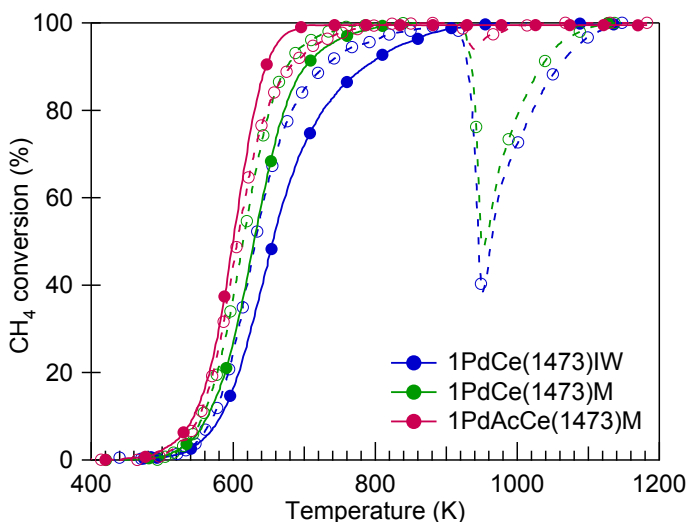


Figure 6.3: Methane combustion activity of samples 1PdAcCe(1473)M, 1PdCe(1473)M and 1PdCe(1473)IW. Solid line, closed symbols: heating; dashed line, open symbols: cooling.

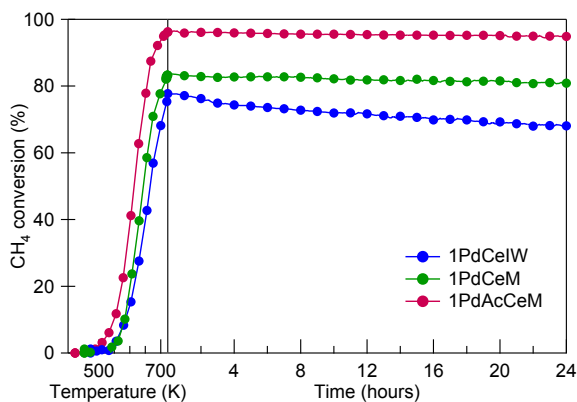


Figure 6.4: Methane combustion activity of 1wt%Pd/CeO₂ samples in stability tests performed at 723 K for 24 hours, dry conditions.

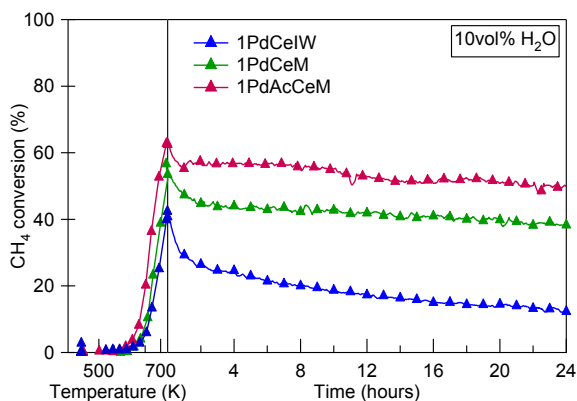


Figure 6.5: Methane combustion activity of 1wt%Pd/CeO₂ samples in stability tests performed at 723 K for 24 hours, wet conditions (10vol% H₂O).

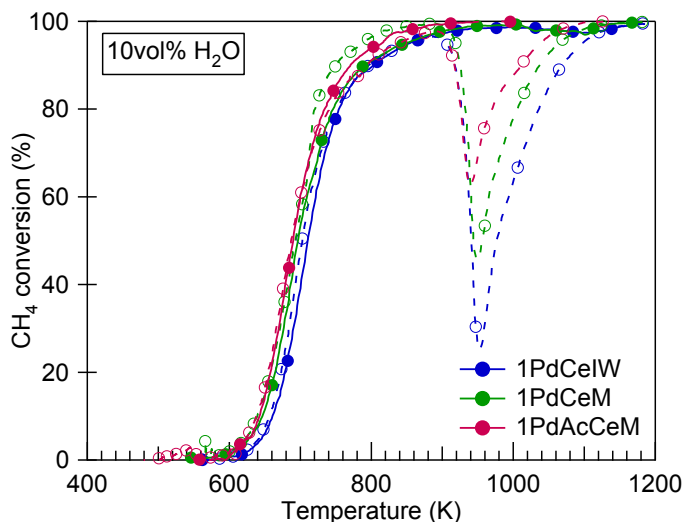


Figure 6.6: Methane combustion activity of 1 wt%Pd/CeO₂ samples in wet conditions (10 vol% H₂O in the feed). Solid line, closed symbols: heating; dashed line, open symbols: cooling.

Increasing Pd loading up to 4 wt% enhances significantly the overall conversion of PdAcCe(1473)M, and it is worth noting that in this case there is no loss in methane conversion during cooling (Figure 6.8). On the other side, sample 4PdCe(1473)M shows a worse performance compared to the impregnated counterpart, as shown in Figure 6.7 and clearly observed by the calculated reaction rates reported in Table 6.1. This indicates that the low surface area ceria is not able to accommodate efficiently higher metallic Pd loadings, as inferred by comparing the light-off curves of 1 wt% and 4 wt% PdCe(1473)M illustrated in Figure 6.8, with the low loaded catalyst showing higher conversion. The preparation of 4 wt% Pd catalysts on ceria calcined at 1173 K (S.A. ca. 25 m²/g) improves only slightly the activity of the impregnated sample and of the one obtained by milling with metallic Pd, both remaining well below the activity of 4PdAcCe(1173)M (Figure 6.9). The use of Pd acetate as Pd precursor allows to introduce up to 10 wt% of palladium on ceria calcined at 1173 K (Figure 6.10), but since from 4 wt% to 10 wt% the improvement is minimal we focused our work on sample 4PdAcCe(1173)M for further characterization. Despite similar activity of the 4PdAcCe(1173)M and 4PdAcCe(1473)M catalysts, the choice to focus on the sample prepared on higher surface area ceria was dictated by several reasons, including easier characterization due to its smaller ceria crystallites and the possibility of use in other reactions.

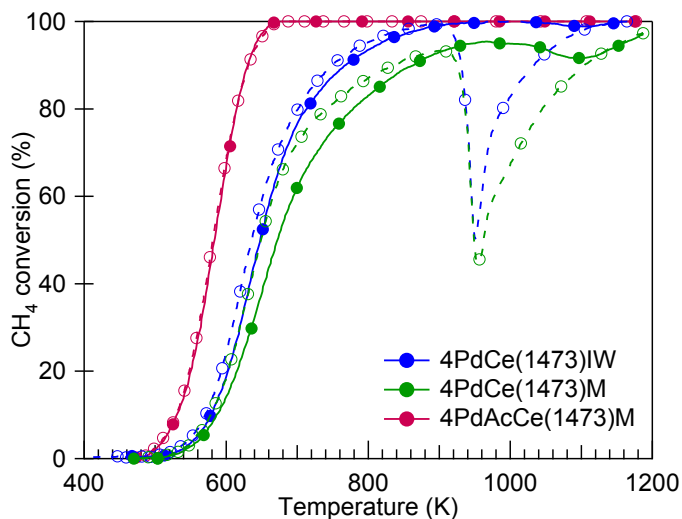


Figure 6.7: Methane oxidation activity for 4wt%Pd/CeO₂ samples prepared by different syntheses on Ce1473. Solid line, closed symbols: heating; dashed line, open symbols: cooling.

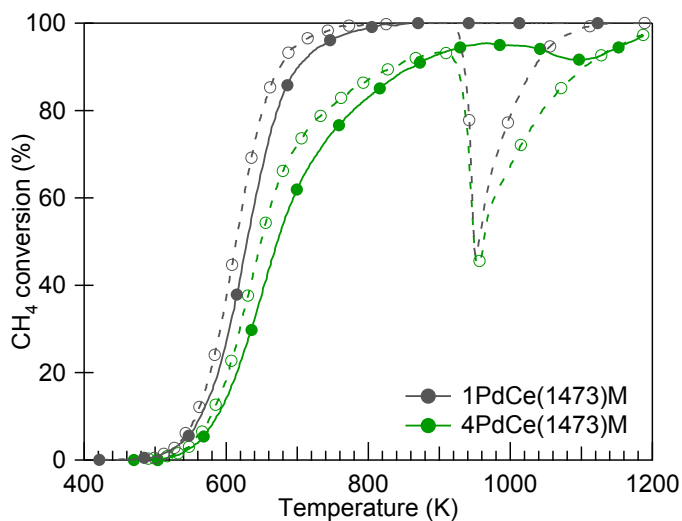


Figure 6.8: Methane combustion activity of 1 wt% and 4 wt% PdCe(1473)M. Solid line, closed symbols: heating; dashed line, open symbols: cooling.

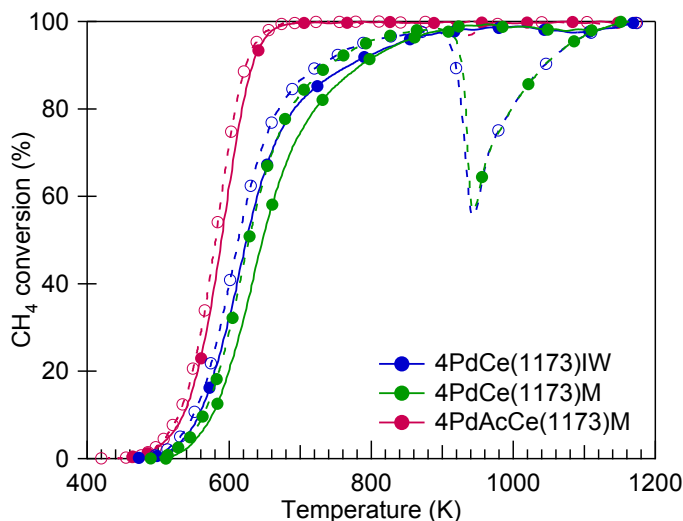


Figure 6.9: Methane oxidation activity of 4wt%Pd/CeO₂ samples prepared by different syntheses on Ce1173. Solid line, closed symbols: heating; dashed line, open symbols: cooling.

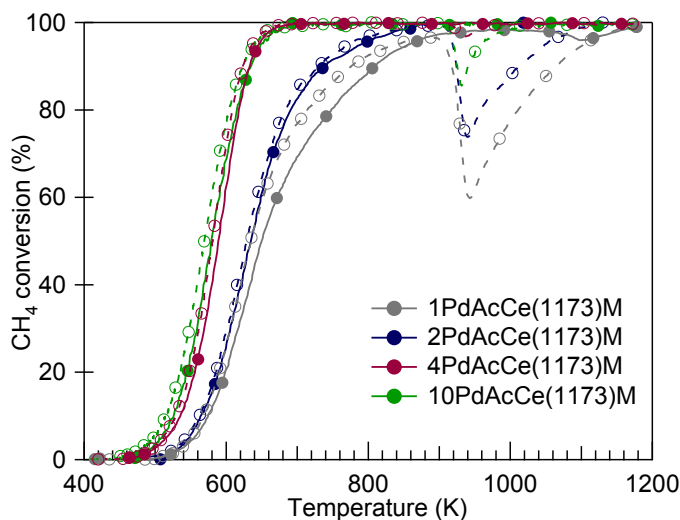


Figure 6.10: Catalytic activity of dry milled samples prepared from Pd acetate precursor with increased palladium loading. Solid line, closed symbols: heating; dashed line, open symbols: cooling.

6.3.2 HRTEM Characterization

The HRTEM characterization of 1PdAcCe(1473)M (Figure 6.11) reveals the formation of an amorphous layer similar to the one observed for sample 1PdCeM prepared starting from metallic Pd and described in Chapter 3.¹³ On this sample, the layer is less homogeneous and its thickness spans from 1 up to 6 nm, as shown in Figure 6.11(A,B). In Figure 6.11(C) an

area with a thick shell along with some uncovered ceria crystallites can be observed. It should be reminded that, for samples prepared from Pd acetate, the HRTEM analysis has been carried out after one light-off cycle up to 1173 K, in order to observe the Pd species formed after the decomposition of the precursor salt. Overall, the morphology of samples prepared from Pd acetate and metallic Pd over low surface area ceria does not differ significantly, with palladium embedded in an amorphous layer covering the ceria crystallites.

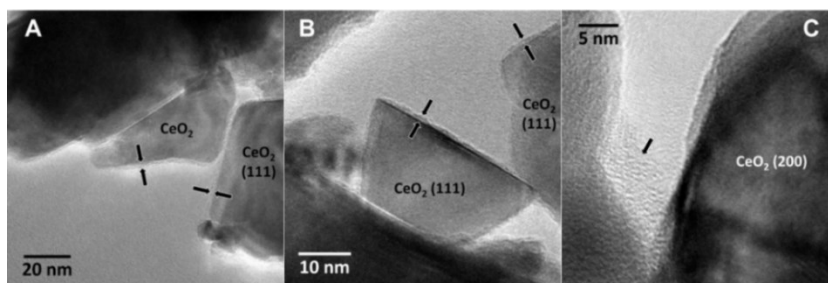


Figure 6.11: HRTEM images of 1PdAcCe(1473)M after one CH₄ combustion cycle up to 1173 K, displaying thinner (A,B) and thicker (C) regions of amorphous shell structure.

Conversely, the HRTEM images of 4PdAcCe(1173)M, reported in Figure 6.12, reveal the presence of different Pd species, together with the characteristic amorphous layer covering ceria nanoparticles (Figure 6.12(D)). Figure 6.12(A) corresponds to a high magnification image of a CeO₂ particle, showing {200} planes of ceria along with defocused darker entities on the surface. By careful analysis of the HRTEM images and through intentional defocus, the entities can be recognized to occur at the surface of the ceria crystallite and are not confused with artifacts originating from the thickness of the particle and/or the carbon film of the TEM grid. A similar HRTEM image is shown in Figure 6.12(B). Again, the ceria crystallites are round-shaped and, under defocus, the tiny entities are unambiguously recognized. From Figure 6.12(A,B) it can be estimated that the size of the entities is below 0.5 nm and their higher electron contrast indicates they probably contain Pd.

Figure 6.12(C) shows an HRTEM image resolved at an atomic scale. The ceria crystallite is oriented along the {112} crystallographic direction. It is noteworthy the lack of well-defined edges of the ceria crystallite, as commonly outlined on the milled samples containing Pd (see Chapter 3), and in addition the atomic rows located at the outermost surface look striking. Despite the impossibility to extract any definitive conclusion, the dark rows located just at the surface and parallel to the {111} steps of the crystallite (marked by black arrows)

might indicate the presence of a monolayer of Pd atoms or Pd islands. These rows are slightly bended outwards the surface, suggesting that they are not due to the ceria lattice. At the surface of the {220} face other dark rows are recognized (marked by white arrows). In Figure 6.12(D), the amorphous nature of the shell (marked by arrows) over the ceria crystallites is clearly seen, measuring about 1-2 nm in thickness. In Figure 6.12(E), the darker nanostructures over the ceria crystallites are identified as PdO as deduced from the lattice fringes at 2.6 and 1.7 Å, corresponding to the characteristic {101} and {112} planes of tetragonal PdO. These PdO nanostructures are crystalline and measure about 1-1.5 nm in diameter and are very well dispersed over CeO₂. A careful analysis of the PdO nanostructures over the ceria crystallites suggests that most of the PdO nanostructures are located at steps or other imperfections of the ceria crystallites as a consequence of the mild-milling process. This is clearly seen in Figure 6.12(F), where two steps of a ceria crystallite are marked by arrows and precisely over the steps two PdO nanostructures with triangular shape are visible (see white triangles in the inset). Samples 4PdCe(1173)IW and 4PdCe(1173)M exhibit a different pattern, with the presence of well-defined Pd clusters on the IW sample (Figure 6.13) and, for the milled sample, of patches of Pd below the outmost surface layers of ceria (Figure 6.14). 4PdCe(1173)M shows also some isolated palladium nanoparticles not interacting with ceria (Figure 6.14(A,B)) along with ceria particles surrounded by the amorphous layer (Figure 6.14(C)), not ubiquitous on this sample as it was for 1PdCe(1473)M.

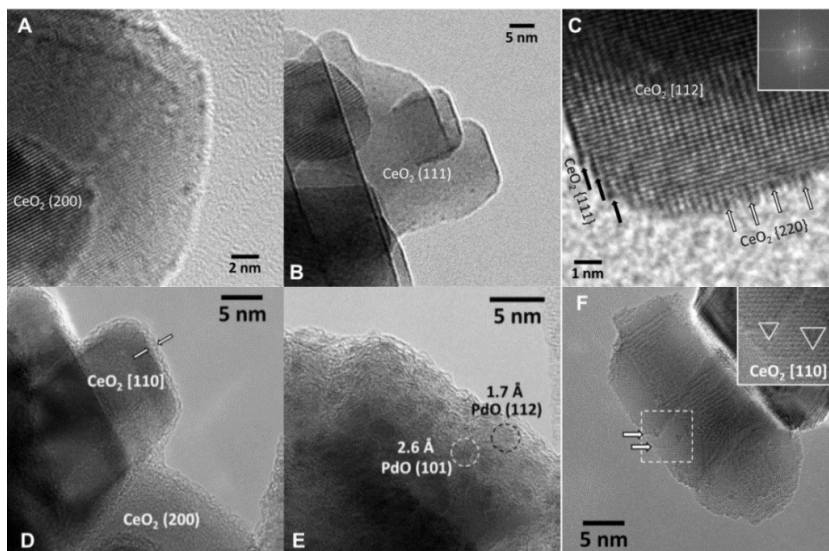


Figure 6.12: HRTEM images of the different Pd species observed on 4PdAcCe(1173)M after one reaction cycle up to 1173 K.

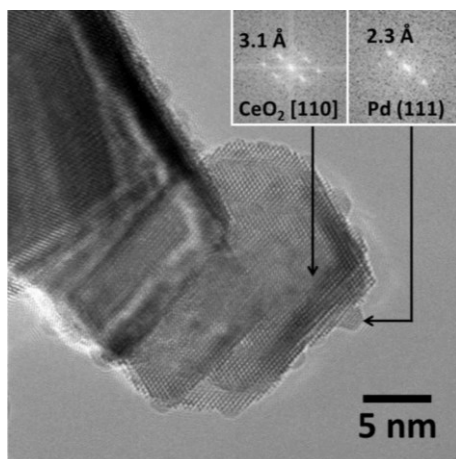


Figure 6.13: HRTEM image of 4PdCe(1173)IW.

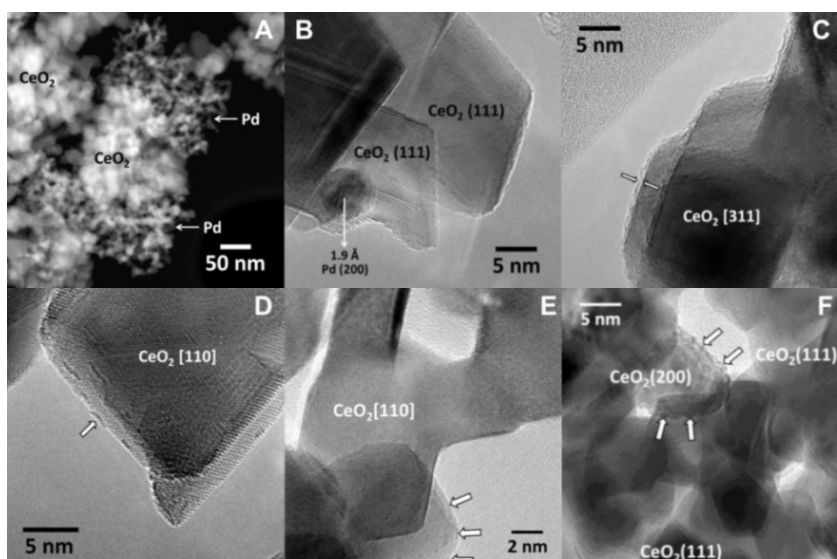


Figure 6.14: HRTEM images of 4PdCe(1173)M before (A-D) and after reaction (E,F).

6.3.3 Temperature Programmed Oxidation (TPO) and Reduction (TPR) Tests

The presence of different Pd species on 4PdAcCe(1173)M can be inferred also from TPO experiments, the oxygen release profile of this sample being very complex compared to 4PdCe(1173)IW and 4PdCe(1173)M (Figure 6.15). On 4PdAcCe(1173)M there is a higher fraction of PdO decomposing at higher temperature, while the IW sample displays a single broad peak centered at around 1060 K. On 4PdCe(1173)M a sharp O₂ release peak is observed at low temperature and a lower amount of cycling palladium is highlighted by the quantitative analysis of oxygen consumed and released, reported in Table 6.2. Conversely,

on the 4PdAcCe(1173)M catalyst there is more PdO decomposing at high temperature, usually indicating a stronger interaction with the support.³⁵ This seems to be a general feature of samples prepared by milling using Pd acetate precursor (Figure 6.16). In fact, the quantitative analysis of the deconvoluted oxygen release profiles on 1PdAcCe(1473)M, 1PdCe(1473)M and 1PdCe(1473)IW (Figure 6.17 and Table 6.3) shows a higher contribution of oxygen released at high temperature (1127 K) on the milled samples compared to the IW catalyst, which on the other hand is characterized by a large O₂ release at 1067 K. This peak is usually attributed to the reduction of bulk PdO³⁵ and corresponds to ca. 84% of the loaded palladium. Compared to the 1PdCe(1473)M catalyst, the sample prepared with palladium acetate shows a similar fraction of oxygen release at higher temperature, corresponding to ca. 30% of the loaded palladium. In addition, a 15 K increase in the main peak decomposition temperature can be observed, suggesting a further stabilization of other PdO species.

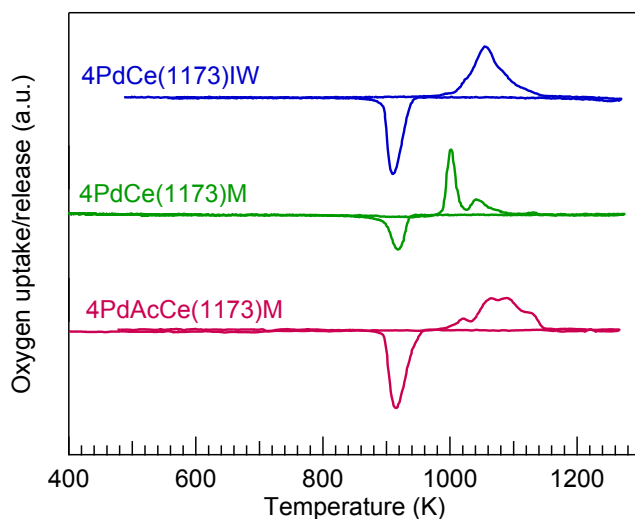


Figure 6.15: Oxygen profiles for 4wt%Pd/CeO₂ samples prepared by different syntheses on HSA ceria, 3rd heating/cooling cycle.

Table 6.2: Quantitative analysis of TPO profiles, 3rd heating/cooling cycle.

Sample	Measured Pd loading (wt%)	O ₂ release (μmoles O ₂ /g) ^a	O ₂ uptake (μmoles O ₂ /g)
4PdCe(1173)IW	3.94	147.6 (80)	123.2 (67)
4PdAcCe(1173)M	3.92	140.3 (76)	133.9 (73)
4PdCe(1173)M	3.69	95.5 (55)	75.1 (43)

a: the amount of Pd (% of total Pd) that is involved in oxidation/decomposition is reported in parentheses.

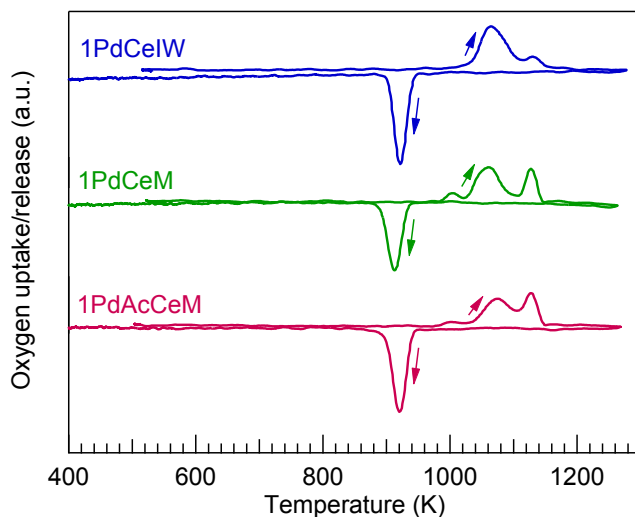


Figure 6.16: Oxygen profiles for 1wt%Pd/CeO₂ samples prepared by different syntheses on LSA ceria, 3rd heating/cooling cycle.

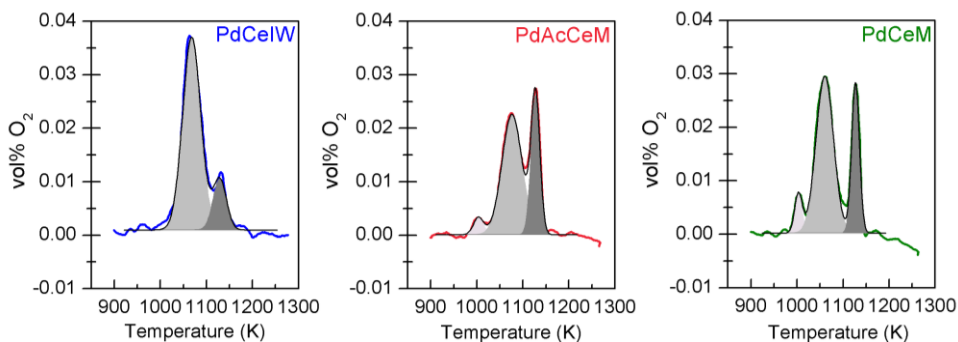


Figure 6.17: Deconvolution of PdO decomposition oxygen profiles for 1wt%Pd/CeO₂ samples, 3rd heating/cooling cycle.

Table 6.3: Quantitative analysis of the deconvoluted O₂ release peaks of Figure 6.17.

Peak	Center Temperature (K)			Area (%)		
	1PdCeIW	1PdAcCeM	1PdCeM	1PdCeIW	1PdAcCeM	1PdCeM
1	-	1003	1003	-	4.6	7.1
2	1067	1076	1060	83.8	63.2	65.1
3	1128	1127	1127	16.2	32.2	27.8

The nature of palladium particles formed after one combustion cycle on 4%Pd/CeO₂(1173) samples can also be inferred from H₂-TPR profiles. The evolution of hydrogen consumption at low temperature indicates that on 4PdCeIW and 4PdCeM PdO particles of different sizes are present, as suggested by the bimodal reduction peak below 323 K^{36,37} and the subsequent H₂ release at 333 K, which is attributed to the decomposition of palladium hydride species and whose formation is promoted on large PdO particles.³⁸ Conversely, on 4PdAcCeM only one sharp peak at 318 K can be observed followed by a negligible hydrogen release, suggesting that only small Pd species exist on the ceria surface. The higher reduction temperature is also generally attributed to Pd²⁺ species strongly interacting with ceria,³⁶ further corroborating the improved Pd-Ce interaction at nanoscale. The reduction of bulk ceria is not affected by the preparation synthesis but a higher degree of surface ceria reduction at around 500 K can be observed on the milled samples, likely due to their higher surface area (see Table 6.1) or to a higher amount of surface defects created by mechanical stresses during the dry-milling synthesis.³⁹

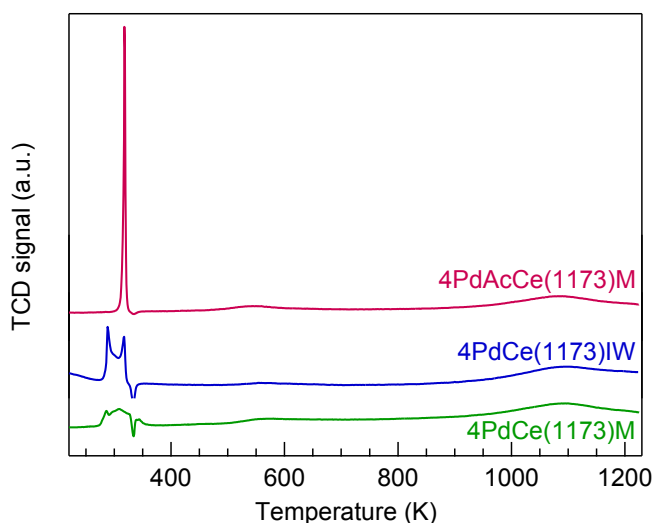


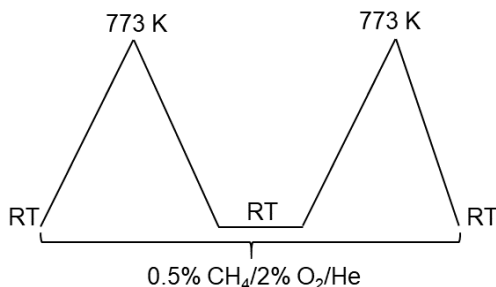
Figure 6.18: H₂-TPR profiles for 4%Pd/CeO₂ samples after combustion test up to 1173 K.

6.3.4 *In-situ* Synchrotron XRD

The peculiarities and higher activity of 4PdAcCe(1173)M prompted us to a deeper characterization through *in-situ* techniques. The surface palladium species and electronic states were evaluated and compared to the reference 4PdCe(1173)IW, which represents the state-of-the-art preparation method. It should be highlighted that in this chapter the

advanced characterization carried out with the help of synchrotron light techniques has involved typically the temperature range in which methane activation takes place (423-773 K), with the aim of understanding the role of different Pd-ceria arrangements, whereas the investigation of the high temperature behavior and stability of the samples will be object of further research.

In-situ synchrotron x-ray diffraction analysis was carried out on the milled and the impregnated samples following Scheme 6.1. A pretreatment up to 773 K in reaction atmosphere was used in order to remove the carbonate species originating from the Pd acetate precursor. This pretreatment was shown to be the most effective to preserve the catalytic activity of PdAcCe milled samples for methane oxidation, as reported in Chapter 5.



Scheme 6.1: Experimental detail of the *in-situ* XRD methane combustion tests. Total gas flow: 10 ml/min, ramp rate 10 K/min (heating), 50 K/min (cooling). First heating/cooling cycle is the pretreatment.

Comparative methane oxidation tests were performed in a lab-scale reactor setup to evaluate the catalytic activity of samples under the Clausen cell conditions (heating ramp up to 773 K, GHSV \approx 400'000 h⁻¹ (Figure 6.19). At higher space velocity, on 4PdAcCe(1173)M methane conversion starts at around 500 K and full conversion is reached at 673 K, outperforming the reference 4PdCe(1173)IW sample by more than 70 K. By keeping the maximum temperature below 973 K, PdO rearrangement or sintering due to decomposition and re-oxidation is prevented,⁴⁰ therefore higher activity is observed for 4PdOCe(1173)M compared to the standard light-off cycle up to 1173 K. Nevertheless, all samples are significantly outperformed by 4PdAcCe(1173)M.

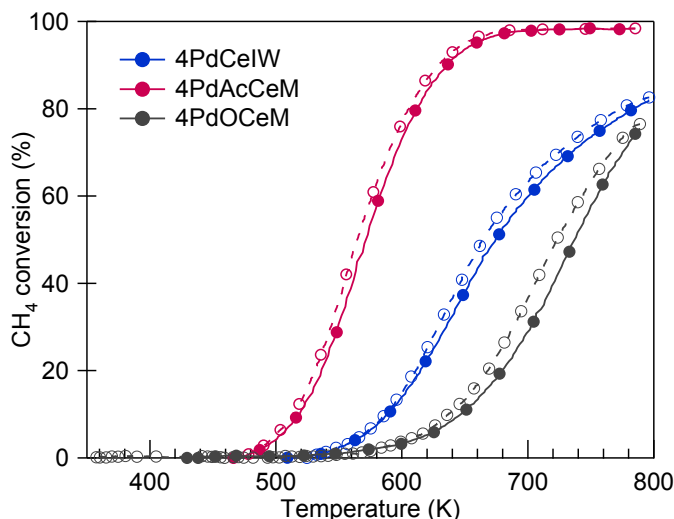


Figure 6.19: Methane combustion activity of samples investigated by *in-situ* XRD, 2nd heating/cooling ramp to 773 K. Solid line, full symbols: heating; dashed line, open symbols: cooling.

Figure 6.20 and Figure 6.21 show the *in-situ* XRD profiles of 4PdCe(1173)IW and 4PdAcCe(1173)M, respectively. The presence of crystalline PdO together with a small feature of metallic Pd can be inferred for the impregnated catalyst. Conversely, on the milled sample broader and less intense Pd and PdO peaks are detected in the whole temperature range after the decomposition of PdAc, indicating a smaller palladium particle size and a higher degree of metallic Pd in coexistence with PdO. On both samples, the size of the ceria crystallites remains constant throughout reaction. The same is observed for methane oxidation on pure ceria (Figure 6.22) and on 4PdOCe(1173)M (Figure 6.23). On the latter, PdO nanoparticles are extremely small, initially escaping detection and then gradually undergoing sintering during methane oxidation pretreatment at around 673 K.

Rietveld refinement of the XRD spectra does not reveal any substitution of Pd into CeO₂ lattice for any of the samples, the variation in the lattice parameter being due only to thermal expansion. This can be inferred from the comparison of the variation in the lattice parameter of Pd-containing samples with that of pure CeO₂ subjected to the same *in-situ* characterization (Figure 6.24). Rietveld refinement of the supported metal species on 4PdAcCeM is challenging due to the small peak size of Pd and PdO, while on 4PdCeIW an average PdO particle size of 5 nm can be calculated.

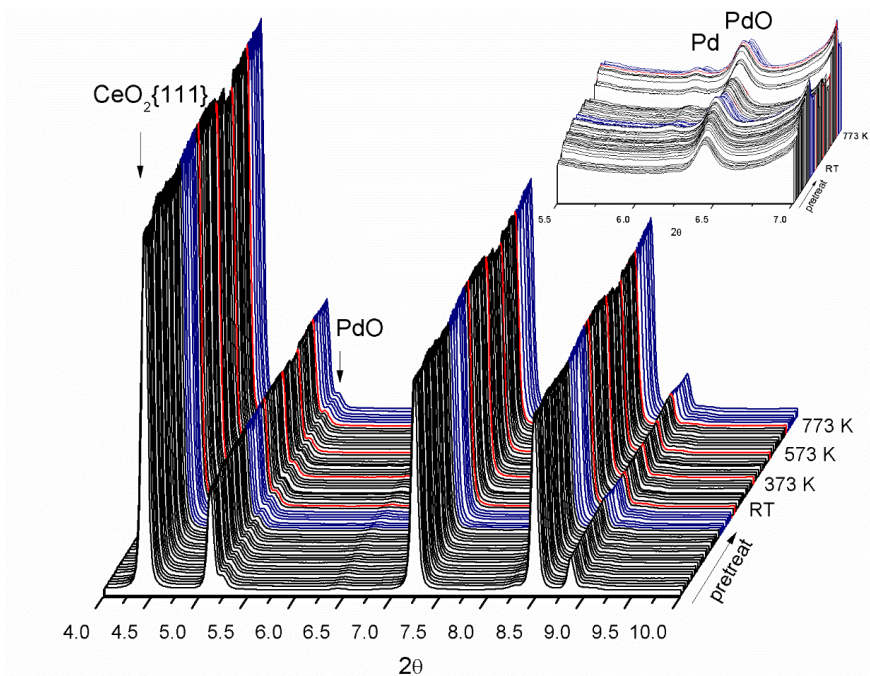


Figure 6.20: *In-situ* synchrotron XRD spectra of 4PdCe(1173)IW. Red lines indicate significant reaction temperatures, blue lines represent cooling, first heating ramp to 773 K is the pretreatment.

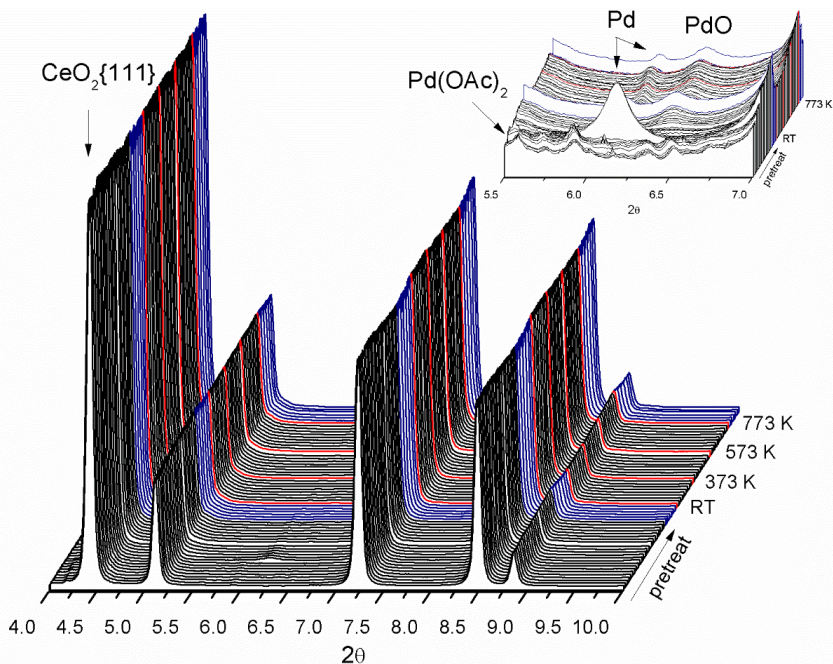


Figure 6.21: *In-situ* synchrotron XRD spectra of 4PdAcCe(1173)M. Red lines indicate significant reaction temperatures, blue lines represent cooling, first heating ramp to 773 K is the pretreatment.

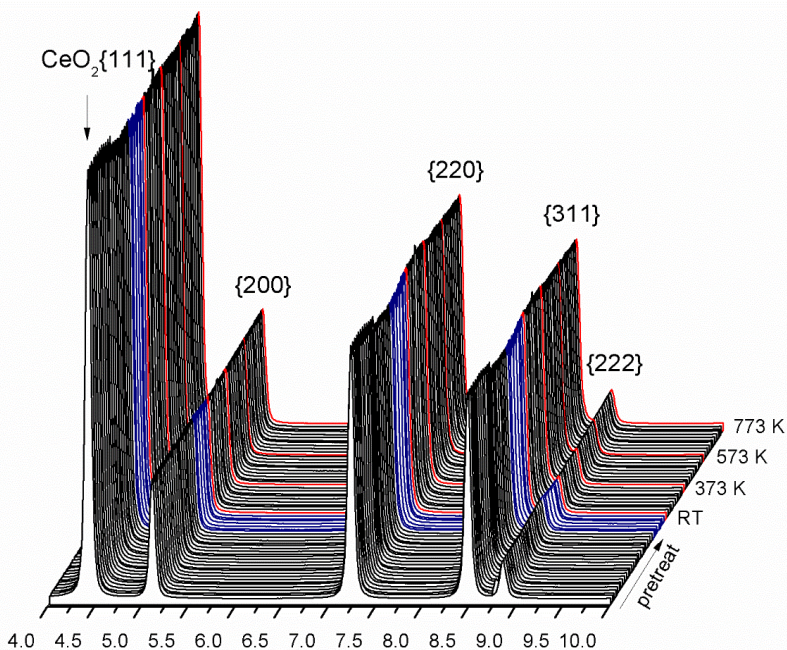


Figure 6.22: *In-situ* synchrotron XRD spectra of CeO₂-M. Red lines indicate significant reaction temperatures, blue lines represent cooling, first heating ramp to 773 K is the pretreatment.

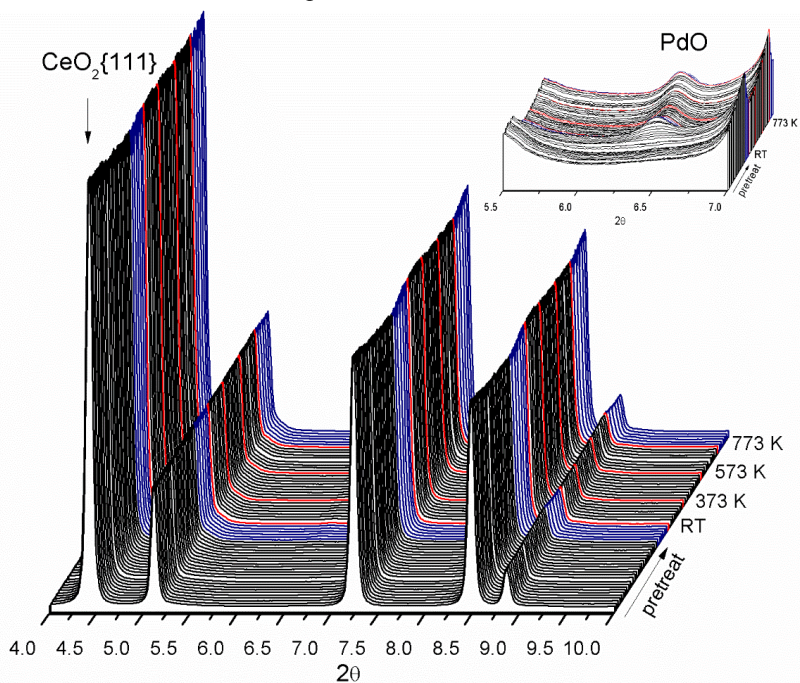


Figure 6.23: *In-situ* synchrotron XRD spectra of 4PdOCe(1173)M. Red lines indicate significant reaction temperatures, blue lines represent cooling, first heating ramp to 773 K is the pretreatment.

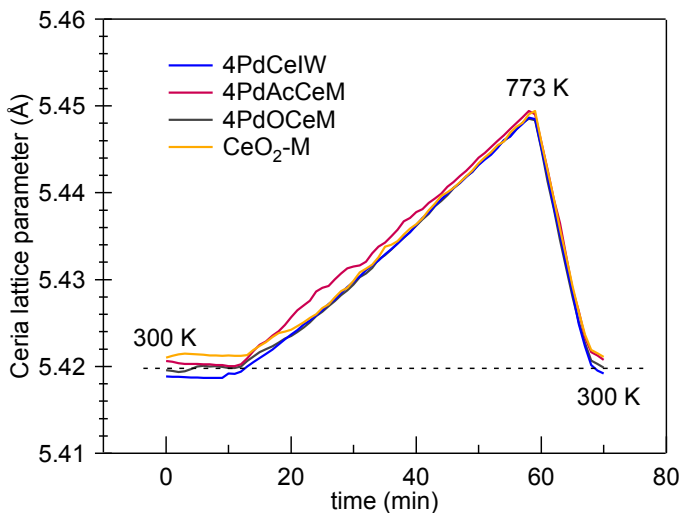


Figure 6.24: Rietveld refinement of CeO_2 lattice parameter during methane oxidation test; only thermal expansion is observed.

The *ex-situ* XRD characterization of the samples after one methane oxidation cycle up to 1173 K is reported in Figure 6.25. In agreement with the *in-situ* tests, on the impregnated catalyst only crystalline PdO can be observed, while on 4PdAcCe(1173)M both Pd and PdO peaks are present.

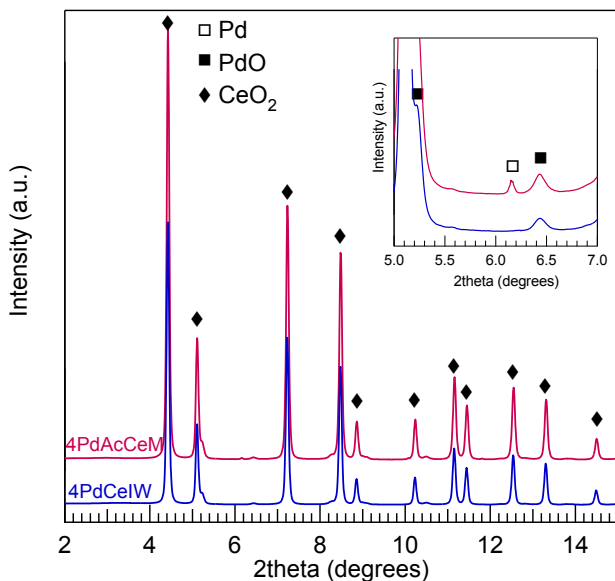


Figure 6.25: *Ex-situ* synchrotron XRD of 4wt%Pd/ CeO_2 samples after one reaction cycle up to 1173 K. Inset: focus on the Pd-PdO region.

6.3.5 Raman Spectroscopy

The presence of a higher amount of crystalline PdO on 4PdCe(1173)IW was confirmed by Raman spectroscopy. Prior to Raman characterization, the samples were exposed to the reaction mixture up to 773 K, to mimic the experimental conditions of *in-situ* XRD. Representative 100 μm^2 maps of the surface of milled and impregnated catalysts showing the ratio between PdO and CeO₂ signals are reported in Figure 6.26. Coherently with XRD results, the IW sample presents a higher amount of crystalline PdO structure on the surface with respect to 4PdAcCe(1173)M, amorphous oxidized PdO and metallic Pd species not providing any Raman signal. In fact, the Raman signal originates from the symmetric stretching of the O-Pd-O bond in a PdO₄ configuration,^{23,41} which is mostly found in the bulk core of crystalline particles; the surface layers of particles and amorphous structure lack the symmetry needed to provide a detectable signal. The situation is similar also after a combustion cycle up to 1173 K, with 4PdCe(1173)IW having a higher PdO/CeO₂ intensity ratio on the surface (Figure 6.26(c,d)). On 4PdOCeM the Raman signal of PdO is very weak, as shown in Figure 6.27, likely due to the smaller particle size of the precursor PdO powders detected by *in-situ* XRD (inset, Figure 6.23). Representative Raman spectra collected on the investigated samples, treated at 773 K under reaction mixture prior to measurement, are compared in Figure 6.28. In addition to the characteristic peaks at 461 cm^{-1} and at 646 cm^{-1} , corresponding to the F_{2g} mode of CeO₂ and the B_{1g} vibrational mode of PdO, respectively, the spectra in Figure 6.28 highlight a broad band between 550 and 600 cm^{-1} on 4PdAcCe(1173)M, suggesting a higher degree of ceria lattice defects are present on its surface.

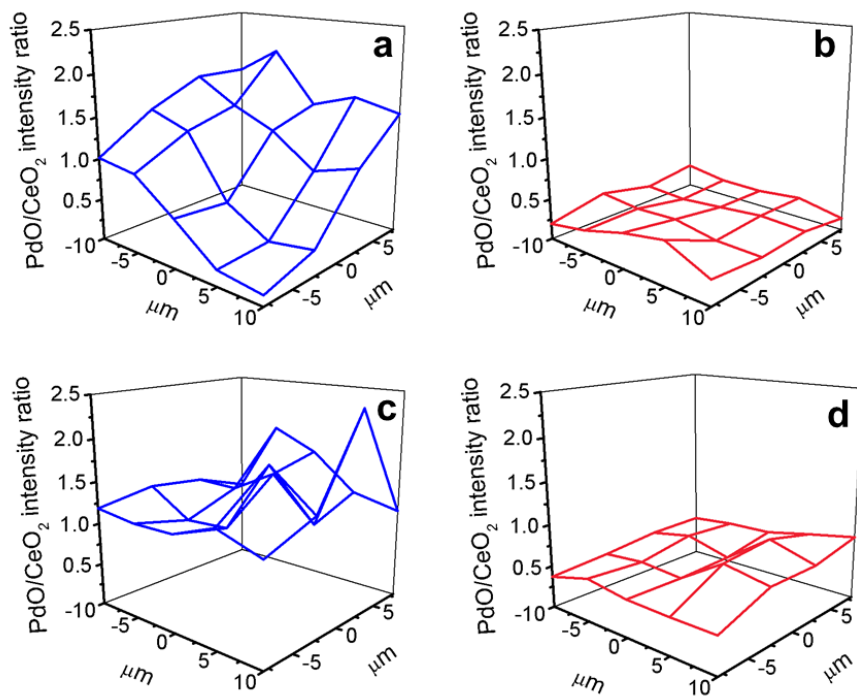


Figure 6.26: Intensity ratio of the PdO and CeO₂ Raman signals for 4PdCe(1173)IW (a,c) and 4PdAcCe(1173)M (b,d) after combustion test up to 773 K.(a,b) and 1173 K (c,d).

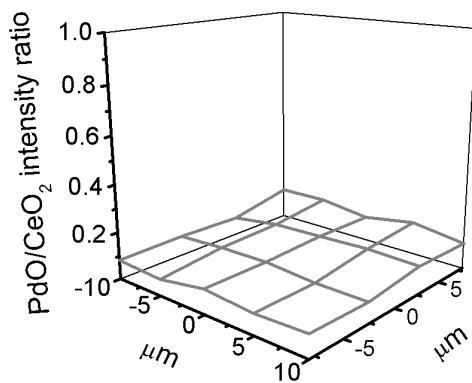


Figure 6.27: Intensity ratio of the PdO and CeO₂ Raman signal for 4PdOCe(1173)M after combustion test at 773 K.

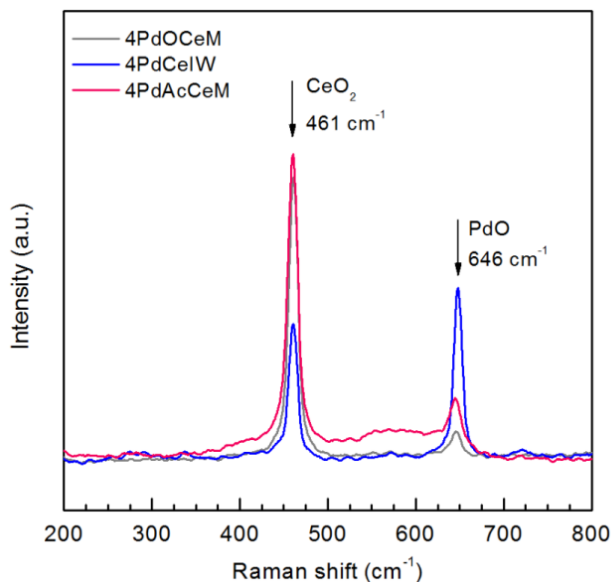
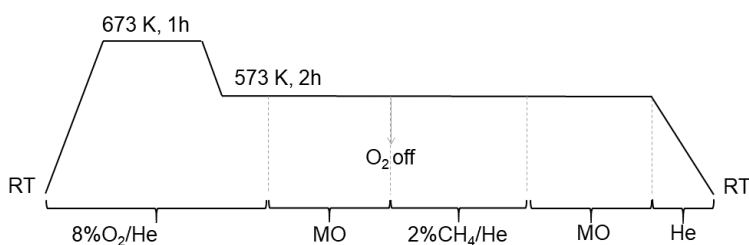


Figure 6.28: Comparison of representative Raman spectra collected on 4PdCe(1173)IW, 4PdAcCe(1173)M and 4PdOCe(1173) after one combustion cycle up to 773 K.

6.3.6 *In-situ* DRIFTS

The transformations occurring on the surface and the nature of Pd species have been followed also by *in-situ* DRIFTS analysis. Experimental conditions have been chosen to optimize the *in-situ* measurements in the apparatus and are reported in Scheme 6.2.



Scheme 6.2: Experimental detail of the *in-situ* DRIFTS methane oxidation (MO) tests. Total gas flow: 50 ml/min; heating/cooling ramps: 20 K/min; reaction mixture: 2%CH₄/8%O₂/He.

The higher reactivity of 4PdAcCeM compared to the impregnated counterpart can be clearly observed by looking at the evolution of gaseous CO₂ in the first few minutes of experiment (band at 2350 cm⁻¹ in Figure 6.29(a,b)). Moreover, the reduction of PdO during the treatment in methane only is much faster for the milled sample, as it can be observed by the shift in the background due to the formation of darker metallic Pd that occurs after 5

minutes on 4PdAcCe(1173)M with respect to 13 minutes on 4PdCe(1173)IW. This suggests that not only the reactivity towards methane oxidation is higher on the milled sample, but also the intrinsic reactivity of the Pd-PdO active phase obtained by the dry milling of Pd acetate and ceria. On pure CeO₂ no reaction occurs, as expected, and carbonate species are formed on the ceria surface during the first methane oxidation step (bands at 1550 and 1350 cm⁻¹,^{42,43} Figure 6.29(c)).

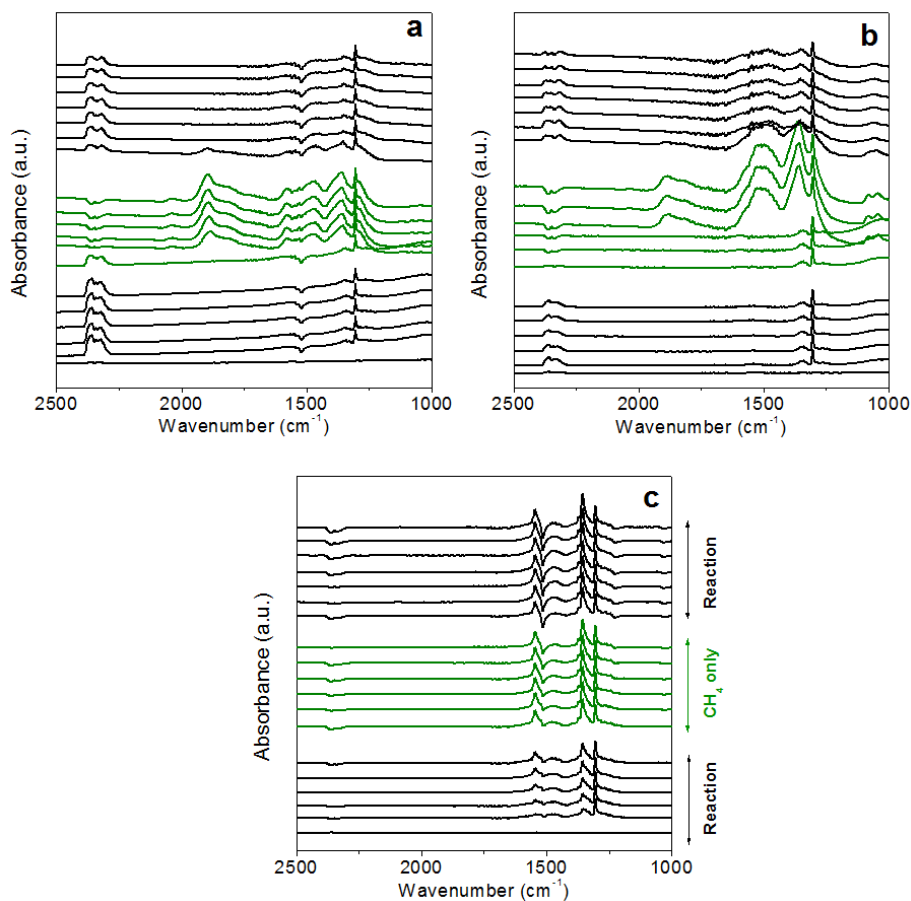


Figure 6.29: Full *in-situ* DRIFTS spectra collected during methane oxidation test at 573 K on 4PdAcCe(1173)M (a), 4PdCe(1173)IW (b) and CeO₂-M (c). Spectra are shown every 5mins; green spectra correspond to the methane reduction step.

A comparison of the most significant spectra, collected on 4PdAcCe(1173)M and 4PdCe(1173)IW at the first and last minute per step (first methane oxidation step, methane-only after O₂ removal, second oxidation step) is reported in Figure 6.30, where it can be clearly observed that the formation of carbonate species on ceria is promoted on the sample

prepared by incipient wetness, as inferred by the broad peaks around 1600-500 cm^{-1} and 1350 cm^{-1} .⁴²⁻⁴⁴ These species remain stable even when oxygen is re-added to the gas feed and may be linked to the higher amount of bare ceria surface available on 4PdCe(1173)IW compared to 4PdAcCe(1173)M, as suggested by HRTEM and further confirmed by XPS measurements.

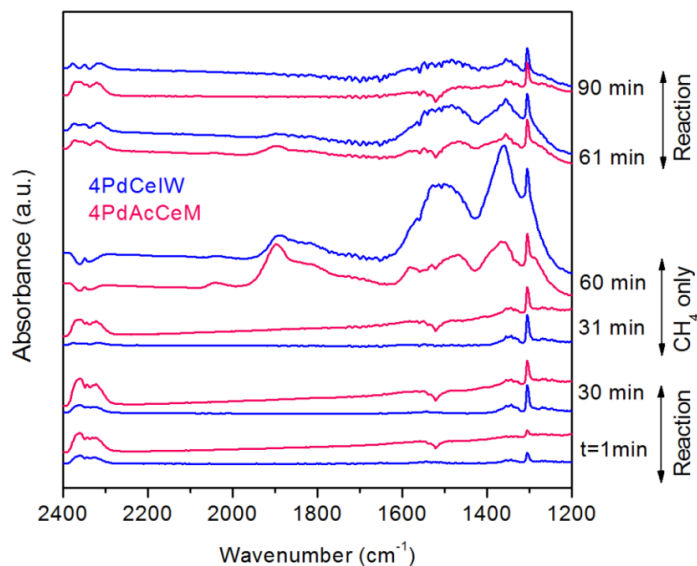


Figure 6.30: Comparison of DRIFTS spectra at time 1 and 30 min for each reaction step (see Scheme 6.2), for 4PdAcCe(1173)M and 4PdCe(1173)IW.

In Figure 6.31, the differential spectra reported on the bottom represent the amount of surface species which are removed by the re-introduction of O_2 in the feed. As also observed in Figure 6.30, on 4PdAcCe(1173)M all carbonates species quickly disappear after oxygen is introduced in the feed, and the differential profile mirrors the final ‘CH₄-only’ spectrum (yellow line). On the other hand, on 4PdCe(1173)IW the spectra look different and a large portion of the carbonates remains on the catalyst surface.

A closer look at the region of CO-bonds on palladium (2100-1800 cm^{-1} , Figure 6.30 and Figure 6.31) reveals that, during the reduction in methane, on the milled catalyst more Pd is available on the surface to react with the CO formed, indicating a higher Pd dispersion. This is further confirmed by the presence of the band at about 2050-2090 cm^{-1} which is commonly attributed to CO linearly bonded to metallic Pd^{43,45,46} and that is evidenced after CO chemisorption (Figure 6.32). A summary of the main frequencies of interest and their assigned species from the literature is reported in Table 6.4.

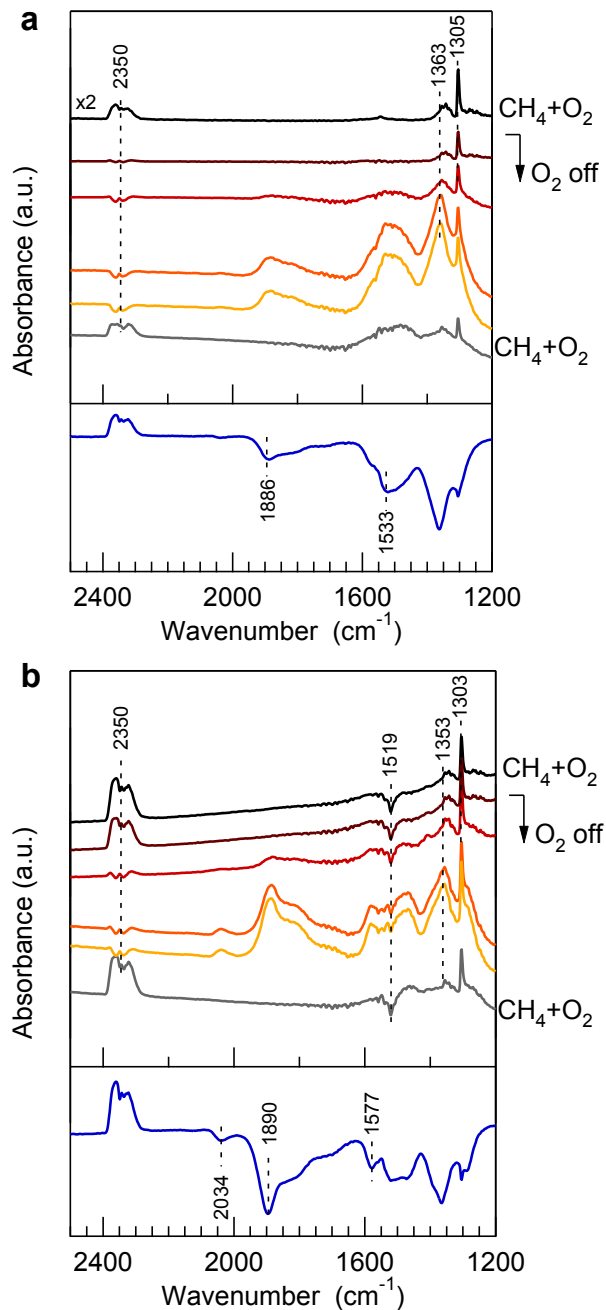


Figure 6.31: *In-situ* DRIFTS spectra collected over 4PdCe(1173)IW (a) and 4PdAcCe(1173)M (b) during methane oxidation at 573 K and an intermediate O_2 -switch off step. The bottom dash line was obtained by subtracting the last ‘ CH_4 -only’ spectrum (yellow line) from the second ‘ $\text{CH}_4 + \text{O}_2$ ’ spectrum (grey line), corresponding to re-introduction of O_2 in the feed. For 4PdCeIW the scale was doubled compared to 4PdAcCeM.

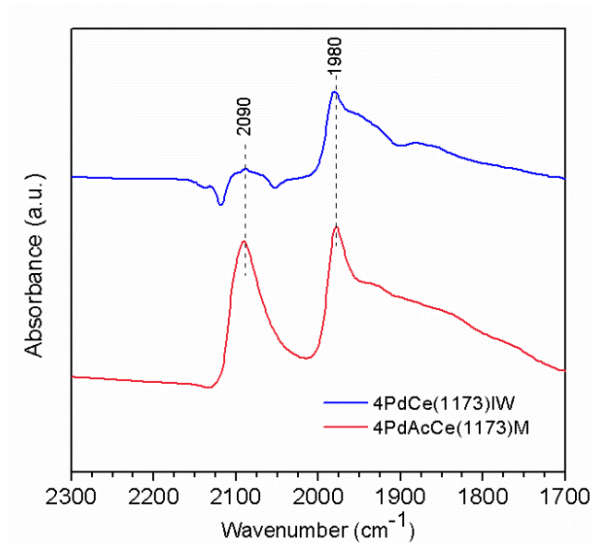


Figure 6.32: DRIFTS spectra after CO adsorption on 4PdCe(1173)IW and 4PdAcCe(1173)M.

Table 6.4: Assignments of the main IR bands observed during methane oxidation and CO-chemisorption tests.

Frequency (cm ⁻¹)	Assignment	Reference
2350	CO _{2,gas}	43
1305	CH _{4,gas}	47,48
2090-2034	CO-Pd ⁰ linear	43,45
1980-1890	CO-Pd ⁰ bridged	43,45,46,49
1577-1519,1353	carbonates	42,43

6.3.7 Ambient Pressure XPS

The oxidation state of palladium and ceria during low temperature methane combustion was followed by *in-situ* Ambient-Pressure X-ray Photoelectron Spectroscopy (AP-XPS) experiments. Both samples display a relatively stable state throughout the whole temperature range (RT to 673 K), as shown in Figure 6.33. However, on the IW catalyst the spectra collected in the Pd 3d region demonstrate that palladium is present mostly in a superoxidized state (~70-80% Pd⁴⁺) and its Signal-to-Noise Ratio (SNR) is much lower compared to the Ce 3d signal (Figure 6.34), suggesting a large amount of bare ceria surface. On the dry milled sample (Figure 6.35) surface Pd²⁺ species are predominant, accompanied by smaller amounts of Pd⁴⁺ (ca. 5%) and Pd⁰ (ca. 10%). The strong Pd 3d signal indicates an improved dispersion of palladium on the ceria surface, resulting in a weaker Ce 3d signal.

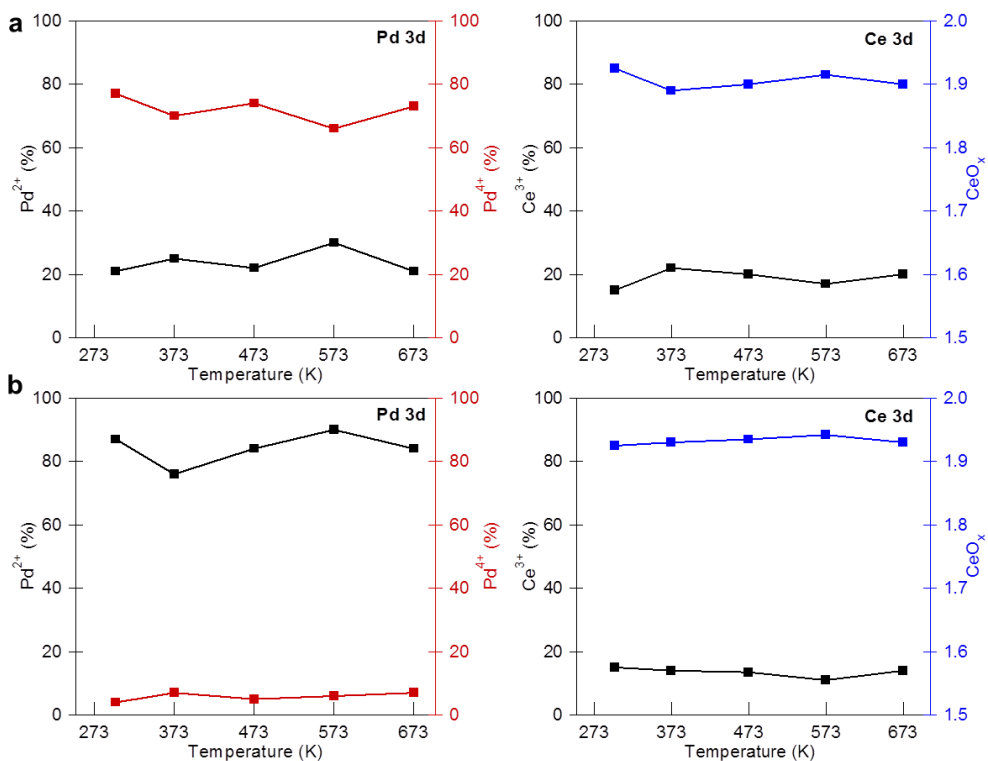


Figure 6.33: Evolution of the Pd and Ce oxidation states as measured by AP-XPS analysis of Pd 3d and Ce 3d regions on 4PdCe(1173)IW (a) and 4PdAcCe(1173)M (b) during methane oxidation tests.

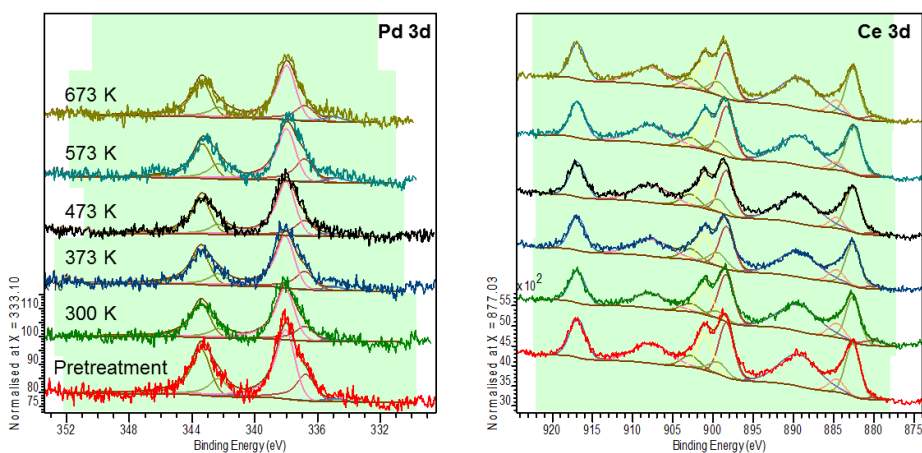


Figure 6.34: AP-XPS spectra collected in the Pd 3d and Ce 3d regions on 4PdCe(1173)IW during methane oxidation tests.

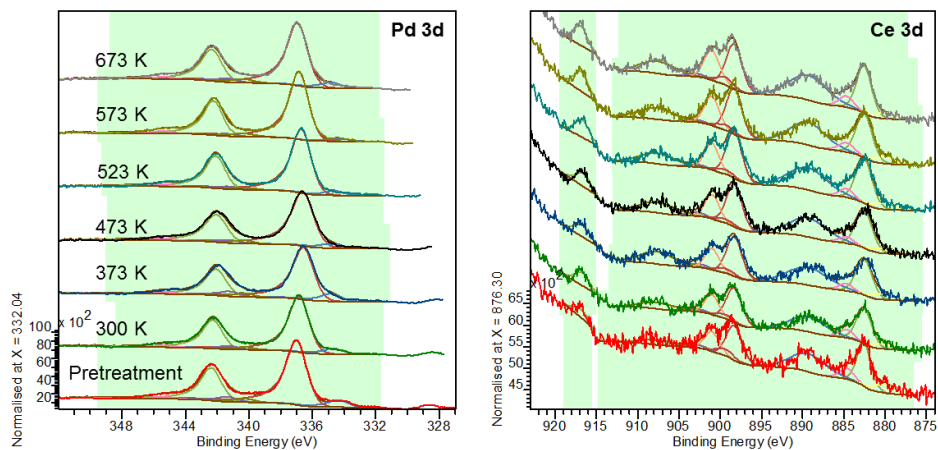


Figure 6.35: AP-XPS spectra collected in the Pd 3d and Ce 3d regions on 4PdAcCe(1173)M during methane oxidation tests.

6.4 Discussion

By milling palladium acetate with low surface area cerium oxide powders (calcined at 1473 K) highly active methane oxidation catalysts were prepared, displaying a remarkable low temperature light-off activity and improving by 15 K the performance of 1PdCe(1473)M (obtained from metallic Pd and previously reported as the most active). Moreover, these catalysts show a significant reduction in the activity loss at high temperature linked to PdO-Pd decomposition (Figure 6.3). To our best knowledge, a decrease in the activity loss during the cooling branch of the light-off cycle on Pd-based catalysts was reported only once before in the work by Cargnello et al., in which the methane oxidation performance of Pd@CeO₂ units supported on alumina was investigated.⁸ In that case, the authors attributed the improved performance to the Pd core-CeO₂ shell configuration capable to maximize the metal-support interface stabilizing the PdO active phase at high temperature. Here the catalyst still maximizes the metal-support interface, even though presenting an opposite physical arrangement (CeO₂ core surrounded by a Pd shell). From TPO experiments (Figure 6.15 and Figure 6.16) it appears that the PdO-Pd transformation takes place on these samples, as also inferred from methane oxidation experiments carried out at very high space velocity showing again the loss in conversion.⁵⁰ This indicates that the reduction in the activity loss is likely due to their overall superior activity with respect to conventional catalysts. 1PdAcCeM sample is also characterized by improved stability in the presence of water with respect to both 1PdCeM and 1PdCeIW (Figure 6.5 and Figure 6.6). Water is known to strongly deactivate the catalyst in methane oxidation due to competitive

adsorption of O₂ and H₂O on active sites and/or the formation of inactive Pd(OH)₂ species.^{34, 47, 51–54} The wide metal-support interface can help the oxygen mobility between Pd and ceria, which is recognized as a key property for the high resistance to deactivation in presence of water.^{30, 52} While no relevant morphological differences can be observed by HRTEM between 1PdAcCeM and 1PdCeM, both samples exhibiting an amorphous shell structure covering the ceria crystallites (Figure 6.11), the enhanced catalytic activity and stability may be attributed to a closer Pd-Ce nanoscale interaction which in turn affects the type and amount of Pd species present on the Pd acetate milled samples compared to the impregnated counterpart.

Further investigation of the Pd active sites on this 1PdAcCeM sample is challenging due the low palladium loading, consequently a new set of samples with increased noble metal loading was prepared (up to 10 wt%) on ceria calcined at two different temperatures to obtain higher (25 m²/g) and lower (4 m²/g) surface area. Catalytic results (Figure 6.7 to Figure 6.10) show that PdAc/CeO₂ milled samples are able to accommodate high loadings of Pd in very active configurations, even on low surface area CeO₂. On the other hand, the 4PdCeIW and 4PdCeM samples display worse performances, indicating that the low surface area ceria is not able to accommodate efficiently higher metallic Pd loadings, as inferred also by comparing the light-off curves of 1 wt% and 4 wt% PdCe(1473)M (see Figure 6.8). The use of a ceria support with higher thermal stability and, consequently, a higher surface area at high temperature improves only partially the overall catalytic activity for the samples prepared by impregnation or by milling with metallic Pd (Figure 6.9).

Morphological characterization of these samples by HRTEM shows a uniform distribution of palladium clusters on 4PdCe(1173)IW, highly crystalline and with an average size of ca. 2 nm (Figure 6.13), while 4PdCe(1173)M presents a non-homogeneous Pd distribution with the presence of isolated particles, flake-like features and limited regions of amorphous shell structure (Figure 6.14). It is evident that the dry milling synthesis using metallic Pd as precursor, which was very effective at 1wt% loading, is not able to successfully distribute higher (4 wt%) Pd content on the ceria surface, resulting in a significant activity loss (Figure 6.8). Conversely, the use of palladium acetate enables the successful deposition of higher loadings of Pd on CeO₂ with higher surface area (Figure 6.10) through the formation of a variety of Pd species on the ceria surfaces, as observed by HRTEM images in Figure 6.12. In addition to a thin amorphous layer, other smaller palladium entities can be identified on the ceria surface: some are below 0.5 nm and appear as sparse darker spots, some are larger

(1-2 nm) and exhibit {101} and {112} planes of tetragonal PdO, others are triangle-shaped and found on ceria steps or terraces sites. The insertion of Pd atoms in the outermost ceria lattice was also observed (Figure 6.12(C)). It should be emphasized that the most recent experimental and theoretical works investigating the catalytic activity for methane oxidation of Pd-based catalysts indicate clearly that there are specific Pd-O configurations, ionic Pd species and/or Pd-PdO exposed facets that are more effective in methane activation with respect to Pd with different arrangements,^{15,47} and this is true also when considering ceria-supported Pd catalysts.^{25,55} The deep characterization carried out in this work allowed to understand that, compared to samples prepared by impregnation or by milling with metallic Pd, the catalysts obtained from Pd acetate present a larger variety of Pd species.

The higher reactivity of 4PdAcCe(1173)M compared to the impregnated counterpart is clearly observed also by looking at the DRIFTS spectra collected during reaction, with the gaseous CO₂ band being more pronounced on the milled sample and showing faster recovery after O₂ re-introduction, coherently with the slower deactivation rate observed in stability tests. The reduction of PdO during the treatment in methane, indicated by the shift in the background due to the formation of darker metallic Pd, is also noteworthy. This transition is much faster for the milled sample, suggesting that not only the reactivity towards methane oxidation is higher on 4PdAcCe(1173)M, but also the intrinsic reactivity of the Pd-PdO active phase obtained by the dry milling of Pd acetate and ceria. Conversely, the formation of stable carbonate species on ceria is promoted on the sample prepared by incipient wetness. These species are only partially removed when oxygen is re-added to the gas feed and may be linked to the higher amount of bare ceria surface available on 4PdCe(1173)IW compared to 4PdAcCe(1173)M, as suggested by HRTEM and further confirmed by XPS measurements.

The wide array of Pd species created and stabilized on 4PdAcCe(1173)M likely stems from the Pd⁰/Pd²⁺ combination created after decomposition of the palladium salt during pretreatment, as previously reported in Chapter 5 and further observed by *in-situ* XRD (Figure 6.21, inset). TPO profiles (Figure 6.15) confirm the existence of multiple Pd species on 4PdAcCe(1173)M with several degrees of interaction with ceria support, compared to predominant bulk PdO species on 4PdCe(1173)IW.³⁵ On 4PdAcCe(1173)M there is a higher fraction of PdO decomposing at higher temperature, usually indicating a stronger interaction with the support.³⁵ This seems to be a general feature of samples prepared by milling from Pd acetate precursor. Conversely, on the 4PdCe(1173)M sample the looser contact of Pd and

CeO₂, suggested by palladium oxide decomposition occurring at lower temperatures (1000 K) and by the smaller amount of palladium undergoing re-oxidation, results in poorer methane oxidation activity (Figure 6.9).

The presence of larger PdO particles on the sample prepared by wet synthesis is also confirmed by HRTEM characterization, (Figure 6.13), by the anticipated reduction profile in H₂-TPR tests (Figure 6.18) and by Rietveld refinement of the palladium peaks. Their larger size also implies a highly crystalline structure, which is reflected in the sharper PdO peak at $2\theta = 6.45^\circ$ in XRD spectra collected *in-situ* and *ex-situ* (Figure 6.20 and Figure 6.25, respectively) and in the stronger intensity of the Raman shift at 646 cm⁻¹ (Figure 6.26 and Figure 6.28). Conversely, the smaller size of palladium species on the milled sample are characterized by a lower degree of crystallinity coupled to a fully amorphous shell structure, resulting in weaker signal in XRD analysis and Raman spectra (Figure 6.21 and Figure 6.26, respectively). The substitution of Pd into the ceria lattice is not detected by Rietveld refinement of the *in-situ* XRD spectra, but its local occurrence inside the amorphous shell cannot be excluded,²³ as the shell/bulk volume ratio identified by HRTEM is very small and the bulk CeO₂ signal could prevent its detection. Certainly, on 4PdAcCe(1173)M the peculiar local Pd/Ce arrangement is able to maintain highly dispersed palladium species during reaction in a Pd⁰/Pd²⁺ combination, while also providing a large number of active sites. Moreover, the variety of Pd species present on 4PdAcCe(1173)M are likely to expose different Pd-PdO planes, which are known to have different reactivity towards methane activation.⁵⁶⁻⁵⁸ An unambiguous identification of the exposed PdO surfaces is impossible due to the small size of most Pd features, below the HRTEM instrument resolution, and the amorphous nature of the shell, but the round PdO entities shown in Figure 6.12(E) clearly exhibit both {101} and {112} planes.

On 4PdAcCe(1173)M the high metal dispersion results in a smaller amount of bare ceria exposed on the surface, as shown by AP-XPS measurements (Figure 6.35) and by the slow deposition of carbonate species on ceria under methane-only and methane oxidation conditions (Figure 6.29 and Figure 6.30). The high reactivity of the PdO_x species of the milled sample results in faster removal of the carbonates, as shown in Figure 6.31, which does not occur on the IW sample. In fact, on 4PdCe(1173)IW the arrangement of palladium in highly crystalline PdO clusters allows more ceria surface to be exposed, as highlighted by HRTEM and AP-XPS spectra of the Ce 3d region (Figure 6.34), which could affect negatively its low temperature methane activation performance and the catalytic stability.

Moreover, the Pd 3d spectra highlight a superoxidized state of palladium on the IW sample (Figure 6.34), exhibiting mostly Pd⁴⁺ and Pd²⁺ species. In our previous paper¹³ we observed the coexistence of Pd²⁺ and Pd⁴⁺ also on 1PdCeM after 1 (or 6) light-off cycle. The exposure at temperatures up to 1173 K can result in a deeper oxidation of the surface also for milled samples and, according to the theoretical work by Senftle et al.,²⁵ the presence of Pd⁴⁺ is important to achieve low methane activation barriers. Nevertheless, our results indicate clearly that the different Pd species present on 4PdAcCe(1173)M constitute a unique environment favoring not only low temperature methane activation but also catalyst stability over a wider temperature range.

It is noteworthy that the morphology of 4PdOCe(1173)M, characterized by highly dispersed PdO nanoparticles (Figure 6.23), results in poor methane oxidation activity (Figure 6.19). Our hypothesis is that the supported PdO nanoparticles, even if with a very small particle size but in weak interaction with ceria (as observed on 4PdOCeM)¹³ and/or PdO nanoparticles in fully oxidized state (as those observed on IW) are not able to activate methane at low temperature. For this purpose, the heterogeneous mixture of Pd⁰/Pd²⁺ species, likely arising from the strong interaction with ceria support and stabilized on its outermost layers, is needed, such as the one formed on 4PdAcCe(1173)M, where the nanoscale surface arrangement enables enhanced methane oxidation performance at low temperature and increased activity and stability at high temperatures. Indeed, a thin PdO layer on Pd^{56,57,59} or Pd⁴⁺ ions on PdO_x²⁵ were indicated as extremely active for low temperature methane oxidation, exhibiting a very low activation barrier for methane dissociation. Moreover, the intimate interaction of Ce³⁺/Ce⁴⁺ and palladium ions in a stable arrangement maintained throughout reaction (Figure 6.33) likely promotes oxygen mobility and, consequently, a higher CH₄ oxidation rate and improved resistance against steam deactivation. Conversely, dispersed PdO nanoparticles exhibiting mostly Pd⁴⁺ and Pd²⁺ species, as those observed on the sample prepared by incipient wetness impregnation and likely on the milled sample prepared using PdO nanoparticles, display poorer methane oxidation activity (Figure 6.19). The improved reactivity observed by *in-situ* DRIFTS under CH₄-only atmosphere (Figure 6.30) further suggests that the Pd⁰/Pd²⁺/CeO_x surface environment developed on 4PdAcCe(1173)M might provide enhanced performances also in other methane activation reactions, whereas Pd entities in an overoxidized state and in a highly crystalline PdO arrangement are less active for the activation of C-H bond and the low temperature oxidation of CH₄.

6.5 Conclusions

Catalytic materials were successfully prepared by dry mechano-chemical synthesis carried out using Pd(OAc)₂ and CeO₂ powders. PdAc/CeO₂ milled (M) samples exhibited higher methane oxidation activity and stability compared to their counterparts prepared by traditional incipient wetness impregnation (IW) and by mechanical milling starting from Pd black, previously reported as the most active among evaluated materials.¹³ The use of a palladium precursor salt also allowed for the successful loading of higher Pd content on low and high surface area ceria. Catalysts containing 4 wt% Pd displayed outstanding methane oxidation, outperforming the reference 4PdCeIW sample.

The combination of *in-situ* and *ex-situ* characterization techniques carried out on the 4PdAcCe(1173)M milled sample revealed a wide array of Pd species in a Pd⁰/Pd²⁺ combination. These palladium species appear very stable, exhibiting small particle size (below 1.5 nm) and high dispersion. The diverse PdO_x entities likely expose a variety of crystallographic planes, providing multiple active sites and of different nature,^{56,57} and their close interaction with the ceria surface and sub-surface layer results in improved oxygen mobility, higher reaction rates and steam deactivation resistance. Conversely, on 4PdCe(1173)IW highly crystalline PdO particles are observed, measuring ca. 2 nm in size and comprised by Pd²⁺ and Pd⁴⁺ species predominantly, leading to worse metal dispersion and a larger amount of free ceria surface. Such PdO/CeO₂ arrangement with more oxidized Pd species results in lower reactivity and a catalyst more prone to deactivation.

On 4PdAcCe(1173)M, the improved reactivity displayed even in presence of methane only in the feed and the stronger CO-Pd binding suggest a generalized enhanced reactivity towards methane activation, which will be further investigated in Chapter 7. Further XAS analysis (which is planned to be carried out in the near future) could be useful in the determination of the nearest neighbors for supported Pd species, providing an additional insight into the Pd-Ce configuration inside of the amorphous layer.

6.6 References

- (1) Ma, Z.; Xiong, X.; Song, C.; Hu, B.; Zhang, W. Electronic Metal–Support Interactions Enhance the Ammonia Synthesis Activity over Ruthenium Supported on Zr-Modified CeO₂ Catalysts. *RSC Advances* **2016**, *6* (56), 51106–51110. <https://doi.org/10.1039/C6RA10540H>.
- (2) Gao, W.; Hood, Z. D.; Chi, M. Interfaces in Heterogeneous Catalysts: Advancing Mechanistic Understanding through Atomic-Scale Measurements. *Accounts of Chemical Research* **2017**, *50* (4), 787–795. <https://doi.org/10.1021/acs.accounts.6b00596>.
- (3) Liu, Y.; Ning, Y.; Yu, L.; Zhou, Z.; Liu, Q.; Zhang, Y.; Chen, H.; Xiao, J.; Liu, P.; Yang, F.; et al. Structure and Electronic Properties of Interface-Confined Oxide Nanostructures. *ACS Nano* **2017**, *11* (11), 11449–11458. <https://doi.org/10.1021/acsnano.7b06164>.
- (4) Suchorski, Y.; Kozlov, S. M.; Bepalov, I.; Datler, M.; Vogel, D.; Budinska, Z.; Neyman, K. M.; Rupprechter, G. The Role of Metal/Oxide Interfaces for Long-Range Metal Particle Activation during CO Oxidation. *Nature Materials* **2018**, *17* (6), 519–522. <https://doi.org/10.1038/s41563-018-0080-y>.
- (5) Aneggi, E.; Boaro, M.; Colussi, S.; de Leitenburg, C.; Trovarelli, A. Ceria-Based Materials in Catalysis: Historical Perspective and Future Trends. In *Handbook on the Physics and Chemistry of Rare Earths*; Bünzli, J.-C. G., Pecharsky, V. K., Eds.; Elsevier, 2016; Vol. 50, pp 209–242. <https://doi.org/10.1016/bs.hpcre.2016.05.002>.
- (6) Zhu, K.-J.; Liu, J.; Yang, Y.-J.; Xu, Y.-X.; Teng, B.-T.; Wen, X.-D.; Fan, M. A Method to Explore the Quantitative Interactions between Metal and Ceria for M/CeO₂ Catalysts. *Surface Science* **2018**, *669*, 79–86. <https://doi.org/10.1016/j.susc.2017.11.009>.
- (7) Colussi, S.; Gayen, A.; Farnesi Camellone, M.; Boaro, M.; Llorca, J.; Fabris, S.; Trovarelli, A. Nanofaceted Pd-O Sites in Pd-Ce Surface Superstructures: Enhanced Activity in Catalytic Combustion of Methane. *Angewandte Chemie International Edition* **2009**, *48* (45), 8481–8484. <https://doi.org/10.1002/anie.200903581>.
- (8) Cargnello, M.; Jaen, J. J. D.; Garrido, J. C. H.; Bakhmutsky, K.; Montini, T.; Gamez, J. J. C.; Gorte, R. J.; Fornasiero, P. Exceptional Activity for Methane Combustion over Modular Pd@CeO₂ Subunits on Functionalized Al₂O₃. *Science* **2012**, *337* (6095), 713–717. <https://doi.org/10.1126/science.1222887>.
- (9) Gomathi, A.; Vickers, S. M.; Gholami, R.; Alyani, M.; Man, R. W. Y.; MacLachlan, M. J.; Smith, K. J.; Wolf, M. O. Nanostructured Materials Prepared by Surface-Assisted Reduction: New Catalysts for Methane Oxidation. *ACS Applied Materials & Interfaces* **2015**, *7* (34), 19268–19273. <https://doi.org/10.1021/acsami.5b05189>.
- (10) Hoffmann, M.; Kreft, S.; Georgi, G.; Fulda, G.; Pohl, M.-M.; Seeburg, D.; Berger-Karin, C.; Kondratenko, E. V.; Wohlrab, S. Improved Catalytic Methane Combustion of Pd/CeO₂ Catalysts via Porous Glass Integration. *Applied Catalysis B: Environmental* **2015**, *179*, 313–320. <https://doi.org/10.1016/j.apcatb.2015.05.028>.
- (11) Guo, T.; Du, J.; Wu, J.; Li, J. Palladium Catalyst Supported on Stair-like Microstructural CeO₂ Provides Enhanced Activity and Stability for Low-Concentration Methane Oxidation. *Applied Catalysis A: General* **2016**, *524*, 237–242. <https://doi.org/10.1016/j.apcata.2016.06.040>.

- (12) Wang, N.; Li, S.; Zong, Y.; Yao, Q. Sintering Inhibition of Flame-Made Pd/CeO₂ Nanocatalyst for Low-Temperature Methane Combustion. *Journal of Aerosol Science* **2017**, *105*, 64–72. <https://doi.org/10.1016/j.jaerosci.2016.11.017>.
- (13) Danielis, M.; Colussi, S.; de Leitenburg, C.; Soler, L.; Llorca, J.; Trovarelli, A. Outstanding Methane Oxidation Performance of Palladium-Embedded Ceria Catalysts Prepared by a One-Step Dry Ball-Milling Method. *Angewandte Chemie International Edition* **2018**, *57* (32), 10212–10216. <https://doi.org/10.1002/anie.201805929>.
- (14) Khader, M.; Al-Marri, M.; Ali, S.; Abdelmoneim, A. Active and Stable Methane Oxidation Nano-Catalyst with Highly-Ionized Palladium Species Prepared by Solution Combustion Synthesis. *Catalysts* **2018**, *8* (2), 66. <https://doi.org/10.3390/catal8020066>.
- (15) Lott, P.; Dolcet, P.; Casapu, M.; Grunwaldt, J.-D.; Deutschmann, O. The Effect of Prereduction on the Performance of Pd/Al₂O₃ and Pd/CeO₂ Catalysts during Methane Oxidation. *Industrial & Engineering Chemistry Research* **2019**, *58* (28), 12561–12570. <https://doi.org/10.1021/acs.iecr.9b01267>.
- (16) Roy, S.; Hegde, M. S. Pd Ion Substituted CeO₂: A Superior de-NO_x Catalyst to Pt or Rh Metal Ion Doped Ceria. *Catalysis Communications* **2008**, *9* (5), 811–815. <https://doi.org/10.1016/j.catcom.2007.09.019>.
- (17) Cargnello, M.; Montini, T.; Polizzi, S.; Wieder, N. L.; Gorte, R. J.; Graziani, M.; Fornasiero, P. Novel Embedded Pd@CeO₂ Catalysts: A Way to Active and Stable Catalysts. *Dalton Trans.* **2010**, *39* (8), 2122–2127. <https://doi.org/10.1039/B916035C>.
- (18) Misch, L. M.; Kurzman, J. A.; Derk, A. R.; Kim, Y.-I.; Seshadri, R.; Metiu, H.; McFarland, E. W.; Stucky, G. D. C–H Bond Activation by Pd-Substituted CeO₂: Substituted Ions versus Reduced Species. *Chemistry of Materials* **2011**, *23* (24), 5432–5439. <https://doi.org/10.1021/cm202709y>.
- (19) Gulyaev, R. V.; Stadnichenko, A. I.; Slavinskaya, E. M.; Ivanova, A. S.; Koscheev, S. V.; Boronin, A. I. In Situ Preparation and Investigation of Pd/CeO₂ Catalysts for the Low-Temperature Oxidation of CO. *Applied Catalysis A: General* **2012**, *439–440*, 41–50. <https://doi.org/10.1016/j.apcata.2012.06.045>.
- (20) Hu, Z.; Liu, X.; Meng, D.; Guo, Y.; Guo, Y.; Lu, G. Effect of Ceria Crystal Plane on the Physicochemical and Catalytic Properties of Pd/Ceria for CO and Propane Oxidation. *ACS Catalysis* **2016**, *6* (4), 2265–2279. <https://doi.org/10.1021/acscatal.5b02617>.
- (21) Si, G.; Yu, J.; Xiao, X.; Guo, X.; Huang, H.; Mao, D.; Lu, G. Boundary Role of Nano-Pd Catalyst Supported on Ceria and the Approach of Promoting the Boundary Effect. *Molecular Catalysis* **2018**, *444*, 1–9. <https://doi.org/10.1016/j.mcat.2017.10.025>.
- (22) Mayernick, A. D.; Janik, M. J. Methane Oxidation on Pd–Ceria: A DFT Study of the Mechanism over Pd_xCe_{1-x}O₂, Pd, and PdO. *Journal of Catalysis* **2011**, *278* (1), 16–25. <https://doi.org/10.1016/j.jcat.2010.11.006>.
- (23) Gulyaev, R. V.; Kardash, T. Yu.; Malykhin, S. E.; Stonkus, O. A.; Ivanova, A. S.; Boronin, A. I. The Local Structure of Pd_xCe_{1-x}O_{2-xδ} Solid Solutions. *Phys. Chem. Chem. Phys.* **2014**, *16* (26), 13523–13539. <https://doi.org/10.1039/C4CP01033G>.
- (24) Senftle, T. P.; van Duin, A. C. T.; Janik, M. J. Role of Site Stability in Methane Activation on Pd_xCe_{1-x}O_δ Surfaces. *ACS Catalysis* **2015**, *5* (10), 6187–6199. <https://doi.org/10.1021/acscatal.5b00741>.

- (25) Senftle, T. P.; van Duin, A. C. T.; Janik, M. J. Methane Activation at the Pd/CeO₂ Interface. *ACS Catalysis* **2017**, *7* (1), 327–332. <https://doi.org/10.1021/acscatal.6b02447>.
- (26) Su, Y.-Q.; Filot, I. A. W.; Liu, J.-X. Stable Pd-Doped Ceria Structures for CH₄ Activation and CO Oxidation. *ACS Catalysis* **2018**, *8* (1), 75–80. <https://doi.org/10.1021/acscatal.7b03295>.
- (27) Palomino, R. M.; Hamlyn, R.; Liu, Z.; Grinter, D. C.; Waluyo, I.; Rodriguez, J. A.; Senanayake, S. D. Interfaces in Heterogeneous Catalytic Reactions: Ambient Pressure XPS as a Tool to Unravel Surface Chemistry. *Journal of Electron Spectroscopy and Related Phenomena* **2017**, *221*, 28–43. <https://doi.org/10.1016/j.elspec.2017.04.006>.
- (28) Anderson, R. B. Kinetics of Catalytic Reactions. In *Experimental Methods in Catalytic Research*; Anderson, R. B., Ed.; Academic Press, 1968; Vol. 15, pp 1–43. <https://doi.org/10.1016/B978-0-12-058650-9.50006-2>.
- (29) Willis, J. J.; Gallo, A.; Sokaras, D.; Aljama, H.; Nowak, S. H.; Goodman, E. D.; Wu, L.; Tassone, C. J.; Jaramillo, T. F.; Abild-Pedersen, F.; et al. Systematic Structure–Property Relationship Studies in Palladium-Catalyzed Methane Complete Combustion. *ACS Catalysis* **2017**, *7* (11), 7810–7821. <https://doi.org/10.1021/acscatal.7b02414>.
- (30) Toso, A.; Colussi, S.; Padigapaty, S.; de Leitenburg, C.; Trovarelli, A. High Stability and Activity of Solution Combustion Synthesized Pd-Based Catalysts for Methane Combustion in Presence of Water. *Applied Catalysis B: Environmental* **2018**, *230*, 237–245. <https://doi.org/10.1016/j.apcatb.2018.02.049>.
- (31) Šepelák, V.; Bégin-Colin, S.; Le Caër, G. Transformations in Oxides Induced by High-Energy Ball-Milling. *Dalton Transactions* **2012**, *41* (39), 11927. <https://doi.org/10.1039/c2dt30349c>.
- (32) Furlani, E.; Aneggi, E.; de Leitenburg, C.; Maschio, S. High Energy Ball Milling of Titania and Titania–Ceria Powder Mixtures. *Powder Technology* **2014**, *254*, 591–596. <https://doi.org/10.1016/j.powtec.2014.01.075>.
- (33) Danielis, M.; Colussi, S.; de Leitenburg, C.; Soler, L.; Llorca, J.; Trovarelli, A. The Effect of Milling Parameters on the Mechanochemical Synthesis of Pd–CeO₂ Methane Oxidation Catalysts. *Catal. Sci. Technol.* **2019**, *9* (16), 4232–4238. <https://doi.org/10.1039/C9CY01098J>.
- (34) Gholami, R.; Alyani, M.; Smith, K. Deactivation of Pd Catalysts by Water during Low Temperature Methane Oxidation Relevant to Natural Gas Vehicle Converters. *Catalysts* **2015**, *5* (2), 561–594. <https://doi.org/10.3390/catal5020561>.
- (35) Colussi, S.; Trovarelli, A.; Vesselli, E.; Baraldi, A.; Comelli, G.; Groppi, G.; Llorca, J. Structure and Morphology of Pd/Al₂O₃ and Pd/CeO₂/Al₂O₃ Combustion Catalysts in Pd–PdO Transformation Hysteresis. *Applied Catalysis A: General* **2010**, *390* (1–2), 1–10. <https://doi.org/10.1016/j.apcata.2010.09.033>.
- (36) Ferrer, V.; Moronta, A.; Sanchez, J.; Solano, R.; Bernal, S.; Finol, D. Effect of the Reduction Temperature on the Catalytic Activity of Pd-Supported Catalysts. *Catalysis Today* **2005**, *6*.
- (37) Lieske, H.; Voelter, J. Palladium Redispersion by Spreading of Palladium(II) Oxide in Oxygen Treated Palladium/Alumina. *The Journal of Physical Chemistry* **1985**, *89* (10), 1841–1842. <https://doi.org/10.1021/j100256a001>.

- (38) Seshu Babu, N.; Lingaiah, N.; Gopinath, R.; Reddy, P. S. S.; Prasad, P. S. S. Characterization and Reactivity of Alumina-Supported Pd Catalysts for the Room-Temperature Hydrodechlorination of Chlorobenzene. *2007*, *111*, 6447–6453. <https://doi.org/0.1021/jp065866r>.
- (39) Buyanov, R. A.; Molchanov, V. V.; Boldyrev, V. V. Mechanochemical Activation as a Tool of Increasing Catalytic Activity. *Catalysis Today* **2009**, *144* (3–4), 212–218. <https://doi.org/10.1016/j.cattod.2009.02.042>.
- (40) McCarty, J. G. Kinetics of PdO Combustion Catalysis. *Catalysis Today* **1995**, *26* (3–4), 283–293. [https://doi.org/10.1016/0920-5861\(95\)00150-7](https://doi.org/10.1016/0920-5861(95)00150-7).
- (41) McBride, J. R.; Hass, K. C.; Weber, W. H. Resonance-Raman and Lattice-Dynamics Studies of Single-Crystal PdO. *Physical Review B* **1991**, *44* (10), 5016–5028. <https://doi.org/10.1103/PhysRevB.44.5016>.
- (42) Li, C.; Sakata, Y.; Arai, T.; Domen, K.; Maruya, K.; Onishi, T. Carbon Monoxide and Carbon Dioxide Adsorption on Cerium Oxide Studied by Fourier-Transform Infrared Spectroscopy. Part I.—Formation of Carbonate Species on Dehydroxylated CeO₂, at Room Temperature. *Journal of the Chemical Society, Faraday Transactions 1: Physical Chemistry in Condensed Phases* **1989**, *85* (4), 929. <https://doi.org/10.1039/f19898500929>.
- (43) Demoulin, O.; Navez, M.; Ruiz, P. Investigation of the Behaviour of a Pd/γ-Al₂O₃ Catalyst during Methane Combustion Reaction Using in Situ DRIFT Spectroscopy. *Applied Catalysis A: General* **2005**, *295* (1), 59–70. <https://doi.org/10.1016/j.apcata.2005.08.008>.
- (44) Li, Z.; Xu, G.; Hoflund, G. B. In Situ IR Studies on the Mechanism of Methane Oxidation over Pd/Al₂O₃ and Pd/Co₃O₄ Catalysts. *Fuel Processing Technology* **2003**, *84* (1–3), 1–11. [https://doi.org/10.1016/S0378-3820\(02\)00099-1](https://doi.org/10.1016/S0378-3820(02)00099-1).
- (45) Khivantsev, K.; Jaegers, N. R.; Koleva, I. Z.; Aleksandrov, H. A.; Kovarik, L.; Engelhard, M.; Gao, F.; Wang, Y.; Vayssilov, G. N.; Szanyi, J. Stabilization of Super Electrophilic Pd²⁺ Cations in Small-Pore SSZ-13 Zeolite. *J. Phys. Chem. C* **2020**, *124* (1), 309–321. <https://doi.org/10.1021/acs.jpcc.9b06760>.
- (46) Jbir, I.; Couble, J.; Khaddar-Zine, S.; Ksibi, Z.; Meunier, F.; Bianchi, D. Individual Heat of Adsorption of Adsorbed CO Species on Palladium and Pd–Sn Nanoparticles Supported on Al₂O₃ by Using Temperature-Programmed Adsorption Equilibrium Methods. *ACS Catalysis* **2016**, *6* (4), 2545–2558. <https://doi.org/10.1021/acscatal.5b02749>.
- (47) Stotz, H.; Maier, L.; Boubnov, A.; Gremminger, A. T.; Grunwaldt, J.-D.; Deutschmann, O. Surface Reaction Kinetics of Methane Oxidation over PdO. *Journal of Catalysis* **2019**, *370*, 152–175. <https://doi.org/10.1016/j.jcat.2018.12.007>.
- (48) Liu, Z.; Zhang, F.; Rui, N.; Li, X.; Lin, L.; Betancourt, L. E.; Su, D.; Xu, W.; Cen, J.; Attenkofer, K.; et al. Highly Active Ceria-Supported Ru Catalyst for the Dry Reforming of Methane: In Situ Identification of Ru^{δ+}–Ce³⁺ Interactions for Enhanced Conversion. *ACS Catalysis* **2019**, *9* (4), 3349–3359. <https://doi.org/10.1021/acscatal.8b05162>.
- (49) Bensalem, A.; Muller, J.-C.; Tessier, D.; Bozon-Verduraz, F. Spectroscopic Study of CO Adsorption on Palladium-Ceria Catalysts. *J. Chem. Soc., Faraday Trans.* **1996**, *92* (17), 3233–3237. <https://doi.org/10.1039/FT9969203233>.

- (50) Danielis, M.; Colussi, S.; de Leitenburg, C.; Trovarelli, A. The Role of Palladium Salt Precursors in Pd-PdO/CeO₂ Catalysts Prepared by Dry Milling for Methane Oxidation. *Catalysis Communications* **2020**, *135*, 105899. <https://doi.org/10.1016/j.catcom.2019.105899>.
- (51) Persson, K.; Pfefferle, L. D.; Schwartz, W.; Ersson, A.; Järås, S. G. Stability of Palladium-Based Catalysts during Catalytic Combustion of Methane: The Influence of Water. *Applied Catalysis B: Environmental* **2007**, *74* (3–4), 242–250. <https://doi.org/10.1016/j.apcatb.2007.02.015>.
- (52) Schwartz, W. R.; Ciuparu, D.; Pfefferle, L. D. Combustion of Methane over Palladium-Based Catalysts: Catalytic Deactivation and Role of the Support. *The Journal of Physical Chemistry C* **2012**, *116* (15), 8587–8593. <https://doi.org/10.1021/jp212236e>.
- (53) Alyani, M.; Smith, K. J. Kinetic Analysis of the Inhibition of CH₄ Oxidation by H₂O on PdO/Al₂O₃ and CeO₂/PdO/Al₂O₃ Catalysts. *Industrial & Engineering Chemistry Research* **2016**, *55* (30), 8309–8318. <https://doi.org/10.1021/acs.iecr.6b01881>.
- (54) Huang, W.; Goodman, E. D.; Losch, P.; Cargnello, M. Deconvoluting Transient Water Effects on the Activity of Pd Methane Combustion Catalysts. *Industrial & Engineering Chemistry Research* **2018**, *57* (31), 10261–10268. <https://doi.org/10.1021/acs.iecr.8b01915>.
- (55) Su, Y.-Q.; Liu, J.-X.; Filot, I. A. W.; Zhang, L.; Hensen, E. J. M. Highly Active and Stable CH₄ Oxidation by Substitution of Ce⁴⁺ by Two Pd²⁺ Ions in CeO₂ (111). *ACS Catalysis* **2018**, *8* (7), 6552–6559. <https://doi.org/10.1021/acscatal.8b01477>.
- (56) Kinnunen, N. M.; Hirvi, J. T.; Suvanto, M.; Pakkanen, T. A. Role of the Interface between Pd and PdO in Methane Dissociation. *The Journal of Physical Chemistry C* **2011**, *115* (39), 19197–19202. <https://doi.org/10.1021/jp204360c>.
- (57) Hellman, A.; Resta, A.; Martin, N. M.; Gustafson, J.; Trincherro, A.; Carlsson, P.-A.; Balmes, O.; Felici, R.; van Rijn, R.; Frenken, J. W. M.; et al. The Active Phase of Palladium during Methane Oxidation. *J. Phys. Chem. Lett.* **2012**, *3* (6), 678–682. <https://doi.org/10.1021/jz300069s>.
- (58) Chin, Y.-H. (Cathy); Buda, C.; Neurock, M.; Iglesia, E. Consequences of Metal–Oxide Interconversion for C–H Bond Activation during CH₄ Reactions on Pd Catalysts. *Journal of the American Chemical Society* **2013**, *135* (41), 15425–15442. <https://doi.org/10.1021/ja405004m>.
- (59) Martin, N. M.; Van den Bossche, M.; Hellman, A.; Grönbeck, H.; Hakanoglu, C.; Gustafson, J.; Blomberg, S.; Johansson, N.; Liu, Z.; Axnanda, S.; et al. Intrinsic Ligand Effect Governing the Catalytic Activity of Pd Oxide Thin Films. *ACS Catalysis* **2014**, *4* (10), 3330–3334. <https://doi.org/10.1021/cs5010163>.

7 Preliminary Study of the Methane Activation Performance of Pd/CeO₂ Milled Catalysts in Dry Reforming of Methane

Abstract

In this chapter synergistic interaction at the Pd-Ce interface on a 4 wt%Pd/CeO₂ sample prepared by dry mechano-chemical synthesis is reported, leading to rapid catalytic turnover in the dry reforming of methane (DRM: CH₄ + CO₂ → 2CO + 2H₂) where the activation of the C-H bond is the most limiting step. Mechanical mixing of Palladium acetate nanoparticles with polycrystalline CeO₂ powder (4PdAcCeM) yielded an active arrangement of the Pd-O-Ce interface highly active for DRM, with Pd-based formulations being effective in methane activation and CeO₂ support promoting the dispersion and the Pd-Ce interfacial interaction. The milled sample exhibited a remarkable activity, greatly surpassing that of 4 wt.%Pd/CeO₂ synthesized using the conventional incipient wetness method (4PdCeIW) on activity tests carried out in a bed-flow reactor setup. These drastic changes were traced to the unique Pd-CeO₂ interface that is promoted during milling. The catalyst structural integrity and chemical state evolution during reaction were probed via *in-situ* characterization techniques. The surface chemistry and electronic distribution were monitored by *in-situ* ambient-pressure X-ray photoelectron spectroscopy (AP-XPS) and X-ray absorption spectroscopy (XAS) measurements, while the reaction was closely followed by *in-situ* XRD to examine the structural evolution of the catalyst. A combined *in-situ* approach was the key to unravel how Pd-Ce interfacial interactions ultimately play a role in the overall activity and stability of the catalyst.

7.1 Introduction

Converting or activating methane efficiently is essential for the profitable use of abundant natural gas resources along with the reduction of greenhouse gas emissions.¹ Traditional fuel sources for energy production, such as oil and coal, are finite resources that have been heavily consumed in the latest decades due to rapid development processes, exponential increase in world population and higher life expectancy.² The Dry Reforming of Methane (DRM, $\text{CH}_4 + \text{CO}_2 \rightleftharpoons 2\text{H}_2 + 2\text{CO}$; $\Delta H_{298} = 246 \text{ kJ/mol}$) is a promising pathway for syngas (H_2/CO) production at a ratio of almost unity, exploiting methane from natural gas, a cheap and abundant fuel stock, and offering simultaneous removal of CO_2 . Syngas production through DRM becomes even more relevant when coupled with the selective long-chain hydrocarbon synthesis via the Fisher-Tropsch reaction, converting syngas into upgraded chemicals.^{3,4} However, the dry reforming of methane is thermodynamically hindered by the stable nature of methane (C-H bond energy: 104 kcal/mol) as well as by the activation of CO_2 , a poor source of O to the C-H bond activation process. Therefore, initiating this reaction requires a catalyst that is not only very effective in activating those molecules, but also able to withstand the high temperatures involved while maintaining high thermal stability.⁵

DRM has been investigated on numerous supported metal catalysts, amongst which both noble (Rh, Ru, Pd, Pt and Ir) and non-noble (Ni and Co) metals are found.^{6,7} Although the non-noble metals are attractive due to their cost effectiveness, they deactivate on account of either carbon formation or sintering,⁸ which are exacerbated by the high temperatures involved in the reaction. Supported noble metal catalysts exhibited improved performances and higher resistance to coke formation,^{7,9} offering great stability due to their metal-support interaction. The anchoring of an active metal onto high-surface-area oxides represents a promising approach for the preparation of active DRM catalysts, creating a metal-support interface and tuning the electronic and chemical properties of the metal catalyst.¹⁰ Among many support oxides, CeO_2 is a promising material with stable sites for the incorporation of Pd nanoparticles.¹¹⁻¹³ Ceria redox chemistry has been extensively evaluated under a reducing environment, where several studies have identified the inclusion of hydrogen into the fluorite lattice.¹⁴⁻¹⁶ On the other hand, the presence of noble metal nanoparticles greatly influences the redox chemistry of ceria, as in a reducing atmosphere it has been demonstrated to result in the removal of oxygen and formation of oxygen vacancies, simultaneously reducing Ce^{4+} ions present in the fluorite lattice.¹⁷

The barriers associated to the two slowest reaction steps for methane dissociation, $\text{CH}_4 \rightarrow \text{CH}_3 + \text{H}$ and $\text{CH} \rightarrow \text{C} + \text{H}$, have been previously studied using density functional theory methods on Pd substrates. Nano-structuring of Pd notably increased the order of reactivity, $\text{Pd}(111) \leq \text{Pd}(211) < \text{Pd}_{140} < \text{Pd}_{79}$, where low coordinated metal atoms showed higher reactivity.¹⁸ Pd-Ceria interaction promotes a similar arrangement, enhancing interfacial interactions and facilitating CH_4 activation,^{19,20} making Pd/CeO₂ a promising material for DRM. By DFT calculations, it has been shown that methane activation is highly dependent on the PdO_x/CeO₂ interface arising from the CeO₂ lattice, which provides a coordination environment for the Pd^{δ+} species facilitating Pd²⁺ and Pd⁴⁺ oxidation states, thereby highly reducible sites for methane activation.²¹ Previous work from our group showed how the incorporation of Pd atoms in the CeO₂ lattice *via* solution combustion synthesis (SCS) results in a remarkable improvement of methane oxidation rates compared to Pd/CeO₂ catalysts prepared by incipient wetness impregnation (IW)^{20,22,23} and in an outstanding resistance to steam deactivation.²⁴

It has been suggested that CeO₂ is able to promote the oxidation of Pd, serving as the active phase for catalytic oxidation reactions through metal support interactions.^{25,26} The dynamic surface state of Pd⁴⁺ sites can be tuned by the methodology used to incorporate the metal onto the CeO₂ lattice, producing an active arrangement highly active for methane activation. In the previous chapter (Chapter 6) a synergistic interaction at the Pd/CeO₂ interface of a mechanically mixed sample was reported, leading to rapid catalytic turnover at low temperatures. Highly active PdO_x species, embedded into CeO₂ surface layers, created highly reactive and stable sites for the methane oxidation reaction, lowering light-off temperatures and accelerating reaction rate.

In this work we explore the performance of Pd/CeO₂ catalysts prepared by mechanical milling and incipient wetness impregnation for the dry reforming of methane, highlighting the importance of metal-oxide interactions in DRM. The detailed dynamic evolution of the catalysts bulk and surface properties was probed by a combination of *in-situ* analyses, which already proved to be excellent tools to unravel the active sites on M-CeO₂ catalysts.^{27,28}

7.2 Experimental

A series of 4 wt%Pd/CeO₂ samples were prepared by dry mechano-chemical synthesis (M) and incipient wetness impregnation (IW). A commercial ceria with high surface area was used as support oxide after calcination at 1173 K for 3 hours in static air, with a final surface

area of 25 m²/g. Milled samples were prepared following the mild milling synthesis reported in the previous chapters using Pd(OAc)₂ and PdO nanoparticles as palladium precursors, representing the best (4PdAcCeM) and worst (4PdOCeM) surface Pd-Ce interaction, as observed in previous chapters (Chapters 3 and 6). In detail, 84.4 mg of Palladium acetate (Sigma-Aldrich, 99.9%) or 46.0 mg of PdO nanoparticles (Sigma-Aldrich) were milled with 960 mg of CeO₂(1173) in a Pulverisette 23 mini-mill operating at 15 Hz for 20 or 10 minutes, respectively. To provide a blank comparison for the support oxide, 1 g of ceria was milled in the same setup for 15 minutes and the sample is denoted as CeO₂-M. A reference Pd/CeO₂ sample was prepared by incipient wetness impregnation using an appropriate amount of commercial palladium nitrate solution (Sigma-Aldrich, 99.999%) to reach a final Pd loading of 4 wt%. After complete wetting, the powders were dried at 373 K overnight and then calcined at 1173 K for 3 hours in static air. Further details on the synthesis methods are reported in Chapter 2, section 2.1.

Activity tests for the DRM reaction were performed on the as-prepared samples at the Chemistry Department at Brookhaven National Laboratory, Upton (NY). CH₄-TPR tests were performed in order to evaluate the reactivity of prepared samples towards methane only. The surface chemistry was monitored by *in-situ* ambient-pressure X-ray photoelectron spectroscopy (AP-XPS), the structural evolution of the catalysts was followed by *in-situ* XRD and the electronic distribution was probed by XAS measurements. HR-TEM was carried out at Universitat Politècnica de Catalunya to evaluate the morphological evolution of catalysts before, during and after reaction. Details on the experimental techniques for characterization and catalytic activity evaluation are reported in full in Chapter 2, in sections 2.2 and 2.3 respectively.

Briefly, DRM activity tests were performed on 10 mg of powder catalysts diluted by ~10 mg of pre-calcined quartz (1173 K, 400-800 μm), loaded into a quartz tube and mounted on a bed-flow system. The gas ratio of CH₄ and CO₂ was set at 1:1 (10 ml/min CH₄ with 10 ml/min CO₂) and diluted with N₂ (10 ml/min), for a final weight hourly space velocity (WHSV) of ca. 180'000 ml/(g_{cat} h). Prior to the reaction, the catalysts were reduced under a 50%H₂/N₂ atmosphere (20 ml/min) at 673 K for 1 hour. The DRM activity was measured at 673 K, 773 K, 873 K and 973 K with 1 h of isothermal at each step.

Quantitative CH₄-TPR experiments were carried out in a lab-scale reactor setup at the Heterogeneous Catalysis Lab in Udine on 60 mg of sample loaded in a quartz tubular reactor (6mm ID) on a quartz wool bed. A 25%CH₄/He gas flow was introduced at 180 ml/min (GHSV≈360'000 h⁻¹) and the temperature was increased from RT to 973 K at 5 K/min. CH₄ concentration was monitored every 10 s with an in-line ABB Uras 14 IR gas analyzer.

A commercial SPECS AP-XPS chamber equipped with a PHOIBOS 150 EP MCD-9 analyzer at the Chemistry Division of Brookhaven National Laboratory (BNL), Upton (NY), was used for XPS analysis.²⁹ For CH₄ TPR, a 20 mTorr amount of O₂ was used to pretreat the sample at 673 K for 1 h before adding 10 mTorr of CH₄ into the reaction chamber through a high-precision leak valve. For DRM, the sample was pretreated in 10 mTorr of H₂ at 673 K for 1 h before introduction of a mixture of 10 mTorr of CH₄ and 10 mTorr of CO₂. O 1s, Ce 3d, and C 1s + Pd 3d XPS regions were collected from 300 K to 773 K under the reaction gas environment.

Time-resolved XRD measurements were performed at beamline 17 BM ($\lambda = 0.24169 \text{ \AA}$) at the Advanced Photon Source (APS), Argonne (IL), using a Clausen cell flow reactor.³⁰ In DRM tests, a 10 ml/min flow rate of 50%H₂/He was first used to pretreat the catalyst at 673 K for 30 min. The gas line was subsequently purged by helium at room temperature before introducing a 10 ml/min flow of a gas mixture containing 25% CO₂, 25% CH₄, and 50% He for a 1:1 CO₂/CH₄ molar ratio. The samples were stepwise heated to 673 K, 773 K, 873 K and 973 K at a 10 K/min ramping rate, with a soaking time of 30 minutes for each isothermal step. CH₄-TPR experiments were performed on as-prepared samples by introducing a 50%CH₄/He mixture (10 ml/min) and gradually heating the sample to 973 K at a 5 K /min heating rate.

In-situ X-ray absorption fine structure (XAFS) measurements of 4Pd/CeO₂ catalysts were performed at 8-ID (ISS) beamline at National Synchrotron Light Source II (NSLS-II), Brookhaven National Laboratory, Upton (NY). In methane activation (CH₄-TPR) experiments the catalyst was ramped at a 10 K/min heating rate to 973 K under a 25%CH₄/He flow (20 ml/min). For DRM, the same procedure as *in-situ* XRD measurements was used. The Pd K-edge data were collected in fluorescence yield mode using a passivated implanted planar silicon (PIPS) detector. Data processing was performed using the IFEFFIT package.³¹ Pd foil was used as standard references for XAFS fitting.

7.3 Results and Discussion

7.3.1 DRM Catalytic Activity

The catalytic performance for the DRM reaction of the as-prepared 4 wt.%Pd/CeO₂ catalysts was evaluated in the temperature range of 673 K to 973 K under a space velocity of 180,000 ml/(g_{cat}·h). As shown in Figure 7.1, at 973 K the milled 4PdAcCeM sample exhibited similar CH₄ conversion as 4PdCeIW, while 4PdOCeM and the bare ceria support showed negligible activity under the same reaction conditions. Nonetheless, it can be noted that all milled samples are characterized by a higher CO₂/CH₄ conversion ratio than PdCeO₂ IW, especially relevant for 4PdAcCeM. Concurrently, from selectivity results (Figure 7.2) it can be observed that at 973 K 4PdAcCeM exhibited higher H₂ production (260 μmol/(g_{cat}·s)) compared to the impregnated catalyst (154 μmol/(g_{cat}·s)), along with increased CO rate and lower H₂O production.

These differences might be ascribed to different side reactions taking place on the two samples. In general, the deposition of Pd nanoparticles on the surface of CeO₂ creates oxygen vacancies leading to stronger anchoring sites for Pd nanoparticles while increasing Pd-dispersion simultaneously. As it interacts with Pd nanoparticles, methane dissociates into hydrogen and carbon, which is then oxidized by the oxygen species provided by CeO₂ in contact with the Pd nanoparticles, producing CO as a main product. However, the carbon that is produced may participate in CO formation by dissociative adsorption of CO₂, thus starting the DRM reaction. At increased temperatures, the production of hydrogen by methane dissociation leads to a reducing environment, facilitating CO₂ dissociation and increasing CO₂ conversions. Moreover, H₂/CO conversion decreases due to the competing reverse water gas shift (RWGS) reaction, which was observed to be prominent on 4PdCeIW. On the other hand, 4PdAcCeM showed a greater conversion for CO₂, possibly ascribed to the simultaneous removal during reaction of deposited carbon ($C + O \rightarrow CO$) by CeO₂ surface oxygen species and CO₂ decomposition ($CO_2 + C \rightleftharpoons 2CO$).

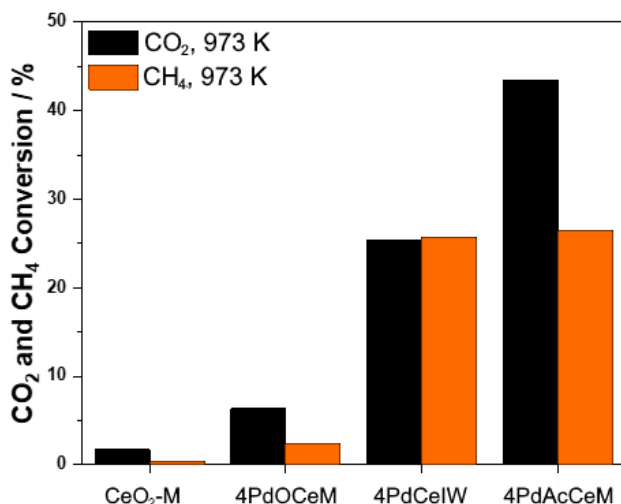


Figure 7.1: CO₂ and CH₄ conversion measured during DRM reaction at 973 K over 4wt.%Pd/CeO₂ samples and bare CeO₂-M support.

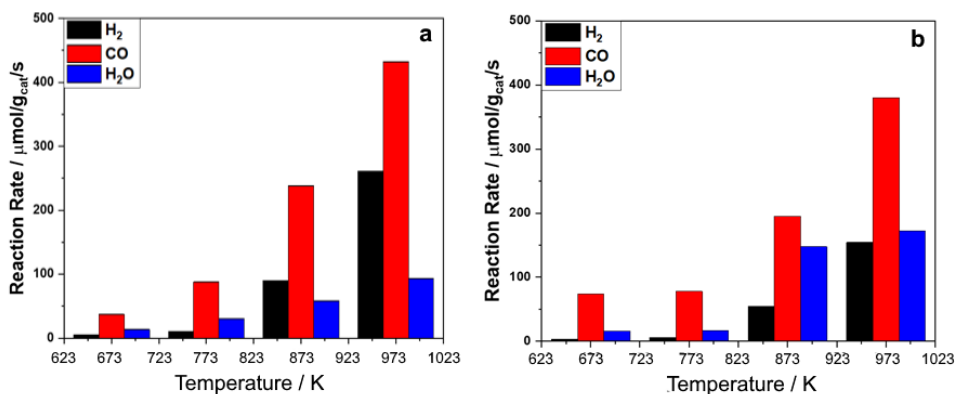


Figure 7.2: Comparison of the measured H₂, CO and H₂O reaction rates during DRM reaction over 4PdAcCeM (a) and 4PdCeIW (b).

To understand the underlying motivations for the observed differences in catalytic behavior, structural features of the bulk phase and surface properties were analyzed during the DRM reaction and activation of pure methane (Section 7.3.2) and after prolonged exposure to reaction conditions (Section 7.3.3). In fact, catalyst deactivation by carbon deposition was indicated as the main drawback for the DRM reaction,^{6,8,32} greatly hindering the overall performance.

7.3.2 *In-situ* Methane Activation

Methane activation is the most limiting step in dry reforming. During reaction, the catalyst undergoes chemical and structural changes and *in-situ* techniques can be used to understand the interplay between Pd and CeO₂ and its effect on catalytic performance.⁷ The structural changes of the bulk phase and the reactivity of the surface states during activation of CH₄ were followed by *in-situ* time resolved XRD analysis and AP-XPS, respectively.

The time resolved XRD profiles corresponding to the 4PdAcCeM and 4PdCeIW under a reductive CH₄ atmosphere with a ramping temperature from 300 to 973 K are shown in Figure 7.3. The ceria fluorite-type crystal structure can be easily distinguished throughout the TPR experiment, as well as the presence of Pd phases, most notably around $2\theta = 6^\circ$. At around 750 K a drastic shift of the ceria peaks to lower 2θ is observed, corresponding to a sharp increase in the CeO₂ lattice parameter consistent with the partial reduction of ceria layers near the surface.

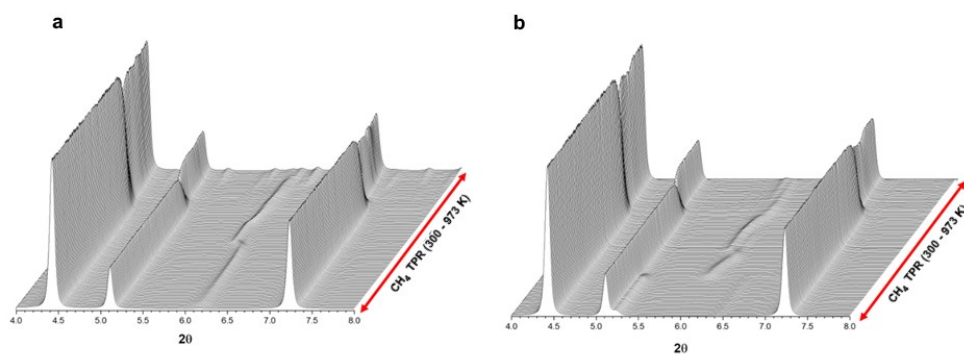


Figure 7.3: *In-situ* XRD profiles of 4PdAcCeM (a) and 4PdCeIW (b) samples in CH₄-TPR experiments.

The dynamic changes on the Pd peak can be appreciated in Figure 7.4, clearly exhibiting high reducibility as methane dissociates into carbon and hydrogen. From the highlighted Pd region on the diffraction peak, it can be observed that on the milled sample the precursor Pd(OAc)₂ salt is reduced already at room temperature and gradually increases its crystallinity as reaction progresses. On the impregnated sample PdO crystallites are reduced into metallic Pd at approximately 573 K. As the temperature increases, Pd undergoes further transformations as dissociated carbon is oxidized by the oxygen species provided by CeO₂ in contact with Pd nanoparticles, producing CO as a main product. On the milled 4PdAcCeM, a peculiar crystalline structure appears above 873 K, likely belonging to a

carbide-like structure and suggesting a higher amount of deposited carbon, i.e. higher CH₄ activation performance, on the milled sample compared to the 4PdCeIW catalyst. The additional crystalline phase can be well observed in the last spectra of the time resolved *in-situ* XRD profiles shown in Figure 7.5 for the milled catalyst (a) and the sample prepared by incipient wetness (b).

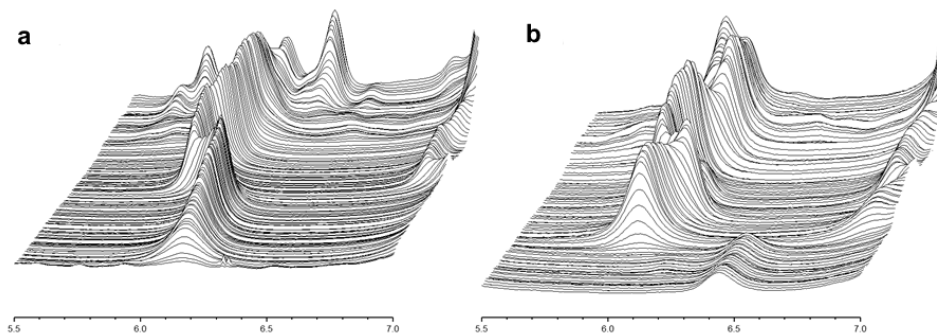


Figure 7.4: Zoomed *In-situ* XRD Pd (111) profile of 4PdAcCeM (a) and 4PdCeIW (b) samples in CH₄-TPR experiments.

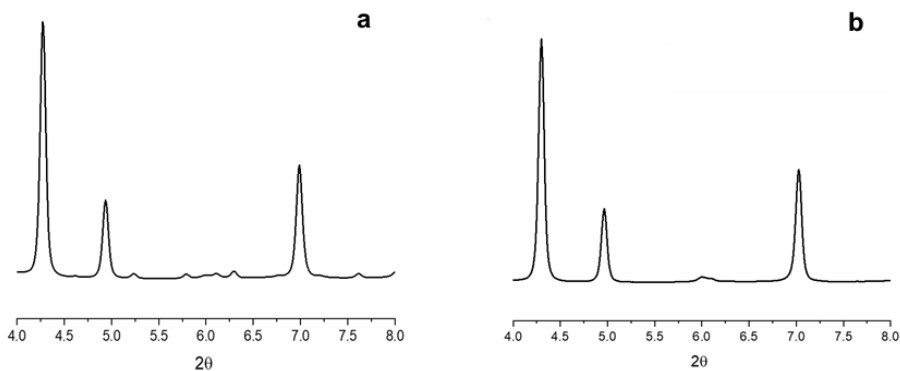


Figure 7.5: *In-situ* XRD profiles at 973 K of 4PdAcCeM (a) and 4PdCeIW (b) samples in a CH₄ atmosphere.

XRD under methane exposure were also taken for bare ceria and the milled 4PdOCeM sample (Figure 7.6(a) and (b), respectively), which showed virtually no changes in the CeO₂ or Pd crystal structure throughout the temperature ramp. For 4PdOCeM, the milling of PdO powder onto CeO₂ does not lead to a close interaction between Pd and CeO₂ (as reported in Chapter 3) consequently exhibiting very low catalytic activity and no significant change in the ceria lattice parameter, only exhibiting thermal lattice expansion and some ceria reduction at elevated temperatures, much alike bare ceria (Figure 7.6(a)).

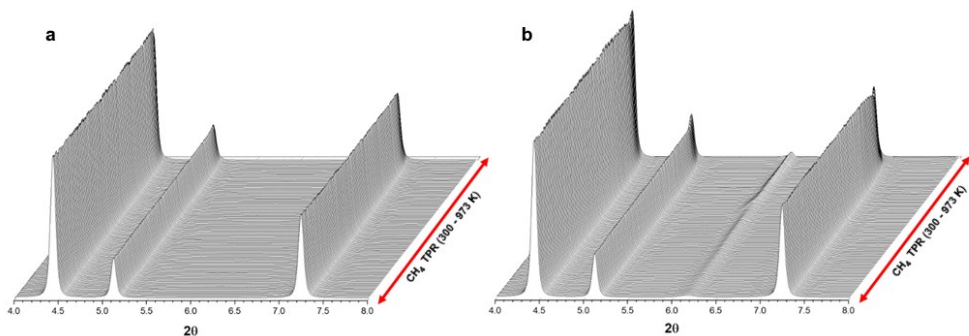


Figure 7.6: *In-situ* XRD profiles of CeO₂-M (a) and 4PdOCeM (b) samples in CH₄-TPR experiments.

Rietveld refinement of *in-situ* XRD spectra for methane TPR experiments shows that indeed ceria lattice parameter and crystallite size are strongly influenced by palladium content and Pd-support interaction (Figure 7.7). An abrupt transition at 723 K can be observed for 4PdAcCeM and 4PdCeIW, accompanied by Pd phase transformations (Figure 7.3 and Figure 7.4), suggesting that a stronger Pd-Ce interaction promotes ceria reduction resulting in a lower transition temperature to smaller crystallite size and higher lattice parameter. PdO nanoparticles in loose interaction with the support, as those observed on 4PdOCeM, induce changes to the ceria lattice only at higher temperatures (> 823 K).

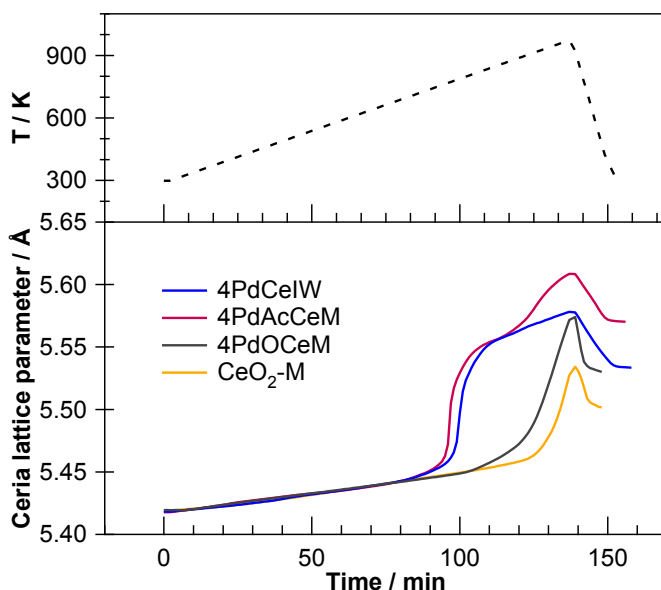


Figure 7.7: Ceria lattice parameter calculated by Rietveld refinement of the *in-situ* time resolved XRD spectra during CH₄-TPR experiments.

It is interesting to note that all samples exhibit a permanent lattice transformation after CH₄-TPR, displaying an increased lattice parameter of the ceria structure after cooling to RT. This is likely due to the surface reduction of Ce⁴⁺ ions to Ce³⁺, induced by methane activation, as well as a possible breaking down of the ceria crystallites to smaller particles. Among evaluated samples, 4PdAcCeM displays the most significant phase transformations compared to its initial state, and it was consequently investigated in more detail.

By semi-quantitative CH₄-TPR measurements (Figure 7.8) it is evident that the milled sample is able to activate a larger amount of methane compared to its IW counterpart, displaying a lower activation temperature and a significant CH₄ uptake increase at high temperatures (above 823 K), corresponding to the transition temperature observed for the additional crystalline phase formation observed in Figure 7.3 and Figure 7.4.

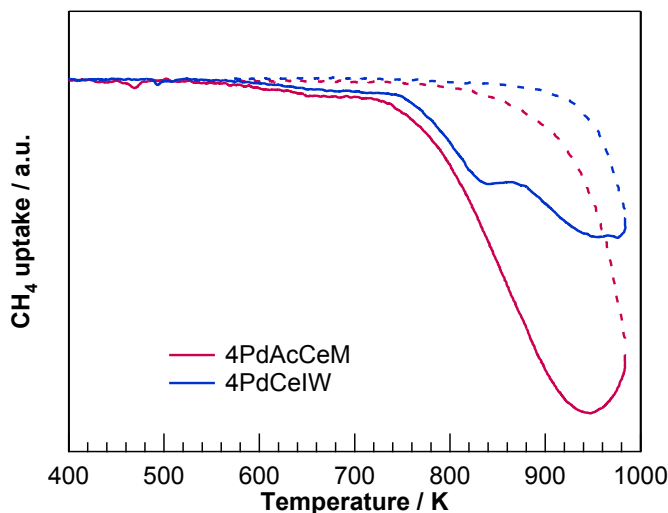


Figure 7.8: CH₄ uptake measurements under a 25%CH₄/He atmosphere at a GHSV \approx 400*000 h⁻¹. Solid line: heating; dashed line: cooling.

Evidence of the huge carbon deposition on 4PdAcCeM after CH₄-TPR was further provided by HRTEM analysis. Images collected on the spent sample are reported in Figure 7.9, displaying a large amount of carbon filaments among which catalysts particles can be observed. In HAADF-STEM images, ceria particles decorated with relatively large Pd nanoparticles (Figure 7.9(A)) can be identified, indicated by their brightness due their high Z number, along with bare CeO₂ particles and isolated Pd nanoparticles (Figure 7.9(B)), where the absence of ceria is corroborated by EDX analysis. Figure 7.9(C) shows a high resolution image of these isolated particles, measuring ca. 3 nm in size, dispersed in the

poorly-ordered carbon filaments. FT in the inset of Figure 7.9(C) indicates they are comprised by laminar structures separated by 3.6 Å, which is typical of poorly-ordered graphite. A low magnification image of these structures is shown in Figure 7.9(D), and the area in the black rectangle is displayed at higher magnification in Figure 7.9(E). In addition to well-defined ceria particles, extremely small ceria crystallites can be observed, such as the one isolated in the inset measuring only about 2 nm in size. The corresponding FT image results in a 3.3 Å and 2.8 Å measured spacing, slightly larger than the {111} and {200} planes of ceria, possibly indicating these particles are comprised by a different phase. Similar structures are observed in Figure 7.9(F), where nanoparticles exhibiting lattice fringes at 3.2 Å and 2.3 Å are identified, possibly related to a ceria or palladium carbide phase. The extremely small size of these nanoparticles hinders further characterization by HRTEM, nonetheless the presence of additional phases and a reduction of ceria crystallite size are in good agreement with the *in-situ* XRD observations.

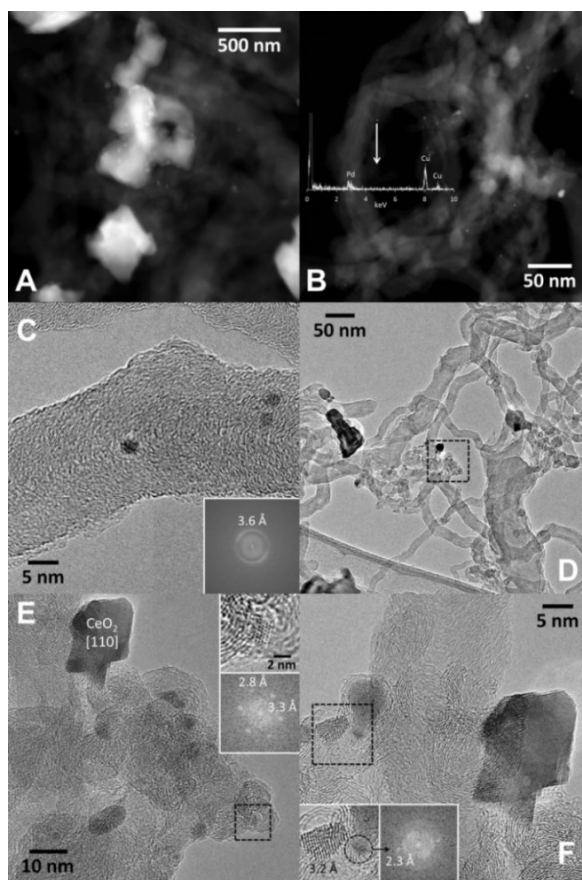


Figure 7.9: HAADF-STEM (A,B) and HRTEM images (C-F) of 4PdAcCeM after CH₄-TPR.

In-situ ambient-pressure XPS was used to evaluate the surface sensitive information for the chemical state and surface species in the presence of gas reactants. The gradual surface changes upon a 10 mTorr CH₄ atmosphere were monitored by AP-XPS on 4PdAcCeM and 4PdCeIW, collecting spectra in the Pd 3d and Ce 3d regions from RT to 673 K. Their evolution is displayed in Figure 7.10 and Figure 7.11, respectively.

The Pd 3d spectra show important differences already after pretreatment in O₂, with palladium found mainly as Pd²⁺ on the milled sample while 4PdCeIW exhibits a mixed Pd⁴⁺/Pd²⁺ arrangement. The higher Pd oxidation state of the impregnated catalyst reflects the results reported in Chapter 6. After removing O₂ and introducing 10 mTorr CH₄ in the chamber, 4PdAcCeM undergoes reduction already at 300 K, exhibiting a mixed Pd²⁺/Pd⁰ oxidation state up to 372 K (Figure 7.10(a)). Between 373 K and 473 K there is a clear reduction of the Pd oxide, with a peak shift of approximately 1.7 eV consistent with the full reduction to metallic Pd. On the conventional 4PdCeIW sample (Figure 7.10(b)), reduction of oxidized Pd^{4+/2+} begins at 373 K and is completed only at 773 K, suggesting a slower H-spillover effect, in agreement with the smaller amount of activated methane observed by CH₄-uptake experiments (Figure 7.8) and by the lower reactivity observed by *in-situ* XRD (Figure 7.3).

From the Ce 3d spectra in Figure 7.11, collected upon CH₄ exposure, on both samples the reduction of Pd oxides was accompanied by the removal of lattice oxygen in ceria, evidenced by a Ce⁴⁺ reduction to Ce³⁺ observed between 373 and 573 K, which progresses as the temperature increases all the way to 773 K. As bare ceria surface exhibits reduction only at temperatures higher than 573 K,³³ the lower surface reduction temperature can be attributed to Pd interaction with the CeO₂ support, promoting a H-spillover effect facilitated by metal-support interaction. The reduction of PdO followed by the removal of lattice oxygen in the oxide support was also confirmed by *in-situ* XRD-TPR (Figure 7.3). Unlike chemical states of surface Pd, Ce 3d spectra display minor differences between the milled and the wet-synthesized sample.

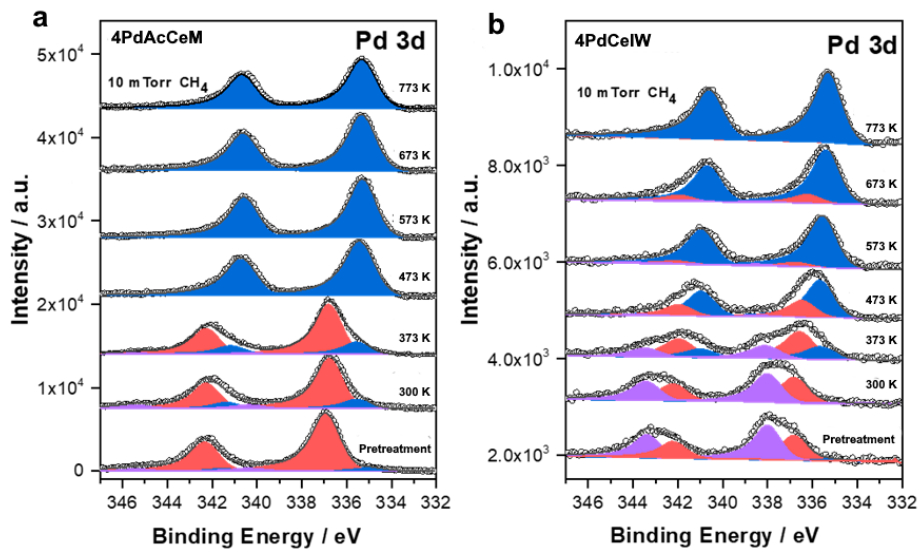


Figure 7.10: Pd 3d AP-XPS spectra of 4PdAcCeM (a) and 4PdCeIW (b) samples in a 10 mTorr CH_4 atmosphere, from 300 to 773 K.

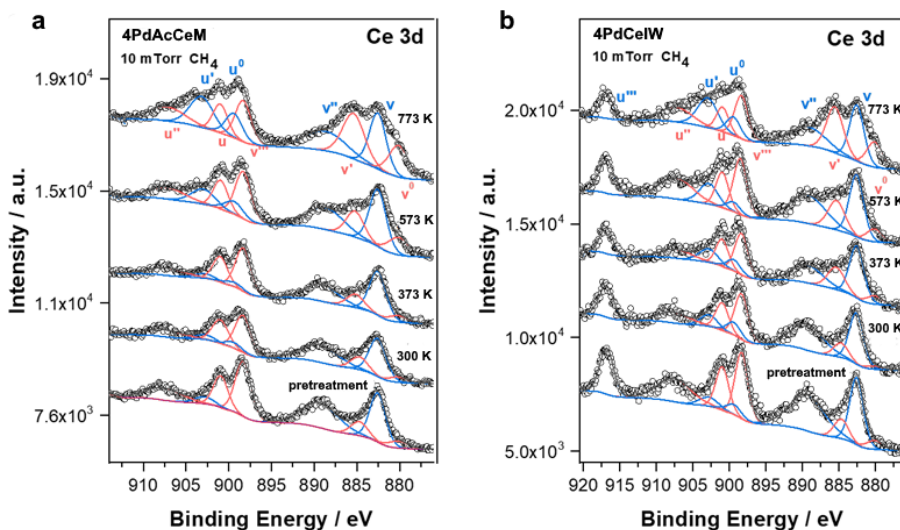


Figure 7.11: Ce 3d AP-XPS spectra of 4PdAcCeM (a) and 4PdCeIW (b) samples in a 10 mTorr CH_4 atmosphere, from 300 to 773 K.

Adding CO_2 in the feed generates additional O adatoms, with respect to O atoms provided by oxygen transfer from the ceria to the metal through metal-support interactions, thus facilitating the re-oxidation of surface carbon formed by methane. As a consequence, the catalysts display significant differences compared to CH_4 -only activation.

In-situ time resolved XRD analysis under DRM conditions (Figure 7.12) shows that on both samples palladium is reduced after treatment in H₂, forming crystalline Pd structures. On 4PdCeIW these Pd species remain stable after switching to the reactant gas (25% CH₄/25% CO₂/He), virtually undergoing no changes from 673 K to 973 K (Figure 7.12(b)) and indicating that metallic palladium was not oxidized by the CO₂ in the reactant stream. Conversely, 4PdAcCeM shows some structural transformations (possibly due to a slight oxidation) between 673 K and 773 K (see inset in Figure 7.12(a)), which is attributed to higher O-transfer capabilities in the catalyst ultimately responsible for the enhanced DRM conversion. Rietveld refinement of the *in-situ* XRD spectra shows that only thermal expansion occurs (Figure 7.13).

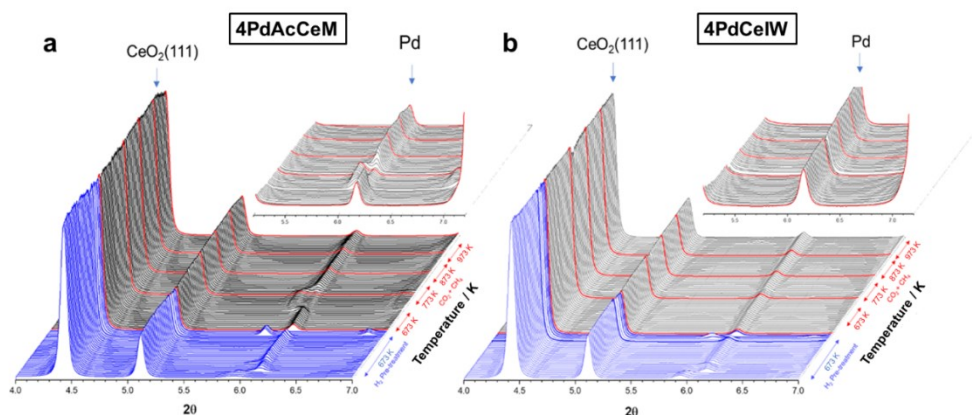


Figure 7.12: *In-situ* XRD profiles of 4PdAcCeM (a) and 4PdCeIW (b) in DRM conditions. Catalyst was pretreated under H₂ at 673 K for 30 min (blue lines) before switching the gas to a 25%CO₂/25%CH₄/50%He mixture at RT.

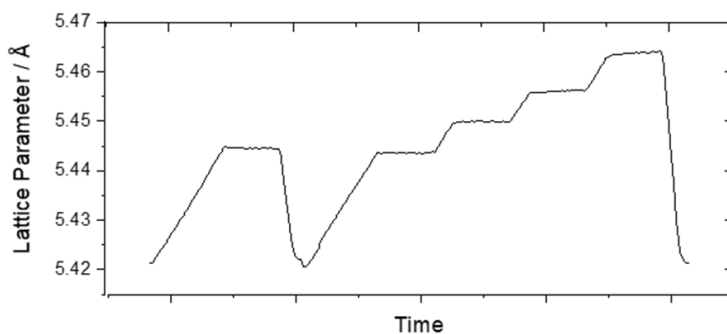


Figure 7.13: Representative Rietveld refinement of the ceria lattice parameter of 4PdCeIW under DRM conditions.

7.3.3 Catalyst Stability and Deactivation

The DRM reaction is strongly hindered by carbon deposition at high temperatures.⁸ Strategies have been developed to circumvent this issue by operating the reaction at lower temperatures or developing catalysts with a high resistance towards coking during DRM.^{6,32}

To evaluate the deactivation resistance of the prepared 4 wt.%Pd/CeO₂ samples, stability tests were performed by holding the samples at 973 K for 24 hours. From the conversion profiles reported in Figure 7.14 it can be seen how under prolonged exposure to DRM conditions the milled catalyst was able to retain its initial activity, whereas the impregnated sample exhibited a 10% reduction in CH₄ conversion. In agreement with the activity measurements reported in Figure 7.1, 4PdAcCeM shows higher CO₂ conversion, which remarkably further increases after 16 hours. The peculiar behavior exhibited by 4PdAcCeM suggests that its surface Pd-Ce interaction is not only able to resist deactivation but also undergoes some yet unexplained transformations during reaction, likely activating side reactions for additional CO₂ conversion.

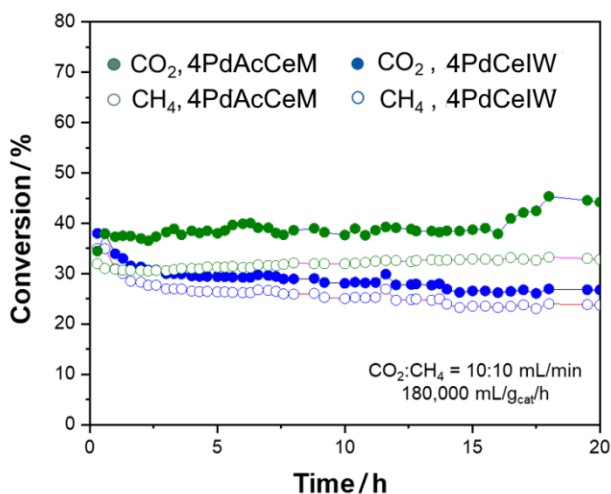


Figure 7.14: Catalytic stability test in DRM conditions for 24 h at 973 K on the 4PdAcCeM and 4PdCeIW samples.

For a preliminary investigation of the reasons behind the increased stability and CO₂ conversion of 4PdAcCeM compared to 4PdCeIW, the initial and final states of considered catalysts were studied by means of HRTEM and *in-situ* XAFS.

To evaluate their morphology before and during reaction, HRTEM was performed on samples after H₂ pretreatment at 673 K and after 3 h and 24 h in DRM isothermal conditions at 973 K. HRTEM images of 4PdAcCeM and 4PdCeIW after reduction in hydrogen are shown in Figure 7.15 and Figure 7.16, respectively. In Figure 7.15 large ceria particles are observed decorated by very well dispersed palladium nanoparticles. Irregular surfaces for the ceria can be easily distinguished, most likely obtained after the milling process, while their large size is a consequence of the elevated calcination temperature (1173 K). The support exhibits lattice fringes at 3.1 Å, which correspond to the {111} crystallographic planes of the ceria particles, while Pd nanoparticles exhibit lattice fringes at 2.2 Å and 1.9 Å corresponding to the {111} and {200} crystallographic planes of Pd metal, respectively. Pd nanoparticles exhibit an average particle sizes of ~ 5 nm and no amorphous Pd-Ce-O shell is distinguishable, as was reported in previous chapters after treatment in oxygen (Chapters 3 and 6).¹⁹

Figure 7.16 shows HRTEM images of the nanostructures obtained on the sample prepared by incipient wetness impregnation (4PdCeIW) after reduction in H₂. Lattice fringes at 3.1 Å correspond to the {111} crystallographic planes of the ceria support, while the fringes at 2.2 Å correspond to the {111} planes of Pd metal. The size of the Pd nanoparticles is about 2 nm, slightly smaller than in sample 4PdAcCeM. Pd metal particles are quite homogeneous in size and very well dispersed on ceria.

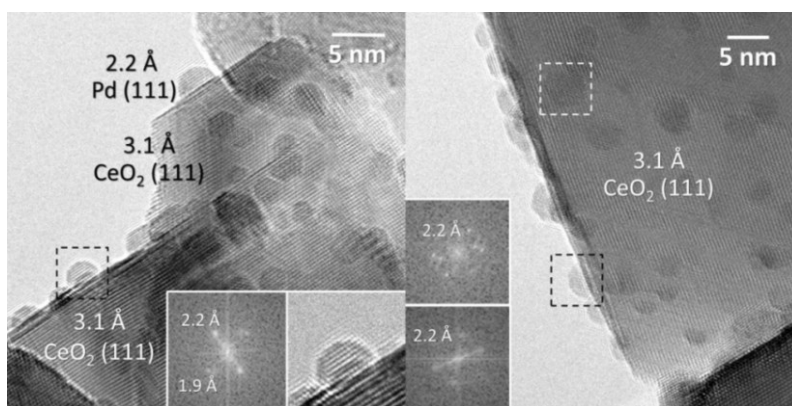


Figure 7.15: HRTEM images of 4PdAcCeM after H₂ reduction treatment at 673 K. Insets show the Fourier Transform corresponding to the respective image inside the rectangle under high magnification.

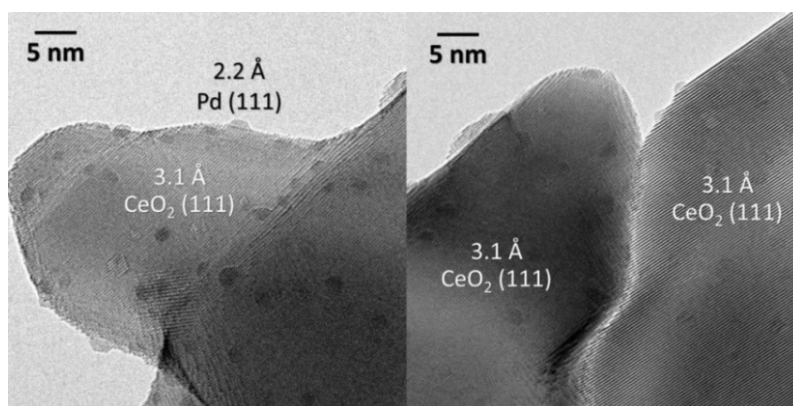


Figure 7.16: HRTEM images of 4PdCeIW after H₂ reduction treatment at 673 K.

During reaction, the morphology of the samples changes significantly. After 3 hours, no visible Pd nanoparticles can be observed on 4PdAcCeM (Figure 7.17) while 4PdCeIW displays the buildup of carbon filaments (Figure 7.18). High magnification HRTEM images in Figure 7.17 shows ceria nanoparticles displaying lattice fringes at 3.1 Å, corresponding to the {111} ceria crystallographic planes, and a slight sintering of the ceria particles can be noted. The area inside the white rectangle of Figure 7.17(A) is shown in the inset, where subnanometric entities are recognized and marked by circles. Other entities decorating the surface (marked by circles) can be appreciated in Figure 7.17(B). Given their subnanometric nature it is not possible to conclude if they correspond to Pd or PdO and/or if they are partly incorporated into the ceria lattice. It is remarkable that the initial Pd metal nanoparticles, observed after H₂ pretreatment in Figure 7.15, completely transform under DRM at 973 K after 3 hours and that no evident palladium phase is visible. Conversely, 4PdCeIW displays a very different arrangement, as seen in Figure 7.18. After 3 hours in DRM conditions there is evidence of carbon deposition in the sample, with carbon filaments that oscillate between 10 and 100 nm of diameter and micron-sized length. The carbon filaments are poorly organized and show a stacking of planes at 3.4 Å which correspond to the {002} distance in carbon structures. No subnanometric entities can be detected on this sample.

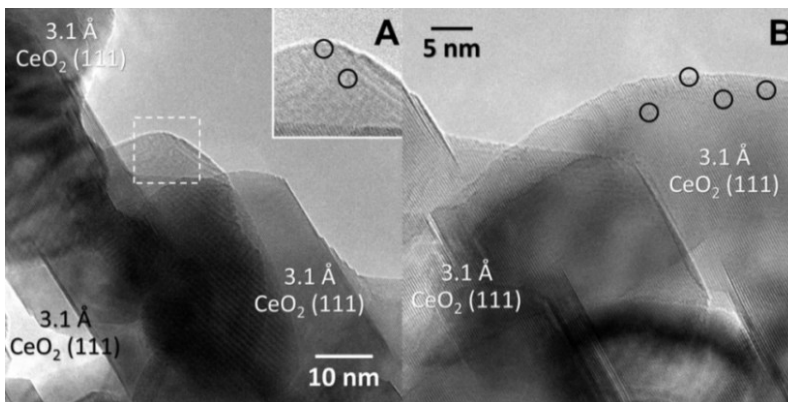


Figure 7.17: HRTEM images of 4PdAcCeM after 3 hours at 973 K in DRM conditions.

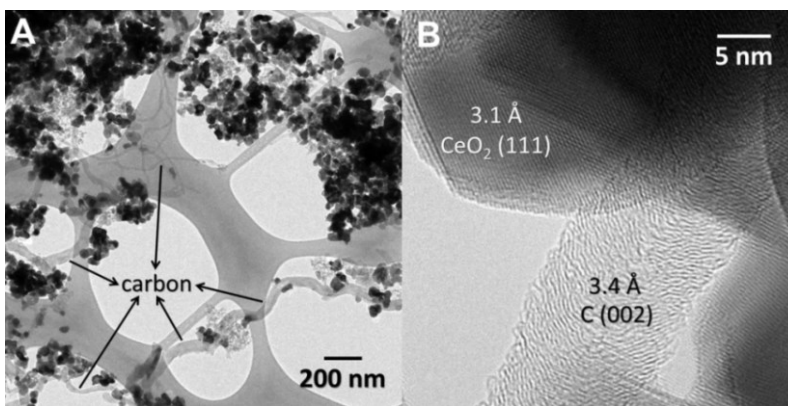


Figure 7.18: HRTEM images of 4PdCeIW after 3 hours at 973 K in DRM conditions under low (A) and high (B) magnification.

After 24 hours in DRM, no additional sintering of the ceria crystallites is observed on 4PdAcCeM and, once again, no Pd nanoparticles are encountered (Figure 7.19). More subnanometric entities are observed, marked by arrows in the inset in Figure 7.19(A), along with some voids in the ceria lattice. These voids are particularly abundant, and the subnanometric entities are visible and extremely well dispersed through the entire sample (Figure 7.19(B), marked by circles). On 4PdCeIW, a higher occurrence of carbon deposition can be observed (Figure 7.20(A)), displaying more abundant and compact carbon filaments. Figure 7.20(B) shows that carbon becomes more structured, with lattice fringes better defined at 3.4 Å (see FT in the inset). Again, no clear subnanometric entities are observed on ceria.

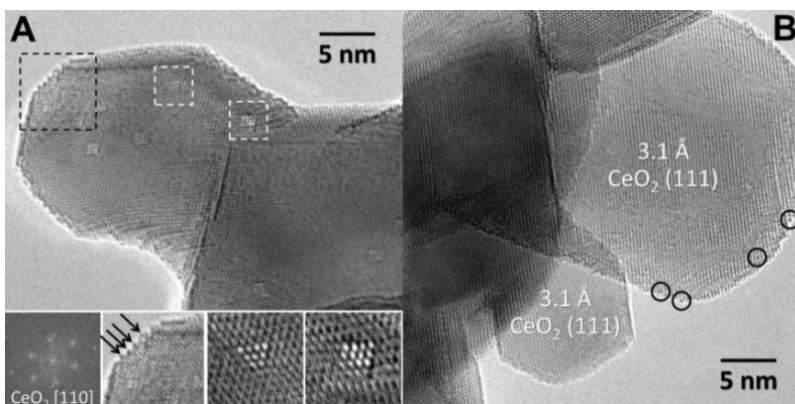


Figure 7.19: HRTEM images of 4PdAcCeM after 24 hours at 973 K in DRM conditions.

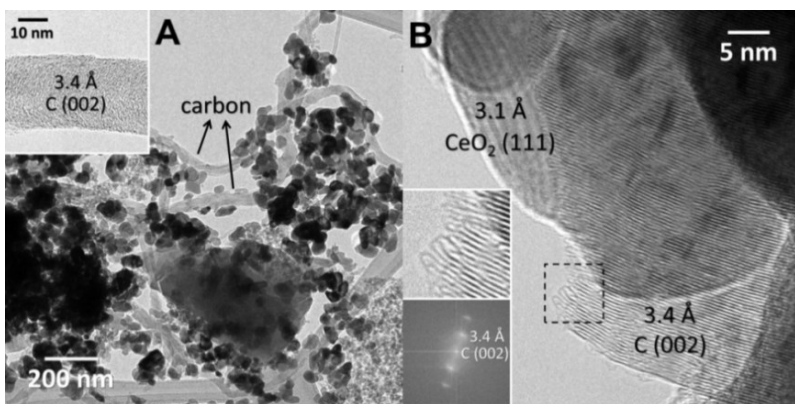


Figure 7.20: HRTEM images of 4PdCeIW after 24 hours at 973 K in DRM conditions under low (A) and high (B) magnification.

Preliminary *in-situ* XAFS analysis was performed, collecting spectra at the Pd K edge after H₂ pretreatment and 24 hours in DRM reaction at 973 K. The energy profiles and Fourier transform in the R space are reported in Figure 7.21(a,b) for 4PdAcCeM and 4PdCeIW, respectively. On the milled sample only metallic Pd is seen after reduction in hydrogen, and it appears virtually unchanged through reaction. On the other hand, on 4PdCeIW some contribution at radial distances around 1.2 Å is observed after pretreatment, likely attributed to residual Pd-O bonds. After reaction, the intensity of the 1.2 Å contribution increases noticeably, likely due to the formation of Pd-C bonds.

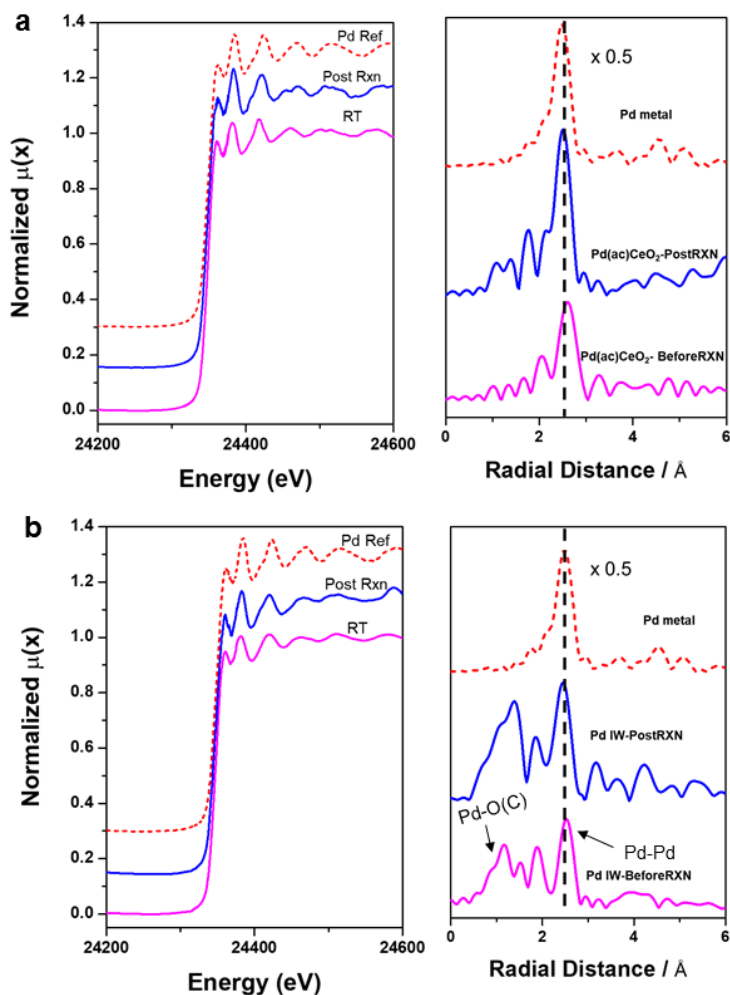


Figure 7.21: Preliminary XAS analysis of 4PdAcCeM (a) and 4PdCeIW (b) after H₂ pretreatment and after 24h stability test.

7.4 Conclusions

Reactivity tests carried out on the prepared samples clearly point to an improved performance obtained by 4PdAcCeM, exhibiting higher reaction yield for H₂ and CO compared to the impregnated 4PdCeIW sample, as well as higher CO₂ conversion and increased stability under prolonged exposure to DRM conditions. Our preliminary results indicate that the origin of the unique activity relates to the specific characteristic of the Pd-CeO₂ interface that is promoted during milling.

In-situ measurements unraveled the catalyst active phase at reaction conditions, allowing close examination of the reaction while in progress. Upon exposure to methane and carbon dioxide, transitions between the metal and support were observed at the reaction onset (673-773 K), suggesting enhanced O and H mobility between Pd and Ce on the milled sample promoting CH₄ and CO₂ activation to initiate the DRM reaction. The nanoscale Pd-Ce interplay has also a key role in the deactivation resistance of 4PdAcCeM, preventing carbon buildup under prolonged exposure to DRM conditions, which was reported in the literature as the main source of deactivation for DRM catalysts.^{6,32}

Under methane only, the promotional effect of the Pd-Ce surface arrangement for the C-H bond activation becomes even more evident, with 4PdAcCeM undergoing substantial transformations already at room temperature and leading to an outstanding methane activation performance. Differently from what observed in the presence of CO₂ in the feed, a large carbon buildup is observed on the milled sample as a consequence of the increased CH₄ activation, resulting in the formation of a secondary phase comprising Pd and/or CeO₂. The nature of this additional crystalline phase is yet to be understood, and further studies are planned in order to investigate its role in the enhanced CH₄ reactivity.

Nevertheless, from DRM stability tests and CH₄ activation tests it clearly appears that the Pd-Ce surface arrangement on 4PdAcCeM, constituted by Pd^{0/2+} moieties in strong interaction with ceria, enhance surface O and H mobility, simultaneously promoting CO₂ and CH₄ activation and resulting in a promising catalyst for DRM applications. Hence, the incorporation of Pd into the CeO₂ lattice and the resulting strong metal-support interaction play a key role in the complex CO₂ and CH₄ activation pathways that lead to the production of CO and H₂.

7.5 References

- (1) Tang, P.; Zhu, Q.; Wu, Z.; Ma, D. Methane Activation: The Past and Future. *Energy Environ. Sci.* **2014**, *7* (8), 2580–2591. <https://doi.org/10.1039/C4EE00604F>.
- (2) Kondratenko, E. V.; Mul, G.; Baltrusaitis, J.; Larrazábal, G. O.; Pérez-Ramírez, J. Status and Perspectives of CO₂ Conversion into Fuels and Chemicals by Catalytic, Photocatalytic and Electrocatalytic Processes. *Energy & Environmental Science* **2013**, *6* (11), 3112. <https://doi.org/10.1039/c3ee41272e>.
- (3) Dry, M. E.; Steynberg, A. P. Chapter 5 - Commercial FT Process Applications. In *Studies in Surface Science and Catalysis*; Steynberg, A., Dry, M., Eds.; Elsevier, 2004; Vol. 152, pp 406–481. [https://doi.org/10.1016/S0167-2991\(04\)80462-2](https://doi.org/10.1016/S0167-2991(04)80462-2).
- (4) Krylova, A. Yu. Products of the Fischer-Tropsch Synthesis (A Review). *Solid Fuel Chemistry* **2014**, *48* (1), 22–35. <https://doi.org/10.3103/S0361521914010030>.
- (5) Lavoie, J.-M. Review on Dry Reforming of Methane, a Potentially More Environmentally-Friendly Approach to the Increasing Natural Gas Exploitation. *Frontiers in Chemistry* **2014**, *2*. <https://doi.org/10.3389/fchem.2014.00081>.
- (6) Li, D.; Nakagawa, Y.; Tomishige, K. Methane Reforming to Synthesis Gas over Ni Catalysts Modified with Noble Metals. *Applied Catalysis A: General* **2011**, *408* (1–2), 1–24. <https://doi.org/10.1016/j.apcata.2011.09.018>.
- (7) Pakhare, D.; Spivey, J. A Review of Dry (CO₂) Reforming of Methane over Noble Metal Catalysts. *Chem. Soc. Rev.* **2014**, *43* (22), 7813–7837. <https://doi.org/10.1039/C3CS60395D>.
- (8) Rostrupnielsen, J. R.; Hansen, J. H. B. CO₂-Reforming of Methane over Transition Metals. *Journal of Catalysis* **1993**, *144* (1), 38–49. <https://doi.org/10.1006/jcat.1993.1312>.
- (9) Rodriguez, José. A. Physical and Chemical Properties of Bimetallic Surfaces. *Surface Science Reports* **1996**, *24* (7–8), 223–287. [https://doi.org/10.1016/0167-5729\(96\)00004-0](https://doi.org/10.1016/0167-5729(96)00004-0).
- (10) Senanayake, S. D.; Zhou, J.; Baddorf, A. P.; Mullins, D. R. The Reaction of Carbon Monoxide with Palladium Supported on Cerium Oxide Thin Films. *Surface Science* **2007**, *601* (15), 3215–3223. <https://doi.org/10.1016/j.susc.2007.05.037>.
- (11) Misch, L. M.; Kurzman, J. A.; Derk, A. R.; Kim, Y.-I.; Seshadri, R.; Metiu, H.; McFarland, E. W.; Stucky, G. D. C–H Bond Activation by Pd-Substituted CeO₂: Substituted Ions versus Reduced Species. *Chemistry of Materials* **2011**, *23* (24), 5432–5439. <https://doi.org/10.1021/cm202709y>.
- (12) Trovarelli, A.; Fornasiero, P. *Catalysis By Ceria And Related Materials*, 2nd ed.; Catalytic Science; Imperial College Press: London, United Kingdom, 2013.
- (13) Boaro, M.; Colussi, S.; Trovarelli, A. Ceria-Based Materials in Hydrogenation and Reforming Reactions for CO₂ Valorization. *Front. Chem.* **2019**, *7*, 28. <https://doi.org/10.3389/fchem.2019.00028>.
- (14) Fierro, J. L. G.; Soria, J.; Sanz, J.; Rojo, J. M. Induced Changes in Ceria by Thermal Treatments under Vacuum or Hydrogen. *Journal of Solid State Chemistry* **1987**, *66* (1), 154–162. [https://doi.org/10.1016/0022-4596\(87\)90230-1](https://doi.org/10.1016/0022-4596(87)90230-1).
- (15) Sohlberg, K.; Pantelides, S. T.; Pennycook, S. J. Interactions of Hydrogen with CeO₂. *Journal of the American Chemical Society* **2001**, *123* (27), 6609–6611. <https://doi.org/10.1021/ja004008k>.

- (16) Wu, Z.; Cheng, Y.; Tao, F.; Daemen, L.; Foo, G. S.; Nguyen, L.; Zhang, X.; Beste, A.; Ramirez-Cuesta, A. J. Direct Neutron Spectroscopy Observation of Cerium Hydride Species on a Cerium Oxide Catalyst. *Journal of the American Chemical Society* **2017**, *139* (28), 9721–9727. <https://doi.org/10.1021/jacs.7b05492>.
- (17) Acerbi, N.; Golunski, S.; Tsang, S. C.; Daly, H.; Hardacre, C.; Smith, R.; Collier, P. Promotion of Ceria Catalysts by Precious Metals: Changes in Nature of the Interaction under Reducing and Oxidizing Conditions. *The Journal of Physical Chemistry C* **2012**, *116* (25), 13569–13583. <https://doi.org/10.1021/jp212233u>.
- (18) Kozlov, S. M.; Neyman, K. M. Insights from Methane Decomposition on Nanostructured Palladium. *Journal of Catalysis* **2016**, *337*, 111–121. <https://doi.org/10.1016/j.jcat.2016.02.010>.
- (19) Danielis, M.; Colussi, S.; de Leitenburg, C.; Soler, L.; Llorca, J.; Trovarelli, A. Outstanding Methane Oxidation Performance of Palladium-Embedded Ceria Catalysts Prepared by a One-Step Dry Ball-Milling Method. *Angewandte Chemie International Edition* **2018**, *57* (32), 10212–10216. <https://doi.org/10.1002/anie.201805929>.
- (20) Colussi, S.; Gayen, A.; Farnesi Camellone, M.; Boaro, M.; Llorca, J.; Fabris, S.; Trovarelli, A. Nanofaceted Pd-O Sites in Pd-Ce Surface Superstructures: Enhanced Activity in Catalytic Combustion of Methane. *Angewandte Chemie International Edition* **2009**, *48* (45), 8481–8484. <https://doi.org/10.1002/anie.200903581>.
- (21) Mayernick, A. D.; Janik, M. J. Methane Oxidation on Pd–Ceria: A DFT Study of the Mechanism over Pd_xCe_{1-x}O₂, Pd, and PdO. *Journal of Catalysis* **2011**, *278* (1), 16–25. <https://doi.org/10.1016/j.jcat.2010.11.006>.
- (22) Colussi, S.; Trovarelli, A.; Cristiani, C.; Lietti, L.; Groppi, G. The Influence of Ceria and Other Rare Earth Promoters on Palladium-Based Methane Combustion Catalysts. *Catalysis Today* **2012**, *180* (1), 124–130. <https://doi.org/10.1016/j.cattod.2011.03.021>.
- (23) Colussi, S.; Trovarelli, A.; Groppi, G.; Llorca, J. The Effect of CeO₂ on the Dynamics of Pd–PdO Transformation over Pd/Al₂O₃ Combustion Catalysts. *Catalysis Communications* **2007**, *8* (8), 1263–1266. <https://doi.org/10.1016/j.catcom.2006.11.020>.
- (24) Toso, A.; Colussi, S.; Padigapaty, S.; de Leitenburg, C.; Trovarelli, A. High Stability and Activity of Solution Combustion Synthesized Pd-Based Catalysts for Methane Combustion in Presence of Water. *Applied Catalysis B: Environmental* **2018**, *230*, 237–245. <https://doi.org/10.1016/j.apcatb.2018.02.049>.
- (25) Senftle, T. P.; van Duin, A. C. T.; Janik, M. J. Methane Activation at the Pd/CeO₂ Interface. *ACS Catalysis* **2017**, *7* (1), 327–332. <https://doi.org/10.1021/acscatal.6b02447>.
- (26) Su, Y.-Q.; Filot, I. A. W.; Liu, J.-X. Stable Pd-Doped Ceria Structures for CH₄ Activation and CO Oxidation. *ACS Catalysis* **2018**, *8* (1), 75–80. <https://doi.org/10.1021/acscatal.7b03295>.
- (27) Liu, Z.; Zhang, F.; Rui, N.; Li, X.; Lin, L.; Betancourt, L. E.; Su, D.; Xu, W.; Cen, J.; Attenkofer, K.; et al. Highly Active Ceria-Supported Ru Catalyst for the Dry Reforming of Methane: In Situ Identification of Ru^{δ+}–Ce³⁺ Interactions for Enhanced Conversion. *ACS Catalysis* **2019**, *9* (4), 3349–3359. <https://doi.org/10.1021/acscatal.8b05162>.

- (28) Zhang, F.; Liu, Z.; Zhang, S.; Akter, N.; Palomino, R. M.; Vovchok, D.; Orozco, I.; Salazar, D.; Rodriguez, J. A.; Llorca, J.; et al. In Situ Elucidation of the Active State of Co–CeO_x Catalysts in the Dry Reforming of Methane: The Important Role of the Reducible Oxide Support and Interactions with Cobalt. *ACS Catalysis* **2018**, *8* (4), 3550–3560. <https://doi.org/10.1021/acscatal.7b03640>.
- (29) Palomino, R. M.; Hamlyn, R.; Liu, Z.; Grinter, D. C.; Waluyo, I.; Rodriguez, J. A.; Senanayake, S. D. Interfaces in Heterogeneous Catalytic Reactions: Ambient Pressure XPS as a Tool to Unravel Surface Chemistry. *Journal of Electron Spectroscopy and Related Phenomena* **2017**, *221*, 28–43. <https://doi.org/10.1016/j.elspec.2017.04.006>.
- (30) Chupas, P. J.; Chapman, K. W.; Kurtz, C.; Hanson, J. C.; Lee, P. L.; Grey, C. P. A Versatile Sample-Environment Cell for Non-Ambient X-Ray Scattering Experiments. *Journal of Applied Crystallography* **2008**, *41* (4), 822–824. <https://doi.org/10.1107/S0021889808020165>.
- (31) Ravel, B.; Newville, M. *ATHENA*, *ARTEMIS*, *HEPHAESTUS*: Data Analysis for X-Ray Absorption Spectroscopy Using *IFEFFIT*. *Journal of Synchrotron Radiation* **2005**, *12* (4), 537–541. <https://doi.org/10.1107/S0909049505012719>.
- (32) Lu, J.; Fu, B.; Kung, M. C.; Xiao, G.; Elam, J. W.; Kung, H. H.; Stair, P. C. Coking- and Sintering-Resistant Palladium Catalysts Achieved Through Atomic Layer Deposition. *Science* **2012**, *335* (6073), 1205–1208. <https://doi.org/10.1126/science.1212906>.
- (33) Liu, Z.; Grinter, D. C.; Lustemberg, P. G.; Nguyen-Phan, T.-D.; Zhou, Y.; Luo, S.; Waluyo, I.; Crumlin, E. J.; Stacchiola, D. J.; Zhou, J.; et al. Dry Reforming of Methane on a Highly-Active Ni-CeO₂ Catalyst: Effects of Metal-Support Interactions on C–H Bond Breaking. *Angewandte Chemie International Edition* **2016**, *55* (26), 7455–7459. <https://doi.org/10.1002/anie.201602489>.

8 Methane Oxidation and Steam Reforming Activity of Pd/CeO₂ Milled Catalysts in NGVs Aftertreatment Applications

Abstract

The increasing diffusion of natural gas fueled vehicles (NGVs) requires careful control of their unburned methane emissions and an improvement of the current aftertreatment system in order to minimize their global greenhouse gas (GHG) emissions. A preliminary feasibility study for the application of catalysts prepared by dry milling in NGVs after-treatment systems was carried out in collaboration with Ford Motor Company, Dearborn (MI). Powder catalysts were tested for CH₄ oxidation and steam reforming, which are the main methane abatement reactions occurring in a three-way catalyst (TWC) under lean and rich conditions, respectively. Catalytic monoliths were prepared by washcoating a cordierite core with the best performing milled sample, whose catalytic performance was then compared to a series of commercial standards. The dry-milled Pd/CeO₂ catalyst displayed comparable activity to its commercial counterpart, prepared by incipient wetness impregnation, but appeared less resistant to the industrial aging processes. In addition, commercial samples with a more complex composition displayed higher activity and stability, suggesting that further work would be needed to optimize the composition, synthesis and coating procedure of dry milled samples for industrial application.

8.1 Introduction

In the latest decades, natural gas has emerged as one of the most appealing and competitive alternative fuel due to its ready availability, lower price compared to liquid fuels, and technological maturity.¹⁻⁴ Its chemical composition, comprising mostly methane and some short-chain hydrocarbons (C_2H_6 , C_3H_8 and C_4H_{10} , up to 5%), allows for a significant reduction of CO_2 emissions due to its low C:H ratio and the possible integration with biogas.⁵ Furthermore, the higher flame stability and lower flame temperature of CH_4 reduce the amount of NO_x formed in the engine,^{1,6} making its abatement to increasingly stringent legislation limits easier and, consequently, cheaper. Nevertheless, methane has a global warming potential that is 25 times higher than CO_2 and its leakage needs to be carefully controlled.⁷ Unburned methane may leak from the production and distribution network and during vehicle use, through evaporation from the fuel tank or by release of residual unburned CH_4 from the exhaust gases.^{8,9} The latter is the focus issue for catalysts manufacturers, whose goal is the design of catalytic converters able to transform all residual CH_4 into CO_2 and H_2O at the lowest possible temperature and with the least amount of noble metal loading, whose price has rapidly grown due to extensive use in the aftertreatment industry¹⁰ and accounts for a large share of the catalytic converter cost.

Along with total methane conversion and price, another key issue for the design of catalytic converters is their durability, as legislation limits are imposed over a certain minimum time (5-7 years) or mileage (150'000-200'000 km).¹¹ This is especially critical for NGVs catalysts, where the high amount of steam produced by CH_4 combustion (ca. 10-15%) acts as a strong inhibitor of methane oxidation.¹²⁻¹⁵ Moreover, the most common technology currently employed are Pd-based three-way catalysts (TWC), in which simultaneous oxidation of CO and HC and reduction of NO_x is achieved by working around the stoichiometric air-to-fuel ratio value (A/F)_s.¹⁶⁻¹⁸ The working operation in a strict lambda window is controlled by an O_2 sensor at the catalyst outlet.¹⁷ Due to the feedback control system, the metal-metal oxide catalyst experiences brief lean-rich oscillations going from oxidative to reducing atmosphere very quickly.¹⁹⁻²¹ The transient and cycling behavior further affects catalytic performance by modifying the palladium active sites or by enabling methane abatement via reforming reactions, as such it was widely investigated in the literature.²¹⁻²⁷

We have previously reported the synthesis of Pd/CeO₂ catalysts with enhanced methane oxidation activity and stability, as tested in lab-scale reactor equipment (Chapter 3). A class of materials with increased Pd loading, prepared by dry mechano-chemical synthesis using Palladium acetate as precursor, exhibited outstanding methane conversion performances both in lean (methane oxidation, Chapter 6) and rich (dry reforming of methane, Chapter 7) conditions. Here we investigate the activity of Pd/CeO₂ dry-milled catalysts in typical exhaust methane abatement applications, namely methane oxidation and methane steam reforming reactions. Catalytic materials were prepared by a scaled-up synthesis and tested both in powder form and as washcoated monoliths in collaboration with Ford Motor Company, Dearborn (MI).

8.2 Experimental

Catalytic materials containing 1 wt% and 4 wt% Pd were prepared on commercial ceria provided by Ford Motor Company, calcined at 1173 K or 1473 K prior to metal deposition. Samples were prepared by dry mechano-chemical synthesis and by incipient wetness impregnation following the synthesis procedures as reported in detail in Chapter 2, section 2.1. Further reference samples, with 4 wt% Pd supported on commercial ceria or alumina calcined at 873 K, were prepared and tested at Ford Motor Company, along with commercial fully formulated TWC. To prepare the necessary amount of catalyst for the washcoating process, the synthesis of a 4 wt%Pd/CeO₂(1473) milled sample was scaled up in a Pulverisette 6 planetary ball mill, using a 250 ml ZrO₂ jar filled with two ZrO₂ grinding balls of 20 mm diameter, each weighting ca. 24 g. 9.60 g of CeO₂(1473) and 0.844 g of Palladium acetate powders were loaded in the grinding bowl and milled for 10 minutes at 100 rpm. The scale up was designed to mimic the same operating conditions employed in the Pulverisette 23 Minimill: the low operating rpm ensures mostly shear stresses are developed during milling, while the Ball-to-Powder weight Ratio (BPR) was decreased from 10 to 5 to account for the increased number of impact and released energy caused by the use of two grinding balls instead of a single one.

Characterization of prepared materials was carried out by means of BET surface area measurements and ICP-mass elemental analysis. Evaluation of catalytic activity was performed at the Heterogeneous Catalysis Lab in Udine and at Ford Motor Company, Dearborn (MI), as described in detail in Section 2.3. Briefly, in Udine combustion tests were performed in a lab-scale microreactor, loading 120 mg of catalytic sample in a quartz

tubular reactor under 180 ml/min of a dry lean gas mixture (0.5%CH₄, 2%O₂, He to balance) to reach a final GHSV of ca. 180'000 h⁻¹. At Ford Motor Company catalytic tests were carried out on powder and monolith samples. Powder catalysts were pressed and sieved, then 500 mg of Pd/CeO₂ sample were diluted with 500 mg of ground up cordierite and loaded in a 0.50" OD quartz reactor tube between two beds of quartz wool. For methane oxidation (MO) tests, 2 L/min of reaction mixture (0.1% CH₄, 1% O₂, 5% H₂O, 5% CO₂ in N₂, λ=1.03) were introduced and the sample heated from 373 K to 1173 K for three consecutive heating/cooling cycles (GHSV ≈ 480'000 h⁻¹). An oxidative or reducing pretreatment at 1173 K was performed before reaction by adding 1% O₂ or 1% CO to a 0.1%CH₄/5%H₂O/5%CO₂/N₂ mixture.

For steam reforming (SR) tests, an oxidative pretreatment at 1173 K under 0.1% CH₄, 1% O₂, 5% H₂O, 5%CO₂ in N₂ was performed before reaction, then oxygen was removed and 0.15% CO was added to the gas feed (λ=0.99). Monoliths were prepared by depositing the prepared dry-milled catalysts on a cordierite core to reach a final washcoat loading of 3 gci. A 0.70" D x 1.0" L sized core was inserted in a quartz tube and exposed to the same reaction atmosphere and powder experiments to reach a final GHSV of 19'000 h⁻¹. Monolithic samples were tested fresh (or degreened) and after two established procedures for synthetic aging (2-modes or 4-modes). The 2-modes synthetic aging process consisted in holding the sample at 1223 K for 50 hours, repeating 60-second-long cycles of 54 s lean (4% O₂/10% H₂O) and 6 s rich pulses (3% CO/1% H₂/10% H₂O). The 4-modes procedure involved holding the coated core for 100 hrs at an effective temperature of 1183 K, with temperature spikes reaching over 1273 K. Combusted fuel resulting in a full gas mixture of various HC types, NO_x, CO, H₂, CO₂, and H₂O was employed, repeating 60 s cycles of stoichiometric, rich, and lean gas mixtures. Methane conversion on fresh (de-greened) and aged samples was evaluated during three consecutive heating/cooling cycles from 373 K to 1173 K; the third cycle is reported in the following as representative of the stable catalytic behavior.

8.3 Results and Discussion

A summary of the physico-chemical properties of the catalytic samples prepared in this study is reported in Table 8.1. A first evaluation of the best performing Pd/CeO₂ combinations was carried out by testing 1wt.% Pd/CeO₂ catalysts prepared by incipient wetness impregnation (1PdCe1173M) and by dry mechano-chemical synthesis using PdAc

supported on high surface area ceria calcined at 1173 K and 1473 K prior to synthesis (1PdAcCe1173M and 1PdAcCe1473M, respectively).

Table 8.1: Physico-chemical properties of catalytic samples and support oxides used in this study.

Sample	BET surface area (m ² /g)	Nominal Pd loading (wt%)	Measured Pd loading (wt%)
CeO ₂ (1173)	23.4	-	-
CeO ₂ (1473)	3.8	-	-
1PdCe1173IW	19.6	1	0.93
1PdAcCe1173M	24.9	1	0.99
1PdAcCe1473M	5.2	1	1.01
4PdCe1173IW	14.6	4	3.94
4PdAcCe1173M	22.1	4	3.92
4PdAcCe1473M	3.1	4	4.03

Prepared samples were tested under methane oxidation (Figure 8.1) and steam reforming (Figure 8.2) conditions at Ford Motor Company Lab, Dearborn (MI). Comparative methane oxidation tests were also carried out at the Heterogeneous Catalysis Lab, Udine (Figure 8.3).

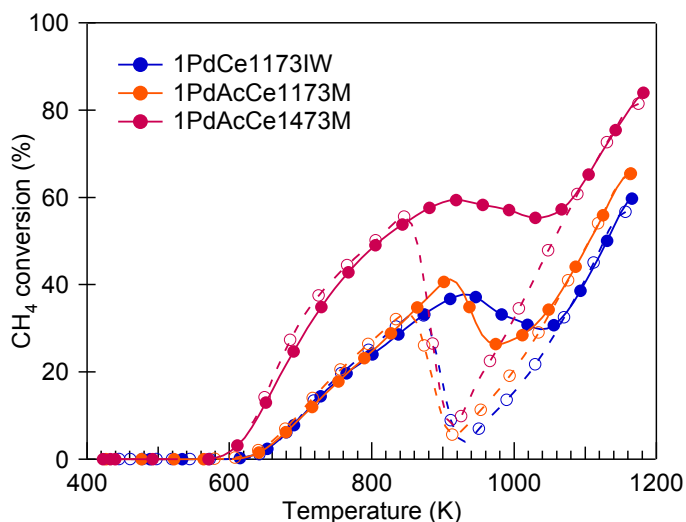


Figure 8.1: Methane oxidation activity on representative 1%Pd/CeO₂ samples (GHSV \approx 480'000 h⁻¹).

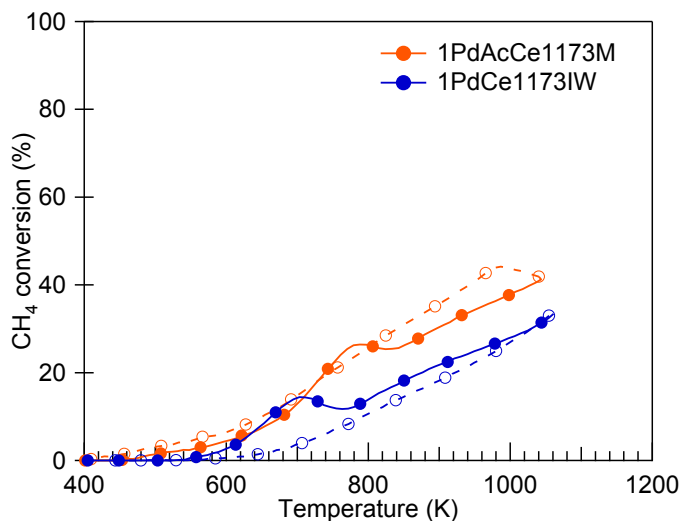


Figure 8.2: Steam reforming activity of 1%Pd/CeO₂ samples (GHSV≈480'000 h⁻¹).

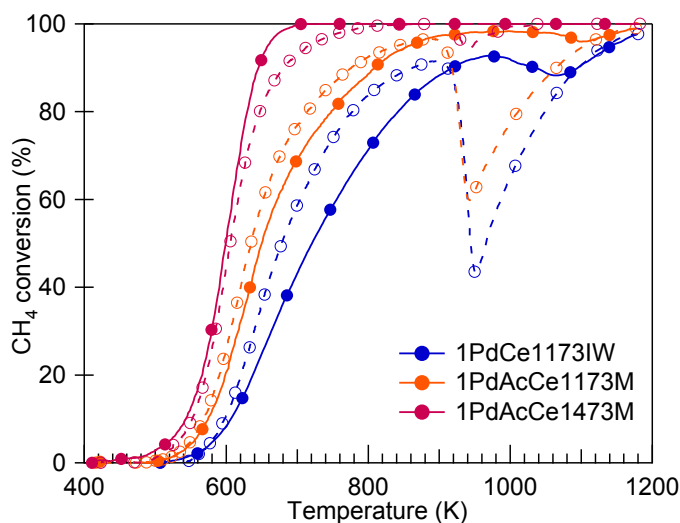


Figure 8.3: Methane oxidation tests performed on 1%Pd/CeO₂ samples (GHSV≈180'000 h⁻¹).

Figure 8.1 and Figure 8.3 clearly point out that the highest methane oxidation activity is obtained by 1PdAcCe1473M, as also reported in previous chapters (Chapters 3 and 6). Indeed, the combination of PdAc milled on low surface area ceria (calcined at 1473 K, ~4m²/g surface area) simultaneously ensures low temperature methane activation and a negligible activity loss at temperatures above 900 K. This was attributed to the peculiar Pd⁰/Pd²⁺ arrangement stabilized on the ceria surface, promoting surface oxygen mobility and resulting in higher methane oxidation reaction rate.

Sample 1PdAcCe1473M even outperformed a commercial 1.5wt.%Pd/La-Al₂O₃ catalyst (Figure 8.4), kindly provided by Ford Motor Company, further confirming the synergistic Pd-PdO/CeO₂ behavior and the possibility to simultaneously reduce palladium loading and improve catalytic performance.

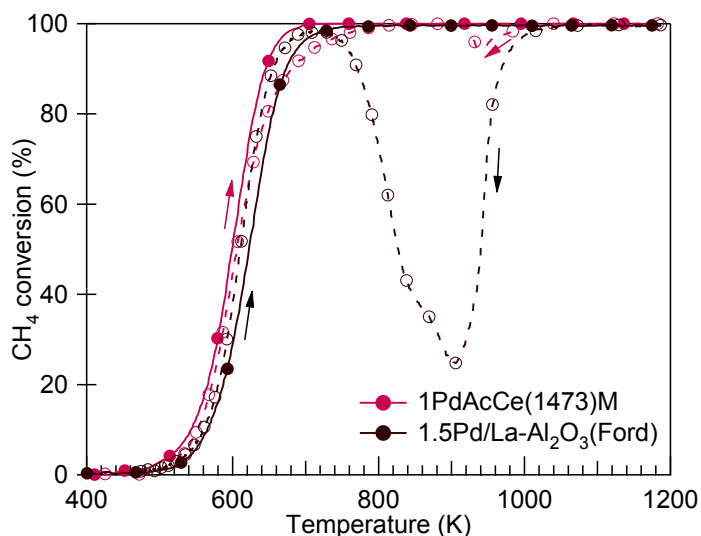


Figure 8.4: Comparison of methane oxidation activity for 1PdAcCe(1473)M and a reference 1.5%Pd/La-Al₂O₃ sample (GHSV \approx 180'000 h⁻¹).

At high space velocity (GHSV \approx 480'000 h⁻¹) the milled sample displays an improved performance compared to the sample prepared by the commercial wet synthesis, both in oxidizing (Figure 8.1) and reducing (Figure 8.2) conditions. Moreover, steam deactivation resistance tests carried out for CH₄ oxidation under a 10 vol% H₂O atmosphere reported in the previous chapters (Chapter 3 and 6) showed that milled catalysts are less deactivated in the 24-hour period and retain a higher conversion value in isothermal conditions compared to samples prepared by incipient wetness impregnation. These preliminary results seem very promising for the application of the dry-milled catalysts to industrial levels.

Nevertheless, at 1 wt.% loading they could not reach full conversion at 480'000 h⁻¹, which was the set goal to comply to the current legislation limits at tailpipe. In fact, a fully formulated TWC was tested as reference in methane oxidation and steam reforming conditions (Figure 8.5). The noble metal loading corresponds to ca. 4% Pd on the oxide support, some Rh being also present (in traces) on the CeO₂-ZrO₂-Al₂O₃ mixed oxide support.

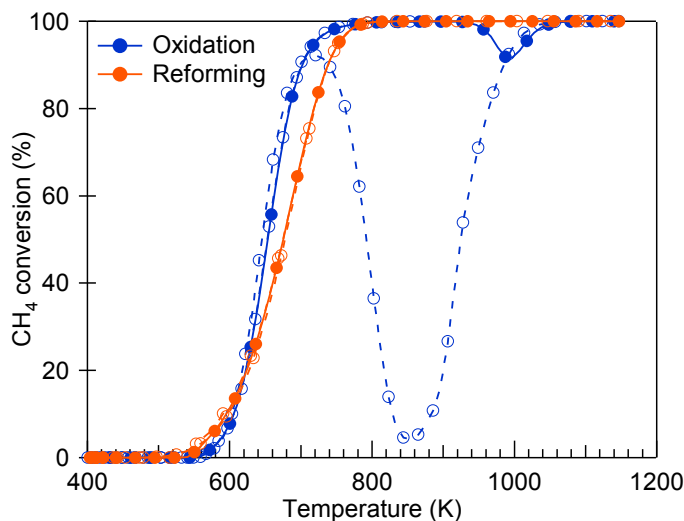


Figure 8.5: Methane oxidation and steam reforming activity of a commercial fully formulated TWC ((0/196/04), 900/2) after 2-modes aging (GHSV \approx 480'000 h⁻¹).

Consequently, aiming at achieving full methane conversion at 480'000 h⁻¹ a corresponding series of 4wt%Pd/CeO₂ samples (4PdCe1173IW, 4PdAcCe1173M, 4PdAcCe1473M) was prepared and evaluated for methane oxidation. The light-off curves are reported in Figure 8.6, where the sample prepared by dry milling PdAc on ceria calcined at 1473 K prior to synthesis (4PdAcCe1473M) showed the highest activity and reached 95% conversion at 860 K, while samples prepared on higher surface area ceria (Ce1173) displayed lower activity. Further oxidation tests clearly showed that the 4PdAcCe1473M sample outperformed commercial samples prepared on ceria calcined at 873 K, as well as a fully formulated TWC (Figure 8.7). A commercial 4Pd/Al₂O₃ IW reference sample displayed lower light-off temperatures compared to the milled 4PdAcCe1473M, but on this sample the activity undergoes a severe drop during cooling and it is not recovered until 700 K, which is typical of alumina-supported Pd catalysts.²⁸⁻³⁰ This behavior is especially undesirable on TWC applications, as the activity loss during cooling accounts for unburned methane release during operation. In fact, in real-life applications the operating temperature depends on the engine regime conditions, hence the cooling process to 700 K cannot be controlled and on Al₂O₃-based catalysts it might result in prolonged release of large amounts of CH₄, above legislation limits. The ceria capacity to reduce this loss by promoting Pd re-oxidation during cooling and thus exhibiting a higher methane conversion averaged on the whole temperature range is much more favorable for methane abatement applications.³¹⁻³⁴

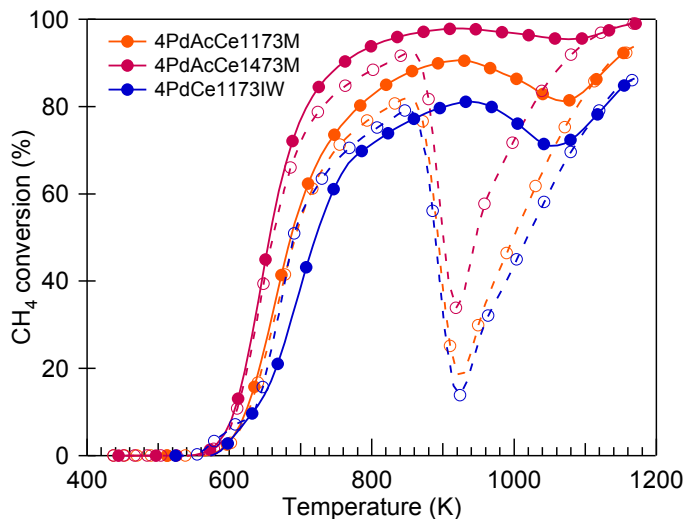


Figure 8.6: Methane oxidation activity of 4 wt% Pd/CeO₂ samples (GHSV≈480'000h⁻¹).

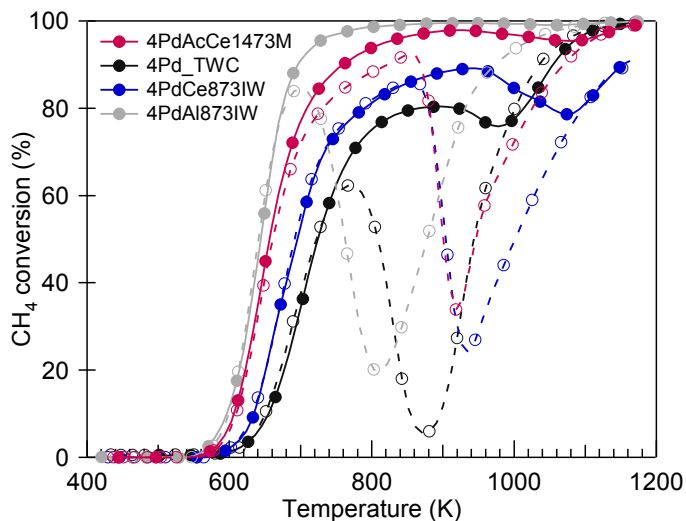


Figure 8.7: Methane oxidation activity of 4PdAcCe1473M compared to 4PdCe(873)-Ford-IW, 4PdAl(873)-Ford-IW and 4Pd_TWC(0/290/10) (GHSV≈480'000 h⁻¹).

Confirmed the remarkable performance of 4PdAcCe1473M in powder form, further testing was carried out on the milled sample coated on a cordierite core. Due to the larger amount of catalytic powders needed for industrial lab-scale washcoating process, the dry mechano-chemical synthesis was scaled up from 1 g to 10 g using a planetary ball-mill instead of a vibratory mini-mill. The synthesis scale-up was not straightforward and comparative 4PdAcCe1473M samples did not exhibit the same catalytic activity (Figure 8.8). Further studies should be conducted to optimize the scale-up synthesis, nonetheless, due to time and

cost constraints and the relatively minor performance discrepancies observed, this sample was used for further catalytic cores washcoating and testing.

It should be mentioned that the established process for cordierite cores washcoating involves dipping the cores into a slurry containing the Pd/CeO₂ catalytic powders and an alumina-based binder. Several dipping steps are usually performed to reach the desired catalyst or noble metal loading, with low temperature calcination treatments (usually at 873 K) in air between each step. The coating process was not optimized for this system, possibly leading to a slight worsening in the catalytic activity exhibited by milled samples. Indeed, as we have shown in a previous chapter (Chapter 5), a poorer methane oxidation performance is achieved on PdAc/CeO₂ milled samples when treated in air.

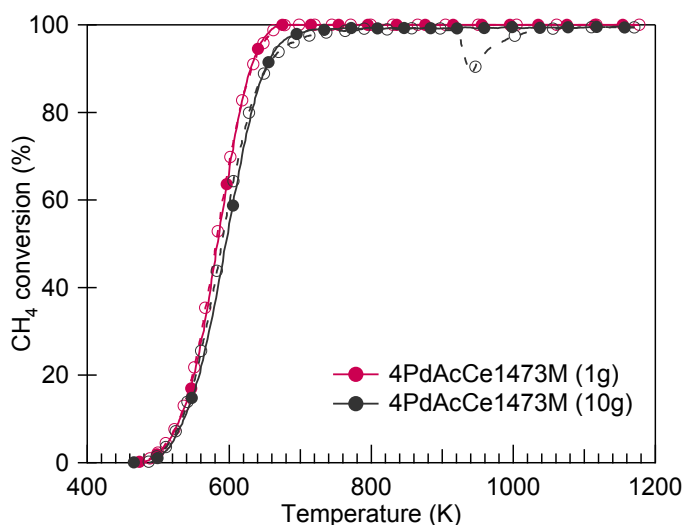


Figure 8.8: Comparison of methane oxidation activity of 4PdAcCe1473M samples prepared in the optimized setup (Pulverisette 23 mini-mill, 1 g) and in a planetary ball-mill (Pulverisette 6, 10 g); (GHSV \approx 180'000 h⁻¹).

The activity of the 4PdAcCe1473M coated monolith was compared to its 4PdCeIW counterpart and an alumina reference under methane oxidation and steam reforming conditions, before and after synthetic aging. The performance of degreened (fresh) samples is shown in Figure 8.9 and Figure 8.10 for methane oxidation and steam reforming, respectively. As already observed in tests carried out on samples in powder form, the fresh milled sample outperforms its 4PdCeIW counterpart in lean methane oxidation (Figure 8.9), while 4%Pd supported on alumina onsets the reaction at lower temperatures (ca. 25 K) but displays a significant conversion loss during cooling. In rich steam reforming conditions

(Figure 8.10) all samples exhibit virtually identical activity. Under this reducing atmosphere palladium is found mostly as Pd metal, consequently no hysteric behavior is observed during reaction.

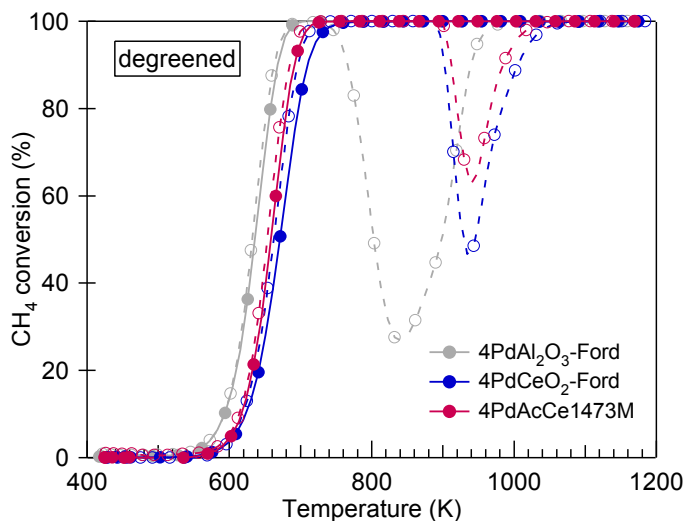


Figure 8.9: Methane oxidation activity of degreened 4PdAcCe1473M, 4PdCeO₂-Ford-IW, 4PdAl₂O₃-Ford-IW on monolith cores.

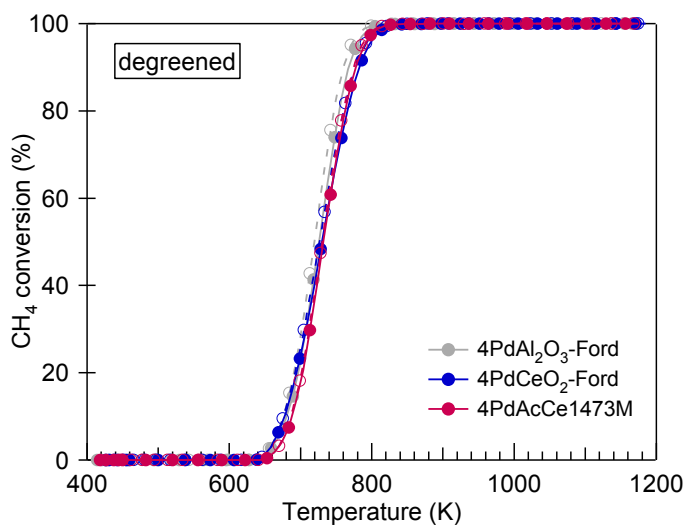


Figure 8.10: Steam reforming activity of degreened 4PdAcCe1473M, 4PdCeO₂-Ford-IW, 4PdAl₂O₃-Ford-IW on monolith cores.

Catalysts were then aged under 2-modes conditions (50 hours at 1223 K), in order to verify the durability performance of evaluated catalysts.³⁵ After aging, the investigated samples exhibit noticeable differences in methane oxidation performance (Figure 8.11), with the milled sample displaying the worst catalytic activity and suffering a 80 K shift to higher

light-off temperatures compared to its degreened conditions. A similar effect is observed under steam reforming conditions (Figure 8.12).

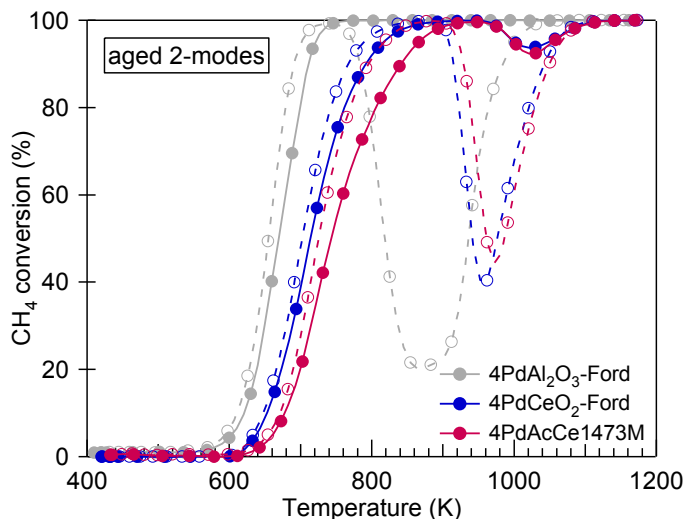


Figure 8.11: Methane oxidation activity of aged 4PdAcCe1473M, 4PdCeO₂-Ford-IW, 4PdAl₂O₃-Ford-IW on monolith cores.

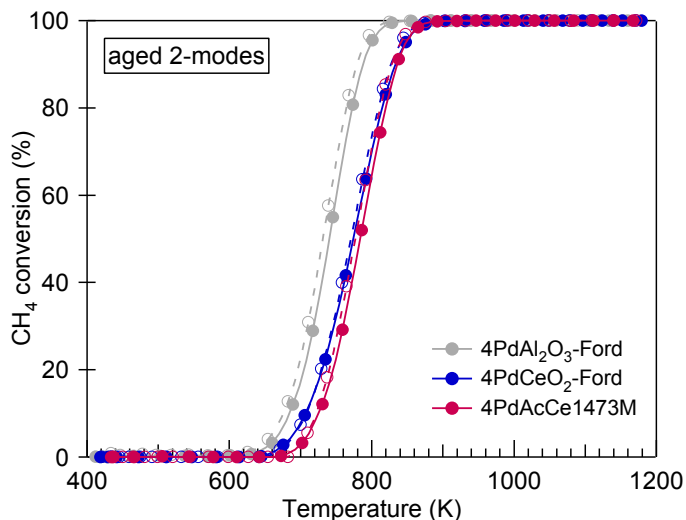


Figure 8.12: Steam reforming activity of aged 4PdAcCe1473M, 4PdCeO₂-Ford-IW, 4PdAl₂O₃-Ford-IW on monolith cores.

Before real life applications, the performance of developed catalysts is usually further evaluated after a strong aging procedure, called 4-modes, where the exhaust gases from combusted fuel are used to modulate the rich, stoichiometric and lean conditions. The methane oxidation and steam reforming activity for the reference 4PdCeIW-Ford sample and the commercial fully formulated TWC after 4-modes aging (100 h, 1183 K) are shown

in Figure 8.13 and Figure 8.14, respectively. Qualitatively, it clearly appears that the different compositions strongly affect the behavior of the materials, as the commercial three-way catalyst displays a hysteretic behavior even under steam reforming conditions (Figure 8.14). As a consequence, a real comparison between the milled sample (comprised only by palladium and ceria) and the commercial reference becomes insignificant. A fully formulated catalytic powder would be needed for a more faithful comparison, which is outside of the scope of the current work.

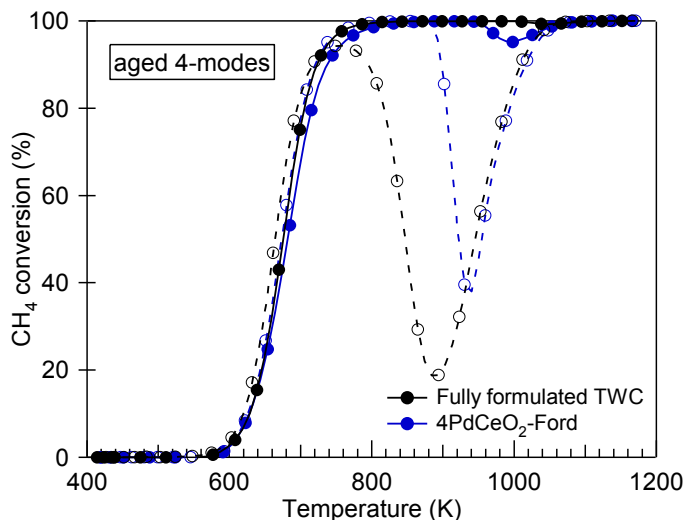


Figure 8.13: Methane oxidation activity of 4PdCeO₂-Ford-IW and a fully formulated TWC after 4-modes aging (100 h, 1183 K).

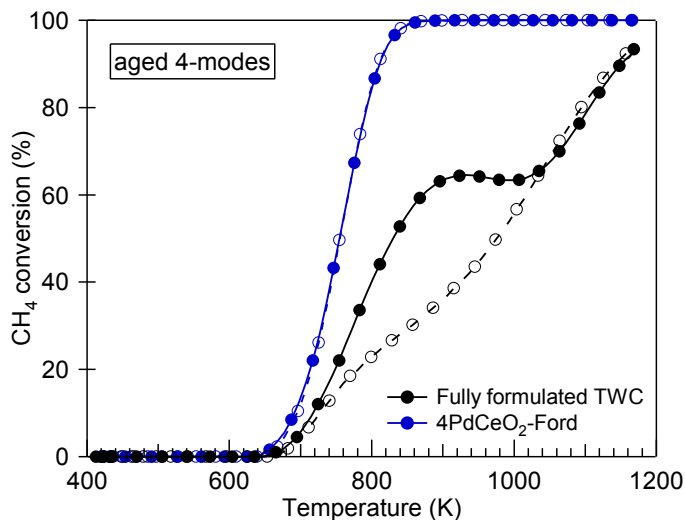


Figure 8.14: Steam reforming activity of 4PdCeO₂-Ford-IW and a fully formulated TWC after 4-modes aging (100 h, 1183 K).

To evaluate the performance of the prepared sample as a function of the (A/F) ratio, i.e. of the λ parameter, the milled catalyst was tested under synthetic gas composition at different λ (0.968 – 1.028) and the CH_4 , CO and NO_x conversions were evaluated as function of temperature. The lambda sweep was evaluated at 773 K and the obtained results are shown in Figure 8.15. From Figure 8.15 it can be observed that, unlike TWC for gasoline engines,¹⁷ the optimum λ is found in the rich region. In fact, the highest conversions for simultaneous NO_x reduction and CO and CH_4 oxidation is found at $\lambda = 0.977$. This confirms previous findings^{20,21} and further suggests methane steam reforming is the most effective methane abatement mechanism in three-way catalyst applications.

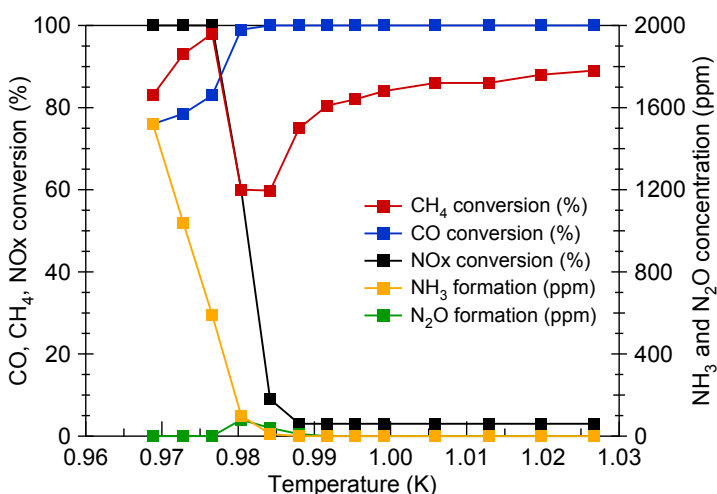


Figure 8.15: Synthetic reactor results with full gas mixture at 873 K.

The catalytic activity observed on a 4PdAcCeM monolith core, before and after aging, might be affected by the preparation and coating process. Nevertheless, the methane oxidation activity on degreened samples follows the same trend observed in lab-scale tests on powder catalysts, with the milled sample outperforming the commercial sample prepared by wet synthesis. Conversely, under steam reforming conditions they exhibit similar methane conversion, suggesting that the milling process does not improve steam reforming performances significantly. It is possible that the peculiar Pd-Ce surface arrangement of 4PdAcCeM plays a minor role under a $\text{CH}_4 + \text{H}_2\text{O}$ atmosphere, as mostly Pd^0 species are involved in the steam reforming reaction.³⁶ Further studies would be needed to understand the mechanisms occurring on the Pd/CeO₂ milled samples under steam reforming conditions.

8.4 Conclusions

The dry milling synthesis allowed for the preparation of highly active Pd/CeO₂ catalysts displaying promising activity for their industrial application in three-way catalysts. Indeed, a 4PdAcCe1473M sample, prepared by milling Palladium acetate nanopowders on a low surface area ceria (~4 m²/g, calcined at 1473 K prior to synthesis), achieved almost full methane conversion (above 95%) in high space velocity testing conditions under a gas mixture containing CO, CO₂ and H₂O, which are known methane oxidation inhibitors^{12,14} but are always present in large quantities in NGVs exhausts.²⁰

When the milled sample was coated on a monolith, it showed improved performance under methane oxidation conditions compared to other commercial reference samples, supported on high surface area ceria and alumina, and comparable activity for the steam reforming of methane. Nevertheless, established aging procedures resulted in significant deactivation, suggesting that either the catalyst composition and/or the washcoating process need further optimization. The evaluation of the simultaneous CH₄, CO and NO_x abatement as a function of λ confirmed the optimum working range of NGVs three-way catalysts to be in the rich region,²¹ indicating steam reforming as a promising methane abatement mechanism in TWC applications. Despite the contradicting results displayed by fresh and aged milled catalysts, the preparation of materials by dry mechano-chemical synthesis is worth further investigation, since it enables drastic reduction of the solvent and energy requirements for catalysts production, which are core issues of the 2030 EU objectives on sustainable processes.^{37,38} Consequently, future studies could be carried out on milled samples to improve the scale up of the synthesis and to investigate the parameters to optimize their coating onto structured supports commonly employed in catalytic converters.

8.5 References

- (1) Chen, H.; He, J.; Zhong, X. Engine Combustion and Emission Fuelled with Natural Gas: A Review. *Journal of the Energy Institute* **2019**, *92* (4), 1123–1136. <https://doi.org/10.1016/j.joei.2018.06.005>.
- (2) Nijboer, M. *The Contribution of Natural Gas Vehicles to Sustainable Transport*; IEA Energy Papers 2010/11; IEA: Paris Cedex 15, France, 2010. <https://doi.org/10.1787/5km4rm5c0pzp-en>.
- (3) Rood Werpy, M.; Santini, D.; Burnham, A.; Mintz, M. *Natural Gas Vehicles: Status, Barriers, and Opportunities*; ANL/ESD/10-4; Argonne National Laboratory, 2010; p 59.
- (4) Yeh, S. An Empirical Analysis on the Adoption of Alternative Fuel Vehicles: The Case of Natural Gas Vehicles. *Energy Policy* **2007**, *35* (11), 5865–5875. <https://doi.org/10.1016/j.enpol.2007.06.012>.
- (5) Han, J. W.; Mintz, M.; Wang, M. *Waste-to-Wheel Analysis of Anaerobic-Digestion-Based Renewable Natural Gas Pathways with the GREET Model*; ANL/ESD/11-6; Argonne National Laboratory, 2011; p 40.
- (6) Korakianitis, T.; Namasivayam, A. M.; Crookes, R. J. Natural-Gas Fueled Spark-Ignition (SI) and Compression-Ignition (CI) Engine Performance and Emissions. *Progress in Energy and Combustion Science* **2011**, *37* (1), 89–112. <https://doi.org/10.1016/j.pecs.2010.04.002>.
- (7) U.S. EPA. Global Greenhouse Gas Emissions Data <https://www.epa.gov/ghgemissions/global-greenhouse-gas-emissions-data>. (accessed Oct 12, 2019).
- (8) Clark, N. N.; McKain, D. L.; Johnson, D. R.; Wayne, W. S.; Li, H.; Akkerman, V.; Sandoval, C.; Covington, A. N.; Mongold, R. A.; Hailer, J. T.; et al. Pump-to-Wheels Methane Emissions from the Heavy-Duty Transportation Sector. *Environ. Sci. Technol.* **2017**, *51* (2), 968–976. <https://doi.org/10.1021/acs.est.5b06059>.
- (9) Engerer, H.; Horn, M. Natural Gas Vehicles: An Option for Europe. *Energy Policy* **2010**, *38* (2), 1017–1029. <https://doi.org/10.1016/j.enpol.2009.10.054>.
- (10) Gandhi, H. S.; Graham, G. W.; McCabe, R. W. Automotive Exhaust Catalysis. *Journal of Catalysis* **2003**, *216*(1–2), 433–442. [https://doi.org/10.1016/S0021-9517\(02\)00067-2](https://doi.org/10.1016/S0021-9517(02)00067-2).
- (11) *Commission Regulation (EU) No 582/2011 of 25 May 2011 Implementing and Amending Regulation (EC) No 595/2009 of the European Parliament and of the Council with Respect to Emissions from Heavy Duty Vehicles (Euro VI) and Amending Annexes I and III to Directive 2007/46/EC of the European Parliament and of the Council Text with EEA Relevance*; p 168.
- (12) Persson, K.; Pfefferle, L. D.; Schwartz, W.; Ersson, A.; Järås, S. G. Stability of Palladium-Based Catalysts during Catalytic Combustion of Methane: The Influence of Water. *Applied Catalysis B: Environmental* **2007**, *74* (3–4), 242–250. <https://doi.org/10.1016/j.apcatb.2007.02.015>.
- (13) Schwartz, W. R.; Ciuparu, D.; Pfefferle, L. D. Combustion of Methane over Palladium-Based Catalysts: Catalytic Deactivation and Role of the Support. *The Journal of Physical Chemistry C* **2012**, *116* (15), 8587–8593. <https://doi.org/10.1021/jp212236e>.

- (14) Gholami, R.; Alyani, M.; Smith, K. Deactivation of Pd Catalysts by Water during Low Temperature Methane Oxidation Relevant to Natural Gas Vehicle Converters. *Catalysts* **2015**, *5* (2), 561–594. <https://doi.org/10.3390/catal5020561>.
- (15) Huang, W.; Goodman, E. D.; Losch, P.; Cargnello, M. Deconvoluting Transient Water Effects on the Activity of Pd Methane Combustion Catalysts. *Industrial & Engineering Chemistry Research* **2018**, *57* (31), 10261–10268. <https://doi.org/10.1021/acs.iecr.8b01915>.
- (16) Einewall, P.; Tunestål, P.; Johansson, B. Lean Burn Natural Gas Operation vs. Stoichiometric Operation with EGR and a Three Way Catalyst; 2005. <https://doi.org/10.4271/2005-01-0250>.
- (17) Heck, R. M.; Farrauto, R. J.; Gulati, S. T. *Catalytic Air Pollution Control: Commercial Technology*, 3rd ed.; John Wiley & Sons, 2012.
- (18) Farrauto, R. J.; Deeba, M.; Alerasool, S. Gasoline Automobile Catalysis and Its Historical Journey to Cleaner Air. *Nat Catal* **2019**, *2* (7), 603–613. <https://doi.org/10.1038/s41929-019-0312-9>.
- (19) Matam, S. K.; Chiarello, G. L.; Lu, Y.; Weidenkaff, A.; Ferri, D. PdO_x/Pd at Work in a Model Three-Way Catalyst for Methane Abatement Monitored by Operando XANES. *Top Catal* **2013**, *56* (1–8), 239–242. <https://doi.org/10.1007/s11244-013-9960-1>.
- (20) Xi, Y.; Ottinger, N.; Liu, Z. G. Development of a Lab Reactor System for the Evaluation of Aftertreatment Catalysts for Stoichiometric Natural Gas Engines; 2017. <https://doi.org/10.4271/2017-01-0999>.
- (21) Ferri, D.; Elsener, M.; Kröcher, O. Methane Oxidation over a Honeycomb Pd-Only Three-Way Catalyst under Static and Periodic Operation. *Applied Catalysis B: Environmental* **2018**, *220*, 67–77. <https://doi.org/10.1016/j.apcatb.2017.07.070>.
- (22) Arosio, F.; Colussi, S.; Trovarelli, A.; Groppi, G. Effect of Alternate CH₄-Reducing/Lean Combustion Treatments on the Reactivity of Fresh and S-Poisoned Pd/CeO₂/Al₂O₃ Catalysts. *Applied Catalysis B: Environmental* **2008**, *80* (3–4), 335–342. <https://doi.org/10.1016/j.apcatb.2007.11.030>.
- (23) Fouladvand, S.; Schernich, S.; Libuda, J.; Grönbeck, H.; Pingel, T.; Olsson, E.; Skoglundh, M.; Carlsson, P.-A. Methane Oxidation Over Pd Supported on Ceria–Alumina Under Rich/Lean Cycling Conditions. *Topics in Catalysis* **2013**, *56* (1–8), 410–415. <https://doi.org/10.1007/s11244-013-9988-2>.
- (24) Bounechada, D.; Groppi, G.; Forzatti, P.; Kallinen, K.; Kinnunen, T. Effect of Periodic Lean/Rich Switch on Methane Conversion over a Ce–Zr Promoted Pd–Rh/Al₂O₃ Catalyst in the Exhausts of Natural Gas Vehicles. *Applied Catalysis B: Environmental* **2012**, *119–120*, 91–99. <https://doi.org/10.1016/j.apcatb.2012.02.025>.
- (25) Hellman, A.; Resta, A.; Martin, N. M.; Gustafson, J.; Trincherro, A.; Carlsson, P.-A.; Balmes, O.; Felici, R.; van Rijn, R.; Frenken, J. W. M.; et al. The Active Phase of Palladium during Methane Oxidation. *J. Phys. Chem. Lett.* **2012**, *3* (6), 678–682. <https://doi.org/10.1021/jz300069s>.
- (26) Huang, F.; Chen, J.; Hu, W.; Li, G.; Wu, Y.; Yuan, S.; Zhong, L.; Chen, Y. Pd or PdO: Catalytic Active Site of Methane Oxidation Operated Close to Stoichiometric Air-to-Fuel for Natural Gas Vehicles. *Applied Catalysis B: Environmental* **2017**, *219*, 73–81. <https://doi.org/10.1016/j.apcatb.2017.07.037>.

- (27) Nilsson, J.; Carlsson, P.-A.; Martin, N. M.; Adams, E. C.; Agostini, G.; Grönbeck, H.; Skoglundh, M. Methane Oxidation over Pd/Al₂O₃ under Rich/Lean Cycling Followed by Operando XAFS and Modulation Excitation Spectroscopy. *Journal of Catalysis* **2017**, *356*, 237–245. <https://doi.org/10.1016/j.jcat.2017.10.018>.
- (28) McCarty, J. G. Kinetics of PdO Combustion Catalysis. *Catalysis Today* **1995**, *26* (3–4), 283–293. [https://doi.org/10.1016/0920-5861\(95\)00150-7](https://doi.org/10.1016/0920-5861(95)00150-7).
- (29) Datye, A. K.; Bravo, J.; Nelson, T. R.; Atanasova, P.; Lyubovsky, M.; Pfefferle, L. Catalyst Microstructure and Methane Oxidation Reactivity during the Pd↔PdO Transformation on Alumina Supports. *Applied Catalysis A: General* **2000**, *198* (1–2), 179–196. [https://doi.org/10.1016/S0926-860X\(99\)00512-8](https://doi.org/10.1016/S0926-860X(99)00512-8).
- (30) Miller, J. B.; Malatpure, M. Pd Catalysts for Total Oxidation of Methane: Support Effects. *Applied Catalysis A: General* **2015**, *495*, 54–62. <https://doi.org/10.1016/j.apcata.2015.01.044>.
- (31) Farrauto, R. J.; Lampert, J. K.; Hobson, M. C.; Waterman, E. M. Thermal Decomposition and Reformation of PdO Catalysts; Support Effects. *Applied Catalysis B: Environmental* **1995**, *6*(3), 263–270. [https://doi.org/10.1016/0926-3373\(95\)00015-1](https://doi.org/10.1016/0926-3373(95)00015-1).
- (32) Groppi, G.; Cristiani, C.; Lietti, L.; Ramella, C.; Valentini, M.; Forzatti, P. Effect of Ceria on Palladium Supported Catalysts for High Temperature Combustion of CH₄ under Lean Conditions. *Catalysis Today* **1999**, *50* (2), 399–412. [https://doi.org/10.1016/S0920-5861\(98\)00518-5](https://doi.org/10.1016/S0920-5861(98)00518-5).
- (33) Colussi, S.; Trovarelli, A.; Cristiani, C.; Lietti, L.; Groppi, G. The Influence of Ceria and Other Rare Earth Promoters on Palladium-Based Methane Combustion Catalysts. *Catalysis Today* **2012**, *180* (1), 124–130. <https://doi.org/10.1016/j.cattod.2011.03.021>.
- (34) McCabe, R. W.; Trovarelli, A. Forty Years of Catalysis by Ceria: A Success Story. *Applied Catalysis B: Environmental* **2016**, *197*, 1. <https://doi.org/10.1016/j.apcatb.2016.04.044>.
- (35) Maunula, T.; Kallinen, K.; Savimäki, A.; Wolff, T. Durability Evaluations and Rapid Ageing Methods in Commercial Emission Catalyst Development for Diesel, Natural Gas and Gasoline Applications. *Topics in Catalysis* **2016**, *59* (10–12), 1049–1053. <https://doi.org/10.1007/s11244-016-0588-9>.
- (36) Mihai, O.; Smedler, G.; Nylén, U.; Olofsson, M.; Olsson, L. The Effect of Water on Methane Oxidation over Pd/Al₂O₃ under Lean, Stoichiometric and Rich Conditions. *Catalysis Science & Technology* **2017**, *7* (14), 3084–3096. <https://doi.org/10.1039/C6CY02329K>.
- (37) Geels, F.; Turnheim, B.; Asquith, M.; Kern, F.; Kivimaa, P.; European Environment Agency. *Sustainability Transitions: Policy and Practice.*; 2019.
- (38) Eurostat. *Sustainable Development in the European Union: Overview of Progress towards the SDGs in an EU Context.*; Publications Office of the European Union: Luxembourg, 2019.

9 Preliminary Study on the Effect of Ceria Exposed Facets on Pd/CeO₂ Methane Oxidation Catalysts

Abstract

The effect of different exposed ceria surfaces on the preparation and methane oxidation activity of Pd/CeO₂ samples was investigated experimentally on ceria nanoparticles with controlled morphology prepared by hydrothermal methods. Palladium was deposited on ceria nanoshapes (nanocubes and nanorods) by incipient wetness impregnation (IW) and dry mechano-chemical synthesis (M), using palladium metal and palladium acetate as metal precursors. Samples were tested for low temperature methane oxidation and their morphological and redox properties were evaluated by means of XRD and HRTEM characterization and temperature programmed oxidation (TPO) and reduction (TPR) tests, respectively. In order to have comparable surface area, reference IW and M samples were prepared on commercial polycrystalline ceria samples calcined at 773 K prior to synthesis. Preliminary results show that undercoordinated {100} and {110} surfaces affect negatively the methane oxidation performance, {100} planes also inhibiting efficient Pd spreading during milling.

9.1 Introduction

The widespread use of ceria as catalytic material is attested by the increasing number of ceria-related publications, where the fundamental¹⁻⁸ and applied⁹⁻¹¹ aspects of cerium oxide are explored in depth. One of the key properties determining its success is its Oxygen Storage Capacity (OSC), representing the ceria capacity to exchange highly reactive oxygen species from the lattice O by a local reduction of Ce⁴⁺ to Ce³⁺ ions while maintaining its crystalline structure,^{1,12} therefore requiring very low energies. In addition, CeO₂ is able to create strong interaction with noble and transition metals alike, creating highly reactive surface species,¹³⁻¹⁹ preventing sintering of the supported nanoparticles²⁰ or promoting the diffusion of metals as single ions on the surface.^{21,22} In order to maximize the surface available for metal-ceria interaction, the synthesis of ceria with high thermal stability and increased surface area²³⁻²⁵ or mesoporous features^{26,27} is currently a matter of great interest.

In addition to the above requirements, the properties of CeO₂ were also observed to be dependent on the exposed surface planes and extensive studies were carried out involving the most stable low index surfaces of CeO₂, namely {111}, {110} and {100} facets.²⁸⁻³⁵ DFT calculations showed that the {110} surface has the lowest oxygen vacancy formation energy, followed by the {100} and {111} surface,^{2,6} the latter being the most stable surface. Experimentally, the effect of the exposed ceria facets was studied on model catalysts⁸ or on ceria nanoparticles with defined morphology, whose synthesis has been optimized through the years.^{29,30} In fact, by treating cerium ions in a solution with controlled pH and temperature, the growth of nanocrystals can be followed resulting in defined nanostructures exposing specific ceria facets.³⁶ Ceria nanocubes are known to expose {100} surfaces, while ceria nanorods expose mainly {110} or {100}+{111} facets.³⁶ The instability of these surfaces makes their unambiguous identification extremely difficult, particularly under reaction conditions.³⁷ Nevertheless, several attempts were made to highlight the structure-activity correlation for different ceria morphologies in a variety of reactions. In particular, the peculiar surface arrangement of undercoordinated planes proved to be especially active in CO activation^{22,31,38,39} and soot oxidation,^{34,40,41} due to the higher oxygen mobility and/or to the formation of reactive peroxide species O₂²⁻,⁶ while hydrogenation reactions are favored on low-vacancy surfaces.⁴²⁻⁴⁴ Due to the low stability of the exposed {110} and {100} planes, studies are usually carried out in reactions occurring at low temperatures or ambient conditions. Consequently, limited work was conducted to evaluate the shape-dependent methane oxidation activity of ceria-based catalysts.^{45,46} Here we investigate experimentally

the effect of ceria nanocubes and nanorods on Pd/CeO₂ catalysts for methane oxidation prepared by conventional incipient wetness impregnation and dry milling synthesis. This chapter presents the preliminary results of activity measurements and characterization carried out on these samples, as the work is still in progress and further in depth characterization is needed to fully address the several issues we have encountered investigating these specific aspects.

9.2 Experimental

Ceria nanocubes and nanorods were obtained following an established hydrothermal synthesis,^{29,34} reported in detail in section 2.1. Briefly, ceria nanocubes (CeNC) were prepared starting from a Ce(NO₃)₃·6H₂O solution, adding dropwise 210 ml of a 6.9M NaOH solution under vigorous mixing to induce precipitation. The obtained suspension was then transferred in a 300 ml Teflon-lined Parr 4843 autoclave and heated at 453 K for 24 hours. After cooling, the precipitate was recovered by centrifugation and washed three times in distilled water and ethanol for further purification and separation. Ceria nanorods (CeNR) were synthesized by adding dropwise 200 ml of a 9.45M NaOH solution to a CeCl₃·7H₂O solution. After precipitation, the suspension was thermally aged in autoclave at 373 K for 48 h, cooled and centrifuged following the same procedure reported above. The obtained precipitates were dried overnight at 333 K and calcined at 723 K for 4 hours prior to their use. A reference polycrystalline ceria was obtained by calcination of commercial cerium oxide (Treibacher Industrie, AG) at 773 K for 3 hours, with a final surface area of 67 m²/g.

On all supports, Pd was deposited by conventional incipient wetness impregnation (IW) and dry milling synthesis (M) using metallic Pd or Palladium acetate as metal precursor to reach a final 1wt.% Pd loading. Pd/CeO₂ IW samples were prepared dropping an appropriate amount of Pd(NO₃)₂ solution (Sigma Aldrich, 99.999%) on the ceria powders; the wet powders were then dried at 373 K overnight and calcined for 3 hours in static air at 723 K or 773 K depending on the support calcination temperature. Pd/CeO₂ milled samples were synthesized by milling the precursor powders (10 mg of Pd black (Sigma-Aldrich) or 21.1 mg of Pd(OAc)₂ (Sigma-Aldrich, 99.9%) with 990 mg of cerium oxide) in a Pulverisette 23 mini-mill, using a 15 ml ZrO₂ grinding jar loaded with a single ZrO₂ sphere (ϕ15 mm, 10 g weight). Milling was carried out at 15 Hz for 10 or 20 minutes for PdCeM and PdAcCeM, respectively.

The morphological, textural and redox properties of prepared samples were characterized by means of TEM and HRTEM analysis, X-ray diffraction analysis, BET surface area, temperature programmed oxidation (TPO) and reduction (TPR) tests. Details of the characterization tests are reported in Chapter 2, section 2.2. Methane oxidation activity was investigated by one first combustion cycle up to 723 K/773 K to avoid sintering of the support and one subsequent cycle up to 1173 K.

9.3 Results

The physico-chemical properties of the support oxides and catalyst samples prepared for this study are reported in Table 9.1. A preliminary comparison of the supports with different morphology was carried out by means of X-ray diffraction and H₂-TPR (Figure 9.1 and Figure 9.2, respectively).

Table 9.1: Physico-chemical properties of catalytic materials and support oxides prepared for this study.

Sample	Calcination Temperature (K)	BET surface area (m ² /g)	Nominal Pd loading (wt%)
Ce(773)	773	67.0	-
CeNC	723	29.0	-
CeNR	723	79.7	-
PdCe(773)IW	773	66.0	0.95 ^b
PdCe(773)M	773 ^a	64.7	0.77 ^b
PdAcCe(773)M	773 ^a	64.9	1
PdCeNC IW	723	28.0	1
PdCeNC M	723 ^a	29.2	1
PdAcCeNC M	723 ^a	29.5	1
PdCeNR IW	723	79.6	1
PdCeNR M	723 ^a	80.6	1
PdAcCeNR M	723 ^a	81.0	1

a: calcination temperature of the support only. b: measured by ICP-mass elemental analysis.

Ceria nanorods and polycrystalline ceria, characterized by high surface area (ca. 80 m²/g and 70 m²/g, respectively), display broad diffraction peaks (Figure 9.1). Conversely, CeNC exhibits sharper diffraction peaks, having a measured surface area of ca. 30 m²/g, and the measured intensity ratio of {200}, {220}, {311}, {400} and {331} planes to the {111} surface is increased compared to the reference (Table 9.2).³⁴ On CeNR, the {200}/{220}

intensity ratio drops from 0.6 of the reference fluorite structure and polycrystalline ceria to 0.52, indicating a {220} preferential growing axis direction for the rods.^{30,47}

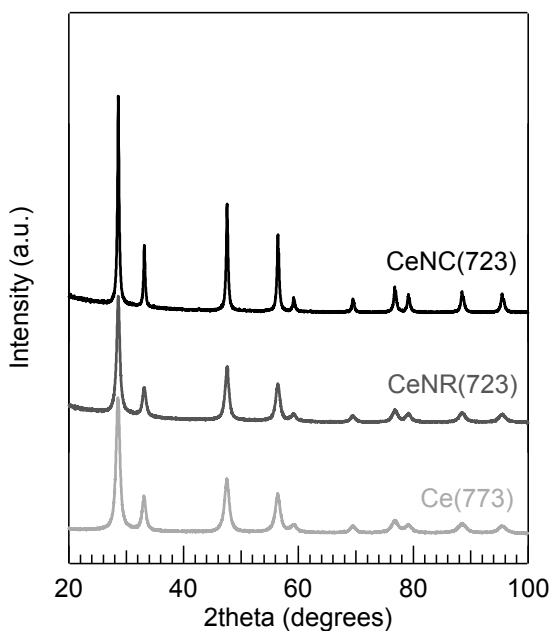


Figure 9.1: XRD profiles of the support oxides considered in this study.

Table 9.2: Measured intensity of the diffraction peaks collected on considered ceria supports.

Planes	Ref (I%) ^a	Ce(773)	CeNC	CeNR
111	100	100	100	100
200	27	24.99	31.45	22.54
220	45	40.16	54.29	42.55
311	33	27.27	39.67	31.33
222	6	4.78	6.88	5.62
400	5	4.64	7.37	5.10
331	10	8.29	14.24	10.67

a: intensity ratio reference of pure fluorite cubic structure of CeO₂ (*Fm3m*, JCPDS 01-075-0120).

Evolution of H₂ uptake during H₂-TPR tests is shown in Figure 9.2 for all support oxides prepared for this study. As expected, the low temperature reducibility increases in the order Ce(773) < CeNC(723) < CeNR(723), in agreement with simulated³⁸ and experimental results.^{31,32,34,46} The quantitative analysis of the consumed moles of H₂, reported in Figure 9.2, shows an increased total H₂ uptake for Ce(773) and CeNR likely due to the higher surface area.

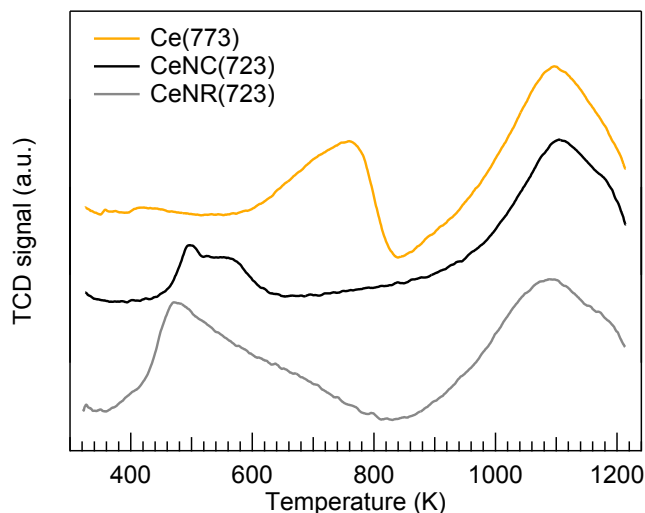


Figure 9.2: H₂-TPR profiles of the prepared support oxides.

Table 9.3: H₂ consumption on CeO₂ supports with different morphology (μmol H₂/g).

Sample	Peak 1		Peak 2	
	T (K) ^a	H ₂ uptake	T (K)	H ₂ uptake
Ce(773)	762	436	1098	668
CeNC(723)	495	179	1106	462
CeNR(723)	470	683	1090	498

a: temperature of the main reduction peak.

9.3.1 Polycrystalline CeO₂

Reference samples were prepared on polycrystalline ceria calcined at lower temperature (773 K) in order to have comparable surface area compared to the controlled-morphology ceria supports. HRTEM characterization of the PdCeM sample prepared on CeO₂(773) shows that the support oxide is constituted by small ceria crystallites of about 6-10 nm in size. Figure 9.3(A) shows a general view of the sample, exhibiting an excellent crystallite size distribution. However, neither Pd or PdO nanoparticles are seen, nor the amorphous shell over the ceria crystallites. The lack of segregated Pd/PdO nanoparticles in the sample indicates that palladium has indeed “reacted” with ceria, but the absence of the amorphous shell around ceria prevents any direct evidence for this. Figure 9.3(B,C) shows representative HRTEM images recorded over the sample. Well-defined ceria crystallites are clearly identified, but no evident shell around them is recognized: it can be hypothesized

that the shell is too thin for detection, or that palladium enters the subsurface of ceria crystallites.

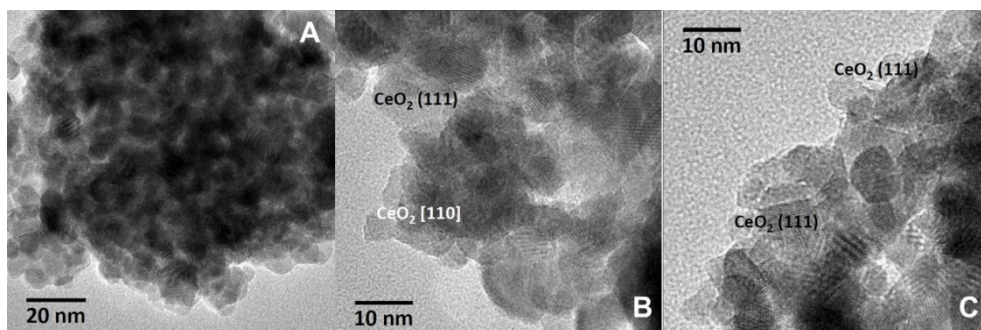


Figure 9.3: Representative HRTEM images of PdCe(773)M.

As shown in Chapter 6, the increased support surface area (with respect to the first studies involving ceria calcined at 1173 K, see Chapter 3) appears to have a negative effect on the catalytic methane combustion performance of both milled and IW samples. Nevertheless, the activity trend is maintained with the milled samples outperforming the reference IW catalyst by over 30 K (Figure 9.4).

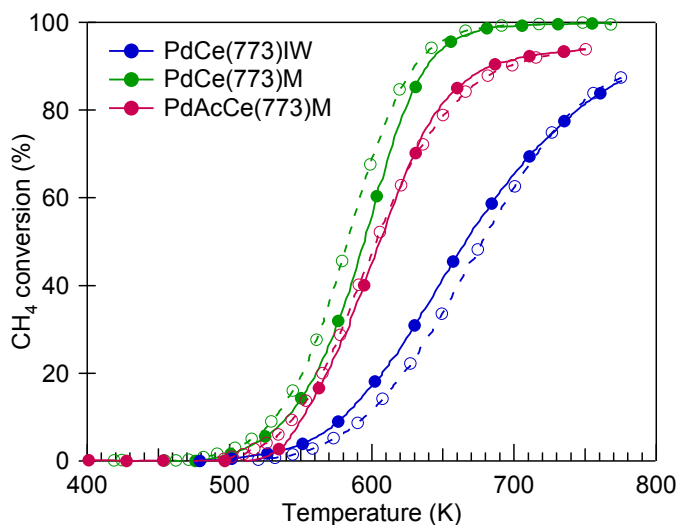


Figure 9.4: Methane oxidation activity of Pd/Ce(773) samples; light-off cycle to 773 K.

Moreover, as shown in Figure 9.5, they are able to retain their activity even after sintering of the support. On PdCeIW, the catalytic activity is completely lost after one heating ramp up to 1173 K, likely due to the collapse of the pores after thermal treatment (Figure 9.6) and the

subsequent encapsulation of Pd. It may be hypothesized that the milling process distributes the active phase mostly on the outer surface of the support oxide compared to the smaller inner pores, as the spreading mechanism is mostly physical,⁴⁸ while the capillary mechanism in wet syntheses enables the distribution of Pd species evenly inside the pores. Consequently, on milled samples less palladium would be lost during sintering of the support at higher temperatures.

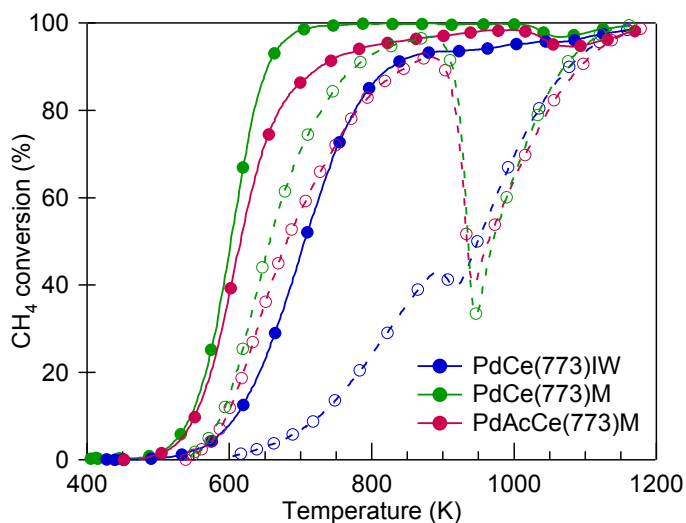


Figure 9.5: Methane oxidation activity of Pd/Ce(773) samples; light-off cycle to 1173 K.

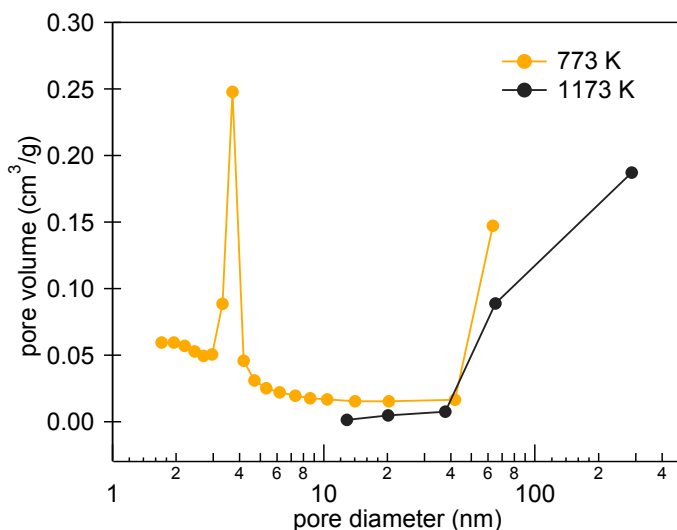


Figure 9.6: Pore size distribution of polycrystalline ceria calcined at 773 K and 1173 K.

More information on the state of Pd/PdO can be inferred from the analysis of O₂ release and uptake during TPO tests, shown in Figure 9.7 (with quantitative analysis reported in Table 9.4). Uptake 0 corresponds to the oxidation of metallic Pd and Pd(OAc)₂ precursors on PdCe(773)M and PdAcCe(773)M, respectively, during the first heating cycle. On the milled samples, the formed PdO species decompose almost completely at around 1030 K (Release 1); during cooling, only 50% of the loaded palladium continues to participate in the cycling behavior, possibly due to encapsulation of some metallic Pd caused by sintering of CeO₂. In addition, the slightly higher PdO decomposition temperature exhibited on PdCe(773)M (Figure 9.7) suggests an enhanced Pd-Ce interaction on this sample compared to PdAcCe(773)M. On PdCe(773)IW, the oxygen uptake and release in the first heating ramp (Uptake 0 and Release 1 in Table 9.4) are barely discernible, and only a 8 μmol O₂/g uptake during cooling can be observed corresponding to 18% of the loaded palladium (Uptake 1). In the following cycles (Release 3 and Uptake 3) only ~25% of Pd contributes to the decomposition/re-oxidation behavior, suggesting an extensive loss of palladium species accessible by the gas phase due to sintering of the support oxide.

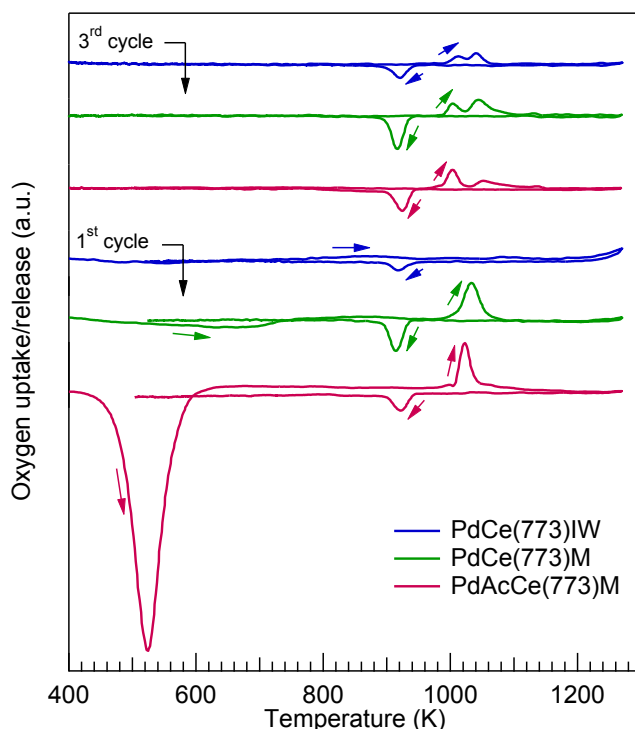


Figure 9.7: TPO profiles of Pd/Ce(773) samples, 1st and 3rd heating/cooling cycle.

Table 9.4: Quantitative analysis of oxygen released and consumed during TPO tests on Pd/Ce(773) samples, 1st and 3rd heating/cooling cycles.

Sample name	I cycle			III cycle	
	Uptake 0 ($\mu\text{mol O}_2/\text{g}$) ^a	Release 1 ($\mu\text{mol O}_2/\text{g}$)	Uptake 1 ($\mu\text{mol O}_2/\text{g}$)	Release 3 ($\mu\text{mol O}_2/\text{g}$)	Uptake 3 ($\mu\text{mol O}_2/\text{g}$)
PdCe(773)IW	-	-	8.0 (18)	10.8 (24)	13.2 (29)
PdCe(773)M	41.9 (116)	34.5 (95)	19.8 (55)	24.4 (68)	19.8 (55)
PdAcCe(773)M	377 (802)	34.6 (74)	16.7 (36)	21.3 (45)	21.0 (45)

a: in parenthesis is reported the corresponding calculated amount of cycling Pd (%).

The nature of the palladium species supported on polycrystalline ceria were further characterized by H₂-TPR experiments. Hydrogen evolution profiles (Figure 9.8) show a single broad peak at around 323 K for PdCe(773)IW, while a bimodal peak with a clear PdH_y decomposition peak at 330 K is observed on the milled samples. Analysis of the hydrogen uptake profiles suggests a uniform dispersion of smaller PdO nanoparticles on the sample prepared by incipient wetness impregnation, while on the milled samples the coexistence of large PdO particles and PdO_x species in strong interaction with ceria can be deduced, based on previous literature studies.^{49,50} PdCe(773)M displays the strongest Pd-Ce interaction, exhibiting a broad decomposition peak between 280 and 400 K. On all samples, the amount of H₂ consumed is much larger than the hydrogen required for stoichiometric PdO reduction, as reported in Table 9.5, indicating a high degree of Pd-promoted surface ceria reduction.

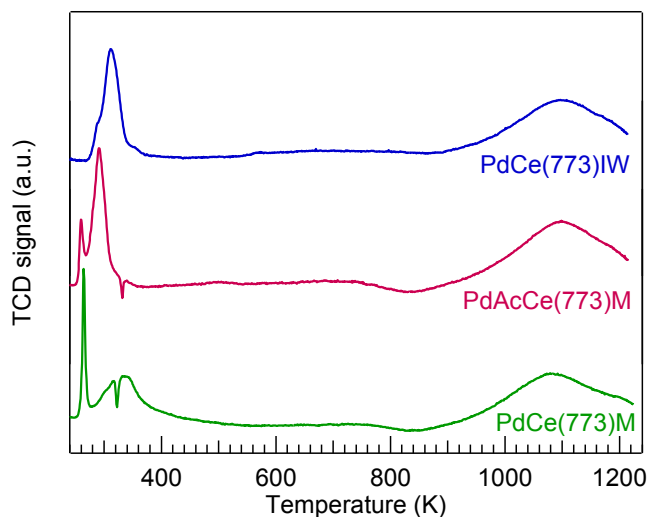


Figure 9.8: H₂-TPR profiles of Pd/Ce(773) samples. Reduction in H₂ was carried out after pretreatment in air at 623 K for 1 hour.

Table 9.5: H₂ consumption during TPR tests performed on Pd/Ce(773) samples (μmol H₂/g).

Sample	Peak 1		Peak 2		Theoretical H ₂ uptake for PdO ^b
	T (K) ^a	H ₂ uptake	T (K)	H ₂ uptake	
PdCe(773)IW	303	374	1100	584	82
PdCe(773)M	264	412	1082	437	72
PdAcCe(773)M	292	440	1098	701	94

a: temperature of the main reduction peak. b: H₂ for stoichiometric PdO reduction.

9.3.2 Ceria Nanocubes (CeNC)

The morphology of prepared nanoparticles was verified by TEM and HRTEM. Through hydrothermal synthesis, ceria nanocubes with an average size of 10-30 nm were obtained, as shown in Figure 9.9. The edges of the ceria nanocubes are sharp and the corners are slightly rounded.^{34,51}

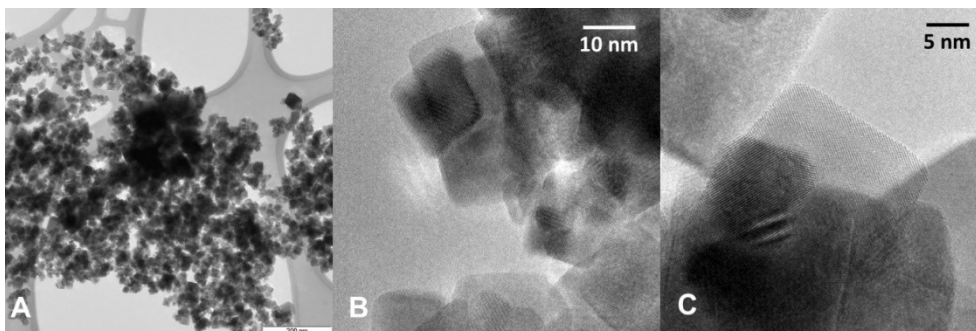


Figure 9.9: Representatives TEM (A) and HRTEM (B,C) images of ceria nanocubes after calcination at 723 K.

As shown in Figure 9.10 and Figure 9.11, which report the HRTEM images of the samples milled with metallic Pd and Palladium acetate after one combustion cycle up to 723 K, respectively, the mild milling process has a minor effect on the morphology of the ceria support. On PdCeNC M (Figure 9.10) the cubic morphology of the ceria nanocubes, again exhibiting rounded corners, can be clearly recognized. No individual Pd nanoparticles are observed and no Pd aggregates are visible, suggesting a good dispersion of Pd. In contrast very small entities are detected in the HRTEM images, which are too small to make an unambiguous identification given the absence of lattice fringes. These entities are encircled for a better identification in Figure 9.10(A,C,D) and measure about 0.5-1 nm in size. On the other hand, the surface of the ceria nanocubes does not appear to be covered by any amorphous layer, except in a few cases where the amorphous structure occurs more in the

form of aggregates rather than as a thin shell over the ceria nanocube crystallites (see arrow in Figure 9.10(B)). In this case, though, the lack of the amorphous shell is not an effect of the surface area, because Pd/ceria samples prepared on ceria of about 27 m²/g (see Chapter 6) show indeed the amorphous layer. PdAcCeNC M exhibits a virtually identical arrangement, except for the size of the Pd ensembles identified in the images (Figure 9.11(A-D)). Their size is below 1 nm and mostly about 0.5 nm. Entities smaller than 0.5 nm may exist in the sample, but they are under the detection limit of the microscope.

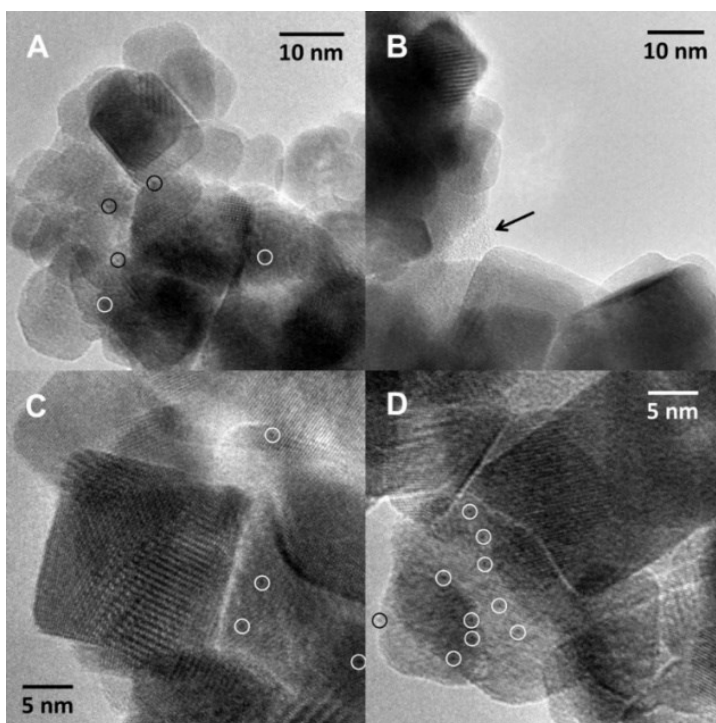


Figure 9.10: HRTEM images of PdCeNC M.

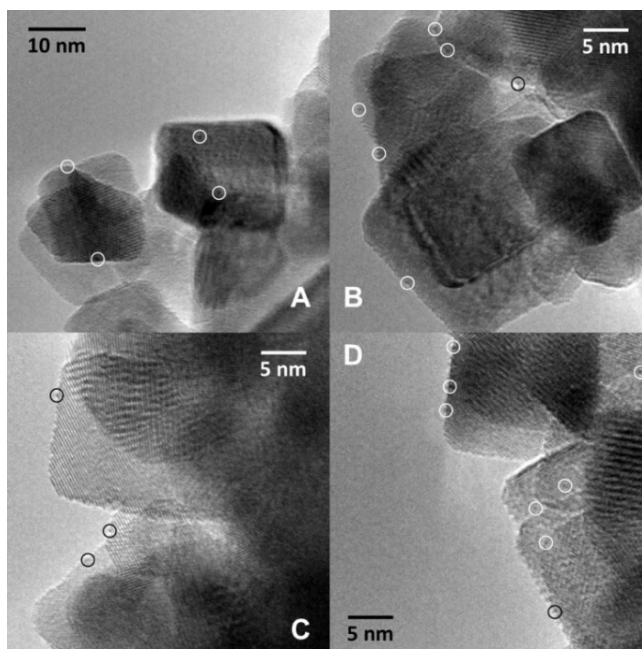


Figure 9.11: HRTEM images of PdAcCeNC M.

On PdCeNC IW, a uniform distribution of palladium nanoclusters on the surface can be observed. Figure 9.12(A) corresponds to BF-TEM image of the sample at low magnification. Nanocubes of about 10-20 nm are identified with rounded corners, but no Pd particles are identified, again suggesting an excellent dispersion of Pd on ceria. Figure 9.12(B) shows a HRTEM image of a ceria nanocube oriented along the $\{100\}$ crystallographic direction, with ceria $\{200\}$ planes at 2.7 \AA . The surface of the ceria nanocubes are decorated with nanoparticles of about 0.5-1 nm in size, which likely correspond to Pd entities (see particles marked by arrows in the inset in Figure 9.12(B)). Another similar HRTEM image is shown in Figure 9.12(C). Pd mostly occurs as sub-nanometric nanoparticles.

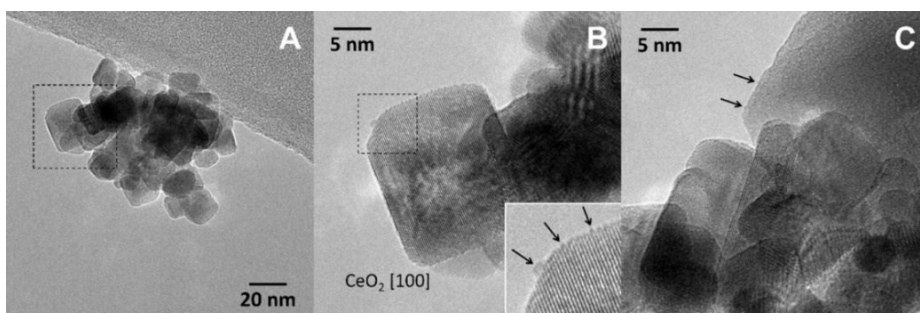


Figure 9.12: HRTEM images of PdCeNC IW.

Interestingly, despite the uniform dispersion of sub-nanometric particles reported by HRTEM images in Figure 9.10 - Figure 9.12, palladium supported on nanocubic ceria exhibits poor methane oxidation activity, irrespective of the catalyst synthesis route (Figure 9.13). When combustion tests are performed up to 1173 K, the sample prepared by incipient wetness displays the best catalytic performance and is able to recover some activity during cooling (Figure 9.14), unlike Pd/CeNC samples prepared by dry milling.

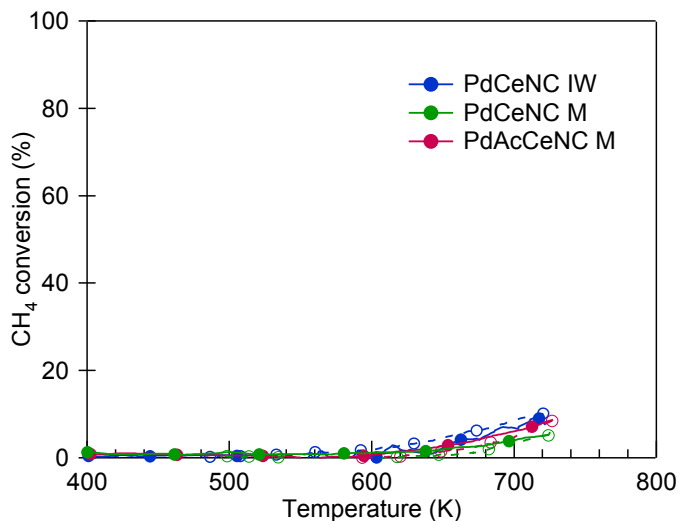


Figure 9.13: Methane oxidation activity of Pd/CeNC samples; light-off cycle to 723 K.

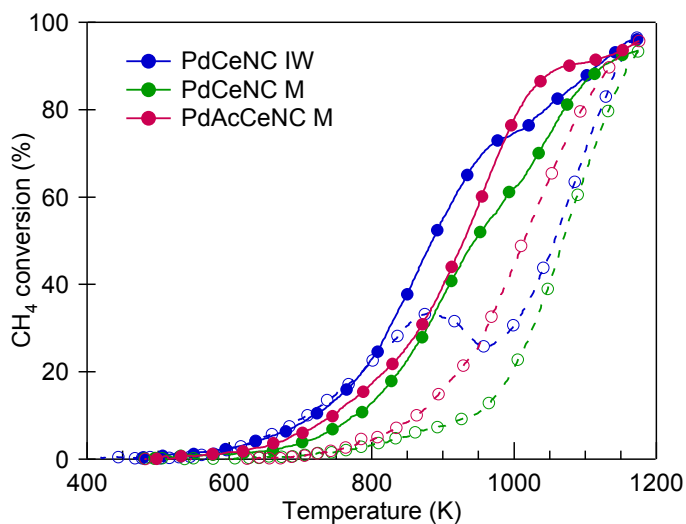


Figure 9.14: Methane oxidation activity of Pd/CeNC samples; light-off cycle to 1173 K.

TPO and TPR profiles provide further insight into the redox properties of the supported palladium species. Qualitative analysis of oxygen release and uptake profiles during TPO experiments (Figure 9.15) indicates the presence of close interacting species on PdAcCeNC M, decomposing at around 1100 K, while PdCeNC M and PdCeNC IW exhibit a predominant bulk PdO decomposition feature at 1030 K and a lower amount of cycling palladium.⁵²

Conversely, H₂-TPR profiles, reported in Figure 9.16 for nanocubes-supported samples, suggest a uniform dispersion of small PdO nanoparticles on PdCeNC IW and PdAcCeNC M, in good agreement with the palladium species observed in HRTEM images (Figure 9.12 and Figure 9.11, respectively). On PdCeNC M the coexistence of small PdO entities with large PdO particles can be deduced by the two reduction peaks at 273 K and 315 K, followed by the decomposition of hydride species.⁵⁰ On this sample, the formation of larger palladium oxide clusters might be linked to the amorphous clusters indicated by HRTEM in Figure 9.10(B). Quantitative analysis of the hydrogen consumption (Table 9.6) clearly indicates a stronger Pd-Ce interaction developed on PdCeNC IW, where the Pd-promoted ceria reduction at low temperature differs significantly from the one measured on milled samples (530 $\mu\text{mol H}_2/\text{g}$ for the IW sample against ca. 230 $\mu\text{mol H}_2/\text{g}$ for both M samples).

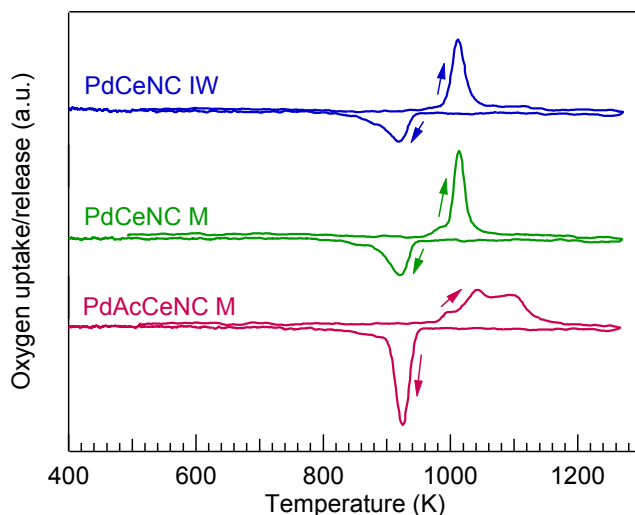


Figure 9.15: Oxygen uptake and release profiles of Pd/CeNC samples; 3rd TPO cycle.

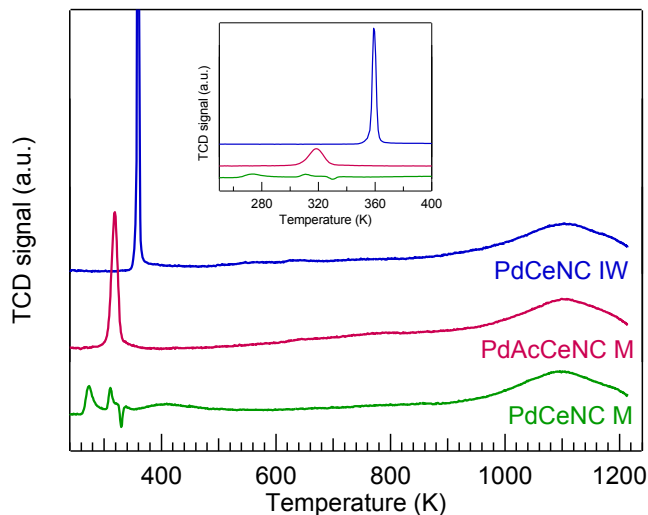


Figure 9.16: H₂-TPR profiles of Pd/CeNC samples. Reduction in H₂ was carried out after pretreatment in air at 623 K for 1 hour. Inset: focus on the H₂ uptake during PdO decomposition.

Table 9.6: H₂ consumption during TPR tests performed on Pd/CeNC samples ($\mu\text{mol H}_2/\text{g}$).

Sample	Peak 1		Peak 2		Theoretical H ₂ uptake for PdO ^b
	T (K) ^a	H ₂ uptake	T (K) ^a	H ₂ uptake	
PdCeNC IW	359	530	1105	532	94
PdCeNC M	273	220	1100	464	94
PdAcCeNC M	318	235	1105	508	94

a: temperature of the main reduction peak. b: H₂ for stoichiometric PdO reduction.

9.3.3 Ceria Nanorods (CeNR)

TEM analysis was performed on ceria nanorods after synthesis and calcination at 723 K. The average size of the prepared nanorods ranges between 100 and 500 nm of length and 10 nm of diameter (Figure 9.17(A,B)), corresponding to the desired $L \gg D$ aspect ratio. In addition many defects can be observed due to nucleation of side branches along the rod length, which appear as darker spots in the lower magnification TEM images (Figure 9.17(A,B) and are clearly shown in Figure 9.17(C,D). Their formation was promoted by using CeCl₃ as cerium precursor in the hydrothermal synthesis.⁵³

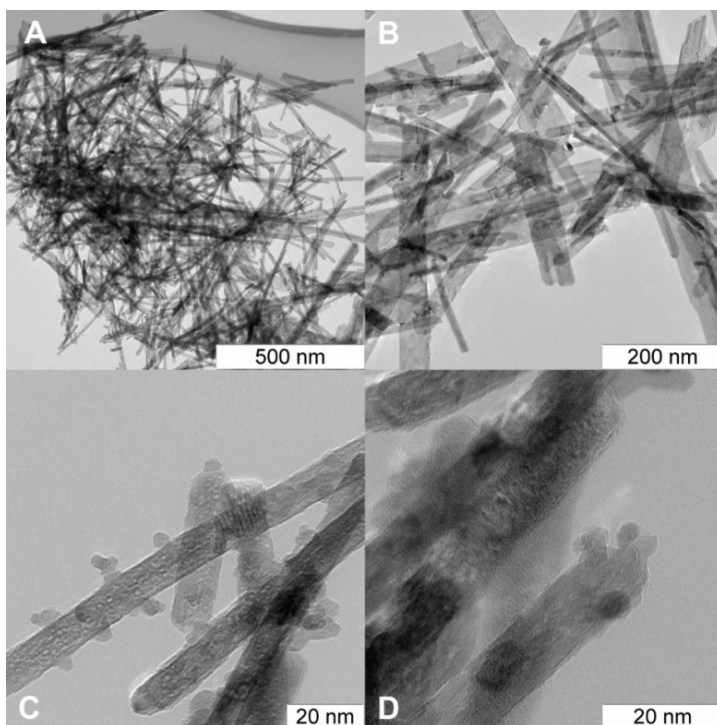


Figure 9.17: TEM images of ceria nanorods, as prepared.

Mild mechano-chemical treatment (20 minutes at 15 Hz, 1 ZrO₂ grinding ball) causes the breaking down of longer rods, reducing the average rod length to about 200 nm (Figure 9.18) but without other significant change in their morphology. On PdAcCeNR M, identification of palladium is not possible due to low resolution of TEM analysis; darker spots appearing on the rods (Figure 9.18(B)) might be equally due to the side branches or large palladium particles. High Resolution TEM, which is planned to be carried out in the future, would be needed for unambiguous identification.

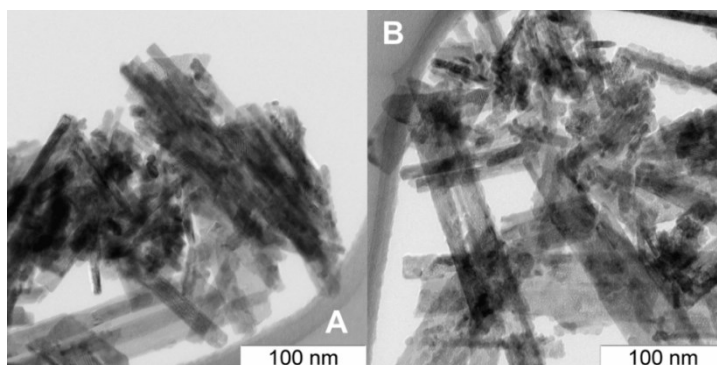


Figure 9.18: TEM images of PdAcCeNR M sample.

Methane combustion tests performed on samples supported on CeNR display a similar trend as the polycrystalline ceria calcined at 773 K, with the milled samples outperforming the impregnated catalyst in the order PdCeNR IW < PdAcCeNR M < PdCeNR M (Figure 9.19 and Figure 9.20 for methane oxidation tests up to 723 K and 1173 K, respectively). During cooling the activity is lost on all samples, likely due to the collapse of the support oxide and subsequent encapsulation of palladium and loss of active sites.

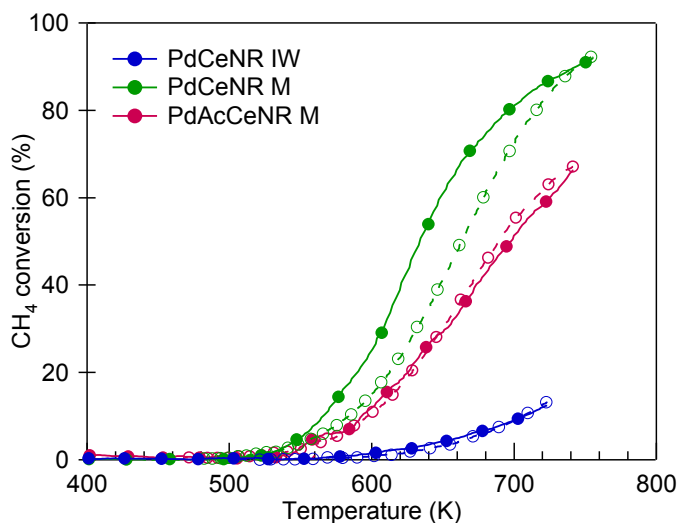


Figure 9.19: Methane oxidation activity of Pd/CeNR samples; light-off cycle to 723 K.

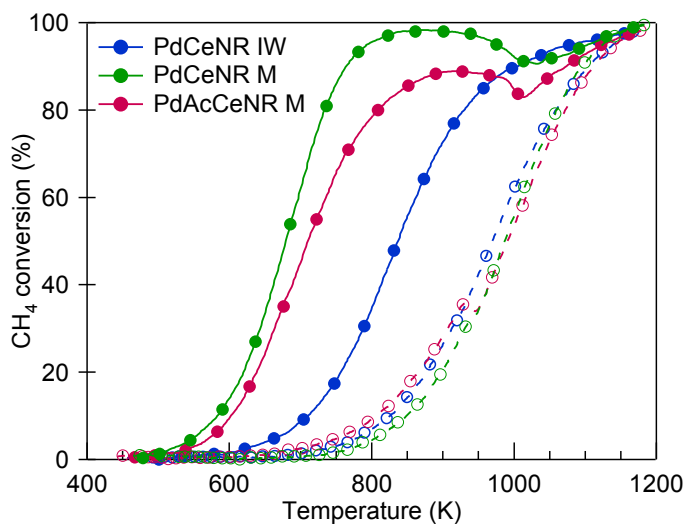


Figure 9.20: Methane oxidation activity of Pd/CeNR samples; light-off cycle to 1173 K.

Likewise, H₂-TPR profiles reported in Figure 9.21 resemble the reduction profiles observed on polycrystalline ceria samples (Figure 9.8), with PdCeNR IW displaying a uniform nanosized PdO dispersion and the milled samples being characterized by larger PdO particles along with Pd-Ce species in close interaction with ceria. Quantitative analysis of consumed hydrogen (Table 9.7) shows negligible differences in the overall H₂ uptake for all considered samples.

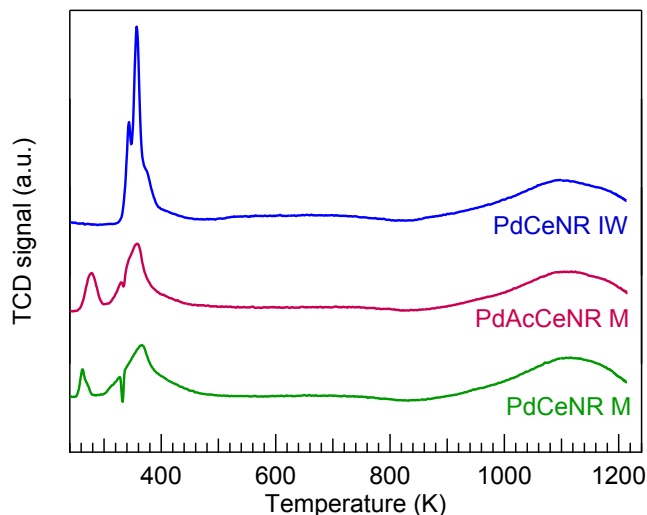


Figure 9.21: H₂-TPR profiles of Pd/CeNR samples. Reduction in H₂ was carried out after pretreatment in air at 623 K for 1 hour.

Table 9.7: H₂ consumption during TPR tests performed on Pd/CeNR samples ($\mu\text{mol H}_2/\text{g}$).

Sample	Peak 1		Peak 2		Theoretical H ₂ uptake for PdO ^b
	T (K) ^a	H ₂ uptake	T (K)	H ₂ uptake	
PdCeNR IW	357	633	1100	579	94
PdCeNR M	367	543	1116	659	94
PdAcCeNR M	358	528	1116	505	94

a: temperature of the main reduction peak. b: H₂ for stoichiometric PdO reduction

9.4 Discussion

Even if the results of this series of experiments are only preliminary and more work is needed, some possible explanations for the outcome of this part of research are discussed in the following.

Overall, the first thing to be highlighted is that the conclusions drawn for Pd supported on polycrystalline ceria cannot be extended straightforwardly to Pd on ceria nanoshapes, irrespective of the synthesis procedure adopted. Comparing the temperatures corresponding to 10% methane conversion measured during light-off experiments (T_{10}), summarized in Table 9.8, two trends can be observed. Regarding the effect of the support oxide, the activity increases following the order CeNC < CeNR < Ce(773), suggesting that surfaces exposing {111} planes are more reactive for assisting Pd mediated C-H activation, as observed in previous works for methane^{45,46} and propane⁵⁴ oxidation. In addition, the properties of the exposed planes affect significantly the efficacy of the dry milling synthesis for Pd deposition. In fact, on polycrystalline ceria and nanorods the sample milled with metallic Pd outperforms its counterpart prepared with palladium acetate, both greatly surpassing the sample prepared by incipient wetness impregnation. Conversely, on ceria nanocubes the traditionally prepared IW sample outperforms the milled samples, following the inverse order PdCeNC M < PdAcCeNC M < PdCeNC IW. In this regard, it is likely that the different electronic structure and surface energy of the low index planes,^{2,6,55} reported in Figure 9.22, influence the spreading mechanism occurring during milling and cause palladium species of a different nature to be supported on CeO₂, coherently with the absence of amorphous layer observed by HRTEM (Figure 9.10, Figure 9.11).

Table 9.8: Summary of the T_{10} (K) measured on supports with different morphologies.

	Ce(773)	CeNC	CeNR
IW	580	740	707
Pd / milled	540	777 ^a	566
PdAc / milled	552	746 ^a	595

a: measured from the 2nd light-off curve, heating to 1173 K.

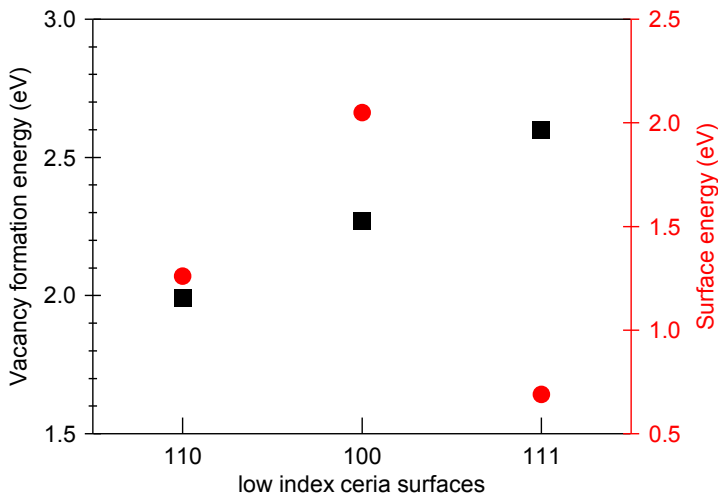


Figure 9.22: Oxygen vacancy formation energy (eV) on low index surfaces of ceria calculated applying DFT+U² and unrelaxed values of surface energies calculated by ab-initio DFT calculations.⁵⁵

According to experimental and theoretical studies, the lower methane oxidation activity observed on nanocubes and nanorods might be due to accumulation of CO₂ species, strongly binding to Pd-O-Ce structures created on the {100} or {110} surfaces and therefore inhibiting CH₄ oxidation,^{56,57} while Pd addition to {111} surfaces was observed to create the highest density of oxygen vacancies,⁴⁶ increasing oxygen mobility and therefore improving catalytic performance. Further experiments on the blank supports (Ce(773), CeNC, CeNR) and *in-situ* spectroscopic characterization of the surface species formed during reaction would be needed to gain further insight on the reaction intermediates and possible inhibition mechanisms.

The negative effect observed on the {100} terminated surfaces for the dry milling of palladium is also quite interesting. Possibly, the dipole generated between O and Ce layers on this facet⁶ results in an electronic configuration that does not allow Pd anchoring and inclusion in the ceria lattice to create an amorphous layer. Additionally, a physical effect could be played by the lower amount of surface defects such as grain boundaries on the nanocubes surface, thus being unable to efficiently promote the atomic interaction during milling. As an experimental evaluation of the interactions occurring during the milling process is rather challenging, perhaps a theoretical approach could be carried out to investigate the possible inhibitions to Pd spreading caused by undercoordinated {100} surfaces.

Another important point involves the correlation between observed palladium redox behavior and catalytic activity, which was proposed in previous chapters (Chapters 3 - 6). On samples based on ceria cubes and rods this correlation is not straightforward. On Ce(773), the sample exhibiting higher methane oxidation activity (PdCe(773)M, Figure 9.4) also displays enhanced Pd-Ce interaction as measured from TPO (Figure 9.7) and TPR (Figure 9.8) experiments. The same correspondence is not observed on samples prepared on ceria with defined morphology. For example on CeNC, the best performing sample (PdCeNC IW, Figure 9.13) exhibits a stronger Pd-Ce interaction based on TPR profiles (Figure 9.16) but TPO analysis in Figure 9.15 suggests a closer interaction on PdAcCeNC M and the presence of sole bulk PdO on PdCeNC IW. These observations are just preliminary, as it is likely that the exposure at high temperature during TPO experiments modifies the Pd-ceria interplay, and the methane oxidation activity has not yet been tested in subsequent light-off cycles up to 1173 K. Nevertheless, it is possible that on these samples other additional factors affect the catalytic activity, not accounted for by bulk TPO and TPR experiments. Other spectroscopic characterization techniques, such as Raman and DRIFTS, could be carried out *in-situ* to investigate further the surface properties of palladium species supported on defined-morphology ceria.⁵⁸

9.5 Conclusions

The effect of undercoordinated ceria surfaces on Pd/CeO₂ interaction and low temperature methane oxidation was studied on samples prepared by dry milling and incipient wetness impregnation on ceria nanocubes, nanorods and polycrystalline nanoparticles. Preliminary results outline two main trends, where {111} surfaces create the best environment for active Pd species for methane oxidation and promote Pd interaction during the milling process. The reasons for the negative effect of {100} and, less evidently, {110} planes is not yet understood, and further characterization techniques such as Raman and DRIFT spectroscopy could be carried out on prepared samples to investigate the Pd-Ce interaction on the surface. Moreover, the controlled aging on nanorods and nanocubes could also provide useful insights in the effect of exposed planes on low temperature methane oxidation performance.

9.6 References

- (1) Trovarelli, A. Catalytic Properties of Ceria and CeO₂-Containing Materials. *Catalysis Reviews* **1996**, *38* (4), 439–520. <https://doi.org/10.1080/01614949608006464>.
- (2) Nolan, M.; Parker, S. C.; Watson, G. W. The Electronic Structure of Oxygen Vacancy Defects at the Low Index Surfaces of Ceria. *Surface Science* **2005**, *595* (1–3), 223–232. <https://doi.org/10.1016/j.susc.2005.08.015>.
- (3) Aneggi, E.; Boaro, M.; Leitenburg, C. de; Dolcetti, G.; Trovarelli, A. Insights into the Redox Properties of Ceria-Based Oxides and Their Implications in Catalysis. *Journal of Alloys and Compounds* **2006**, *408–412*, 1096–1102. <https://doi.org/10.1016/j.jallcom.2004.12.113>.
- (4) Filtschew, A.; Hofmann, K.; Hess, C. Ceria and Its Defect Structure: New Insights from a Combined Spectroscopic Approach. *The Journal of Physical Chemistry C* **2016**, *120* (12), 6694–6703. <https://doi.org/10.1021/acs.jpcc.6b00959>.
- (5) Capdevila-Cortada, M.; Vilé, G.; Teschner, D.; Pérez-Ramírez, J.; López, N. Reactivity Descriptors for Ceria in Catalysis. *Applied Catalysis B: Environmental* **2016**, *197*, 299–312. <https://doi.org/10.1016/j.apcatb.2016.02.035>.
- (6) Trovarelli, A.; Llorca, J. Ceria Catalysts at Nanoscale: How Do Crystal Shapes Shape Catalysis? *ACS Catal.* **2017**, *7* (7), 4716–4735. <https://doi.org/10.1021/acscatal.7b01246>.
- (7) Yang, C.; Yu, X.; Heißler, S.; Nefedov, A.; Colussi, S.; Llorca, J.; Trovarelli, A.; Wang, Y.; Wöll, C. Surface Faceting and Reconstruction of Ceria Nanoparticles. *Angewandte Chemie International Edition* **2017**, *56* (1), 375–379. <https://doi.org/10.1002/anie.201609179>.
- (8) Rodriguez, J. A.; Grinter, D. C.; Liu, Z.; Palomino, R. M.; Senanayake, S. D. Ceria-Based Model Catalysts: Fundamental Studies on the Importance of the Metal–Ceria Interface in CO Oxidation, the Water–Gas Shift, CO₂ Hydrogenation, and Methane and Alcohol Reforming. *Chemical Society Reviews* **2017**, *46* (7), 1824–1841. <https://doi.org/10.1039/C6CS00863A>.
- (9) Trovarelli, A.; Fornasiero, P. *Catalysis By Ceria And Related Materials*, 2nd ed.; Catalytic Science; Imperial College Press: London, United Kingdom, 2013.
- (10) McCabe, R. W.; Trovarelli, A. Forty Years of Catalysis by Ceria: A Success Story. *Applied Catalysis B: Environmental* **2016**, *197*, 1. <https://doi.org/10.1016/j.apcatb.2016.04.044>.
- (11) Montini, T.; Melchionna, M.; Monai, M.; Fornasiero, P. Fundamentals and Catalytic Applications of CeO₂-Based Materials. *Chemical Reviews* **2016**, *116* (10), 5987–6041. <https://doi.org/10.1021/acs.chemrev.5b00603>.
- (12) Monte, R. D.; Kašpar, J. On the Role of Oxygen Storage in Three-Way Catalysis. *Topics in Catalysis* **2004**, *28* (1–4), 47–57. <https://doi.org/10.1023/B:TOCA.0000024333.08447.f7>.
- (13) Xu, W.; Liu, Z.; Johnston-Peck, A. C.; Senanayake, S. D.; Zhou, G.; Stacchiola, D.; Stach, E. A.; Rodriguez, J. A. Steam Reforming of Ethanol on Ni/CeO₂: Reaction Pathway and Interaction between Ni and the CeO₂ Support. *ACS Catalysis* **2013**, *3* (5), 975–984. <https://doi.org/10.1021/cs4000969>.

- (14) Liu, Z.; Grinter, D. C.; Lustemberg, P. G.; Nguyen-Phan, T.-D.; Zhou, Y.; Luo, S.; Waluyo, I.; Crumlin, E. J.; Stacchiola, D. J.; Zhou, J.; et al. Dry Reforming of Methane on a Highly-Active Ni-CeO₂ Catalyst: Effects of Metal-Support Interactions on C–H Bond Breaking. *Angewandte Chemie International Edition* **2016**, *55* (26), 7455–7459. <https://doi.org/10.1002/anie.201602489>.
- (15) Schilling, C.; Hess, C. CO Oxidation on Ceria Supported Gold Catalysts Studied by Combined Operando Raman/UV–Vis and IR Spectroscopy. *Top Catal* **2017**, *60* (1–2), 131–140. <https://doi.org/10.1007/s11244-016-0732-6>.
- (16) Khader, M.; Al-Marri, M.; Ali, S.; Abdelmoneim, A. Active and Stable Methane Oxidation Nano-Catalyst with Highly-Ionized Palladium Species Prepared by Solution Combustion Synthesis. *Catalysts* **2018**, *8* (2), 66. <https://doi.org/10.3390/catal8020066>.
- (17) Si, G.; Yu, J.; Xiao, X.; Guo, X.; Huang, H.; Mao, D.; Lu, G. Boundary Role of Nano-Pd Catalyst Supported on Ceria and the Approach of Promoting the Boundary Effect. *Molecular Catalysis* **2018**, *444*, 1–9. <https://doi.org/10.1016/j.mcat.2017.10.025>.
- (18) Zhang, F.; Liu, Z.; Zhang, S.; Akter, N.; Palomino, R. M.; Vovchok, D.; Orozco, I.; Salazar, D.; Rodriguez, J. A.; Llorca, J.; et al. In Situ Elucidation of the Active State of Co–CeO_x Catalysts in the Dry Reforming of Methane: The Important Role of the Reducible Oxide Support and Interactions with Cobalt. *ACS Catalysis* **2018**, *8* (4), 3550–3560. <https://doi.org/10.1021/acscatal.7b03640>.
- (19) Liu, Z.; Zhang, F.; Rui, N.; Li, X.; Lin, L.; Betancourt, L. E.; Su, D.; Xu, W.; Cen, J.; Attenkofer, K.; et al. Highly Active Ceria-Supported Ru Catalyst for the Dry Reforming of Methane: In Situ Identification of Ru^{δ+}–Ce³⁺ Interactions for Enhanced Conversion. *ACS Catalysis* **2019**, *9* (4), 3349–3359. <https://doi.org/10.1021/acscatal.8b05162>.
- (20) Farmer, J. A.; Campbell, C. T. Ceria Maintains Smaller Metal Catalyst Particles by Strong Metal-Support Bonding. *Science* **2010**, *329* (5994), 933–936. <https://doi.org/10.1126/science.1191778>.
- (21) Jones, J.; Xiong, H.; DeLaRiva, A. T.; Peterson, E. J.; Pham, H.; Challa, S. R.; Qi, G.; Oh, S.; Wiebenga, M. H.; Pereira Hernandez, X. I.; et al. Thermally Stable Single-Atom Platinum-on-Ceria Catalysts via Atom Trapping. *Science* **2016**, *353* (6295), 150–154. <https://doi.org/10.1126/science.aaf8800>.
- (22) Spezzati, G.; Su, Y.; Hofmann, J. P.; Benavidez, A. D.; DeLaRiva, A. T.; McCabe, J.; Datye, A. K.; Hensen, E. J. M. Atomically Dispersed Pd–O Species on CeO₂ (111) as Highly Active Sites for Low-Temperature CO Oxidation. *ACS Catal.* **2017**, *7* (10), 6887–6891. <https://doi.org/10.1021/acscatal.7b02001>.
- (23) Fink, C.; Hagemeyer, A.; Hogan, Z.; Volpe, A.; Yoder, J. High Surface Area Cerium Oxide. *Current Catalysis* **2016**, *5* (3), 182–202. <https://doi.org/10.2174/2211544705666160509161559>.
- (24) Ohtake, N.; Yamane, Y.; Nakagawa, K.; Katoh, M.; Sugiyama, S. Hydrothermally Synthesized Ceria with a High Specific Surface Area for Catalytic Conversion of Ethanol to Ethylene. *Journal of Chemical Engineering of Japan* **2016**, *49* (2), 197–203. <https://doi.org/10.1252/jcej.15we125>.
- (25) Ohtake, N.; Katoh, M.; Sugiyama, S. High Thermal-Stability Ceria Synthesized via Thermal-Hydrolysis Route and Methane-Combustion Performance. *Journal of the Ceramic Society of Japan* **2017**, *125* (2), 57–61. <https://doi.org/10.2109/jcersj2.16255>.

- (26) Kamimura, Y.; Shimomura, M.; Endo, A. Simple Template-Free Synthesis of High Surface Area Mesoporous Ceria and Its New Use as a Potential Adsorbent for Carbon Dioxide Capture. *Journal of Colloid and Interface Science* **2014**, *436*, 52–62. <https://doi.org/10.1016/j.jcis.2014.08.047>.
- (27) Zhan, W.; Yang, S.; Zhang, P.; Guo, Y.; Lu, G.; Chisholm, M. F.; Dai, S. Incorporating Rich Mesoporosity into a Ceria-Based Catalyst via Mechanochemistry. *Chemistry of Materials* **2017**, *29* (17), 7323–7329. <https://doi.org/10.1021/acs.chemmater.7b02206>.
- (28) Huang, P. X.; Wu, F.; Zhu, B. L.; Gao, X. P.; Zhu, H. Y.; Yan, T. Y.; Huang, W. P.; Wu, S. H.; Song, D. Y. CeO₂ Nanorods and Gold Nanocrystals Supported on CeO₂ Nanorods as Catalyst. *J. Phys. Chem. B* **2005**, *109* (41), 19169–19174. <https://doi.org/10.1021/jp052978u>.
- (29) Mai, H.-X.; Sun, L.-D.; Zhang, Y.-W.; Si, R.; Feng, W.; Zhang, H.-P.; Liu, H.-C.; Yan, C.-H. Shape-Selective Synthesis and Oxygen Storage Behavior of Ceria Nanopolyhedra, Nanorods, and Nanocubes. *The Journal of Physical Chemistry B* **2005**, *109* (51), 24380–24385. <https://doi.org/10.1021/jp055584b>.
- (30) Pan, C.; Zhang, D.; Shi, L.; Fang, J. Template-Free Synthesis, Controlled Conversion, and CO Oxidation Properties of CeO₂ Nanorods, Nanotubes, Nanowires, and Nanocubes. *European Journal of Inorganic Chemistry* **2008**, *2008* (15), 2429–2436. <https://doi.org/10.1002/ejic.200800047>.
- (31) Tana; Zhang, M.; Li, J.; Li, H.; Li, Y.; Shen, W. Morphology-Dependent Redox and Catalytic Properties of CeO₂ Nanostructures: Nanowires, Nanorods and Nanoparticles. *Catalysis Today* **2009**, *148* (1–2), 179–183. <https://doi.org/10.1016/j.cattod.2009.02.016>.
- (32) Désaunay, T.; Bonura, G.; Chiodo, V.; Freni, S.; Couzinié, J.-P.; Bourgon, J.; Ringuedé, A.; Labat, F.; Adamo, C.; Cassir, M. Surface-Dependent Oxidation of H₂ on CeO₂ Surfaces. *Journal of Catalysis* **2013**, *297*, 193–201. <https://doi.org/10.1016/j.jcat.2012.10.011>.
- (33) Agarwal, S.; Zhu, X.; Hensen, E. J. M.; Lefferts, L.; Mojet, B. L. Defect Chemistry of Ceria Nanorods. *The Journal of Physical Chemistry C* **2014**, *118* (8), 4131–4142. <https://doi.org/10.1021/jp409989y>.
- (34) Aneggi, E.; Wiater, D.; de Leitenburg, C.; Llorca, J.; Trovarelli, A. Shape-Dependent Activity of Ceria in Soot Combustion. *ACS Catalysis* **2014**, *4* (1), 172–181. <https://doi.org/10.1021/cs400850r>.
- (35) Wu, Z.; Overbury, S. H. *Catalysis by Materials with Well-Defined Structures*; Elsevier, 2015.
- (36) Wu, Q.; Zhang, F.; Xiao, P.; Tao, H.; Wang, X.; Hu, Z.; Lü, Y. Great Influence of Anions for Controllable Synthesis of CeO₂ Nanostructures: From Nanorods to Nanocubes. *J. Phys. Chem. C* **2008**, *112* (44), 17076–17080. <https://doi.org/10.1021/jp804140e>.
- (37) Tinoco, M.; Fernandez-Garcia, S.; Lopez-Haro, M.; Hungria, A. B.; Chen, X.; Blanco, G.; Perez-Omil, J. A.; Collins, S. E.; Okuno, H.; Calvino, J. J. Critical Influence of Nanofaceting on the Preparation and Performance of Supported Gold Catalysts. *ACS Catalysis* **2015**, *5* (6), 3504–3513. <https://doi.org/10.1021/acscatal.5b00086>.
- (38) Sayle, T. X. T.; Parker, S. C.; Catlow, C. R. A. The Role of Oxygen Vacancies on Ceria Surfaces in the Oxidation of Carbon Monoxide. *Surface Science* **1994**, *316* (3), 329–336. [https://doi.org/10.1016/0039-6028\(94\)91225-4](https://doi.org/10.1016/0039-6028(94)91225-4).

- (39) Spezzati, G.; Benavidez, A. D.; DeLaRiva, A. T.; Su, Y.; Hofmann, J. P.; Asahina, S.; Olivier, E. J.; Neethling, J. H.; Miller, J. T.; Datye, A. K.; et al. CO Oxidation by Pd Supported on CeO₂(100) and CeO₂(111) Facets. *Applied Catalysis B: Environmental* **2019**, *243*, 36–46. <https://doi.org/10.1016/j.apcatb.2018.10.015>.
- (40) Piumetti, M.; Bensaid, S.; Russo, N.; Fino, D. Nanostructured Ceria-Based Catalysts for Soot Combustion: Investigations on the Surface Sensitivity. *Applied Catalysis B: Environmental* **2015**, *165*, 742–751. <https://doi.org/10.1016/j.apcatb.2014.10.062>.
- (41) Sartoretti, E.; Novara, C.; Giorgis, F.; Piumetti, M.; Bensaid, S.; Russo, N.; Fino, D. In Situ Raman Analyses of the Soot Oxidation Reaction over Nanostructured Ceria-Based Catalysts. *Scientific Reports* **2019**, *9* (1). <https://doi.org/10.1038/s41598-019-39105-5>.
- (42) Vilé, G.; Bridier, B.; Wichert, J.; Pérez-Ramírez, J. Ceria in Hydrogenation Catalysis: High Selectivity in the Conversion of Alkynes to Olefins. *Angewandte Chemie International Edition* **2012**, *51* (34), 8620–8623. <https://doi.org/10.1002/anie.201203675>.
- (43) Vilé, G.; Colussi, S.; Krumeich, F.; Trovarelli, A.; Pérez-Ramírez, J. Opposite Face Sensitivity of CeO₂ in Hydrogenation and Oxidation Catalysis. *Angewandte Chemie International Edition* **2014**, *53* (45), 12069–12072. <https://doi.org/10.1002/anie.201406637>.
- (44) Zhao, E. W.; Zheng, H.; Zhou, R.; Hagelin-Weaver, H. E.; Bowers, C. R. Shaped Ceria Nanocrystals Catalyze Efficient and Selective Para-Hydrogen-Enhanced Polarization. *Angewandte Chemie International Edition* **2015**, *54* (48), 14270–14275. <https://doi.org/10.1002/anie.201506045>.
- (45) Guo, T.; Du, J.; Li, J. The Effects of Ceria Morphology on the Properties of Pd/Ceria Catalyst for Catalytic Oxidation of Low-Concentration Methane. *J Mater Sci* **2016**, *51* (24), 10917–10925. <https://doi.org/10.1007/s10853-016-0303-z>.
- (46) Lei, Y.; Li, W.; Liu, Q.; Lin, Q.; Zheng, X.; Huang, Q.; Guan, S.; Wang, X.; Wang, C.; Li, F. Typical Crystal Face Effects of Different Morphology Ceria on the Activity of Pd/CeO₂ Catalysts for Lean Methane Combustion. *Fuel* **2018**, *233*, 10–20. <https://doi.org/10.1016/j.fuel.2018.06.035>.
- (47) Chowdhury, S.; Lin, K.-S. Characterization and Surface Reactivity Analyses of Ceria Nanorod Catalyst for Methanol Interaction. *Materials Chemistry and Physics* **2012**, *133* (1), 163–169. <https://doi.org/10.1016/j.matchemphys.2012.01.002>.
- (48) Munnik, P.; de Jongh, P. E.; de Jong, K. P. Recent Developments in the Synthesis of Supported Catalysts. *Chem. Rev.* **2015**, *115* (14), 6687–6718. <https://doi.org/10.1021/cr500486u>.
- (49) Lieske, H.; Voelter, J. Palladium Redispersion by Spreading of Palladium(II) Oxide in Oxygen Treated Palladium/Alumina. *The Journal of Physical Chemistry* **1985**, *89* (10), 1841–1842. <https://doi.org/10.1021/j100256a001>.
- (50) Ferrer, V.; Moronta, A.; Sanchez, J.; Solano, R.; Bernal, S.; Finol, D. Effect of the Reduction Temperature on the Catalytic Activity of Pd-Supported Catalysts. *Catalysis Today* **2005**, *6*.
- (51) Florea, I.; Feral-Martin, C.; Majimel, J.; Ihiawakrim, D.; Hirlimann, C.; Ersen, O. Three-Dimensional Tomographic Analyses of CeO₂ Nanoparticles. *Crystal Growth & Design* **2013**, *13* (3), 1110–1121. <https://doi.org/10.1021/cg301445h>.

- (52) Colussi, S.; Trovarelli, A.; Vesselli, E.; Baraldi, A.; Comelli, G.; Groppi, G.; Llorca, J. Structure and Morphology of Pd/Al₂O₃ and Pd/CeO₂/Al₂O₃ Combustion Catalysts in Pd–PdO Transformation Hysteresis. *Applied Catalysis A: General* **2010**, *390* (1–2), 1–10. <https://doi.org/10.1016/j.apcata.2010.09.033>.
- (53) Liu, X.; Zhou, K.; Wang, L.; Wang, B.; Li, Y. Oxygen Vacancy Clusters Promoting Reducibility and Activity of Ceria Nanorods. *J. Am. Chem. Soc.* **2009**, *131* (9), 3140–3141. <https://doi.org/10.1021/ja808433d>.
- (54) Hu, Z.; Liu, X.; Meng, D.; Guo, Y.; Guo, Y.; Lu, G. Effect of Ceria Crystal Plane on the Physicochemical and Catalytic Properties of Pd/Ceria for CO and Propane Oxidation. *ACS Catalysis* **2016**, *6* (4), 2265–2279. <https://doi.org/10.1021/acscatal.5b02617>.
- (55) Nolan, M.; Grigoleit, S.; Sayle, D. C.; Parker, S. C.; Watson, G. W. Density Functional Theory Studies of the Structure and Electronic Structure of Pure and Defective Low Index Surfaces of Ceria. *Surface Science* **2005**, *576* (1–3), 217–229. <https://doi.org/10.1016/j.susc.2004.12.016>.
- (56) Wu, Z.; Mann, A. K. P.; Li, M.; Overbury, S. H. Spectroscopic Investigation of Surface-Dependent Acid–Base Property of Ceria Nanoshapes. *J. Phys. Chem. C* **2015**, *119* (13), 7340–7350. <https://doi.org/10.1021/acs.jpcc.5b00859>.
- (57) Ma, J.; Lou, Y.; Cai, Y.; Zhao, Z.; Wang, L.; Zhan, W.; Guo, Y.; Guo, Y. The Relationship between the Chemical State of Pd Species and the Catalytic Activity for Methane Combustion on Pd/CeO₂. *Catal. Sci. Technol.* **2018**, *8* (10), 2567–2577. <https://doi.org/10.1039/C8CY00208H>.
- (58) Wu, Z.; Li, M.; Howe, J.; Meyer, H. M.; Overbury, S. H. Probing Defect Sites on CeO₂ Nanocrystals with Well-Defined Surface Planes by Raman Spectroscopy and O₂ Adsorption. *Langmuir* **2010**, *26* (21), 16595–16606. <https://doi.org/10.1021/la101723w>.

10 Concluding Remarks and Future Perspectives

The PhD research work illustrated in this dissertation was focused on the development and optimization of an ecofriendly, solvent free mechano-chemical synthesis of Pd/CeO₂ methane oxidation catalysts. The outstanding results obtained in terms of catalytic activity and stability of the prepared materials prompted a systematic study of these catalysts in order to gain a better understanding of methane activation and deeper insights into the correlation between methane activation and Pd-Ce interaction, specifically at nanoscale level.

In particular, a novel dry milling methodology was developed as a result of this PhD research work, reducing simultaneously solvent, energy and time requirements with respect to the conventional impregnation techniques, enabling the synthesis of Pd-CeO₂ only methane oxidation catalysts among the most active ever reported. The simultaneous improvement of catalytic performance and synthesis process brought to a deposited Italian patent (n.102017000070360 “Catalysts based on Pd/CeO₂ and preparation method thereof”, granted on Sept 30th, 2019), which is now under evaluation for extension. In fact, despite successful applications of mechano-chemistry in the material science field, the lack of detailed comprehension of the forces developed at nanoscale during the milling process has so far hindered an equally successful application in the preparation of supported metal catalysts, where the state-of-the-art is currently represented by wet chemistry based syntheses.

The enhanced catalytic activity of Pd/CeO₂ catalysts prepared by milling was ascribed to their peculiar core/shell morphology, comprised by an amorphous shell containing both palladium and ceria uniformly covering the ceria crystallites. A similar morphology has never been previously reported in the literature for this catalytic system; consequently, the nanoscale arrangement was investigated in depth by a variety of *in-situ* and spectroscopic characterization techniques. The combination of techniques employed allowed the identification of a variety of Pd⁰/Pd²⁺/Pd⁴⁺ species stabilized in close contact with the ceria

lattice and highlighted the role of the palladium species embedded in the outermost ceria layers in the activation of methane and their evolution during reaction.

Comparing the samples prepared by mild mechanical milling, also obtained by varying the palladium precursor, with the ones prepared by the conventional incipient wetness impregnation method, it clearly appears that the presence of Pd⁰ species in a PdO_x mixture is key for enhanced catalytic performance. This was recently reported in the literature by several groups, yet the beneficial effect of metallic Pd was almost always lost upon oxidation in reaction conditions. A high temperature reducing treatment in H₂ or CO was needed in order to recover the necessary Pd⁰ species, which is impractical and economically unfavorable in real life applications. Conversely, the peculiar arrangement created in the amorphous shell appears to simultaneously stabilize metallic and oxidized palladium species, maintaining this active combination throughout subsequent reaction cycles. Possibly, the shell-like configuration enables the presence of highly reactive Pd⁰-Pd²⁺-Pd⁴⁺ sites and a high oxygen mobility promoted by their strong interaction with ceria, thus resulting in outstanding methane oxidation performance and improved resistance to steam deactivation.

The exact role of Pd⁰ and Pd²⁺ species in methane oxidation is yet to be understood, and further spectroscopic analyses might be carried out in order to disclose the reaction mechanism occurring on the Pd-Ce shell. Remarkably, the peculiar nanoscale arrangement and the strong metal-support interaction developed by milling resulted in improved activity also in other methane activation reactions, even under reducing conditions. Nonetheless, the latest results on methane steam and dry reforming and from methane oxidation tests on CeO₂ nanoshapes are only preliminary and demonstrate that further work is needed in order to better elucidate the C-H bond activation mechanisms occurring on the Pd-Ce interface and the effect of the nanoscale environment on the Pd species created and stabilized during milling.

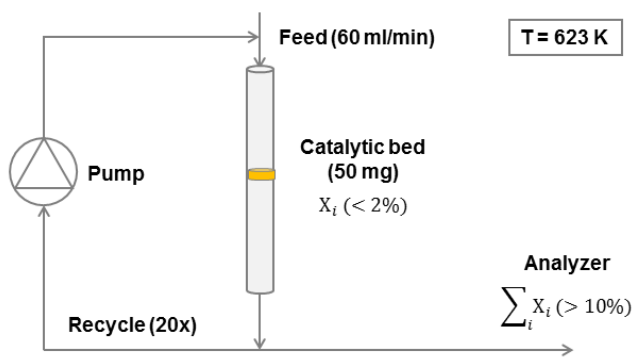
The mechanisms leading to the creation of the amorphous layer are also not yet clear. Potentially, successful applications of mechano-chemistry leading to improved catalytic performance, as the one obtained here for the Pd-CeO₂ system, might promote a focused development of a theoretical model for the mechanical stresses generated by impacts and shear movements of the milling media on the micro- and nanoscale. This would represent a step forward in the development of a comprehensive theoretical background of mechanical

milling forces and, simultaneously, help shed more light on the Pd-Ce-O interactions created during milling. In addition, this would allow for an easier scale up of the milling procedure and facilitate the knowledge transfer to industrial partners, as preliminary applications of the prepared catalysts in industrial bench tests showed that significant steps need to be made to convert a promising lab recipe into a new commercial product.

In that respect, but not limited to three-way-catalyst applications, additional work could be dedicated to further improvement of the Pd/CeO₂ system, for example by analyzing the effect of bi- and multimetallic system deposited by milling over ceria support. The use of palladium salt (instead of metal) as precursor for milling was observed to be extremely promising also if applied on other reducible and non-reducible oxides, namely ZrO₂ and Al₂O₃: therefore the extension of this methodology to the preparation of other Pd-based materials by mechanical processes appears quite favorable. In parallel, and in addition to other methane activation reaction (such as the partial oxidation of methane to methanol or the thermo-catalytic decomposition of methane into highly desired pure hydrogen) the potentiality of the Pd/CeO₂ catalysts prepared by milling is worth investigating in several other reactions, which go from CO and C₃H₆ oxidation to CO₂ hydrogenation, where the interaction of ceria with Pd might play a unique role.

Appendix A: Influence of Mass and Heat Transfer Limitations

To verify the presence of internal and external mass and heat transfer limitations at temperatures below 623 K suitable calculations were carried out on the reaction set-up. As input data, reaction rates were calculated in differential conditions in a recycle reactor¹ at 623 K for the most active samples (PdCeG, PdCeM, PdCeM 1h) considered in Chapters 3-7. A scheme of the recycle reactor set-up is reported in Scheme 1. The calculated reaction rates are summarized in Table 1. For other samples (Chapters 4-6), methane conversion data for reaction rate measurements were extrapolated from the light-off curves at 520 K, 540 K or 623 K, in order to have CH₄ conversion values below 5%. These conditions ensure lower transfer limitations compared to the recycle reactor conditions because of the lower temperatures and conversion values. The hypothesis was verified by performing calculations on the most critical sample, 4PdAcCe(1473)M, due to its high activity and large particle size.



Scheme 1: Recycle reactor.

Table 1: Calculated reaction rates for the most active samples.

Sample	Reaction rate ($\mu\text{mol}/\text{g}_{\text{cat}}\cdot\text{s}$)	Measured Pd loading (wt%) ^a	Reaction rate ($\mu\text{mol}/\text{g}_{\text{Pd}}\cdot\text{s}$)
PdCeG	1.19 ^b	0.8	205
PdCeM	1.66 ^b	0.8	208
PdCeM 1h	1.69 ^b	0.82	206
4PdAcCe(1473)M	0.34 ^c	4.03	8.5

a: Pd loading was measured by ICP elemental analysis. b: Reaction rates are calculated in differential conditions in a recycle reactor at 623 K. c: measured at 520 K in a flow reactor under 5% conversion.

To evaluate the mass and heat transfer limitations, the criteria in equations (eq.1-4) were used.² Given the strong positive dependency on reaction rate and particle size, the calculations are reported in the following for the case most susceptible to mass transfer limitations, i.e. PdCeM and 4PdAcCe(1473)M. The input data are reported in Table 2.

Table 2: Input data for mass and heat transfer limitations calculation.

Parameter		PdCeM	4PdAcCe(1473)M
$-r'_A(\text{obs})$	mol/(g·s)	$1.66 \cdot 10^{-6}$	$3.44 \cdot 10^{-7}$
ρ_b	kg/m ³	2300	2300
ρ_c	kg/m ³	7220	7220
D_p	m	$7 \cdot 10^{-6}$ ^b	$1.52 \cdot 10^{-5}$ ^b
Sh		1.5 ^a	1.5 ^a
$C_{A,b} (\approx C_{A,s})$	mol/m ³	0.0108	0.0129
D_{AB}	m ² /s	$6.1 \cdot 10^{-5}$ ^a	$6.1 \cdot 10^{-5}$ ^a
D_c	m ² /s	$3.8 \cdot 10^{-7}$ ^a	$3.8 \cdot 10^{-7}$ ^a
ΔH_{Rx}	kJ/mol	830	830
E	kJ/kmol	$1.8 \cdot 10^5$	$1.8 \cdot 10^5$
R_g	J/(mol·K)	8.314	8.314
λ_c	J/(m·s·K)	30 ^a	30 ^a
T_s	K	623	520

a: values are assumed based on reference². b: as the tests were carried out in powder form, the pellet size was measured by laser scattering of the catalytic powders in a Horiba LA950 laser scattering particle size analyzer.

External Mass Transfer Limitations

External mass transfer limitations were evaluated by calculating the difference in methane concentration between the gas film surrounding the catalyst particle and the gas bulk. Indeed, for a packed-bed reactor with spherical pellets in steady state conditions the reaction rate can be coupled to the film transport by equation (eq.1)

$$-r'_A = \frac{6 k_c \Delta C_{CH_4}}{\rho_p D_p} \quad (\text{eq.1})$$

where k_c is the mass transfer coefficient ($k_c = Sh D_{AB}/D_p$), Sh is the Sherwood number, D_{AB} is the binary gas diffusivity, ρ_p is the pellet density and D_p is the pellet diameter.

Re-arranging the terms and introducing the observed rate, the film concentration difference can be written as (eq.2):

$$\Delta C_{CH_4} = \frac{-r'_A(obs)\rho_p D_p^2}{6ShD_{AB}} \quad (eq.2)$$

Assuming data values as reported in Table , the resulting concentration difference in the film is equal to $\Delta C_{CH_4} = 1.7 \cdot 10^{-10}$ mol/m³ for the recycle reactor and $1.56 \cdot 10^{-9}$ mol/m³ for the flow reactor, which is negligible compared to the bulk methane concentration ($C_{A,b} = 0.0108$ mol/m³ and 0.0129 mol/m³ at 623 K and 520 K, respectively). It can be therefore assumed that no external resistance to mass transport is present.

Internal Mass Transfer Limitations

Concerning the internal mass transfer limitations, the Weisz-Prater method^{2,3} was applied (eq.3):

$$C_{WP} = \frac{-r'_A(obs)\rho_c R^2}{D_e C_{As}} = \begin{cases} \ll 1 & \text{no mass transfer limitations} \\ \gg 1 & \text{severe mass transfer limitations} \end{cases} \quad (eq.3)$$

where R is the pellet radius ($D_p/2$), ρ_c is the bulk density of the catalytic material, D_e is the effective diffusivity and C_{As} is the methane concentration at the pellet surface (assumed equal to $C_{A,b}$ due to the previous calculations).

Substituting the values of Table , the C_{WP} results equal to $3.59 \cdot 10^{-3}$ for PdCeM and $2.93 \cdot 10^{-3}$ for 4PdAcCe(1473)M, which is indeed $\ll 1$. Consequently, no internal mass transfer limitations are present.

Heat Transfer Limitations

To investigate the heat transfer limitations the Anderson criterion was used (eq.4). If satisfied, it implies that the reaction rate does not differ more than 5% of the rate at constant temperature, i.e. that the heat transfer limitations are negligible.

$$\frac{|\Delta H_{Rx}|(-r'_A)\rho_c R^2}{\lambda_e T_s} < 0.75 \frac{R_g T_s}{E} \quad (eq.4)$$

In the equation above, ΔH_{Rx} is the heat of reaction, λ_e is the effective thermal conductivity, T_s is the particle surface temperature, R_g is the gas constant and E is the activation energy.

Using reasonable values for the parameters, reported in Table 2, on both samples a left term equal to $6.5 \cdot 10^{-9}$ is calculated, while the right term is equal to 0.02. The criterion is thus satisfied.

References

- (1) Colussi, S.; Gayen, A.; Llorca, J.; de Leitenburg, C.; Dolcetti, G.; Trovarelli, A. Catalytic Performance of Solution Combustion Synthesized Alumina- and Ceria-Supported Pt and Pd Nanoparticles for the Combustion of Propane and Dimethyl Ether (DME). *Industrial & Engineering Chemistry Research* **2012**, *51* (22), 7510–7517. <https://doi.org/10.1021/ie2016625>.
- (2) Nilsson, J.; Carlsson, P.-A.; Martin, N. M.; Adams, E. C.; Agostini, G.; Grönbeck, H.; Skoglundh, M. Methane Oxidation over Pd/Al₂O₃ under Rich/Lean Cycling Followed by Operando XAFS and Modulation Excitation Spectroscopy. *Journal of Catalysis* **2017**, *356*, 237–245. <https://doi.org/10.1016/j.jcat.2017.10.018>.
- (3) Fogler, H. S. *Elements of Chemical Reaction Engineering*; Third edition. Upper Saddle River, N.J. : Prentice Hall PTR, 1999.